A Thesis entitled

Optical and Structural Characterisation of InP based Quantum wells and dots

by

Caroline Bryan

submitted for the

Degree of Doctor of Philosophy

of the

University of London

Imperial College of Science, Technology and Medicine

London

1999

To my parents

Abstract

InP based semiconductors which operate at the technologically important wavelengths of 1.3 and 1.55μm have been investigated. Optical analysis of these samples has been performed using photoluminescence (PL) and transmission experiments along with complementary structural methods including x-ray diffraction (XRD) and atomic force microscopy (AFM).

Carrier motion is confined in one dimension and three dimensions for quantum wells (QWs) and quantum dots (QDs) respectively and this significantly alters their electronic properties compared with bulk material. These properties are also strongly dependent on the composition and size/shape of the well or dot. Usually QWs are assumed to have abrupt interfaces, however, there is evidence that group V atoms exchange at the interface in certain material combinations ($In_xGa_{1-x}As/InP$) and this leads to graded interfaces. The extent of the grading at the interface has been deduced by x-ray diffraction measurements in conjunction with optical measurements and the transfer matrix model. Barrier materials such as InGaAsP reduce the effects of the P-As exchange.

For $InAs_xP_{1-x}/InP$ QWs, controlled intermixing at the interfaces can be used to alter the bandgap while retaining strong excitonic features. The ability to continuously vary the effective bandgap is crucial to the integration of optical devices and the variety of potential device applications. After a series of annealing experiments on SiO_2 and Si_3N_4 capped samples, a significant blue shift (~200meV) of the emission peak was observed but strong excitonic effects were retained. The P-As interdiffusion was accurately modelled assuming that the diffusion obeyed Fick's Law to determine the diffusion coefficient.

The work on phosphorus containing QWs has been extended to include preliminary study of self-assembled InAsP/InP quantum dots which should exhibit superior electronic and optical properties. InAs dots are grown by depositing a critical amount of InAs on InP at 600°C. The composition of these dots is not pure InAs and the existence of a wetting layer is revealed in PL measurements.

Contents

List of Figures

1. Chapter 1 - Introduction

Using light rather than an electric current to carry information has revolutionised long-distance communications and data transmission networks as more information can be collected and transmitted at any one time. Photonic telecommunication systems employ semiconductor optoelectronic devices (e.g. lasers and detectors to transmit and receive information) and silica optical fibre waveguides in which the information signal is carried [1]. The increasing demand for higher data rate systems for global telecommunications and the ever expanding internet has pushed technology towards improving existing components and developing new ones to improve the speed and efficiency of transmission.

This thesis focuses on InP semiconductors which operate at the technologically important wavelengths of 1.3 and 1.55μm, corresponding to zero-dispersion and lowest attenuation respectively in a silica optical fibre. Work has been carried out on P-based quantum wells [2D] which are currently used as the active medium in devices. Quantum dots have created a new wave of interest due to their reduced dimensionality which is attractive for laser devices. The benefits of these 0D structures are described in section 1.4.

1.1 Optical Properties of III-V semiconductors

A crystalline solid consists of an array of atoms arranged in a pattern which is periodic in three dimensions, so that along any axis within the crystal the potential energy will vary in a periodic manner. In a semiconductor, the interaction of the atomic energy levels between each atom in the array creates bands of allowed electronic states in which two adjacent bands are separated by a forbidden band (energy gap) where there are no energy

states. For semiconductors of interest, the forbidden energy gap is in the region of 1eV so only a few electrons can be excited from the highest occupied band (valence band) across the energy gap into the next allowed band which is largely empty (conduction band) at room temperature (~300K) [2].

For an electron to be promoted from the valence band (VB) to the conduction band (CB), it must acquire sufficient energy (from a light source or voltage) greater or equal to the bandgap. In a crystal, the motion of electrons in the CB and holes in the VB approximates to free electron motion but is modified by the periodic ionic potential of the crystal. This has the effect of imparting an effective mass to the electron, m*. The relationship between the energy of an electron and its momentum near the bandedge (Eq 1-1) is given from solutions of the Schrödinger equation, $-\left(\frac{\hbar^2}{2m^*}\nabla^2\right)\psi = E\psi$, where it is assumed that the potential inside the crystal is zero. The kinetic energy of the electron is now,

$$E(k) = \frac{\hbar^2 k^2}{2m^*} \qquad \text{Eq 1-1}$$

where k is the electron wavevector and $\hbar$ is Planck's constant. A plot of the energy E(k) versus k (parabolic relationship) for a free electron is shown in figure 1.1. The allowed states form a continuum of states, as a function of k, either side of the forbidden gap.

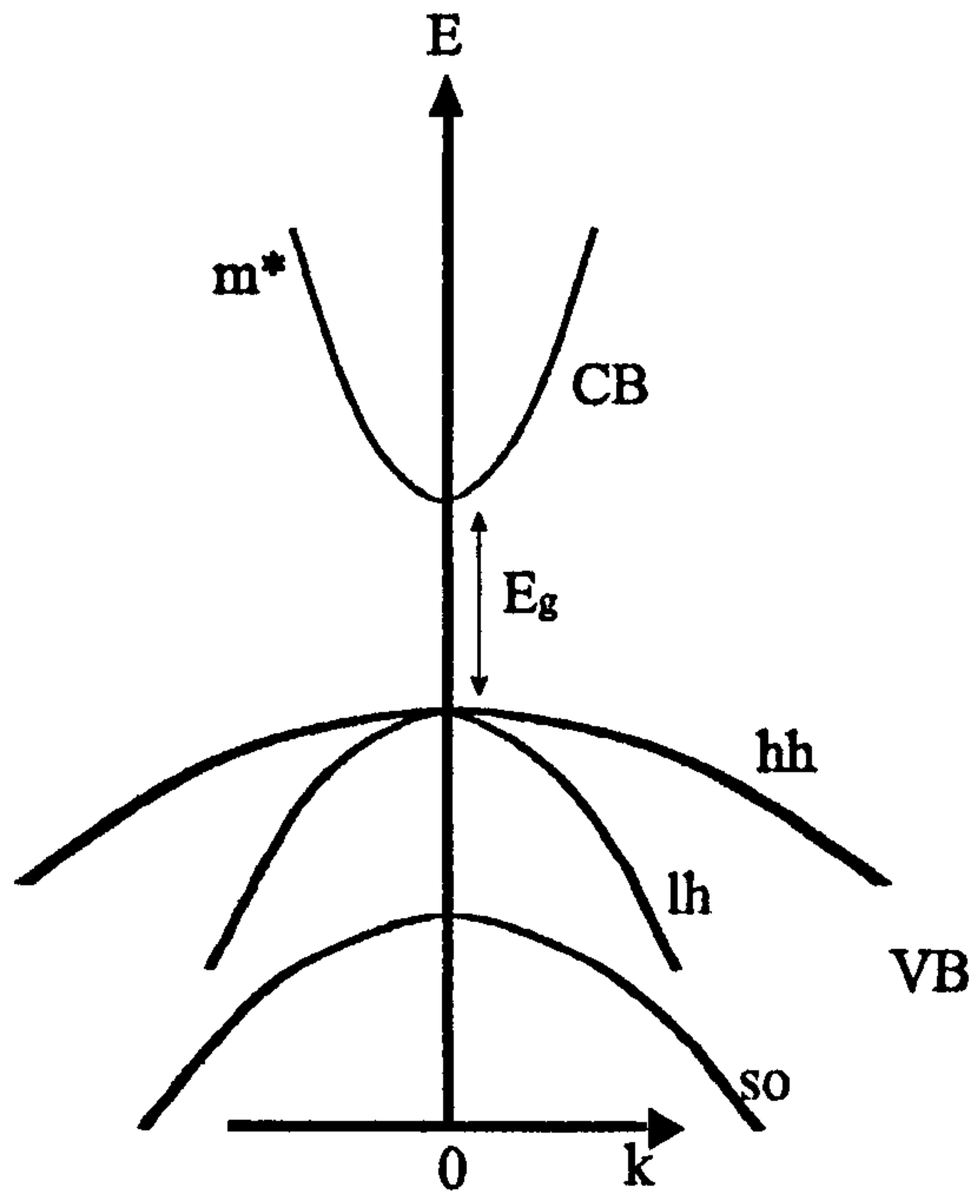

Figure 1-1 *III-V semiconductor band structure (direct) schematic illustrating the CB, hh, lh, split-off (so) band and the energy gap, E_g. The CB is represented by the effective mass (m*) which has been influenced by the periodic potential of the crystal.*

One of the most important parameters is the effective mass (m^*) which is strongly connected to the carrier mobility and therefore transport properties of electrons and holes [3]. The effective masses are proportional to the inverse of the energy / momentum dispersion relationship of the band and near the bandedge,

$$m^* = \frac{\hbar^2}{\left(\frac{d^2E}{dk^2}\right)} \qquad \text{Eq 1-2}$$

This equation shows that the m^* for electrons at any point in a band depends on the curvature of the dispersion curve E(k). Any deviation of the dispersion curve E_k, at the band minima or maxima from the free electron function can be accounted for by choosing the relevant value of m* (Figure 1-1) [4]. For electrons, the value of m^* can be extracted

experimentally from the Shubnikov-de-Haas effect or cyclotron resonance experiments but the valence band masses must be calculated from band theory [5].

In direct gap semiconductors with band edges at the centre of the Brillouin zone, the conduction band is constructed from s-like atomic orbitals. The valence band is constructed from a linear combination of p-like atomic orbitals. At k=0, there are two degenerate hole bands which are described by the Kane model, where the angular momentum for the valence band is J=$\frac{3}{2}$ (doubly degenerate $m_J=\pm\frac{3}{2}$ and $\pm\frac{1}{2}$ for the heavy and light hole respectively) [4,6]. However, the bands are not degenerate for higher momentum values, since the effective masses are quite different. The heavy hole band is 'flatter' and therefore has a large effective mass (m^*_{hh}), while the light hole band has a larger curvature and hence a smaller effective mass (m^*_{lh}) (Figure 1-1). The spin-split off band results from the effects of the spin-orbit coupling where J=$\frac{1}{2}$

1.1.1 The effects of confinement on bulk semiconductor materials

The simplest and the first type of solid state opto-electronic component was the bulk GaAs p-n junction [7]. If a forward bias is applied across the junction a current will pass through it. The homojunction structure was soon superseded by a GaAs/AlGaAs double heterostructure (DH) which introduced a degree of spatial confinement to the carriers arising from the difference in bandgap energy [8].

A potential well is formed in the direction of the growth (z) for both electrons and holes in the material with the smaller bandgap and this configuration of band offsets [9] is known as type I DH (Figure 1-2). If the well width is of the order of 20nm, the particle motion is constrained to discrete energy levels in the direction normal to the plane of the

layer. Motion of carriers in the plane of the layer still retains the character of bulk material. Assuming an infinitely deep well, the energy levels E_e and E_{hh}, can be calculated by solving the Schrödinger equation with the appropriate effective mass for electrons and holes,

$$E_n = \frac{\hbar^2}{2m^*}\left(\frac{n\pi}{L}\right)^2 \qquad \text{Eq 1-3}$$

The free particle energy levels are inversely dependent on $m_{e,hh}$ and the square of the well width L^2. Carrier envelope wavefunctions ψ_e , ψ_{hh} are sinusoidal (sine-like and cosine-like) in nature inside the well and exponentially decreasing into the barrier for a finite barrier height [10]. The presence of m* in the denominator means that the hh and lh bands are no longer degenerate at the band edge in a QW.

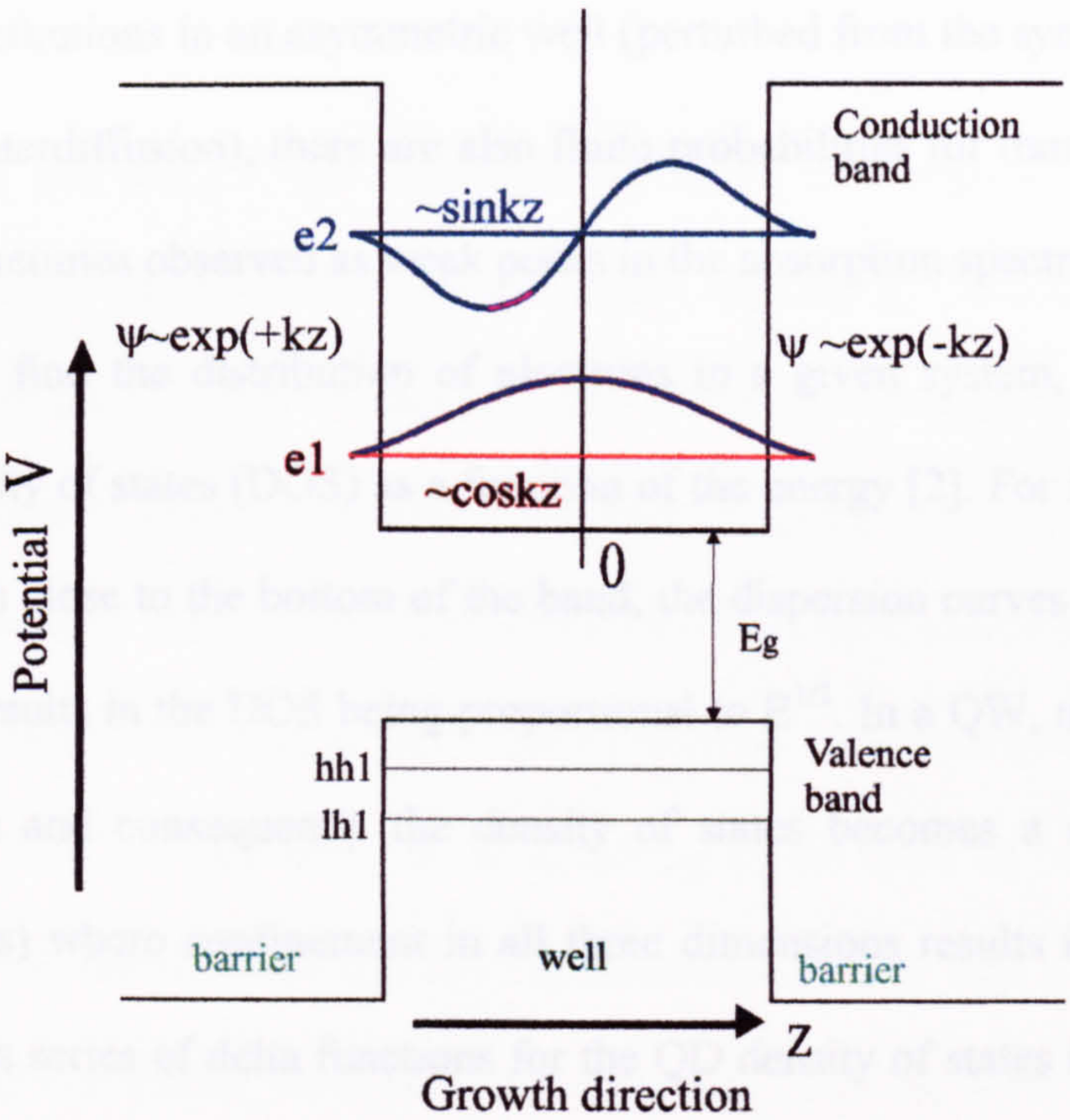

Figure 1-2 *Confined wavefunctions and energy states for the conduction band of a QW.*

The selection rules for optical transitions in QWs are governed by Fermi's Golden rule which depends on the overlap integral of the electron and hole envelope wavefunctions. The Golden rule provides a link between electronic structure of solids (i.e. the wave functions and energies) and the transition probabilities and energies [4]. The probability that an optical transition takes place depends on the form of the wavefunctions of the initial and final quantum states. In the infinite-well approximation [8], due to the orthogonality of the envelope function, only transitions between confined valence and conduction states with the same quantum number n are allowed ($\Delta n=0$ rule) such as e1-hh1 and e2-hh2. These transitions are the strongest observed features in the absorption and excitation spectra. However, due to the penetration of the wavefunctions into the barrier of a finite well or the

asymmetry of wavefuntions in an asymmetric well (perturbed from the symmetric well shape by, for example, interdiffusion), there are also finite probabilities for transitions such as e2-hh1, which are sometimes observed as weak peaks in the absorption spectrum.

In order to find the distribution of electrons in a given system, it is necessary to determine the density of states (DOS) as a function of the energy [2]. For free carrier motion in three dimensions close to the bottom of the band, the dispersion curves are approximately parabolic, which results in the DOS being proportional to $E^{1/2}$. In a QW, motion is restricted to two dimensions and consequently the density of states becomes a series of steps. In quantum dots (QDs) where confinement in all three dimensions results in discrete atomic-like energy levels, a series of delta functions for the QD density of states is found (Figure 1-3).

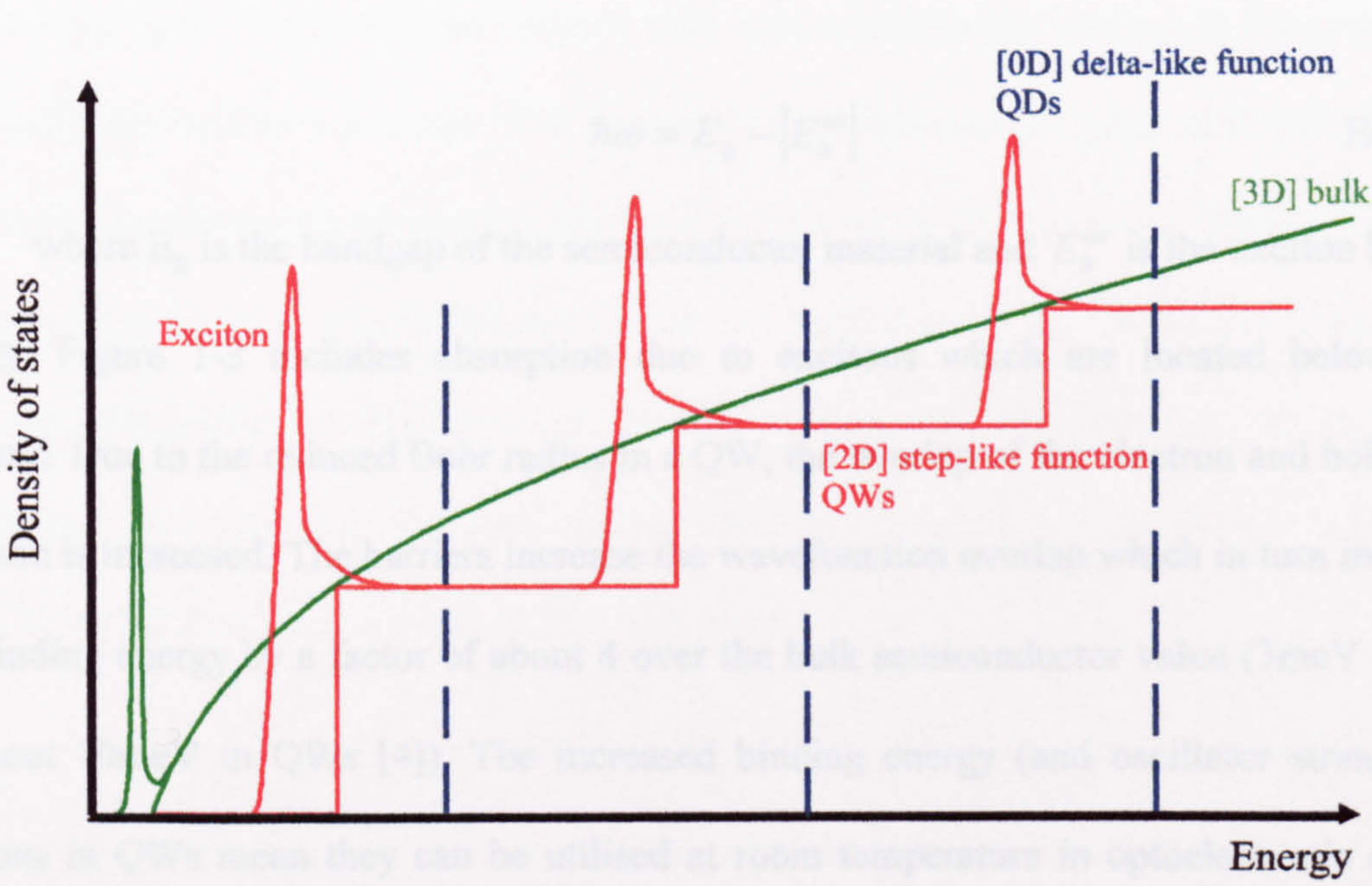

Figure1-3 *Density of states as a function of energy for bulk, QW and QDs*

1.1.2 Excitons

The optical properties of a semiconductor near the band edge in QWs are dominated by excitons [11]. These are electron-hole pairs bound together by Coulombic attraction [12]. The first process in the creation of excitons is to excite electrons from the VB in the CB. This can be achieved by optically pumping the material using a laser with a photon energy greater than the bandgap. The excited electrons which have been elevated to the CB relax to the bottom of the band, disposing of any excess energy in collisions with lattice vibrational waves (phonons). This is a very fast process occurring on the order of picoseconds. Once at the bottom of the CB, the electrons can form an electron-hole pair with a corresponding hole in the VB bound by Coulombic attraction. The exciton in QWs has a lifetime of the order of a few hundred picoseconds and on collasping the electron emits a photon of energy and returns to the VB by recombining with a hole. The energy of the emitted photon,

$$\hbar\omega = E_g - \left|E_b^{ex}\right| \qquad \text{Eq 1-4}$$

where E_g is the bandgap of the semiconductor material and E_b^{ex} is the exciton binding energy. Figure 1-3 includes absorption due to excitons which are located below each subband. Due to the reduced Bohr radius in a QW, the overlap of the electron and hole wave function is increased. The barriers increase the wavefunction overlap which in turn increases the binding energy by a factor of about 4 over the bulk semiconductor value (3meV in bulk to about 10meV in QWs [4]). The increased binding energy (and oscillator strength) of excitons in QWs mean they can be utilised at room temperature in optoelectronic devices [13] However, due to the increased penetration of the carrier wavefunctions into the barriers in QWs of width less than 30Å, the binding energy for very narrow wells is expected to

decrease with further decreasing well width. The exciton binding energy also depends on composition as well as well width.

1.1.3 Photoluminescence Spectroscopy

Photoluminescence spectroscopy is concerned with the light emitted by a crystal after optical excitation and hence can be used for investigating both intrinsic and extrinsic (impurities and defects) radiative recombination of electron-hole pairs in high purity bulk material at low temperatures and low dimensional structures such as QWs and QDs [14] up to room temperature. In PL, the excitation wavelength remains constant whilst the luminescence emitted from the sample is monitored over a range of energies. A laser of suitable energy is usually used as the excitation source and the luminescence is conventionally collected from the surface upon which the excitation light is incident [12,15]. The emitted light is collected and focused onto a monochromator where it is then dispersed and finally directed to a detector. The energy of the luminescence peak in a QW can give information on the well composition, potential shape and width. Analysing the luminescence spectrum as a function of excitation intensity or excitation energy or sample temperature leads to information on the material quality (Figure 1-4). By varying the excitation wavelength, the penetration depth of the light into the structure can be altered so different layers in the structure can to some extent be probed.

At low temperatures, rapid thermalisation of the photogenerated carriers means that only transitions between the ground state and first excited state (e1-hh1) can be observed. Rapid thermalisation of the carriers also occurs at ~300K but at this temperature carriers can have enough energy to occupy the lh band as well as the hh band. The lh band is sometimes

observed as a weak shoulder on the high energy side of the e1-hh1 peak. In pure (undoped) materials, the intrinsic transitions consist of band to band or free exciton recombination. However, even with sophisticated growth techniques such as MBE or MOVPE, impurities such as carbon are unavoidably present leading to extrinsic transitions. There are several different types of extrinsic emission; bound exciton recombination, free to bound recombination etc. As a result, at low temperatures and low excitation levels, transitions involving bound excitons are frequently observed in the emission spectrum.

Excitons can become trapped by an impurity (donor or acceptor), creating a bound exciton. When these complexes recombine, they will emit at a lower energy than the intrinsic exciton emission by an amount corresponding to the binding energy of the exciton to the impurity [16].

Free to bound recombination can take place between free carriers (electrons and holes) and carriers trapped at impurity atoms (donors and acceptors). For example, in GaAs at low temperatures, carbon is a neutral acceptor (C^o) which binds a hole with an energy of ~30meV [4]. Free electrons in the conduction band can recombine with the hole giving rise to free to bound extrinsic emission.

To distinguish between extrinsic (bound excitons) and intrinsic (free excitons) emission, two methods are commonly employed; 1) increasing the sample temperature. 2) increasing excitation power. Increasing the temperature to 30K is usually sufficient to cause de-trapping of the bound excitons as they are very weakly bound to the impurity. Increasing the temperature to 70K in GaAs or InP material results in the ionisation of donors and acceptors and only free excitonic emission (intrinsic) is detected. Increasing the excitation

power causes the intrinsic emission to dominate over the extrinsic emission (saturates the impurity level) and the two processes can be distinguished.

The linewidth and lineshape of the PL emission peak also gives a good indication of the quality of the sample [17]. A narrow linewidth indicates a good quality sample but fluctuations in well width, composition, well to well fluctuations in MQWs and strain inhomogeneity in strained QWs can produce considerable broadening of the PL peak. These broadening mechanisms can be accounted for by a Gaussian linewidth [18]. It should be noted that only radiative processes can be examined by PL. Non-radiative recombination processes where the electron and hole recombine but do not emit a photon can be studied by investigating the quantum efficiency [11].

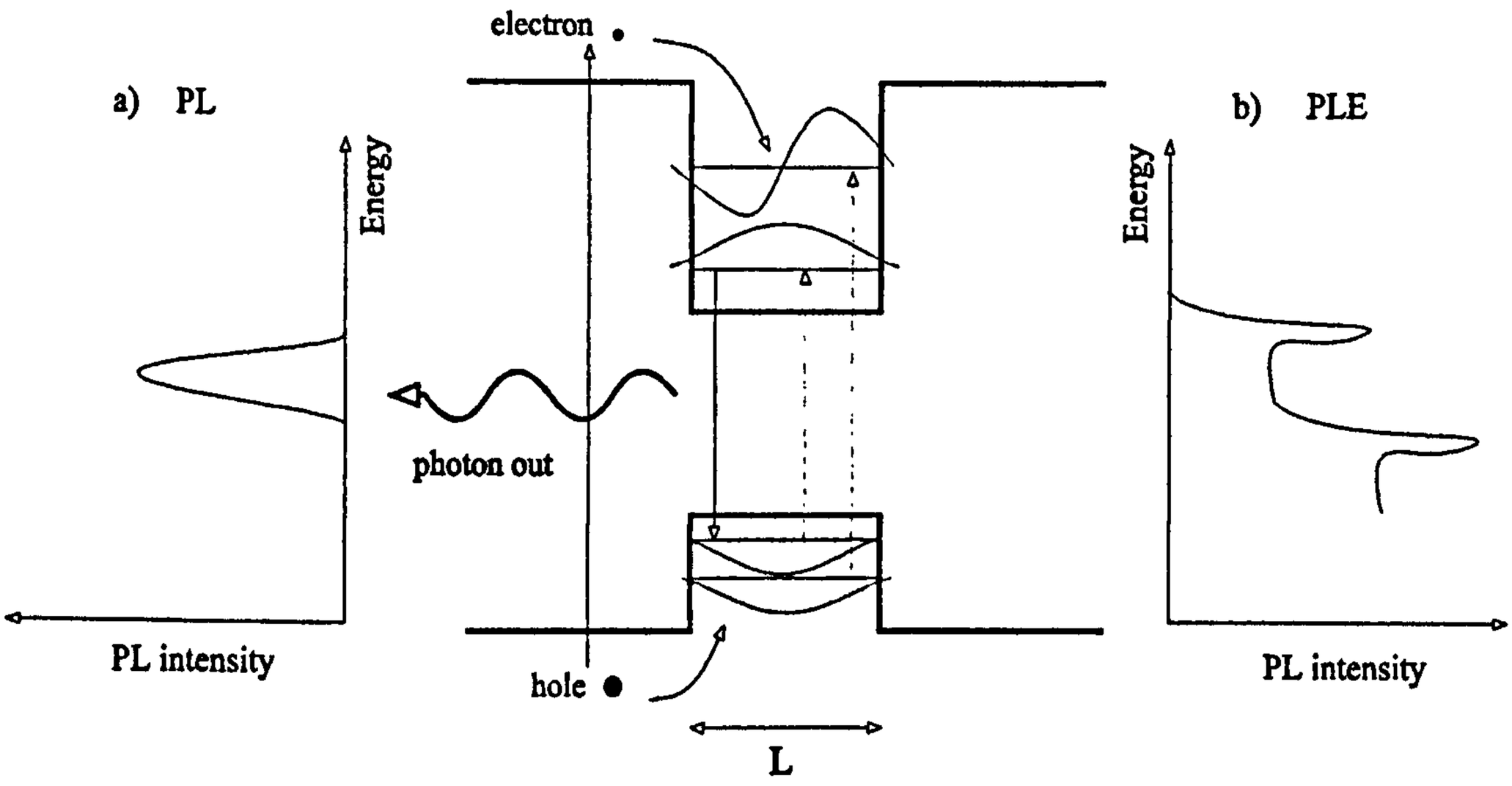

Figure 1-4 *Excitation of an electron from the valence band to the conduction band in a quantum well giving rise to a) an emission spectrum (PL) and b) an excitation spectra (PLE/absorption).*

1.1.4 Absorption / Photoluminescence Excitation (PLE)

Optical absorption is an addition of all the transitions from the ground state to the excited states. The ability of a material to absorb light of a given wavelength (λ) is measured by the absorption coefficient (α). The absorption is calculated (Beer Lambert Law) [19] from the change in intensity of the transmitted light at different wavelengths (ignoring multiple reflections),

$$T = T_0 e^{-\alpha d} \qquad \text{Eq 1-5}$$

where T is the transmitted light, d is the total QW thickness and α the absorption coefficient which is proportional to the number of absorbing centres.

However, for structures containing only a few QWs the change in transmission can be very small and an alternative technique, photoluminescence excitation (PLE) is often used. In PLE measurements, the excitation energy is scanned over a range of energies using a tunable laser source (or a white light source and monochromator), whilst monitoring the intensity of the photoluminescence emission from the sample at a fixed energy. Resonant excitation will occur when the photon energy corresponds to that of the free exciton transitions, e1-hh1, e1-lh1, e2-hh2 i.e. the variation in emission intensity with excitation energy will follow the DOS including exciton effects (Figure 1-4). Provided the relaxation of carriers to the ground state is fast compared with the radiative recombination times, PLE measurements yield the same information as an absorption spectrum.

Free excitons (and/or free electrons and holes depending on the photon energy) are created by the absorption of a photon but recombination can involve bound excitons.

Consequently, the energy of the e1-hh1 exciton peak in PLE is almost always located a few meV higher in energy with respect to the exciton PL peak. The energy difference between this emission and absorption peak is called the Stokes' shift [20] and is usually taken to be an indication of the material quality. A large Stokes shift suggests either well width and/or composition fluctuations. Alternatively, impurities which trap excitons may also be present in the sample. The Stokes shift may not only relate to impurity effects but could arise even in pure samples where an interface shows monolayer ML steps with lateral scale slightly smaller than the exciton diameter [21].

1.2 Growth of Phosphide Semiconductors

Epitaxy is concerned with the growth of high quality crystalline materials on prepared substrates. If the grown layer is different from the substrate, the technique is referred to as heteroepitaxy which distinguishes it from homoepitaxy, the growth of a crystal on itself. All stages of the growth process take place at the surface of the substrate or the growing epilayer. The aim is to grow high quality crystals with atomically abrupt interfaces which can be used in semiconductor devices.

There are two types of growth mechanism for growing semiconductors; one is the deposition from the vapour phase by molecular beam epitaxy (MBE) and the other is chemical vapour deposition (CVD). Several variants have arisen from the above techniques, such as chemical beam epitaxy (CBE), metalorganic molecular beam epitaxy (MOMBE) and metal organic chemical vapour deposition (MOCVD).

The three main growth modes are a) monolayer growth, b) nucleated growth and c) nucleation following monolayer formation known as Stranski-Krastanov growth [22]. Monolayer growth takes place when the atoms deposited on the substrate are bound more strongly to the substrate than each other, forming flat 2D islands. As more atoms are deposited, these islands will increase in size resulting in a complete coverage of the substrate. Nucleated growth occurs when the deposited atoms are more strongly bound to each other than the substrate. Small 3D islands grow which increase in size with increasing deposition until they coalesce to form larger islands. The Stranski-Krastanov growth mode combines aspects of 2D and 3D growth and is thought to be responsible for the growth of self-assembled quantum dots. One or more MLs of atoms form a wetting layer on the substrate followed by nucleation of 3D islands on top. A critical thickness of deposition layer determines the formation of dots. A more detailed account is given in chapter 5.

All samples studied in this thesis were grown by the MOCVD crystal growth method as they contain phosphides which are pyromorphic at very high temperatures. A brief overview of the MOCVD [24] growth processes is given here.

MOCVD is a process in which organo-metallic gaseous compounds such as trimethylgallium, trimethylindium and group V hydrides react on the substrate surface leading to the formation of thin films. In the growth process when switching from barrier to well and vice versa, the flow rate is altered in order to maintain the correct ratio of gases. The growth rate is typically 1.5μm/hour. High group V/III ratios are critical in eliminating carbon from the group V lattice sites within the epilayer. The by-products (unreacted source gases and hydrocarbons) are directed away from the deposition region towards the reactor exit by the carrier gas (Figure 1-5).

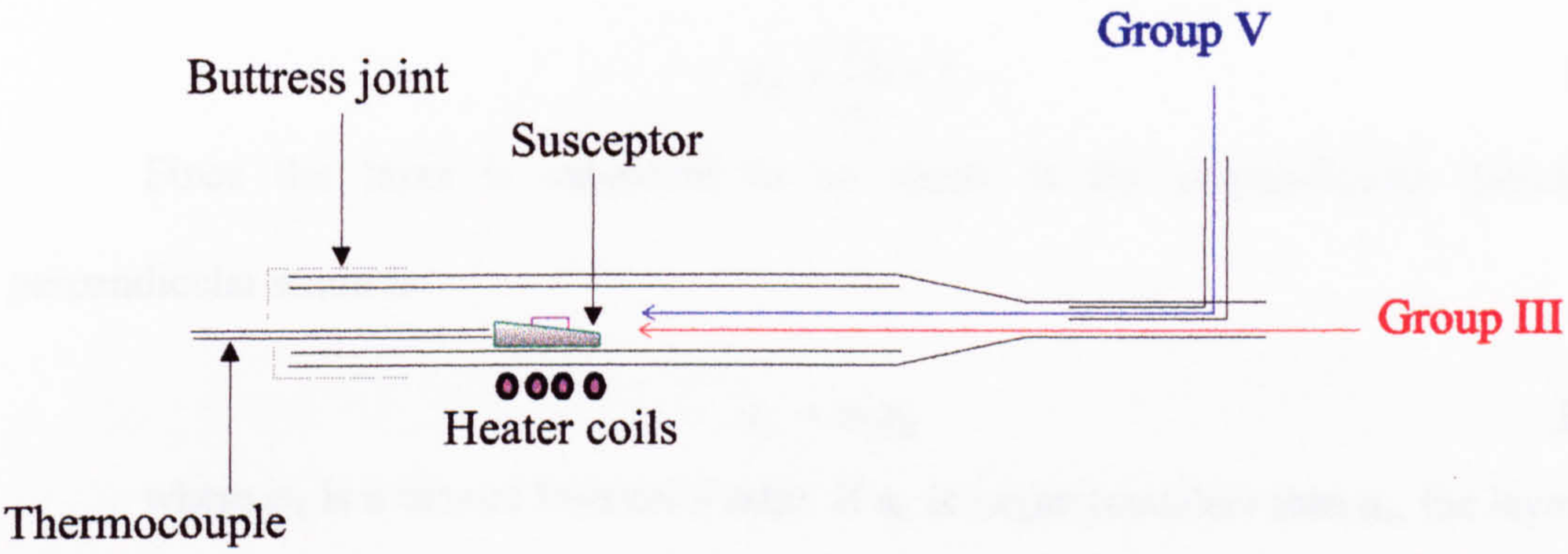

Figure 1-5 *Schematic of an MOCVD reactor.*

1.2.1 The effect of strain on the band structure

In order to study the effects of strain on the electronic properties of semiconductors the strain tensor produced by epitaxy must be established. During epitaxial growth if the strain is incorporated only in the layer (well), the lattice constant of the layer in the direction parallel to the interface is forced to be equal to the lattice constant of the substrate (barrier) and the layer is biaxially strained by an amount ε_{ll}. The lattice constant of the layer in a direction perpendicular to the substrate will also be subject to change because of Poisson's ratio which implies a uniaxial strain of $\varepsilon_{\perp}$. The in-plane lattice constant of the film takes on the lattice constant of the substrate, while the out-of-plane film lattice constant is distorted. Terms such as pseudomorphic or coherent growth are often used to describe the above situation since interfacial coherence is maintained.

For a thick substrate, the in-plane (biaxial) strain of the layer is determined from the bulk lattice constants of the substrate material, a_S and the layer material a_L

$$\varepsilon_{//} = \frac{a_S}{a_L} - 1 \qquad \text{Eq 1-6}$$

Since the layer is subjected to no stress in the perpendicular direction, the perpendicular strain is:

$$\varepsilon_{\perp} = \sigma_2 \varepsilon_{//} \qquad \text{Eq 1-7}$$

where σ_2 is a biaxial Poisson's ratio. If a_L is larger (smaller) than a_s, the layer will be under compressive (tensile) stress. The biaxial strain also induces a shift in the bandgap (ΔE_g) (Eq 1-8). Compressive strain causes an increase in the energy separation between the highest heavy and light hole subbands. The bandgap also increases and the perpendicular lattice constant expands (Figure 1-6 a)). Tensile strain has the opposite effect and leads to a reduction in the splitting of the heavy and light hole states and in some cases causes the hh1 and lh1 positions to swap over. The bandgap decreases in energy and the perpendicular lattice constant contracts (Figure 1-6 b)) [6].

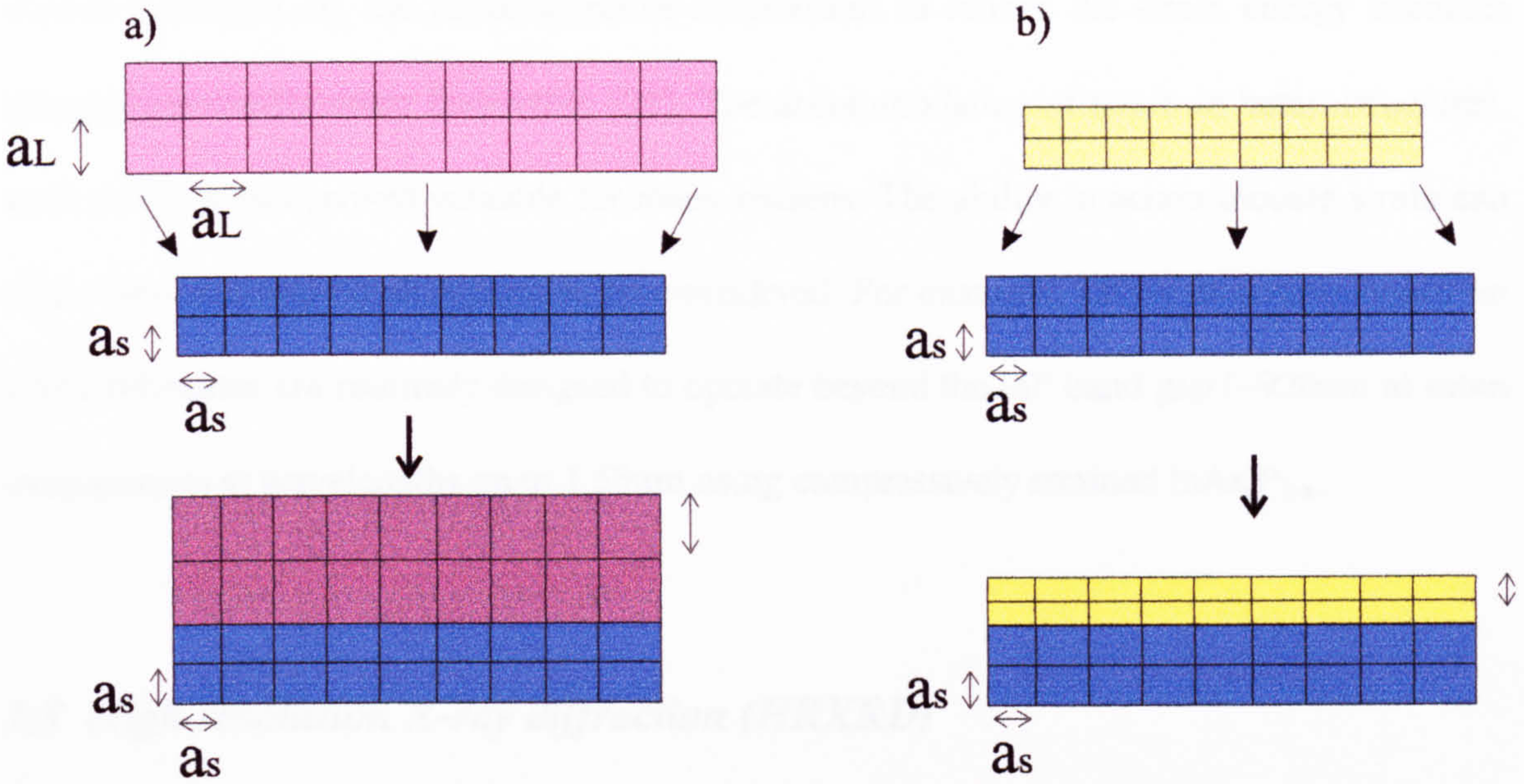

Figure 1-6 *Pseudomorphic strain produced by a layer with a bulk lattice constant, a) larger ($a_L > a_s$) and b) smaller ($a_L < a_s$) than the substrate.*

The bandgap changes experienced, for example, by depositing InAsP on InP can be expressed in the following way: if the unstrained bandgap is $E_0(x)$ then the biaxial compression experienced by the InAsP layer can be deconvolved into a hydrostatic compression and uniaxial tension and the bandgap is [25],

$$E(x) = E_0(x) + \Delta E^H \pm \Delta E^U \qquad \text{Eq 1-8}$$

where ΔE^H and ΔE^U are the strain introduced changes due to the hydrostatic and uniaxial components of the strain and ± signs refer light and heavy hole bands respectively. The expressions for ΔE^H and ΔE^U are given in Eq 4-5 and Eq 4-6 respectively, Chapter 4.

Coherent growth of an epilayer in this manner does not proceed indefinitely. The accommodated strain energy increases with epilayer thickness, h, such that above a certain

critical thickness, h_c, the introduction of dislocations to relieve the strain energy becomes thermodynamically more favourable [26]. The accommodation of strain in heterostructures, such as QWs, has proved valuable for many reasons. The ability to accommodate strain can allow new material combinations to be considered. For example, MQW structures based on GaAs substrates are routinely designed to operate beyond the InP band gap (~920nm at room temperature) at wavelengths up to 1.55μm using compressively strained $InAs_xP_{1-x}$.

1.3 High resolution X-ray diffraction (HRXRD)

X-rays are short wavelength (0.5-2.5Å) electromagnetic waves. High energy electrons incident on solids result in the emission of x-ray spectra. The emission lines arise from transitions between inner shell energy levels in the atoms and their wavelengths are characteristic of the element. A high resolution x-ray machine (Philips MRD) (see section 2.3) employs x-rays from a Cu source of $\lambda(K_{\alpha 1})$=1.54Å and can be used to obtain structural information on semiconductor materials since the interplanar spacing is the same order of magnitude as the x-ray wavelength. A diffraction pattern is produced by Bragg reflections of the x-rays from sets of the lattice planes within the crystal. The condition for constructive interference to occur is given by Bragg's Law (Eq 1-9) and states that the scattered rays will be completely in phase if the path difference is equal to a whole number of wavelengths [27],

$$2d\sin\theta = n\lambda \qquad \text{Eq 1-9}$$

where λ is the wavelength of the x-ray beam, θ is the angle between the incident beam and the diffracting planes in the surface and d is the separation of the planes. As d

varies slightly from the substrate to the layer, there is an angular separation, Δω, between the Bragg peak for the layer and substrate. The differential form of Bragg's Law,

$$\frac{\Delta d}{d} = -\cot\theta\Delta\omega = \frac{\bar{a} - a_s}{a_s} \qquad \text{Eq 1-10}$$

relates the strain and therefore the lattice mismatch $\Delta d/d$ to the angular separation of the Bragg peaks (Δω) [28] where $\bar{a}$ is the mean lattice parameter and a_s is the lattice constant of the substrate. This approximation is valid for small values of Δω.

1.3.1 XRD rocking curve

The x-ray diffractometry study in this thesis was performed using a Philips HR1880 high resolution triple-axis MRD diffractometer described in further detail in section 2.3. X-rays are directed onto the sample (Figure 1-7). The sample is rotated (ω) through the Bragg conditions for the substrate and epilayer whilst simultaneously rotating the detector through an acceptor angle of 2θ giving rise to ω-2θ scans known as *high resolution rocking curves.* Variations in the diffracted x-ray intensity as a function of the angle subtended between the incident x-ray beam and the sample are recorded by the detector and displayed as a rocking curve scan [29].

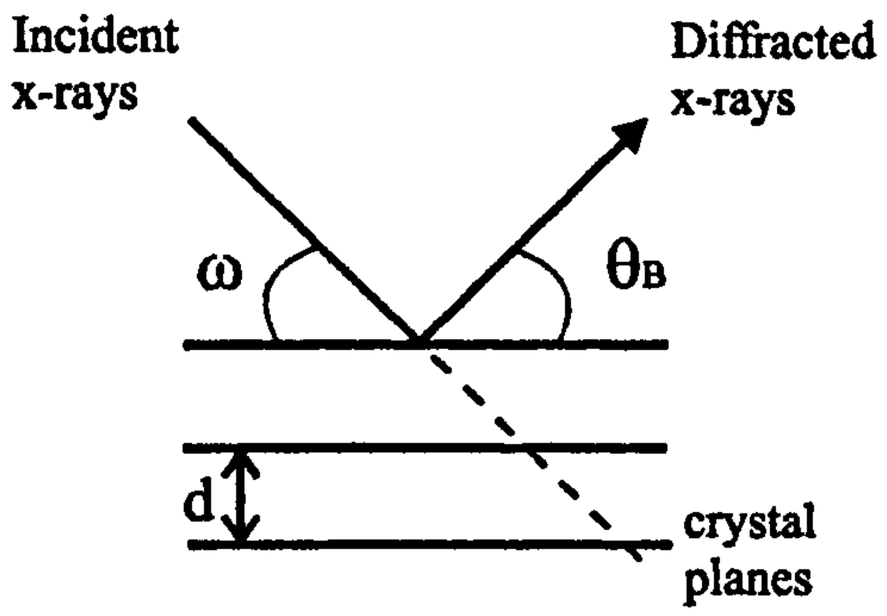

Figure 1-7 *Illustration of reflection geometry for symmetric reflections. The sample is rotated through angle ω. The Bragg angle θ_B is measured between the incident beam and the particular crystal planes under consideration.*

In this thesis, the rocking curves were taken in the symmetric (+m, -m) mode with the (004) reflection of an InP (001) orientated primary crystal. Symmetric (004) reflections are measured because the *structure factor F* of the zinc blende crystal is zero for (002) [27]. The structure factor is simply obtained by adding together all the waves scattered by the individual atoms. The intensity of the beam diffracted by all the atoms of the unit cell in a direction predicted by the Bragg Law is proportional to $|F|^2$ the square of the amplitude of the resultant beam. For semiconductors, such as GaAs and InP, the 004 order reflection is used for XRD analysis since the zinc-blende structure results in systematic absences in the diffraction pattern, and the 004 order reflections are the most intense order (after 000).

In structures that are pseudomorphically strained or lattice matched, the rocking curve provides accurate structural information such as periodicity (p) and the mean lattice parameter ($\bar{a}$) (Eq 1-10) over the whole stack. For a MQW structure with a stack of AB

layers, where A is the substrate material (eg. InP) and B is the alloy ($In_xGa_{1-x}As$) [30] the rocking curve will show the following features:

1) A substrate peak which is the most prominent feature in the rocking curve.

2) A peak caused by the addition of Bragg reflections from the A and B components of the MQW. This is the zero-order peak from which the average composition of the A+B layers may be obtained by differentiation of Bragg's Law (Eq 1-10).

3) A set of subsidiary satellite peaks surrounding the zero-order peak, with spacing determined by the periodicity (total thickness of the repeating layer) of the MQW.

From these peaks, the following information can be deduced,

a) the angular separation between the Bragg peak of the substrate and the zeroth-order peak of the epilayer gives the average lattice parameter ($\bar{a}$) (Eq 1-10) and, thus, the average epilayer composition,

b) the periodicity of the multilayer structure from any two adjacent satellite peak positions can be determined. These satellite peaks are separated by the inverse of the period in reciprocal space which is given by [31],

$$p = \frac{\left(L_i - L_j\right)\lambda}{2\left(\sin\theta_i - \sin\theta_j\right)} \qquad \text{Eq 1-11}$$

where L_i and L_j represent the diffraction orders (e.g. 2 and 3), λ the wavelength and θ_i and θ_j are the Bragg angles for the two satellite peaks,

(c) the FWHM and the intensity of the satellite peaks give information on the quality of the interfaces. Variation in the period causes broadening of satellite peaks. Interface

grading changes the integrated intensities of the satellite peaks with higher order peaks being most sensitive to interface grading,

d) the oscillations between the satellite peaks are called Pendellosung oscillations (interference fringes) and relate to the overall thickness of the stacking layer. The observation of well resolved fringes is a good indication of perfection in the epitaxial layer surface and interface. They are detected in films where the strain is homogeneous and interfaces are smooth. The x-ray measurement yields an unambiguous determination of the strain distribution and allows the composition of the structure to be (indirectly) determined.

Rocking curves were simulated using a computer programme developed at Philips by Paul Fewster [31] which is based on the solution of the Tagaki-Taupin [32,33] equations of dynamical diffraction theory accounting for multiple scattering. The equations relate the value of the diffracted and incident amplitudes at a depth (Z) in a perfect crystal and account for the dynamic interaction between these two amplitudes. The evaluation of strain and structure factor variation is based upon the zinc-blende crystal structure and can be used to generate all the diffraction broadening and interference effects observed experimentally. When simulating a MQW structure using the high resolution simulation software (HRS) [28, 34], initial input parameters for the first trial must be established. As described, the period and the average strain of the MQW can be obtained from the peaks on the rocking curve and hence these parameters can be used to determine the initial composition of the MQWs. These 'start' parameters are entered into the simulation program along with the input fields which define the diffractometer geometry and the best fit is obtained by an iterative process.

1.4 Device Applications

1.4.1 Semiconductor lasers

The enhanced emission properties of QWs are utilised in semiconductor laser structures [38]. The essential components of the laser structure are an active region where electrons and holes recombine to emit photons, a p-n junction which injects electrons and holes into the active region, and an optical cavity formed in the crystal structure to provide optical feedback into the active region. Some of the benefits of using QWs as the laser medium are; (i) the ability to vary the lasing wavelength, (ii) lower threshold current (J_{th}) (iii) improvements in modulation speeds because of the larger differential gain [35]. J_{th} for QW lasers exhibits less temperature sensitivity than double-heterostructure lasers [14]. The threshold current is the minimum injected current required to balance the optical losses within the structure in order for lasing to begin. A combination of choosing an optimum number of QWs for a given cavity length is also important to minimise the threshold current. The optical properties of semiconductor lasers may be further improved by using quantum dots rather than QWs as the active medium. Reducing the dimensionality to 0D [14] is attractive for laser devices as it promises a higher differential gain, lower threshold current density and a higher temperature stability than can be achieved with QW lasers (chapter 5).

In-plane semiconductor lasers are fabricated by cleaving the crystal perpendicular to the QWs and the semiconductor/air interface produces an approximately 30% reflecting surface. In order to increase the interaction within the active region, optical confinement perpendicular to the cavity can be achieved by cladding the active region with a semiconductor which has a low refractive index [10]. A further improvement to laser design

is the vertical cavity surface emitting laser (VCSEL) in which the cavity volume is reduced to <0.05μm [36]. The VCSEL consists of a short cavity containing the active QWs sandwiched between distributed Bragg reflectors (DBR) [36]. These highly reflecting surfaces (>99%) consist of alternating layers with different refractive indices (e.g. AlAs and GaAs). The reduced cavity of a VCSEL results in sub-mA threshold lasing current and helps prevents mode hopping [37]. A combination of this low power usage and their compactness means that large arrays of such lasers can be fabricated.

Lasers with strained layer QWs in the active region are now very common [38]. The improvement in gain arises from the decreased hole effective mass that occurs when the heavy hole and light hole in the valence band are separated. This occurs because the higher lying valence band can be distorted to more closely resemble the shape of the conduction band, i.e. the density of states for holes is reduced [39]. As a result a greater proportion of the available hole states are filled for a given injection current and again the gain is increased. As strain reduces the threshold carrier density, both inter-valence band absorption (IVBA) and free carrier absorption decrease, reducing the internal loss in the laser cavity and increasing the differential efficiency. Chapter 4 investigates strained layers of InAsP grown on InP.

1.4.2 Modulators

Adding dopants to semiconductors results in either electron rich or hole rich material depending on the type of impurity. The addition of an undoped (intrinsic, i) layer in between the p and n region creates a potential gradient between the n and p-type regions (p-i-n structures). Application of a reverse bias across this p-i-n structure increases the gradient in

the i-region. The potential profile of the well is skewed so that the carriers no longer see rectangular barriers on either side (Figure 1-8).

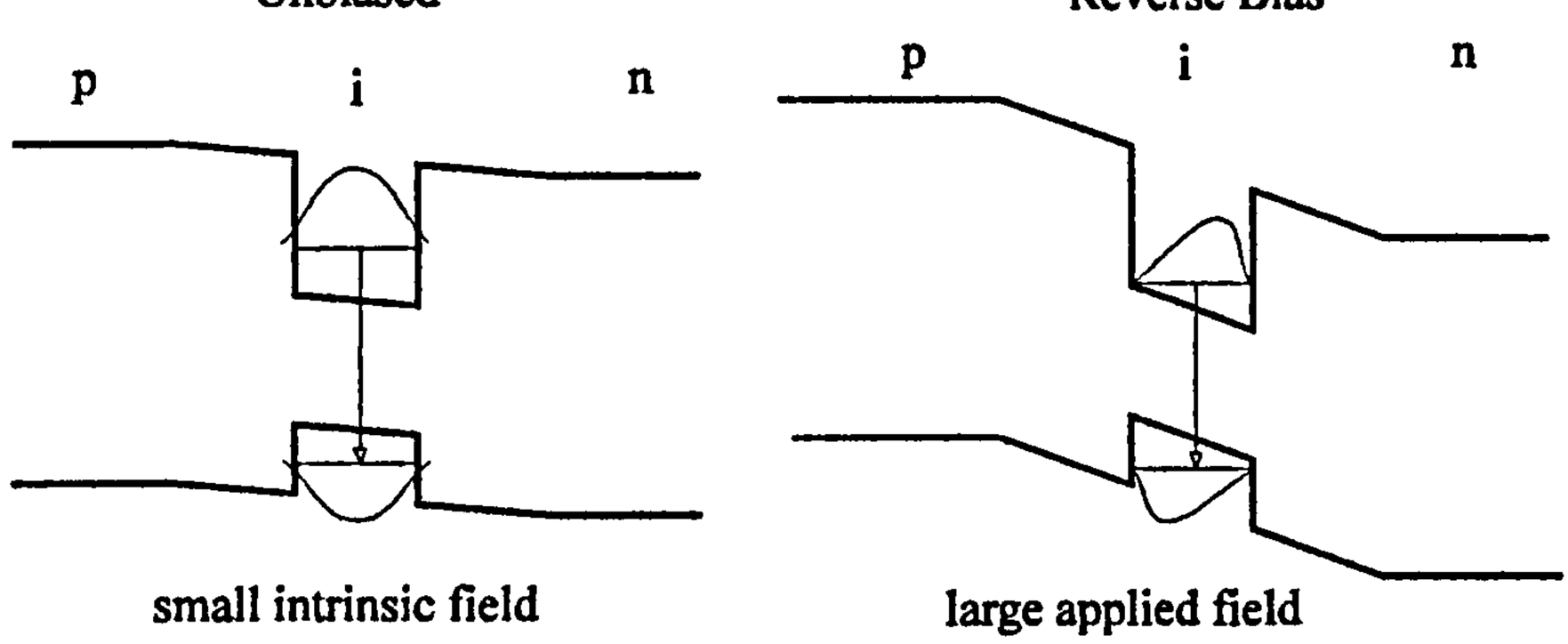

Figure 1-8 *Effect of an electric field on a QW in a p-i-n structure resulting in an e1-hh1 energy redshift and a reduction the transition strength.*

Electron and hole wavefunctions are polarised in opposite directions. This change in the shape of the potential causes the energy levels to red-shift. The electron and hole wavefunctions then have maxima near the opposite sides of the well, reducing the excitonic transition strength due to the decrease in overlap of the wavefunctions. The shift of the subbands is a direct consequence of the QW structure and is different from the Franz-Keldysh electro-absorption [10] observed in bulk semiconductors, which is dominated by field tunnelling broadening effects rather than an actual shift of the edge. Consequently the shape change of the QW caused by application of an electric field results in an excitonic transition energy shift - the quantum confined Stark effect (QCSE) [40]. A large change in the absorption coefficient on application of an electric field due to the QCSE means that modulation can be performed with low voltages (typically 10V) [41]. Hence, when no

external field is applied the QW p-i-n structure absorbs incident light at the excitonic transition energy (off), but if a reverse bias is applied, the absorption coefficient (α_V) is reduced and the structure begins to transmit (on). Chapter 3 investigates the importance of abrupt interfaces in QWs particularly if they are to be used in modulators.

Due to a combination of good electrical and optical properties of QWs, the possibility of monolithic integration (on a single substrate) and hence the fabrication/formation of an optoelectronic integrated circuit (OEIC) can be achieved. Monolithic integration means that component-to-component optical loss is drastically reduced resulting in an improvement in the overall efficiency of the system. To integrate optical functions requires selective area control of the bandgap. Together, semiconductor lasers and modulators are able to produce and switch optical beams with wavelengths ranging from 0.6-1.55μm for a variety of telecommunications and possible optical computing applications. An ability to produce different wavelengths would also lead to new photonic integrated circuit (PIC) configurations (chapter 4).

1.5 Outline of thesis

This thesis focuses on the properties of InP-based 0D and 2D quantum confined structures as they emit at the all important telecommunication wavelength of 1.3 -1.55μm. Chapter 1 has introduced low dimensional semiconductor structures and shown that the intrinsic optical properties are determined by the confining potential resulting from growth of materials of different bandgaps. The experimental techniques and equipment used to assess the optical and structural properties are described in chapter 2. Chapter 3 investigates grading at the InGaAs/InP and InGaAs/InGaAsP interfaces due to As/P exchange. In chapter 4, the interdiffusion of InAsP/InP MQWs by intermixing the well and barrier materials using post-growth annealing techniques was studied. Chapter 5 investigates self-assembled quantum dots which have generated a lot of interest recently. InAsP QDs are grown by depositing a few MLs of InAs on a standard and misorientated InP substrate by MOCVD. Finally, in chapter 6, each chapter is summarised and followed by a discussion on further work.

1.6 References

[1] R. G. Hunsperger: Photonic devices and systems (Marcel Dekker USA, 1994)

[2] H. M. Rosenberg: The Solid State (Oxford Publications, 1998)

[3] P. Dawson, K.J Moore, G Duggan, H.I. Ralph, C.T.B. Foxon, Phys. Rev. B. vol34 no8 p6007 (1986).

[4] M. Jaros, "Physics and Applications of Semiconductor Microstructures", Oxford University Press (1990)

[5] C. Kittel, 1986 "Introduction to Solid State Physics" 6^{thc} edition, Wiley.

[6] J. Singh: Physics of Semiconductors and their heterostructures, McGraw-Hill (1993)

[7] S.M. Sze 1981 "Physics of Semiconductor Devices", 2nd edition, Wiley.

[8] D. A. B Dingle, W. Weigmann, C. H. Henry: Phys Rev Lett 33 p827 (1974)

[9] C. G. Van der Walle: Phys Rev B, vol39, no3 p1871 (1989) [E10]

[10] C. Weisbuch and B. Vinter: Quantum Semiconductor Structures, Fundamentals and Applications, Academic Press, Boston (1991)

[11] L. Pavesi, M. Guzzi: J. Appl. Phys. 75 (10) p.4779 (1994) [E1]

[12] J.I. Pankove: Optical Processes in Semiconductors, Prentice Hill, Englewood Cliffs, (1971)

[13] G. Bastard, E. E. Mendez, L. L. Chang, L. Esaki: Phys Rev B, vol26, no4 p1974 (1982) [E12]

[14] Y. Arakawa, H. Sakaki; Appl. Phys. Lett. 40 (11) p939 (1982) [D65]

[15] H.B. Bebb, E.W. Williams: Semiconductors and Semimetals 8 1972

[16] J. R. Haynes: Phys Rev Lett 64 p361 (1960)

[17] J. Feldmann, G. Peter, E. O. Gobel, P. Dawson, K. Moore, C. Foxon, R. J. Elliot: Phys Rev Lett, vol59, no20 (1987) [E11]

[18] E. F. Shubert, E. O Gobel, Y. Horikoshi, K. Ploog, H. J. Queisser: Phys Rev B 30 p813 (1984)

[19] R.A. Stradling, P.C. Klipstein: Growth and Characterisation of Semiconductors, Adam Hilger (1990)

[20] F. Yang, M. Wilkinson, E.J. Austin, K.P. O'Donnell: Phys. Rev. Letts. 70 no.3 p.323, (1993) [E2]

[21] J.W. Orton, P.F. Fewster, J.P. Gowers, P. Dawson, K.J. Moore, P.J. Dobson, C.J. Curling, C.T. Foxon, K. Woodbridge, G. Duggen, H.I. Ralph. Semicond. Sci. Technol. 2 1987 p.597-606. (M63)

[22] D. Leonard, K. Pond, P. M. Petroff; Phys. Rev. B 50 (16) p11 687 (1994) [D80]

[23] C. T. Foxon, B. A. Joyce: Surface Sci. 50 p434 (1975)

[24] P. D. Dapkus: J of Cryst Growth 68 p345 (1984)

[25] F. Pollack, M. Cardona: Phys Rev 172 p817 (1968)

[26] E. P. O'Reilly: Semicon Sci and Technol 4 p121 (1989)

[27] B. D. Cullity: Elements of X-ray Diffraction, Addison-Wesley Publishing Company (1959)

[28] P. F. Fewster: Semicond Sci Technol, 8 p1915 (1993) [E9]

[29] M. Schuster, N. Herres: An Introduction to High-Resolution X-Ray Diffraction. [E15]

[30] D. K. Bowen, B. K. Tanner: High-Resolution X-Ray Diffractometry and Topography, published by Taylor and Francis.

[31] P. F. Fewster and C. J. Curling: J. Appl Phys 62 p4154 (1987)

[32] S. Takagi: J. Phys Soc Jap 26 p1239 (1969)

[33] D. Taupin: Bull Soc Fran Miner Cryst 87 p469 (1964)

[34] M. Halliwell, G. Daalderop, Philips Analytical X-Ray, Almelo, The Netherlands.

[35] M. Dagenais, R. F. Leheny, J. Crow: Integrated Optoelectronics, Academic Press (1995)

[36] J. L. Jewell, J. P. Harbison, A. Scherer, Y. H. Lee, L. T. Florez: IEEE J of Quant Electron vol 27 no6 p1332 (1991)

[37] R. S. Geels, L. A. Coldren: Appl Phys Lett 57 p1605 (1990)

[38] P. S. Zory Jr.: Academic Press (1993)

[39] D.A. Cohen, L. A. Coldren; IEEE J. of selected topics in Quant Electronics, vol.3, no2, p649 (1997)

[40] D. A. B Miller, D.S Chemla, T. C. Damen, A. C. Gossard, W. Weigmann, T. H. Wood, C. A. Barrus: Phys Rev Lett 53 p2173-6 (1984)

[41] D. A. B Miller, D.S Chemla, T. C. Damen, A. C. Gossard, W. Weigmann, T. H. Wood, C. A. Barrus: Phys Rev B 32 no2 p1043-59 (1985) [E14]

2. Chapter 2 - Experimental Techniques

2.1 Introduction

There are many well established techniques for investigating and characterising the optical, structural and electrical properties of semiconductor quantum wells and dots. The optical methods described in this chapter for examining transitions between confined levels in such structures include photoluminescence (PL), photoluminescence excitation (PLE) and transmission measurements. Structural methods include x-ray diffraction (XRD) and atomic force microscopy (AFM) [1]. All the above techniques are non-destructive ways of analysing semiconductor properties where only a small quantity of the material is needed. Other techniques which yield valuable structural information on low dimensional structures include transmission electron microscopy (TEM) and scanning transmission electron microscopy (STEM) used in conjunction with dispersive x-ray analysis (EDX). However, both these techniques are destructive and the samples cannot be used again. PL, transmission, XRD and AFM experiments were all carried out at the IRC for Semiconductor Materials, Imperial College whereas the STEM and EDX measurements were performed by H. Davock on the STEM facility in Liverpool.

2.2 Optical Characterisation

2.2.1 PL /PLE Equipment

The optical set-up for the PL or PLE experiments consists of an excitation source, usually a laser, a monochromator to disperse the luminescence emitted from the sample, and a detector. This is shown schematically in Figure 2-1.

For PL experiments, either a HeNe or an Argon ion laser was used as the excitation source providing continuous wave emission at 632.8nm or 514.5nm respectively. The tunable laser source used for PLE was a titanium-doped sapphire (Ti:Sapph) laser which delivers an intense beam over a broad range of near infrared wavelengths (700-1000nm). The Ti:Sapph crystal absorbs in the range 400-600nm, making the Argon ion laser an ideal pump source. Continuous variation of the excitation wavelength is achieved by means of a Digiplan stepper motor and driver connected to a micrometer which controls the tuning of the laser using a birefringent filter. Two different mirror sets can be used which provide tuning from 700-850nm (blue set) and 850-1000nm (red set).

Samples are mounted on a cold finger inside a closed cycle helium cryostat (Oxford Instruments or APD) and the sample temperature can be varied between 10K and 300K. The luminescence emitted from the sample is collected by means of two planoconvex lenses (L1 and L2) which focus the light onto the entrance slits of the monochromator. L2 is chosen to match the f-number of the monochromator.The dispersed luminescence is then directed into a detector placed at the exit slit of the monochromator. Two systems were used in the course of this work; system (a) consists of a Spex 0.85m double grating instrument controlled by a CD2A compudrive. The gratings (600grooves/mm) are blazed for a wavelength (λ_B) of 1μm

but the efficiency drops to 50% when λ=1.5μm. System (b) consists of a Spex M500 single grating instrument, again with a grating (600 grooves/ mm) blazed for 1μm. The main difference between these two monochromators is in the rejection of scattered light which is significantly better for system (a). Two detectors have been used in this work; a) Hamamatsu Micro-channel plate (MCP) with an S1 response used for detection in the range below 1.1μm and b) a North Coast Germanium p-i-n diode to detect luminescence in the wavelength range 0.8 - 1.7μm. The Ge diode is cooled to 77K in order to reduce thermal noise. To further improve the signal to noise ratio, the output voltage is input to a lock-in amplifier which is phase matched to a mechanical chopper operating at 326Hz. A muon filter is connected in parallel across the lock-in to reduce voltage spikes which arise due to muons (cosmic rays) which can cause the Ge diode to temporarily overload.

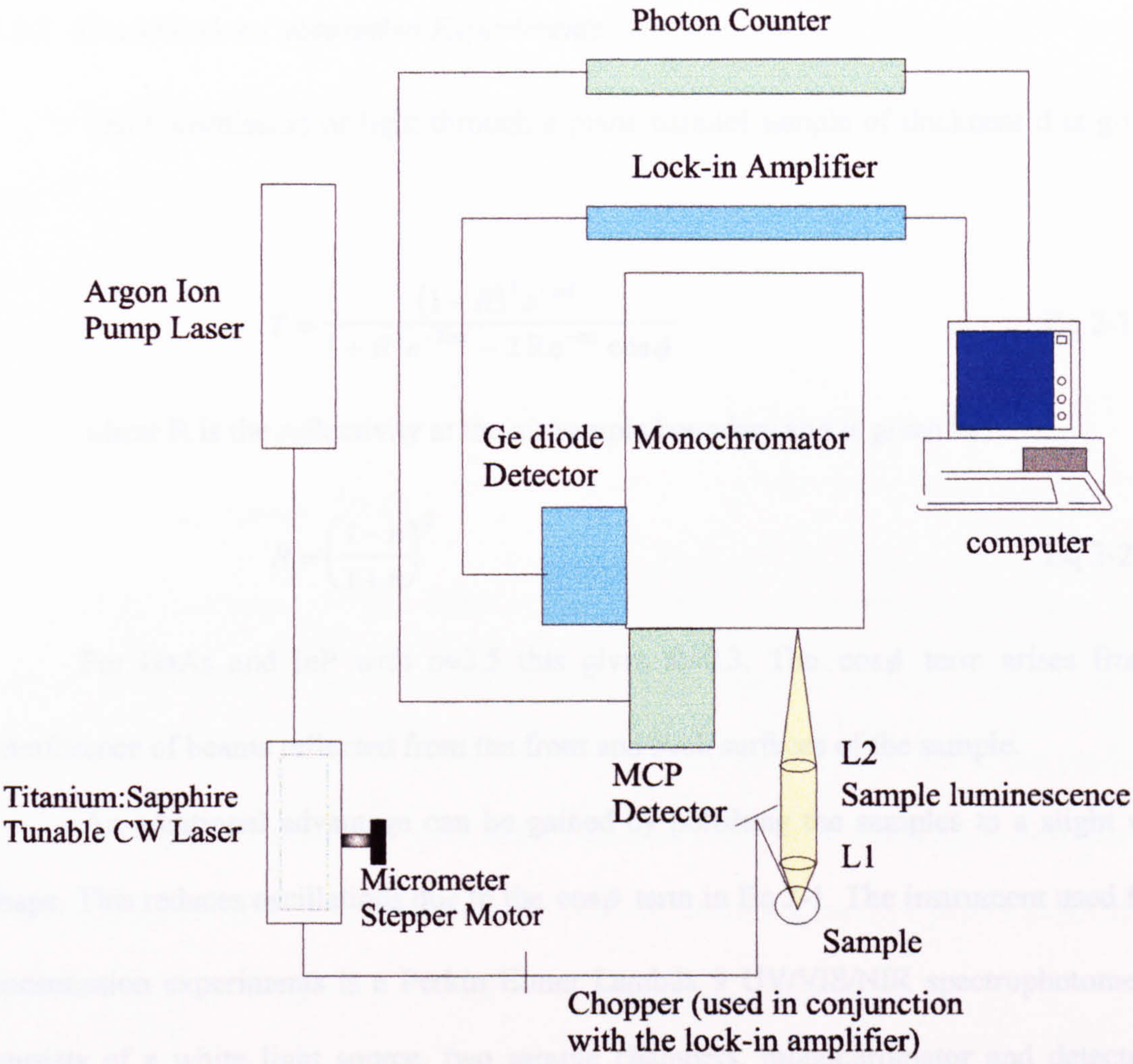

Figure 2-1 *Schematic of optical set-up for PL or PLE experiments consisting of an excitation source, a monochromator and detector.*

2.2.2 Transmission / absorption Experiments

The transmission of light through a plane parallel sample of thickness d is given by [2],

$$T = \frac{(1-R)^2 e^{-\alpha d}}{1 + R^2 e^{-2\alpha d} - 2R e^{-\alpha d}\cos\phi} \qquad \text{Eq 2-1}$$

where R is the reflectivity at the air/sample boundary and is given by,

$$R = \left(\frac{1-n}{1+n}\right)^2 \qquad \text{Eq 2-2}$$

For GaAs and InP with n≈3.5 this gives R≈0.3. The $\cos\phi$ term arises from the interference of beams reflected from the front and back surfaces of the sample.

An additional advantage can be gained by polishing the samples to a slight wedge shape. This reduces oscillations due to the $\cos\phi$ term in Eq 2-1. The instrument used for the transmission experiments is a Perkin Elmer Lambda 9 UV/VIS/NIR spectrophotometer. It consists of a white light source, two sample chambers, monochromator and detectors. A double monochromator set-up is necessary to reduce the amount of stray radiation. Two detectors, a photomultiplier and a PbS cell, are used to cover the UV/VIS and the NIR range. The detector signal is amplified and fed directly to an Analogue - Digital converter. The transmission range, slit width, sensitivity and scan speed are all controlled by a computer linked to the spectrophotometer. Initially, a background correction scan, with no sample, is taken to act as a reference for all further scans. The computer stores this information, uses it as the reference signal, eventually displaying the scans as a percentage transmission. In order to remove some of the effects of substrate absorption the samples are polished to remove some of the substrate in preparation for the transmission experiment. The substrate is

polished with various grades of waterproof silicon carbide paper. This process is completed by using polishing cloth impregnated with 6μm diamond particles until a specularly reflecting surface is obtained.

2.3 Structural Characterisation

2.3.1 X-Ray Diffraction (XRD)

High Resolution X-Ray Diffraction (HRXRD) is a structural technique used to provide information on the composition and lattice strain of ternary or quaternary III-V heteroepitaxial layers [3]. This information is obtained from an analysis of the profile of a particular Bragg reflection. For a complete characterisation it is necessary to measure Bragg reflections from sets of lattice planes parallel to the crystal surface and planes inclined to the surface so strain in the epitaxial layer can be determined [4] (section 1.3).

High resolution rocking curves are measured for the epitaxial layers using a Philips High Resolution X-Ray diffractometer with the four-crystal monochromator aligned in the Ge(440) setting (Figure 2-2 a)). The X-ray source is a sealed Cu anode X-ray tube which emits radiation of wavelength 1.54Å. For high resolution X-ray, the beam must be collimated before it is incident on the sample. This is achieved using the four-crystal monochromator. The collimated beam is directed onto the sample with incident angle θ and the reflected X-rays are then directed through a set of slits into the detector. The sample crystal is rotated through an angle ω whilst simultaneously rotating the detector through an acceptor angle of 2θ giving rise to ω/2θ scans. These are later analysed in the form of a spectrum mapped out

in reciprocal space which provides information on variations in lattice spacing and can therefore be used to determine the position of the substrate peak and various satellites. However, if the crystal sample is bent, the detector will accept diffracted beams from different angles from the different regions of the sample which results in an intrinsic broadening of the diffraction peaks. This problem can be overcome by adding the channel-cut Ge(220) analyser crystal (Figure 2-2 b)) which turns the diffractometer from a high resolution diffractometer into a *triple axis diffractometer.* The triple-axis scan can be displayed in real or reciprocal space. The tilt of the layer with respect to the substrate can be obtained directly, the diffuse scattering (from defects) can be separated from the coherent scattering to give information on these defects, and the strain or mismatch can be distinguished from the tilt of the epilayers. This is important in a strain-relaxation study.

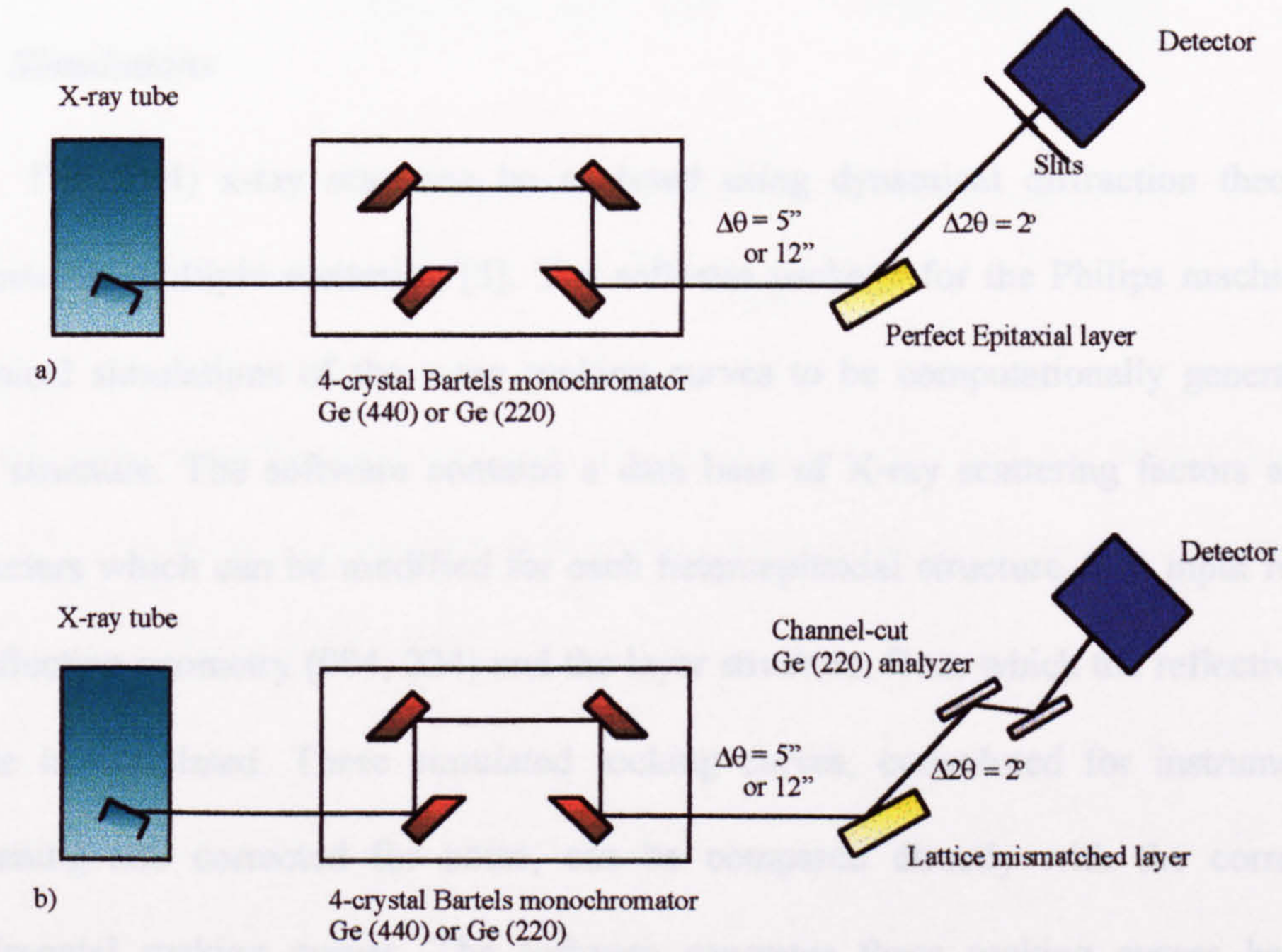

Figure 2-2 *a) High resolution double axis diffractometer, b) Triple axis diffractometer*

The fourth order reflection (004) from (001) planes is found to be the most intense, therefore a symmetrical 004 reflection rocking curve for a layer grown on a (001) substrate is recorded. A periodic structure such as an InGaAs/InP MQW will modify the X-ray diffraction pattern by giving a series of satellite Bragg peaks [3] (Figure 2-3). The central, most intense peak arises from the substrate (InP) with the zero order layer peak directly superimposed on top showing that the layer (InGaAs) and substrate are lattice matched. The intensities of the satellites are related to the the difference in structure factors of the constituent layers. The modulation of the satellite intensities is related to the shape of the individual layers in the MQW and can be used to deduce the abruptness of the interfaces. The higher order satellites are most sensitive to interface grading. A variation in the period of the MQW will cause broadening of the satellite peaks.

2.3.2 Simulations

The (004) x-ray scan can be analysed using dynamical diffraction theory which accounts for multiple scattering [5]. The software package for the Philips machine allows dynamical simulations of the x-ray rocking curves to be computationally generated for a given structure. The software contains a data base of X-ray scattering factors and lattice parameters which can be modified for each heteroepitaxial structure. The input required is the reflection geometry (004, 224) and the layer structure, from which the reflectivity of the sample is calculated. These simulated rocking curves, convoluted for instrumental line broadening and corrected for noise, can be compared directly with the corresponding experimental rocking curves. The software generates these rocking curves based upon composition and well/barrier width profiles [3]. The layers comprising the sample structure

can either be constant in composition or in the case of alloys the ratios of the elements can be varied in a linear or an exponential manner throughout the layer thickness. Layers with a varying composition are referred to as *graded layers* and can be used to ascertain the actual well composition or potential [6]. The MQW period can be determined within about 2Å accuracy.

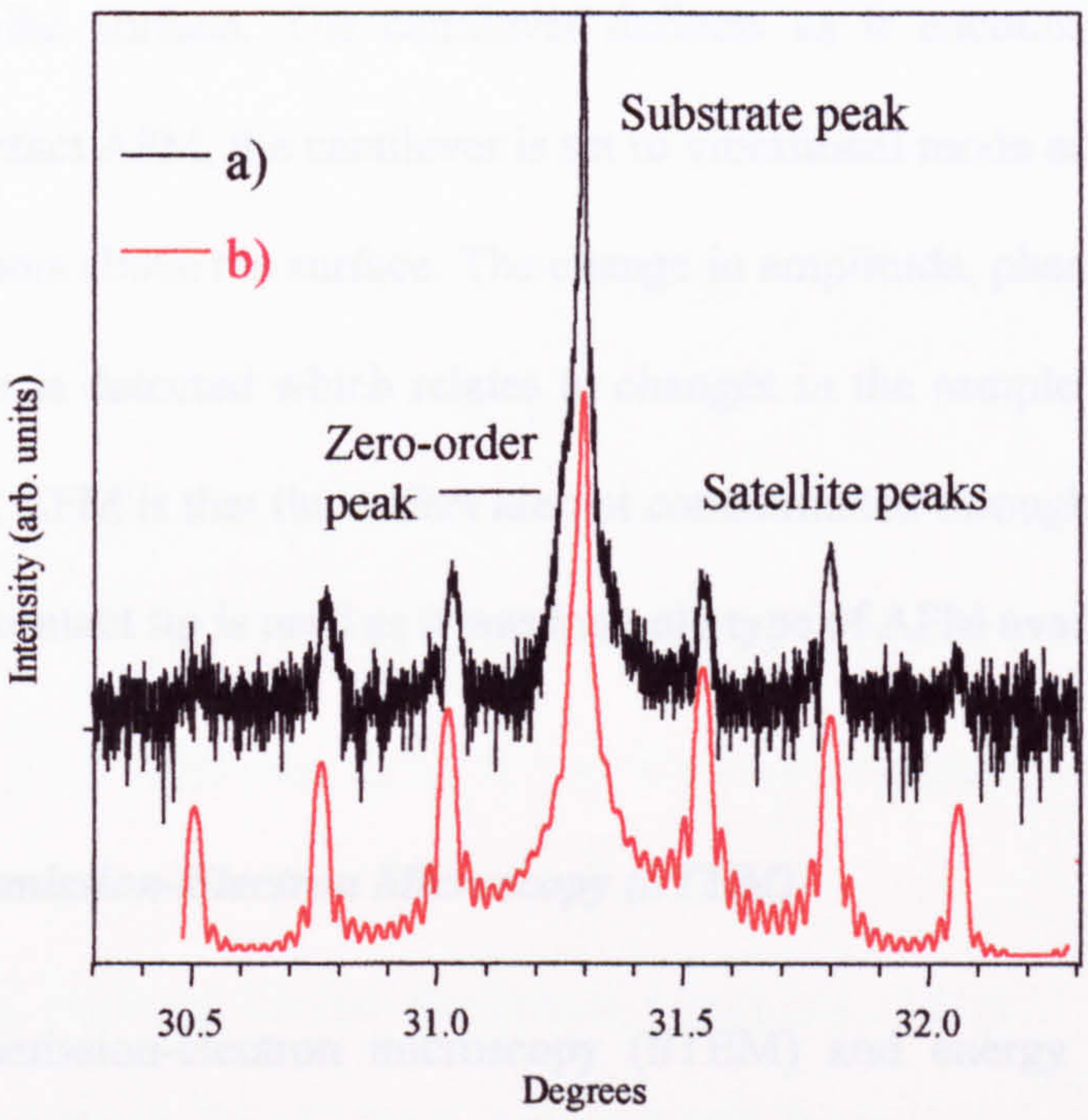

Figure 2-3 XRD *a) (004) experimental rocking curve for lattice matched InGaAs/InP b) (004) simulated rocking curve for InGaAs/InP assuming an asymmetric graded well profile*

2.3.3 Atomic Force Microscopy (AFM)

AFM is used for studying the topography of materials from the atomic to the micron level by imaging a scanned surface. AFM probes the surface with a sharp tip made from Si.

The tip is fixed at the end of a cantilever (100 - 200μm long) and scanned over the sample surface. Inter-atomic and electrostatic forces attract or repel the tip causing the cantilever to deflect. A detector measures the cantilever deflections which allows a computer to generate an image of the surface topography. Two types of AFM can be employed; contact and non-contact [7]. In contact AFM (or repulsive mode) the scanner traces the tip across the sample making contact with the surface. The cantilever deflects as it encounters variations in topography. In non-contact AFM, the cantilever is set to vibrational mode and then scanned a few hundred of angstroms above the surface. The change in amplitude, phase or frequency of the vibrating cantilever is detected which relates to changes in the sample topography. The advantage over contact AFM is that the wafers are not contaminated through contact with the tip. For this work, the contact tip is used as it was the only type of AFM available.

2.3.4 Scanning Transmission-Electron Microscopy (STEM)

Scanning transmission-electron microscopy (STEM) and energy dispersive x-ray (EDX) have been employed to give structural information on semiconductor samples [8]. The experiment was carried out using the facility at Liverpool University. STEM was carried out using a VGHB601 UX 100KeV cold field emission STEM fitted with a windowless X-ray detector and parallel electron energy loss spectroscopy (PEELS). The sample of typical size 3mm x 3mm is ground and thinned using a polishing unit and an ion milling process to an optimum thickness of between 5-10nm which can be measured using PEELS. The thinning helps to restrict loss of resolution through beam broadening. The sample is mounted and heated to remove any oxide and then left to settle for up to eight hours to prevent sample

drift during measurement. The high vacuum (10^{-11}Torr) conditions of the STEM allows the use of a cold field emission tip and the ability to reduce the spot size to 0.2nm. An electron beam (~100keV) scans the thin section of the sample yielding a contrast image. An energy dispersive x-ray microanalysis (EDX) is performed by reducing the 100keV beam size to 1nm and scanning a line across the sample of length 8nm-64nm or rastering an area of up to 64nm x 64nm in 1nm steps along the direction of growth. Detection of the X-rays emitted provides a qualitative description of the elements contained within the sample. Absorption of X-rays is monitored by observing the intensity ratio of K_α and L_α lines for a given material such as GaAs.

2.4 References

[1] R.A. Stradling, P.C. Klipstein: Growth and Characterisation of Semiconductors, Adam Hilger (1990)

[2] E. Hecht: Optics, Addison-Wesley Publishing Company, (1974)

[3] P.F. Fewster: Semicond. Sci. Technol. 8 p.1915 (1993)

[4] C. Bocchi, C. Ferrai: J. Phys. 28 p.A164 (1995)

[5] Halliwell, G. Daalderop, Philips Analytical X-Ray, Almelo, The Netherlands.

[6] J.M. Vandenberg, A.T. Macrander, R.A. Hamm, M.B. Panish: Phys. Rev. B, 44 no.8 (1991)

[7] R. Howland, L. Benatar: A practical guide to scanning probe microscopy, Park Scientific Instruments (1996)

[8] R. J. Keyse, A. J. Garratt-Reed, P. J. Goodhew and G. W. Lorimer: Introduction to Scanning transmission electron microscopy., Bios Scientific Publishers (1998)

3. Chapter 3 - $In_xGa_{1-x}As/InP$ Quantum Wells

3.1 Introduction - Review of InGaAs/InP Quantum wells

$In_xGa_{1-x}As/InP$ multiple quantum well (MQW) structures are an important material system for optoelectronic devices which operate in the wavelength regions of minimum absorption (1.55μm) and zero dispersion (1.3μm) of commercial silica-based optical fibres [1]. Lattice matched (strain free) structures can be obtained for x=0.53 operating at 1.55μm, making this material combination very attractive for InP-based long-haul telecommunications [2]. High quality heterostructures can be grown by MOCVD, CBE and GSMBE and have been used to form optoelectronic devices such as lasers, waveguides or optical switches. The electrical and optical properties of these structures are strongly dependent on the size and shape of the QWs and device design is usually based on the assumption that the interfaces are abrupt.

However, InGaAs/InP structures are more difficult to produce than, for example, InGaAs/GaAs due to the additional requirements of lattice matching and the necessity of changing group V fluxes between successive layers. Gas phase epitaxial techniques such as MOCVD can be prone to flux intermixing [3] during growth of the heterointerfaces and the InGaAs/InP material combination has been shown to be susceptible to interdiffusion on the group V sublattice even at relatively low temperatures [4]. This creates a compositionally graded (interfacial) layer which can give rise to highly strained interface regions [5] which, if sufficiently thick, may contain extended defects which would reduce the electron mobility or enhance non-radiative recombination paths [6]. *Vanderberg et al.* [7] first suggested the

presence of an intrinsic strain at the heterointerfaces of InGaAs/InP and concluded that there may be problems with growing high quality interfaces. These problems are usually referred to as the 'memory effect' and the As-P exchange at the interface [7, 8, 9]. The memory effect is more prevalent in P-based material due to the high sticking coefficient of As relative to P [7, 9, 10] and either arises from small amounts of As found in the reactor during growth or from cross contamination of the sources due to incomplete switching. Excess As is incorporated into the InP and hence a compositionally graded interface is formed [5, 11, 12] Figure 3-1a). As/P exchange occurs at the interface forming intermediate InAsP or InGaAsP layer at the interface [10, 12] (Figure 3-1b).

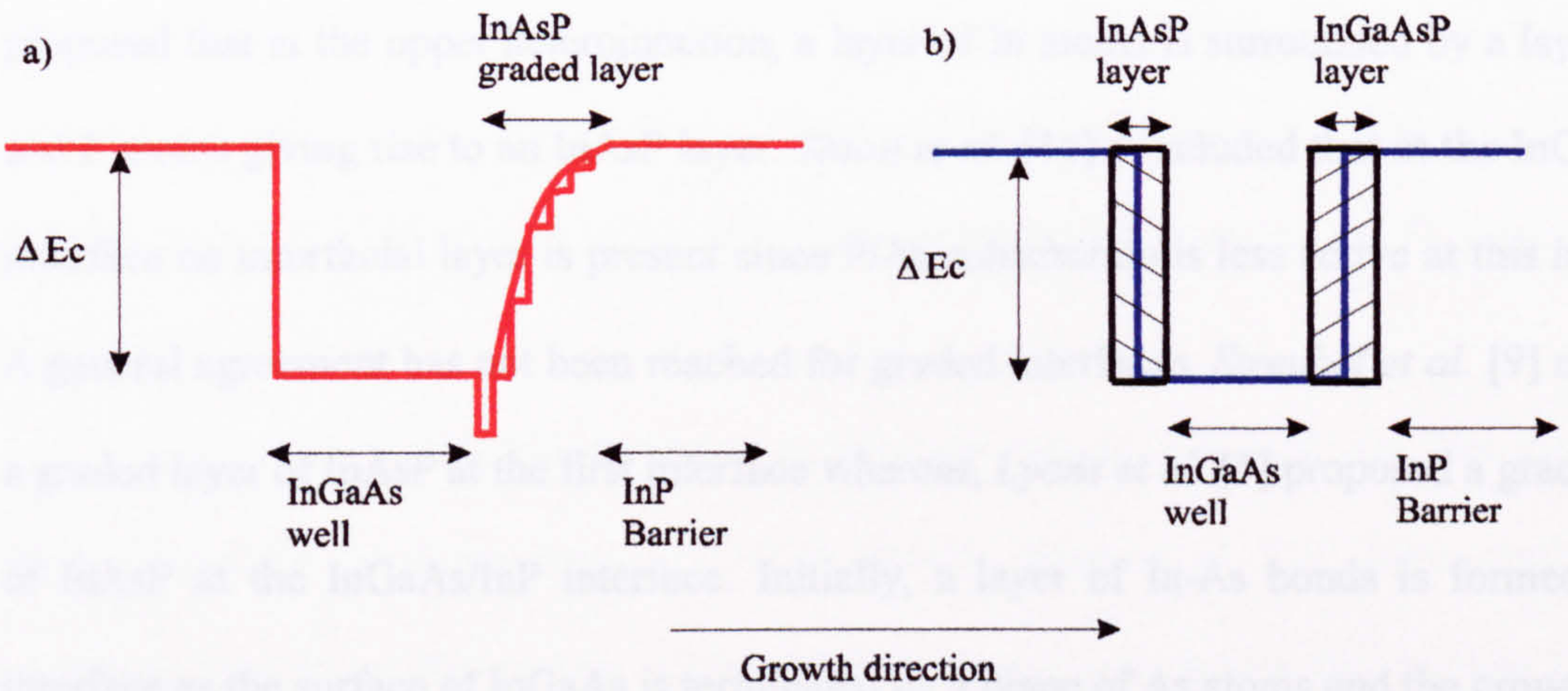

Figure 3-1 *As-P exchange at the interface results in a) a graded layer formed at the interface(s) or b) equal but oppositely strained monolayers at the interface. An InAsP layer at the lower (InP-InGaAs) interface is positively strained (compressive) and a quaternary InGaAsP layer at the upper (InGaAs-InP) interface is negatively strained (tensile).*

3.1.1 As-P exchange

As a result of As-P exchange at the interface, equal but oppositely strained monolayers (MLs) form a graded layer at the interfaces due to the difference in atomic size of As and P which can cause severe degradation of interface quality. This As-P exchange leads to InAs or InAsP interfacial layers at the lower (InP-InGaAs) interface which are positively strained (compressive) and a quaternary InGaAsP layer at the upper (InGaAs-InP) interface which is negatively strained (tensile) after an AsH_3 or PH_3 purge during growth [6, 10, 12, 13]. This is shown schematically in Figure 3-1b). However, a general consensus has not been reached on the composition of the interfacial layers. For example, *Meyer et al.* [7] proposed that at the upper heterojunction, a layer of In atoms is surrounded by a layer of As and P atoms giving rise to an InAsP layer. *Shiau et al.* [14] concluded that at the InGaAs/InP interface no interfacial layer is present since P/As substitution is less active at this interface. A general agreement has not been reached for graded interfaces. *Streubel et al.* [9] modelled a graded layer of InAsP at the first interface whereas, *Lyons et al.* [5] proposed a graded layer of InAsP at the InGaAs/InP interface. Initially, a layer of In-As bonds is formed at this interface as the surface of InGaAs is terminated by a plane of As atoms and the growth of InP is initiated by the deposition of In atoms. It would appear that the exchange process depends on the growth conditions and/or growth interrupts used by each group. However, it is agreed that an exchange of group V elements is the dominant effect.

These interfacial layers can influence the confining potential and therefore the heterostructures may not operate at the desired wavelength [2, 8, 10, 15]. Also, areas at the interface differing in thickness by ML steps (2D terraces) due to these interfacial layers lead to substantial broadening and even splitting of the emission peak due to the potential

fluctuations experienced by the exciton. A further problem encountered at the interfaces is the formation of 3D islands during the flux switching sequence which again affects the optical properties as the PL emission line is split into multiplets [9]. Growth techniques such as MOCVD, CBE and GSMBE are all subject to these As/P exchange problems. The specific growth conditions will determine whether 3D islands [9, 14, 17] graded layers [5] or strained layers at the interfaces are formed [7, 11, 12, 14, 18]. Optical and structural techniques such as PL, absorption, XRD and TEM have been used to analyse the condition of the interfaces [10]. For example, a strong red shift of the PL peak energy caused by the formation of intermediate $InAs_yP_{1-y}$ layers at the interface resulting from As substituting for P atoms on the InP surface during an AsH_3 purge in the growth was observed by *Wang et al.* [11]. *Brown et al.* [18] have observed that the PL is shifted to higher energies due to the formation of an intermediate InGaAsP layer at the InGaAs-InP interface. In both cases, the PL shift is a result of the As/P exchange.

Using *in situ* RHEED studies to monitor the effects of P_2 and As_2 flux exposure to InGaAs and InP surfaces during GSMBE growth, *Anan et al.* [19] have identified the exchange process at the sample surface during growth and shown that surface Ga atoms enhance the substitution of As to P atoms due to the different chemical bond strengths between the atoms. In-As and In-P have nearly equal chemical bond strengths but the energy required to break a Ga-P bond is larger than for the Ga-As bond. and consequently roughening could originate from this substitution of As to P atoms around Ga atoms. However, in general, As tends to incorporate with Ga (or In) preferentially compared to P because of the larger sticking coefficient of As [7, 14].

As the properties of optoelectronic devices may critically depend on compositional uniformity and interfacial perfection, methods of reducing the As/P exchange and eliminating island formation have been investigated and are discussed in the following section.

3.1.2 Growth Interruption Sequences (GIS)

Many groups have tried to eliminate surface roughening caused by As-P substitution when growing InGaAs/InP QWs by utilising various growth schemes such as different growth interruption sequences (GIS) at the upper and lower interfaces, different AsH_3 and PH_3 flow rates at various growth temperatures and pressures to obtain smooth interfaces [7, 13, 18, 19] and introducing an evacuation time during flux switching to avoid the memory effect [14]. In MOCVD, CBE and GSMBE growth processes, GIS are also used to eliminate the formation of 3D surface islands which form during the flux switching sequence. The GIS technique requires exposing the clean InP and InGaAs surfaces to AsH_3 and PH_3 fluxes which tends to increase the size of the 2D terraces (with 1ML thick fluctuations) by allowing the freshly grown surface to relax before the next layer is deposited [13]. The density of ML growth steps is diminished as the smaller terraces relax into larger ones due to the migration of surface atoms during interruption [20], hence increasing the interface abruptness and reducing the size of the atomic step fluctuation.

However, initial attempts at GIS resulted in the same problems as described in section 3.1.1. Some GIS introduced unintentional layers of InAsP and InGaAsP at the heterointerface whose composition and thickness depended on the particular growth sequence [6, 21]. These exposures led to a partial substitution of P with As (As with P) at the InP/InGaAs

(InGaAs/InP) interface. As the position of the confined states and hence optical transitions of QWs with well width, l_w<5nm, are particularly sensitive to well shape, thin QWs were grown where both interfaces were modified using various GIS to avoid an As carry over from InGaAs to InP. *Camassel et al.* [13], *Streubel et al.* [9] and *Bohrer et al.* [16] reported a splitting in the PL emission spectra corresponding to ML steps in the interface plane. This was attributed to a P-As exchange at the lower interface leading to InAsP interface islands that were larger than the excitonic diameter and therefore appeared to act as ML steps [17].

3.1.3 Improving Growth Interruption Sequences

By exposing the surface to different fluxes, over various time intervals and using different switching sequences, interfaces can be formed which are more abrupt than those obtained using conventional sequences [14]. *Benzaquen et al.* [6] have shown that longer exposures to hydrides (over 5s) give rise to interfacial layers with less compositional disorder and/or thickness fluctuation. *Wang et al.* [11] have demonstrated that PL peak energies for QWs grown using different GIS differ by as much as 0.25eV at low AsH_3 flow rates. They attributed this to the different fractions of surface P atoms replaced by As during an AsH_3 purge. Varying the AsH_3 flow rate during growth of the InGaAs well layer significantly influenced the emission energies for the samples grown continuously or with an interruption at the second interface.

Shiau et al. [14], *Streubel et al.* [9] *and Hergeth et al.* [12] have all demonstrated a significant improvement in the interface smoothing by using slightly more elaborate growth interruption (GI) techniques. *Shiau et al.* [18] have shown that a group III stabilised surface in the growth of InGaAs(P)/In(GaAs)P MQWs, As/P substitution can be avoided, improving

the interface quality. This was done by introducing a mixed ML of In and Ga to the freshly grown InP and InGaAs surfaces prior to exposure to the new group V flux. XRD and low temperature PL techniques were used to examine heterointerface abruptness. The results show that the interfaces grown with the modified switching sequence are considerably more abrupt than those obtained using conventional sequences where As/P interdiffusion extends over several MLs. By depositing a ML of In or Ga onto InP, exposure to the new group V structure can reduce the interfacial strain since the transition layer composition is InGaAsP rather than InAsP. InGaAsP has a smaller lattice mismatch with InP than InAsP and hence the strain is decreased at the interface [8].

Streubel et al. [9] have adopted a different approach. Rather than using PH_3 or AsH_3 purges, they have found that employing a GIS with a hydride purge improves the sharpness of the heterointerface. By purging the reactor with H_2 for 20-30s, after growth of InGaAs, an InAsP gradient in the InP barriers can be avoided. At the lower interface, no P carry over from the InP to InGaAs was detected.

Hergeth et al. [12] have grown InGaAs/ InP MQWs using low pressure MOVPE, with 4 different switching sequences of the gas phase at the interfaces: a) with GI at both interfaces, b) without interruption at the transition from InGaAs to InP, c) without interruption at the transition from InP and InGaAs, d) without interruption at both transitions. However, as the surface has to be stabilised during interruption, even a substitution of P by As at the InP surface is hard to avoid. In fact, in some cases, strained interfaces caused by the exchange of As and P at the interfaces may be beneficial, for example, in high performance long wavelength lasers. Usually strained QW systems are employed as the active material since the presence of strain leads to improved efficiency [22].

3.1.4 InGaAs/InGaAsP MQWs

The InGaAsP material system has attracted considerable interest in recent years as it allows a wide range of different bandgap materials to be grown on the two commercially important III-V substrate materials; InP and GaAs. InGaAs/InGaAsP MQWs grown on InP are considered to be suitable candidates for optoelectronic devices, particularly lasers, operating between 1.3 and 1.55μm [23-26]. Again, for such device applications, the interfaces of the QW structure need to be abrupt, otherwise interface roughness will affect the quantum confined levels, the linewidth of the optical emission spectra and the optical properties of the heterostructure. Most studies have focused on the interfaces of InGaAs/InP QWs with relatively few on InGaAs/InGaAsP QWs. Energies of the higher lying states which can give information on the confining potential are usually derived from PLE measurements. However, the lack of tunable laser sources in the required energy range means that these data are difficult to obtain for the InGaAs/InP and InGaAs/InGaAsP system [27].

Optical (PL and absorption spectroscopy) and structural (XRD) techniques have been used to study the interfaces of InGaAs/InP and InGaAs/InGaAsP materials for application in long wavelength optoelectronic devices. In InGaAs/InGaAsP MQWs, as will be shown the effects of interdiffusion of In, Ga and As may be less detrimental to the optical and electronic properties thereby reducing the need to use elaborate GIS [4]. However, quaternary as well as ternary QWs grown on InP are susceptible to interdiffusion which can cause a shift in the emission wavelength from that expected from the nominally grown structure.

The remainder of the chapter is organised as follows. Section 3.2 describes the PL results for InGaAs/InP and InGaAs/InGaAsP MQWs. In section 3.3, absorption results from the same samples are discussed in conjunction with the transfer matrix modelled results.

Section 3.4 describes XRD results and simulations, and finally, section 3.5 presents the conclusions which can be drawn from this work.

3.1.5 Samples

Two nominally lattice matched $In_{0.53}Ga_{0.47}As$ samples (A and B) with different barrier material and designed to emit at 1.55μm at room temperature, were investigated to determine how the barrier material influences the optical properties. As outlined in section 3.1, arsenic atoms are easily incorporated into and readily diffuse through the lattice (replacing P) at typical growth temperatures, leading to non-abrupt interfaces (Figure 3-1). A P-based quaternary barrier, with a room temperature bandgap of 1.26μm (0.98eV), was used for sample B. Sample A has InP barriers. Both samples consist of a 10 period 70/100Å well/barrier width, MQW, grown on an n^+ doped (100) InP substrate cut 0.35° off to (110) and capped with 7500Å of undoped InP. The structures were grown by atmospheric pressure MOCVD at the EPSRC III-V growth facility at Sheffield University. The growth rate was 2ML/s at a temperature of 650°C using arsine and phosphine as group V sources and trimethyl indium and trimethyl gallium as group III sources. The layers were not intentionally doped.

3.2 PL Results

Low temperature (10K) PL spectra obtained from samples A and B are shown in Figure 3-2a) and b) (black line). The spectra are dominated by e1-hh1 excitonic recombination located at 0.86 and 0.87eV for samples A and B respectively. No impurity

lines are evident. The linewidths (Full Width at Half Maximum (FWHM)) for samples A and B are 12meV and 8meV respectively. Compared with previously grown samples from the same MOCVD system, these linewidths are larger (usually FWHM of 3-6 meV) [28] and may indicate that these MQW structures are not of the highest quality. The width of the excitonic peak has been correlated with interface fluctuations [29] and as the FWHM for sample A is greater then for sample B, this implies an increased roughness for the InGaAs/InP interfaces. In addition, the integrated intensity of the emission peak for sample A is four times greater than sample B, for the same experimental conditions. This may be due in part to the quality of the substrate which would need to be characterised before growth.

Also evident in the 10K spectra for both sample A (Figure 3-2a) and sample B (Figure 3-2 b) is a weak emission observed about 33meV to the lower energy side of the main peak. This feature corresponds to the 'GaAs-like' LO phonon mode (or replica) previously reported by *Skolnick et al.* [29] and *Westland et al.* [30]. *Skolnick et al.* [29] observed the LO phonon peak in the PL spectra for a 150Å InGaAs/InP QW.

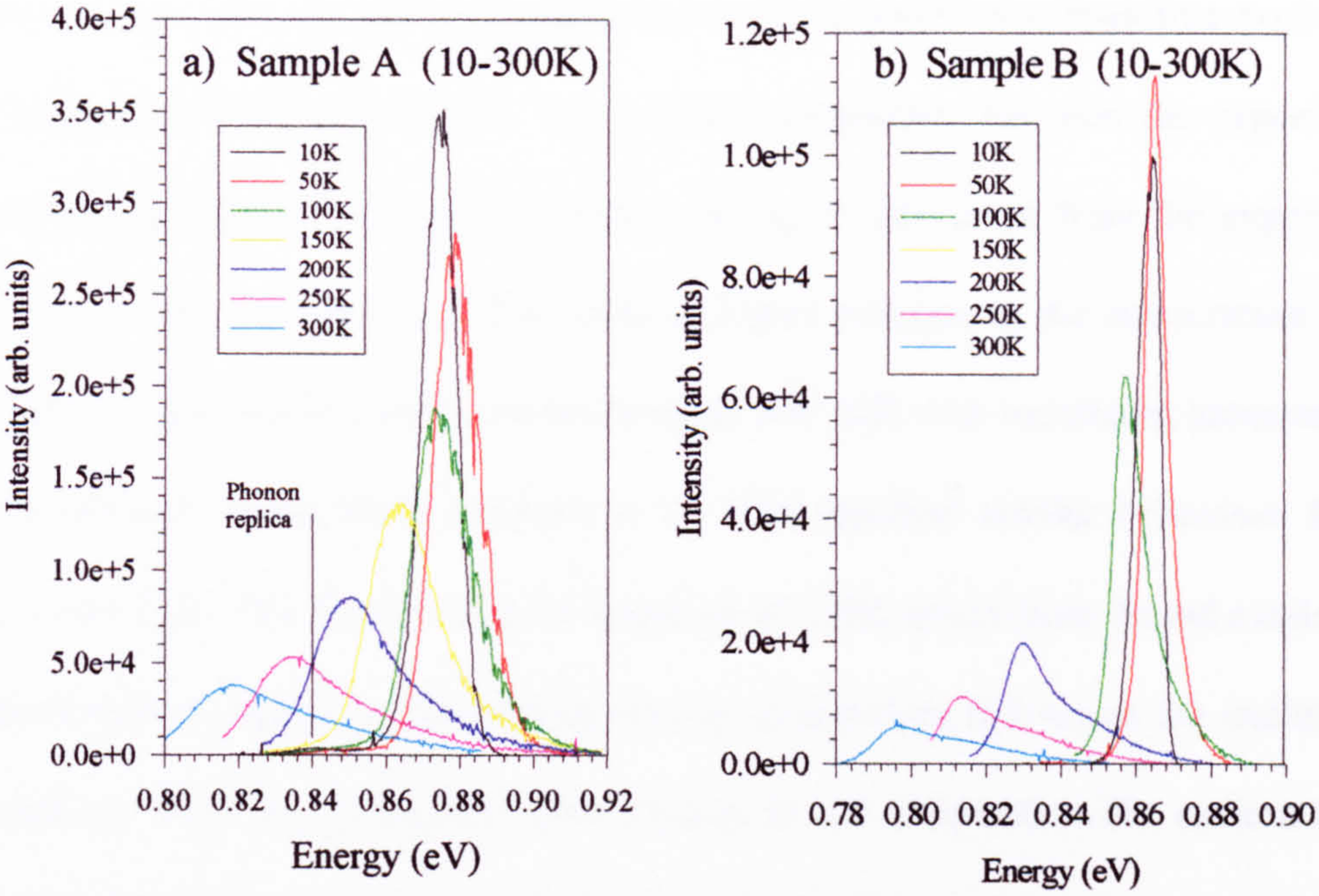

Figure 3-2 *PL spectra at different temperatures for a) sample A and b) sample B. A He-Ne laser with a power density of 2Wcm^{-2} was used as the excitation source.*

Figure 3-2a) also shows the evolution of the PL spectra as a function of increasing temperature. At 300K, the PL peak is still detectable indicating that the emission is intrinsic.

Figure 3-3 compares the temperature dependent experimental bandgap for sample A with the calculated bandgap using the Varshni equation for $In_{0.53}Ga_{0.47}As$, taken from *Schwedler et al.* [17],

$$E(T) = E(0) - \frac{\alpha T^2}{T + \beta} \qquad \text{Eq 3-1}$$

where β=100K and the temperature coefficient, α, is 3.2×10^{-4}eV/K. The values of α and β were obtained from the known bulk values for GaAs, InP and InAs [31]. The e1-hh1

transition value from the absorption measurements (luminescence from free excitons) can be used to determine E(0) in Eq 3-1. For a direct comparison between the experimental and calculated bandgap values, the confinement energy is subtracted from the experimental e1-hh1 PL emission. The emission first shifts to higher energies as the temperature is raised to 50K before following the conventional bandgap red shift with increasing temperature due to electron-phonon interactions. *Skolnick et al.* [32] reported similar behaviour for a 150Å InGaAs/InP QW. This implies that the emission at <50K arises from bound excitons and the observed shift to higher energy with increasing temperature follows as the excitons become unbound. As there are no impurity lines evident at low temperature PL, exciton localisation is assumed to occur at potential (interface) fluctuations arising from variations in well thickness. However, if the InGaAs is not uniformly alloyed, there may be localisation of excitons occurring in the well and/or at the interfaces. Above 50K, the excitons are free (mobile) and the PL peak energy follows the Varshni equation for InGaAs.

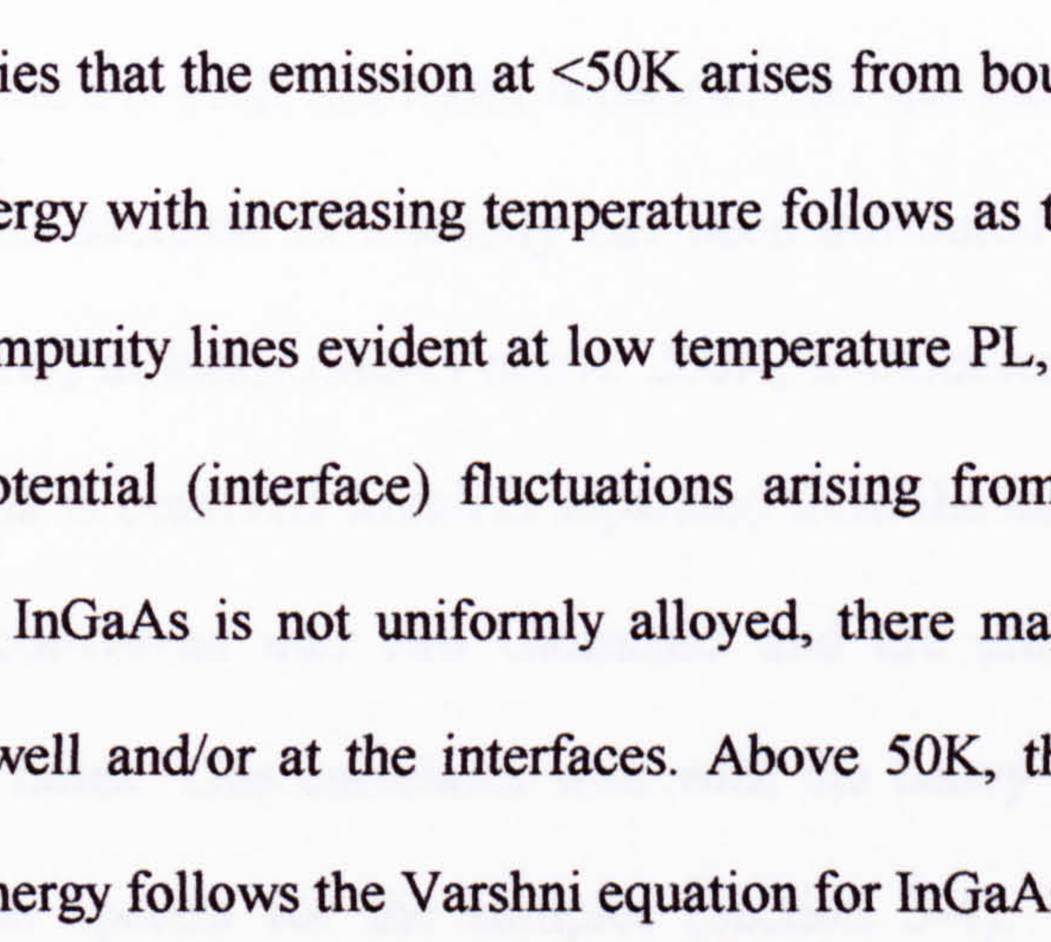

Figure 3-3 *Temperature dependent PL peak position for sample A and calculated peak positions using the Varshni formula.*

Figure 3-2b) also shows the PL peaks as a function of increasing temperature for sample B. In this case, the PL shifts to lower energy following the band-edge variation and luminescence is still detectable at 300K indicating that the emission is intrinsic. An initial blue shift is observed implying that the excitons are not bound to potential (alloy) fluctuations. The blueshift is smaller for sample B than A indicating that the interfaces in sample B are smoother [28].

For both samples, the PL peak linewidth broadens and the intensity decreases with increasing temperature. The decrease in intensity has been attributed to thermal emission from the QW [33]. However, at temperatures above 200K, a shoulder located on the high energy side of the main peak is observed which is separated from the main peak by ~20meV. These spectra can be deconvolved into two Gaussians and are attributed to transitions involving light and heavy holes. This correlates well with the heavy and light hole peaks observed in the absorption spectra for the samples (section 3-4). The FWHM for the Gaussian attributed to the heavy holes is ~16 and 10meV for samples A and B respectively. For the light holes, the corresponding linewidths are ~33 and 25meV. The linewidth for the light holes is likely to be overestimated because of the additional contributions from band to band emission.

The integrated intensity of the PL peaks is displayed as Arrhenius plots in Figure 3-4. Activation energies (E_a) for samples A and B are deduced assuming the luminescence obeys the expression [34],

$$I(T) = \frac{I_o}{1 + C\exp\left(-E_a / k_B T\right)} \qquad \text{Eq 3-2}$$

where I(T) is the integrated intensity of the PL emission peak at temperature T, I_o is the integrated intensity of the PL emission peak at the lowest measurement temperature (10K), k_B is Boltzmann's constant and C is the pre-exponential factor related to impurities and defects within the lattice which acts as a loss mechanism for radiative recombination. E_a is assumed to correspond predominantly to thermal escape of the carriers from the well.

The activation energy measured from the steepest part of the curve yields values of (28±2)meV and (18±2)meV for samples A and B respectively. As the CB and VB potential barriers are higher for sample A than B, the activation energy is expected to be greater for the former. However, the value of E_a for samples A and B is lower than expected assuming the electrons are thermally emitted and taking into account the confinement energy which is ~60 and 50meV respectively. For sample B (Figure 3-4b)) the integrated emission at 50K is greater than 10K due to bound excitons at the interface de-trapping at higher temperatures [29].

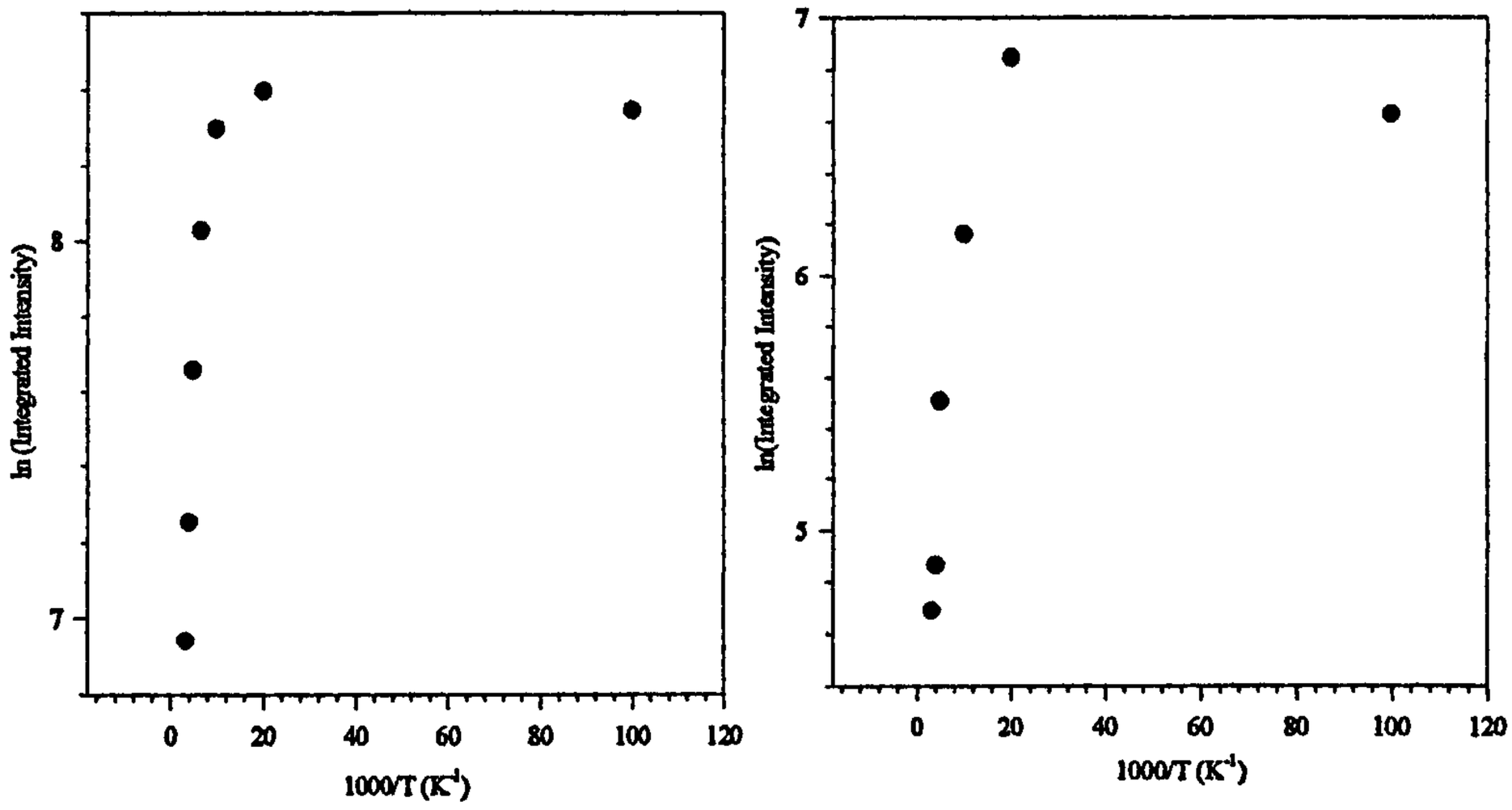

Figure 3-4 *Arrhenius plots for samples A and B yielding activation energies of 28 and 18meV respectively.*

Low temperature PL results yield information only on the e1-hh1 transition energy as the light hole band is insufficiently populated for any significant recombination to occur. In order to determine the higher lying states, PLE and transmission experiments were performed on the samples. Unfortunately, the PLE results (using a lamp and monochromator as excitation source) resulted in a rather weak signal and so transmission experiments were carried out to determine the energies of the higher lying states. These results were then compared with modelled results to determine the shape of the well.

3.3 Absorption Experiments and Computer Modelling

3.3.1 Parameters used in the Transfer Matrix model

The conventional way of displaying transmission data is to plot the optical absorption spectrum which is derived from the intensity of the transmitted light using the Beer-Lambert Law (see introduction 1). The absorption peaks can be assigned to the confined exciton transitions using the transfer matrix model [See Appendix A for details] [9, 35]. The finite potential well can be modelled assuming an ideally smooth interface or grading the first, second (asymmetric) or both interfaces (symmetric). For sample A, the material parameters such as the effective mass of a carrier in an alloy are assumed to follow Vegard's Law and are linearly interpolated between values of the constituent binaries except for the value of the bandgap. As sample B contains a quaternary barrier, the material parameters are calculated using equations taken from the 'Properties of InP' [37].

Sample A - The bandgap of bulk $In_xGa_{1-x}As$ as a function of the In content x at 2K is given in Eq 3-3 [36],

$$E_g = 1.519 - 1.584x + 0.475x^2 \qquad \text{Eq 3-3}$$

The band offset ratio (ΔE_c:ΔE_v) for InGaAs/InP has been reported by many authors and ranges from 36:64 [40], 40:60[30], 42:58[39], and 45:55[30]. *Cavicchi et al.* [40] calculated a CB:VB potential of 210:390meV for a lattice matched InGaAs/InP QW of well width 70Å. As the nominal well width of sample A is 70Å, the 36:64 ratio was chosen which gives a conduction band potential of 213meV and a valence band potential of 396meV. The

effective masses for the electron, heavy and light holes were obtained from *Krijn et al.* [41] and are displayed in Table 3-1.

Table 3-1 *Effective mass values for $In_{0.53}Ga_{0.47}As$ and InP*

	m^*_e/m_0	m^*_{hh}/m_0	m^*_{lh}/m_0
InGaAs	0.041	0.470	0.050
InP	0.080	0.560	0.120

Sample B - As the barriers consist of four elements, the parameters cannot be linearly interpolated between the binaries. All the following equations are taken from *Adachi* [42] assuming the $In_xGa_{1-x}As$ wells and $In_xGa_{1-x}As_yP_{1-y}$ barriers are lattice matched to the InP substrate. The bandgap is given at 300K as a function of the In content x and the As content, y [43];

$$E_g = 1.35 + (0.748x + 0.642)x + (0.101y - 1.101)y - (0.28x - 0.109y + 0.159)xy \qquad \text{Eq 3-4}$$

The band offset potentials were calculated from Eq 3-5 and 3-6 which yield a conduction band potential of 131meV and a valence band potential of 128meV.

$$\Delta E_c(meV) = 271 - 268y + 3y^2 \qquad \text{Eq 3-5}$$

$$\Delta E_v(meV) = 350 - 502y + 152y^2 \qquad \text{Eq 3-6}$$

The effective masses for electrons, heavy and light holes of $In_xGa_{1-x}As_yP_{1-y}$ are calculated according to,

$$m_e^* = 0.077 - 0.050y + 0.014y^2 \qquad \text{Eq 3-7}$$

$$m^*_{hh} = 0.45m_0 \text{ [44]}$$

$$m^*_{lh} = 0.12 - 0.069y \quad \text{[45]}, \qquad \text{Eq 3-8}$$

where m_0 is the free electron mass. An exciton binding energy of 10meV [46] for samples A and B was assumed throughout this chapter.

3.3.2 Absorption and transfer matrix modelled results

Sample A - The optical absorption spectrum for sample A measured at 77K is shown in Figure 3-5 a). Four peaks are clearly resolved which have to be assigned to confined exciton transitions in the QWs.

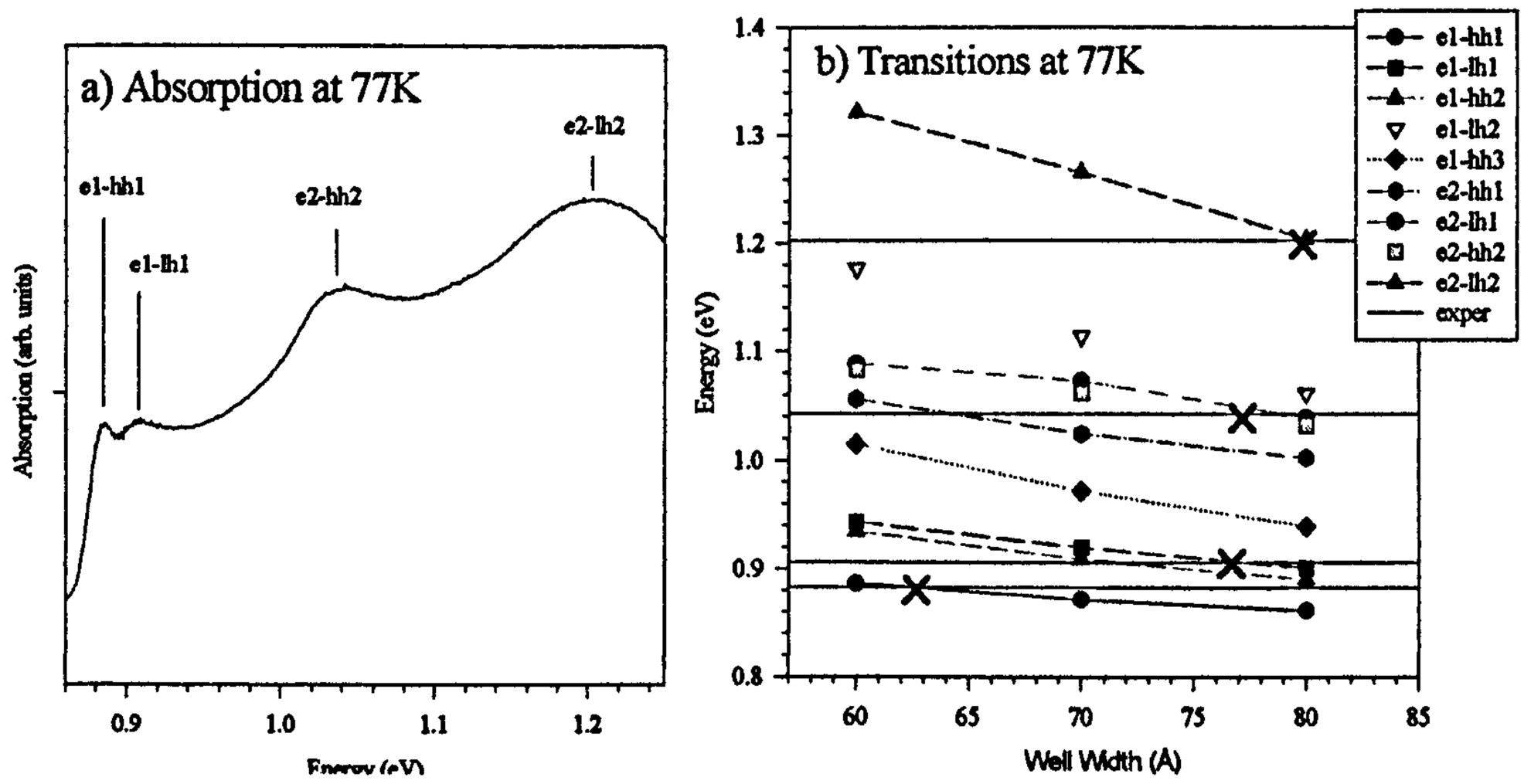

Figure 3-5 *Sample A a) Absorption data at 77K b) predicted heavy and light hole transitions (coloured lines) compared with experimental data (full horizontal lines) at 77K*

The absorption spectrum exhibits the behaviour expected for a QW with exciton effects at each 2D bandedge up to 1.2eV. Above 1.2eV there is a reduction in transmittance

which is due to multiple interference reflections occurring in the substrate sample and becomes apparent after the ratioing procedure. A Stokes shift of ~15meV is measured between the emission and absorption peaks for the e1-hh1. The absorption peak always corresponds to intrinsic processes, that is the production of free excitons, whereas the emission peak occurs at lower energies due to bound excitons. The measured Stokes shift is slightly larger than the value of 12meV obtained by *Skolnick et al.* [32], for a 110Å InGaAs/InP QW. In the present case, no additional impurity peaks were observed in the low temperature PL spectrum (for example, free to bound) and the Stokes shift is attributed to potential fluctuations at the interface [32, 47].

Table 3-2 *Experimental transition values compared with theoretical calculated values for a 70Å square well for sample A*

Transitions at 77K	a) Experimental (eV)	b) Theory (eV)
e1-hh1	0.8828	0.8718
e1-lh1	0.9063	0.9200
e2-hh2	1.0422	1.0616
e2-lh2	1.2030	1.2656

Figure 3-5b) shows the predicted heavy and light hole transitions for a well width ranging from 60-80Å compared with experimental data. The parameters described in section 3.3.1 appropriate to sample A are substituted into the transfer matrix model (Appendix A). Transitions ranging from strong (e1-hh1) to weak (forbidden e1-hh2) have been included in order to assign the experimental transitions. The experimental lines cross the predicted strong transitions as indicated in Figure 3-5b) and hence the experimental lines have been

tentatively ascribed to the strong transitions e1-hh1, e1-lh1, e2-hh2 and e2-lh2. The experimental lines do not cross the predicted lines at the intended well width of 70Å. It can be seen from Table 3-2 that the energy of the e1-hh1 experimental transition is greater than the theoretical result whilst the experimental transition energies of the higher lying confined states are located at lower energies than the corresponding theoretical results. The points where the curves (predicted value) cross the horizontal lines (experimental value), indicate the expected well width for that transition. Although the three higher lying transitions are consistent with a well width of about 75-80Å, this value is inconsistent with the e1-hh1 transition which indicates a rather narrower well around 60Å. As mentioned in section 3.1, such a variation in the well could arise from (i) a non-square well potential due to a compositional variation in the well or (ii) a substantial non-parabolicity in the effective mass. The effect of non-parabolicity on the optical transitions is estimated in section (3.3.3) and is found to make only minor modifications to the predicted energies. In section 3.4 XRD measurements are presented which show that there are significant compositional variations across the QW which can account for the disparity in the predicted and measured optical transitions.

Sample B - The optical absorption spectrum for sample B measured at 77K is shown in Figure 3-6a).

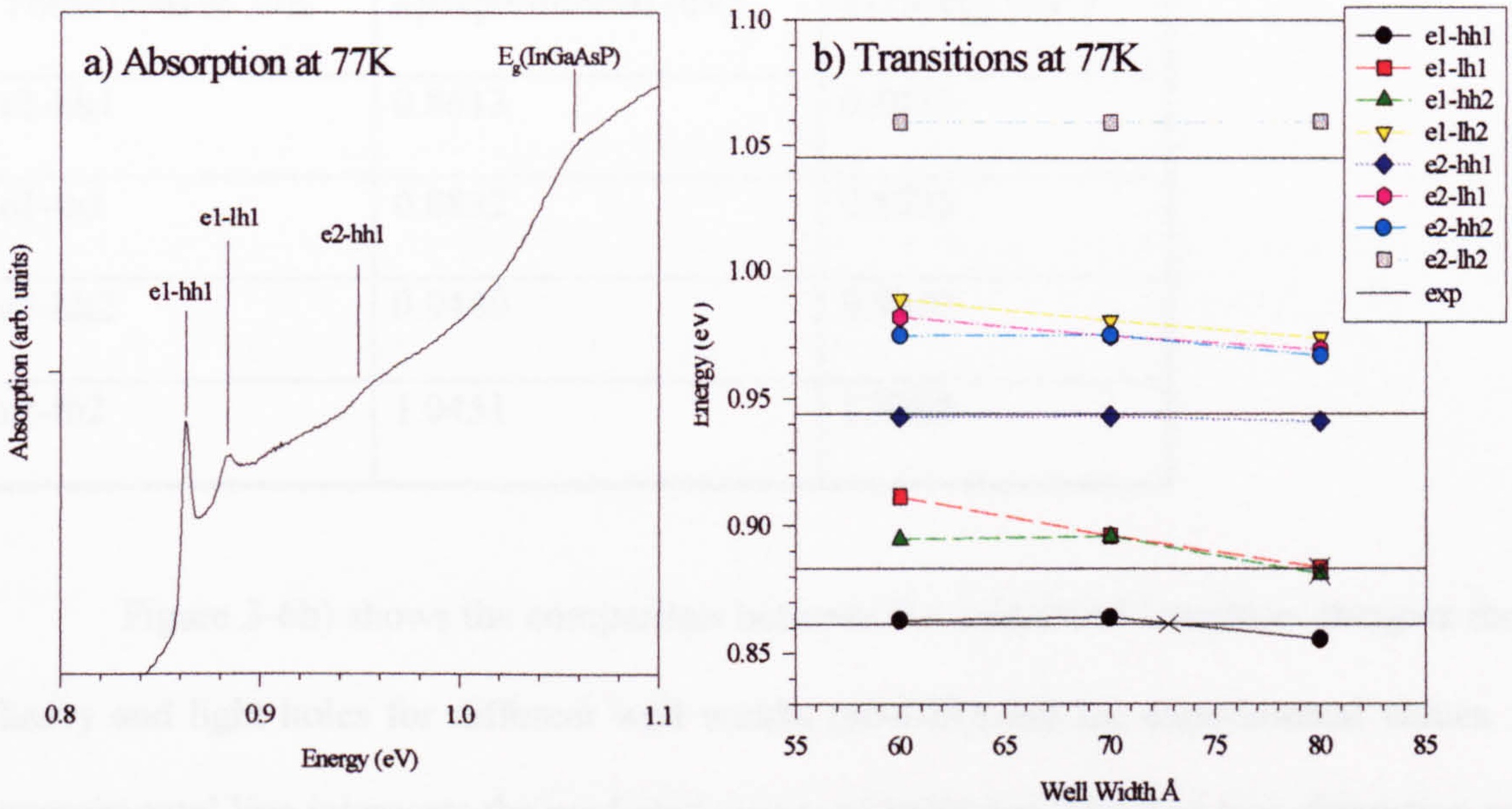

Figure 3-6 Sample B *a) Absorption data b) predicted heavy and light hole transitions (coloured lines) compared with experimental data (horizontal lines) at 77K*

The measured Stokes shift for sample B is ~5meV. Again, as no additional impurity lines were evident in the low temperature PL spectra, the Stokes shift is attributed to interface trapping. This result implies higher quality interfaces for sample B compared with sample A.

A similar analysis to that used for sample A is performed on sample B in order to confirm the identity of the absorption peaks. The first two peaks are strong, whereas the third and fourth absorption peaks are much weaker. The e1-hh1 and e1-lh1 exciton transitions are well resolved for sample B compared with sample A.

Table 3-3 *Experimental transition values compared with calculated values for a 70Å square well for sample B*

Transitions at 77K	a)Experimental (eV)	b)Theory (eV)
e1-hh1	0.8613	0.8410
e1-lh1	0.8832	0.8730
e2-hh2	0.9440	0.9432
e2-lh2	1.0451	1.0362

Figure 3-6b) shows the comparison between the calculated transition energies for the heavy and light holes for different well widths (60-80Å) and the experimental values. The experimental line intercepts the predicted curves as indicated. The first two absorption peaks can be attributed to the strong e1-hh1 and e1-lh1 transitions. The third feature may in fact be the e2-hh1 transition (Figure 3-6b)) as this predicted transition is within a couple of meV of the experimental value. The fourth peak is also weak and is located too close to the bandgap of the InGaAsP barrier (~1.05eV at 77K) to make an unambiguous assignment possible. Table 3-3 compares the experimental transition values shown in Figure 3-6a) with the theoretically calculated values for a square well of width 70Å. The measured e1-hh1 and e1-lh1 transitions are slightly higher in value than the calculated transitions. Again the results are not consistent with a 70Å well. The effect of non-parabolicity in the effective mass is considered in the following section.

3.3.3 Non-parabolicity

Non-parabolicity of the electron effective mass can have a significant effect on the higher lying confined level energies and may account for the discrepancies between experimental and theoretical results obtained for samples A and B [48]. However, the degree of non-parabolicity for the InGaAs QWs is unknown and the procedure adopted here is to use an empirical relationship derived for GaAs/AlGaAs [46]:

$$m_e^* = m_{eb}^*\left(1+2\frac{E_c}{E_g}\right) \qquad \text{Eq 3-9}$$

where m^*_{eb} is the bandedge effective mass, m^*_e the modified effective mass, E_c the confinement energy and E_g the bandgap.

The bandedge effective mass value for $In_{0.53}Ga_{0.47}As$, m^*_{eb}, was calculated by linearly interpolating between the corresponding binaries (Table 3-1) as described in section 3.3.1. The effective mass m^*_{en} for each confined state, n, can then be calculated using Eq 3-9. This value is then substituted into the transfer matrix model to obtain the 'new' value of the transition energy for different well widths. Figure 3-7a) shows the changes in predicted transition energy levels using the new effective masses for sample A. For the e1-hh1 and e1-lh1 confined levels, the electron effective mass increases from $m^*_{eb}=0.041m_0$ to $m^*_{e1}=0.047m_0$ and introduces only a small difference to the position of the transition energy [30]. For the next heavy and light hole transitions e2-hh2 and e2-lh2, the transition energy is lowered by ~25meV for the wider well. The transfer matrix model reveals that the second electron confined state (e2) is barely confined for the narrower (60Å) well and, hence, it cannot be assumed with confidence that the e2 state is confined for such a narrow well. The effect of the non-parabolicity can be disregarded for a well of this width. Changing the

effective mass seems to have a negligible effect on the confined states and the transition energies still correspond to wells of 55-80Å in width.

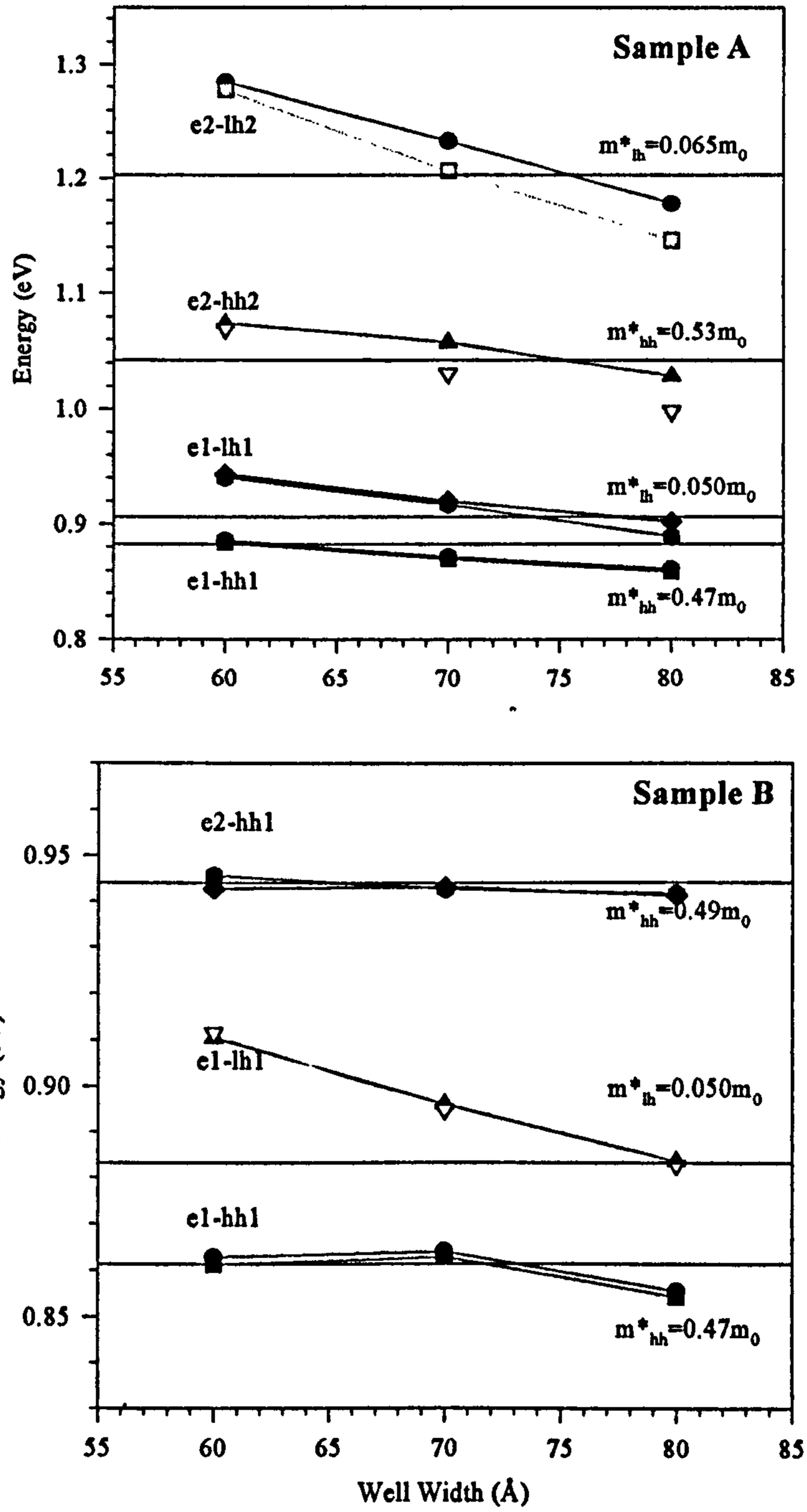

Figure 3-7 *The effect of changing the effective mass and well width for the heavy hole states for a) sample A and b) sample B*

Figure 3-7b) shows the changes to the predicted transition energy levels using the modified electron effective masses for sample B. As expected, the change in effective mass makes only a small difference to the positions of the e1-hh1 and e1-lh1 states. A negligible separation between the transition energies is also observed for the e2-hh2 and e2-lh2 states. According to the transfer matrix model, the e2-hh2 and e2-lh2 transition cannot occur as the second heavy and light hole states are not confined due to the relatively shallow VB potential compared with sample A. Changing the effective mass has an inconsequential effect on these transition energies as shown in Figure 3-7b).

From the optical measurements and confined state modelling, it can be concluded that the QW potential is not square. Unfortunately, the exact shape of the well cannot be determined solely from optical measurements. Therefore another characterisation technique, XRD, has been used to investigate the well compositions for these structures and will be discussed in the following section.

3.4 XRD Results

3.4.1 Preliminary square well simulations

X-ray diffraction (XRD) measurements were performed on the samples in order to obtain information about the crystalline structure [49]. XRD is highly sensitive to changes in lattice parameter due to small deviations in composition even when the layers are only a few monolayers thick [7]. Rocking curves of the (004) reflections were obtained and these were simulated using a model based on dynamical x-ray diffraction [50]. The distribution of strain in the simulated layers was modified until a good fit was obtained with the experimental data.

Sample A - The experimental (004) reflection rocking curve is shown in Figure 3-8. The most prominent feature is the InP substrate peak located at ~31.7°. The satellite peaks, situated on either side of the substrate peak, correspond to (004) reflections from the InGaAs epilayer. The satellite peaks closest to the substrate peak are referred to as the first-order ($m=\pm1$) superlattice peaks, the adjacent satellite peaks are the second order ($m=\pm2$) etc. For lattice matched systems, the zeroth order peak originating from the $In_xGa_{1-x}As$ epilayer is superimposed on the main InP substrate peak and there should be no splitting between the peaks [50]. However, Figure 3-8 shows a slight shoulder to the lower angle side of the main InP peak indicating that the structure is not completely strain free. The angular separation of the substrate and epilayer peaks relates to the strain due to the difference in lattice parameter. The splitting between the substrate peak and the epilayer peak, $\Delta\omega$, (Eq 1-10) is negative implying that the structure is under compressive strain.

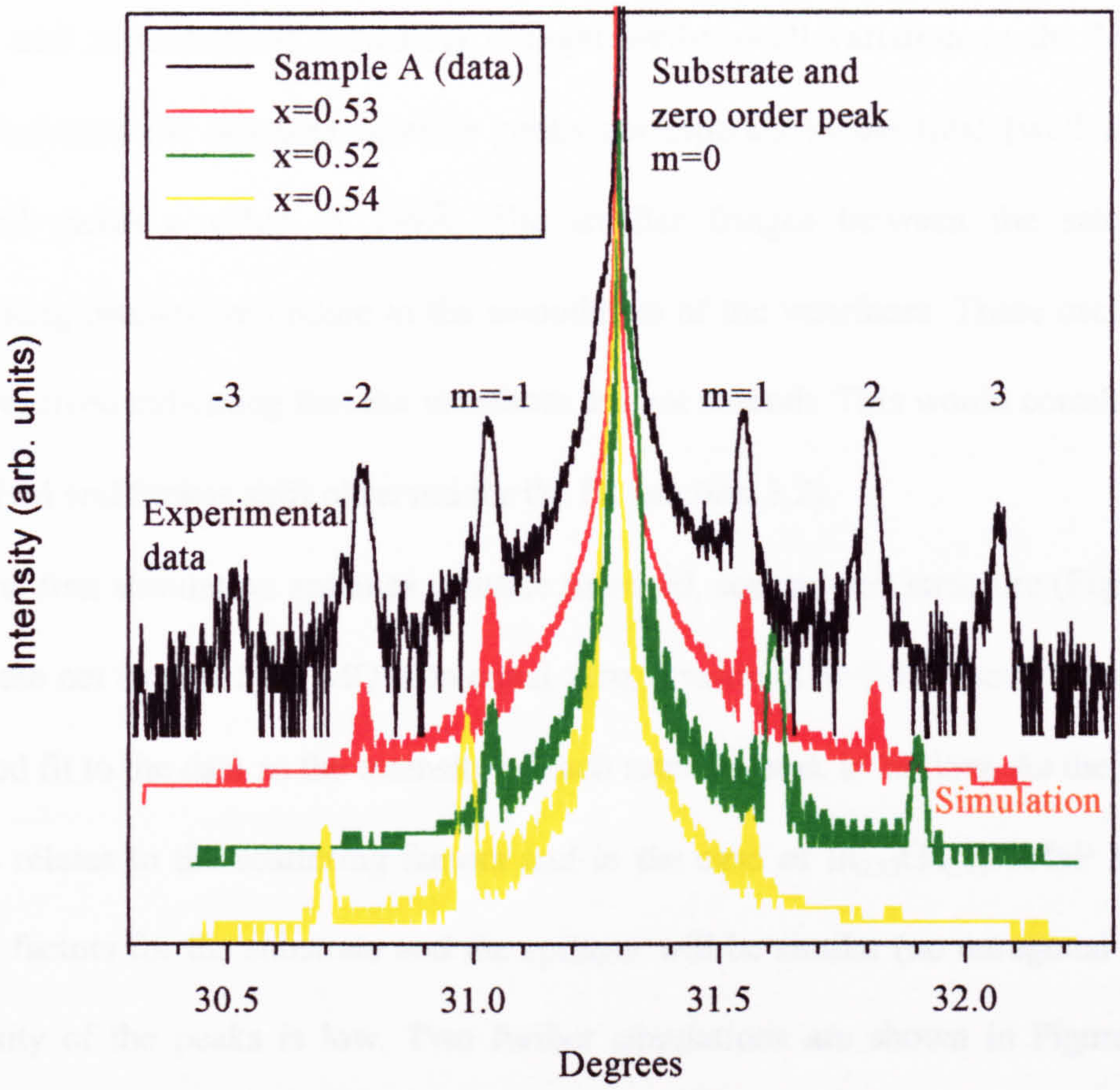

Figure 3-8 *Experimentally determined (004) reflection rocking curve (black). The red simulation represents the rocking curve assuming a square well which is lattice matched* $In_xGa_{1-x}As$ *(x=0.53) to InP. A Ga rich (x=0.52) and an In rich (x=0.54) square well structure is represented by the green and yellow simulation respectively for sample A.*

Benzequen et al. [6] obtained a similar result and concluded that the $In_xGa_{1-x}As$/InP structure was under a small biaxial compressive strain [52]. The slight shoulder to the lower angle side of the main InP peak could also originate from the diffusion of As in the substrate and/or capping layer [53]. The disappearance of the shoulder after etching the capping and substrate layers would confirm As diffusion. The first and second order satellite peaks are clearly visible but the third order peaks, which are most sensitive to interface grading [51],

are weak and asymmetrical indicating a slight well-to-well variation in the MQWs. The distance between the adjacent satellite peaks corresponds to the total (well and barrier) period and yields a value of 199Å. The smaller fringes between the satellite peaks (Pendellosung oscillations) relate to the smoothness of the interfaces. These oscillations are not well resolved indicating that the interfaces are not smooth. This would correlate with the large FWHM and Stokes shift observed for the PL (section 3.2).

The first simulation assumes a lattice matched, square well structure (Figure 3-8). In order for the net strain of the MQW to equal zero, a value of x=0.53 is used which does not give a good fit to the data as the intensity of each satellite peak is too low. As the intensity of the peaks relates to the scattering factors and in the case of $In_{0.53}Ga_{0.47}As$/InP MQWs, the scattering factors for the substrate and the epilayer will be similar (no tetragonal distortion), the intensity of the peaks is low. Two further simulations are shown in Figure 3-8 for a tensile (x<0.53) and compressive (x>0.53) strained SW structure. For the tensile strained SW (green simulation), the satellite peaks shift to higher angles and the peaks on the RHS of the substrate peak are more intense. This correlates with the high intensity satellite peaks on the RHS of the experimental data. For the compressive strained SW (yellow simulation), the satellite peaks are more intense on the LHS of m=0 and shifted to lower angles. This corresponds to the m=0 peak which is situated to the lower angle side of the InP peak. The Pendellosung fringes are more easily distinguished. However, the simulations provide a poor fit to the experimental data as the simulated satellite peaks are less intense than the experimental peaks.

From the XRD data, it has been determined that the InGaAs well is under a slight negative strain as the satellite intensities on the right hand side (RHS) (m>0) of the zero-

order peak are slightly more intense than those on the left hand side (LHS) (m<0) but the net strain of the MQWs is positive as m=0 is situated to the low angle side of the InP peak.

3.4.2 *Graded and strained interfacial layers*

The rather poor agreement between the rocking curve measurement and simulation in Figure 3-8 suggests that the assumption of a square well cannot be correct. To improve the fit, the existence of interfacial strain layers on the scale of MLs is assumed as outlined in section 3.1. *Krost et al.* [10] have shown that both the relative intensity of the satellite peaks can be increased by introducing interfacial layers at both interfaces. In addition these authors showed that the envelope of the intensities depends critically on the correct sign and differences in the strain values. Section 3.1 details how many groups have used different models to explain the well shape. The increased incorporation of As compared with P (memory effect) and group V exchange reactions during growth usually lead to strained interfacial layers and/or graded interfaces. Therefore, rocking curves have been simulated by assuming various interfacial MLs and graded layers as follows:

1) A positively strained $InAs_yP_{1-y}$ interfacial ML at the InP/InGaAs interface or the InGaAs/InP interface [5, 8, 10, 11, 15].

2) A negatively strained $In_xGa_{1-x}As_yP_{1-y}$ interfacial ML at the InGaAs/InP interface [8, 10, 15, 18].

3) Strained MLs on both sides of the well [6, 28].

4) Graded interfacial layers [5, 14, 26, 35].

Strained $InAs_yP_{1-y}$ MLs introduced at the InP/InGaAs interface produces a positive strain value as InAsP has a larger lattice constant than the InP. This results in a phase shift ($\Delta\omega$) between the x-rays reflected from the InGaAs and from the InP lattice which affects the interference conditions [7]. For the simulations, the number of MLs and the compositional values were iteratively varied until the best possible qualitative fit for the relative intensities of the satellite reflections is obtained. The substitution of As and P atoms during the growth process and resulting well shapes are described for each additional interfacial layer. Table 3-4 displays the chemical bond strengths between the group III and V atoms in lattice matched InGaAs/InP QWs [19].

Table 3-4 *Chemical Bonds strengths of In-P, In-As, Ga-As and Ga-P.*

III-V Bond	Bond Strength (kcal/mole)
In-P	47.3
In-As	48.0
Ga-As	50.1
Ga-P	54.9

Figure 3-9 illustrates the growth of the InGaAs/InP QW structure. The TMIn flow is kept constant throughout the growth of the structure. TMGa and group V sources (AsH_3 and PH_3) are switched 'on' and 'off' when required. For sample B, (InGaAs/InGaAsP) a constant flow rate of TMIn was also used throughout the structure but different AsH_3 and TMGa channels, set at different flow rates, are used depending whether the well or barrier is grown.

A large excess of group Vs is used which blocks the incorporation of carbon on the group V lattice sites. There are no growth halts or interruptions at the interfaces.

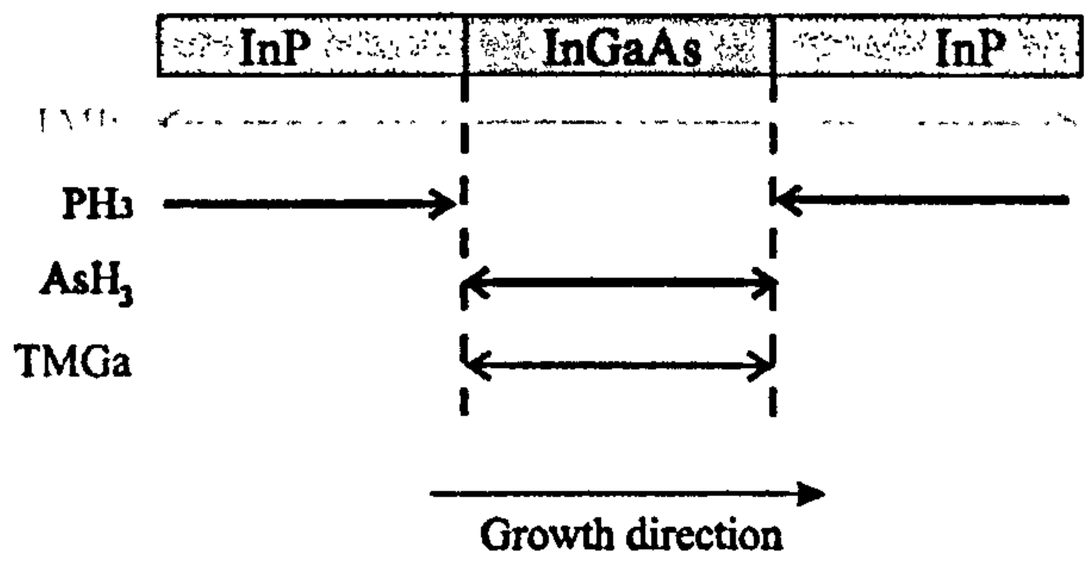

Figure 3-9 *Sequencing of group III and V sources during the growth of $In_{0.53}Ga_{0.47}As/InP$ MQWs. Arrows indicate when the sources are 'on'.*

1) *A positively strained $InAs_yP_{1-y}$ interfacial ML at the InP/InGaAs interface.*

The InP layer will be terminated by a layer of P atoms due to the excess PH_3 source used in the growth process. When the Ga and As sources are switched on to grow the InGaAs well, the higher incorporation rate of arsenic atoms means that arsenic will substitute for P creating a strained InAs(P) layer, due to the differences in the atomic bond lengths between In-As and In-P. The In-P bond is weaker than the In-As bond facilitating As substitution for P so an As/P exchange mechanism dominates (table 3-4). In the extreme case, Figure 3-10a), the top layer of P will be completely displaced by As. This gives rise to a ML of In-As with a strain of 3.2%.

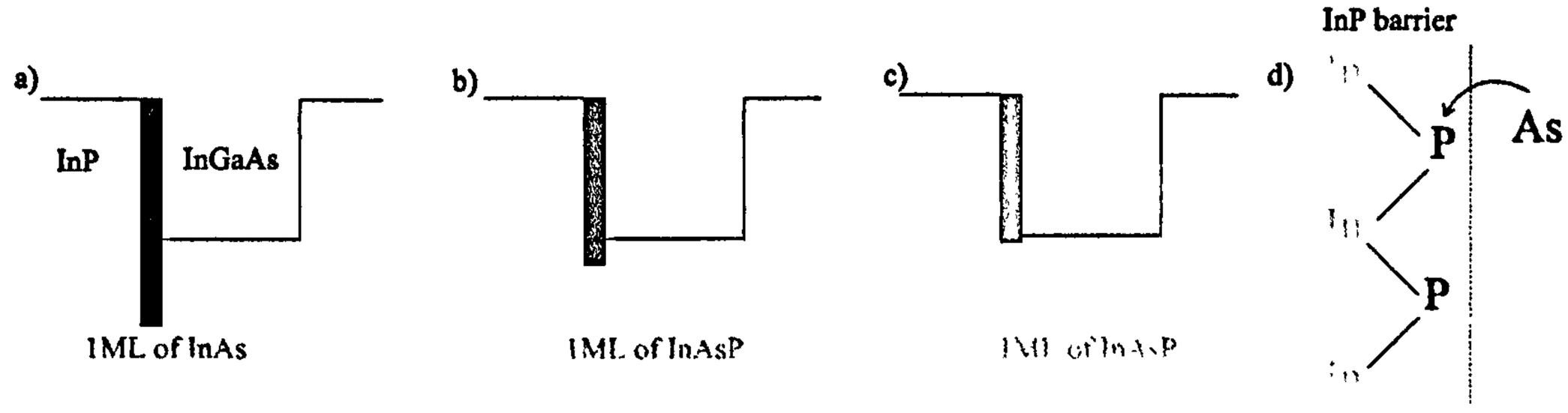

Figure 3-10 *Insertion of a positively strained $InAs_xP_{1-x}$ layer at the InP/InGaAs interface a) 1ML of InAs, b) 1ML of $InAs_{0.5}P_{0.5}$ and 3) 1ML of $InAs_{0.66}P_{0.34}$. c) Schematic of the As atoms substituting for the P atoms at the InP barrier surface.*

Assuming that the $In_{0.53}Ga_{0.47}As$ well remains lattice-matched, one monolayer of InAs is simulated at the InP/InGaAs interface. The satellite peaks are shifted to lower angles implying excess positive strain in the overall structure (Figure 3-11) and a poor fit to the data. Alternatively, a 1ML interfacial layer of $InAs_{0.5}P_{0.5}$ represents the situation where half the P atoms exchange with As (figure 3-10b). Finally a simulation assuming a 1ML interfacial layer of $InAs_{0.66}P_{0.34}$ at the InP/InGaAs interface is shown in figure 3-10c). The As/P exchange is confined to 1ML as it is unlikely that P will substitute for As once P is displaced from its original atomic site. With the inclusion of each of these strained layers, the simulated spectral position of the m=0 order peak and the other satellite peaks shift to smaller angles. This indicates that there is a net positive strain within each period of the MQW and none of these simulations provide a good fit to the data as shown in Figure 3-11.

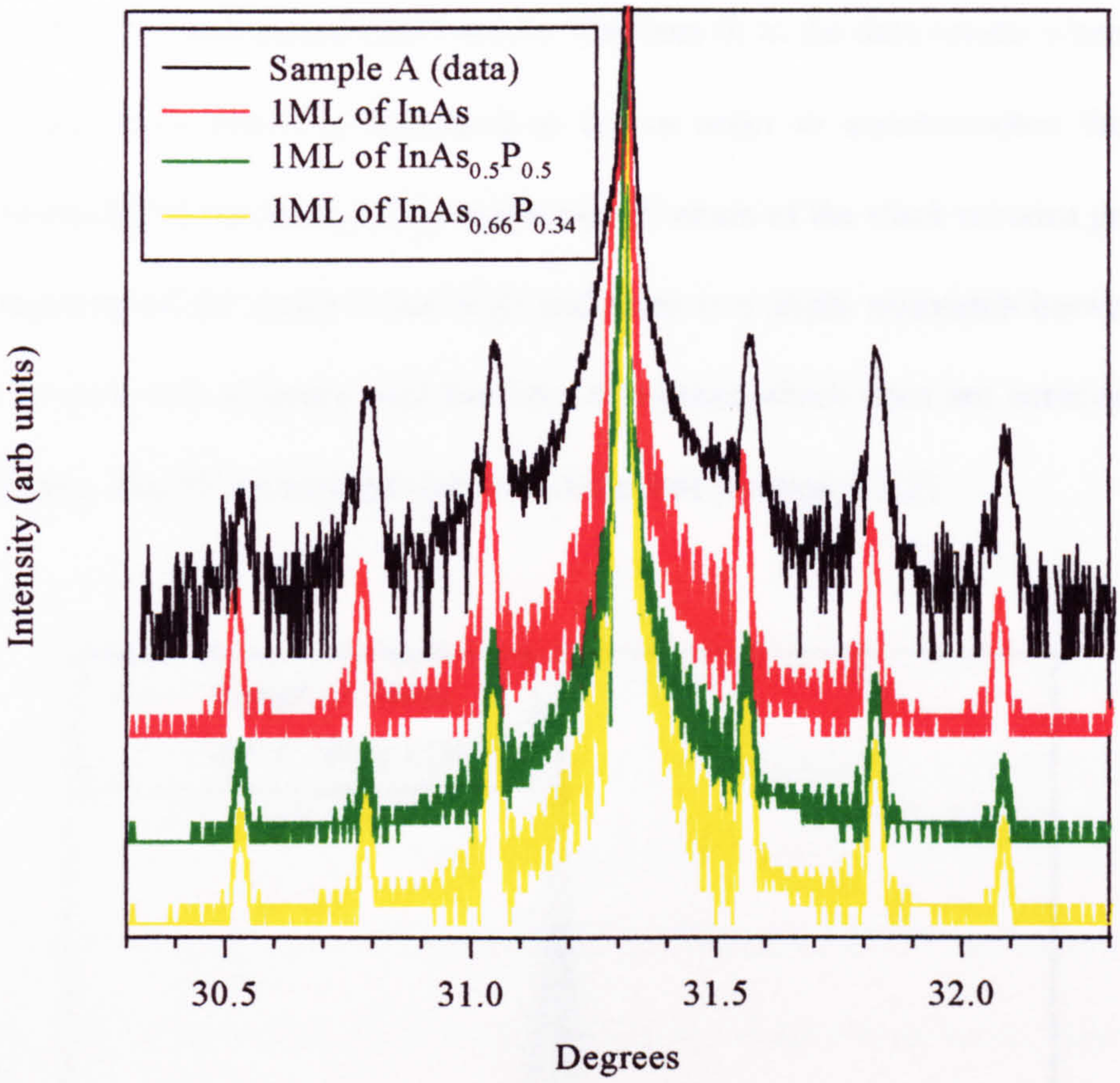

Figure 3-11 *XRD rocking curve (black) and simulations of 1ML of InAs (red), 2MLs of $InAs_{0.5}P_{0.5}$ (green) and 3MLs of $InAs_{0.66}P_{0.34}$ (yellow) strained interfacial layers at the InP/InGaAs interface.*

Figure 3-12 displays the XRD simulation corresponding to the inclusion of positively (compressively) strained MLs of InAsP at the InP/InGaAs interface. In order to produce a better fit to the data, the In concentration in $In_xGa_{1-x}As$ as well as the As concentration in $InAs_yP_{1-y}$ are altered heuristically. The simulation shows that the satellite intensities on the left hand side (LHS) ($m<0$) of the main SL peak are weaker than those on the right hand side (RHS) ($m>0$) as the strain in the $In_xGa_{1-x}As$ wells has become more negative [54], which

correlates well with the experimental XRD results. The best fit to the data results when the In fraction in the $In_xGa_{1-x}As$ layers is decreased to 0.5 in order to accommodate the large positive strain produced by the $InAs_{0.57}P_{0.43}$ so the overall strain of the stack remains positive. However, the intensity of the peaks is too high and there is a slight mismatch between the satellite peaks. In each case a square well has been simulated which does not correlate well with the optical data. The PL reveals that the well is tapered (section 3.3.2).

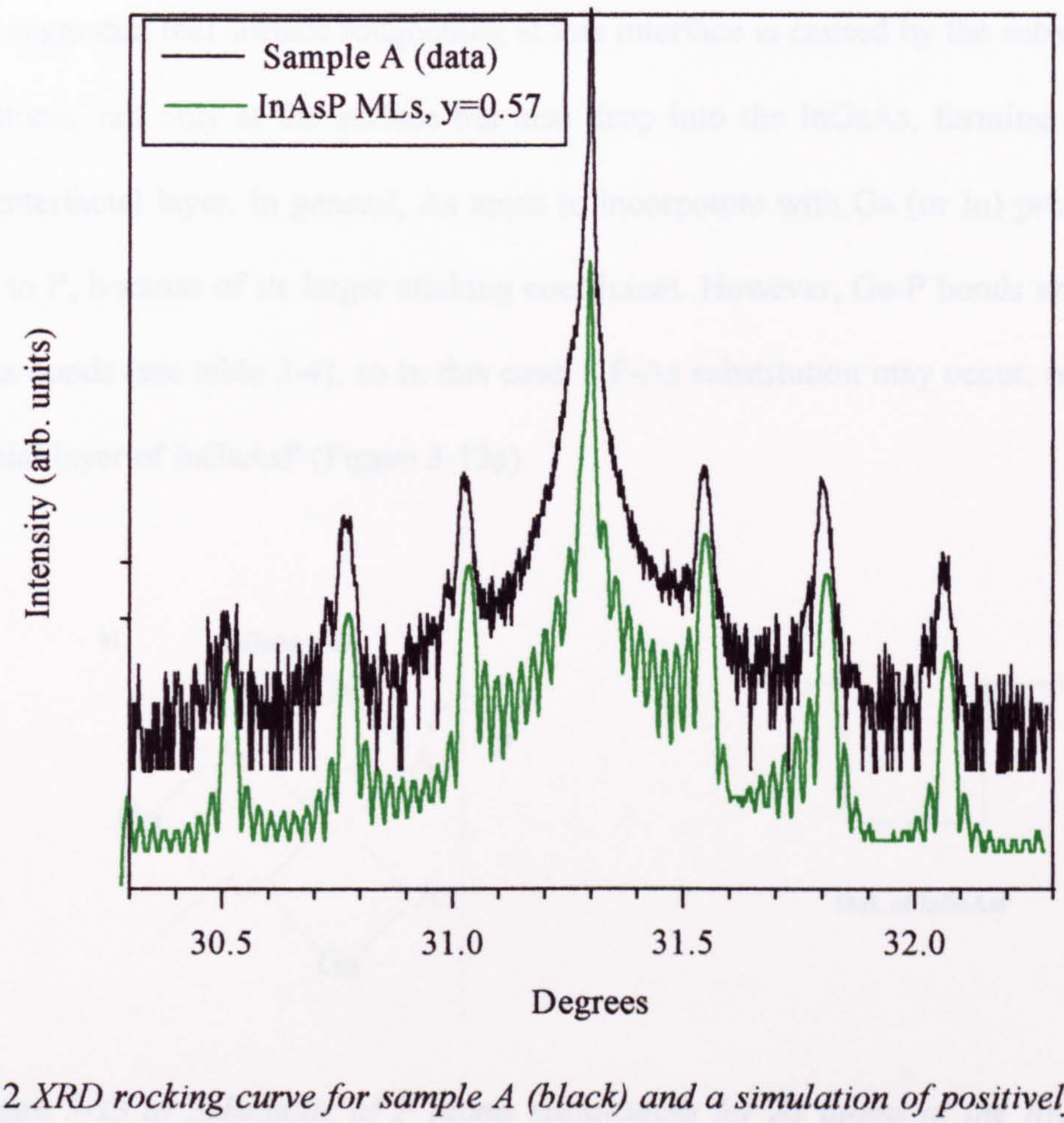

Figure 3-12 *XRD rocking curve for sample A (black) and a simulation of positively strained InAsP interfacial ML at the InP/InGaAs interface (green).*

b) An InAs(P) layer may also be present at the second InGaAs/InP interface although in this case it arises not from As/P exchange but the As memory effect. However, placing this positively strained layer at the upper or lower interface cannot be differentiated in x-ray simulations. Again, the simulation is based on a square well and does not fit the optical data.

2) *A negatively strained $In_xGa_{1-x}As_yP_{1-y}$ interfacial ML at the InGaAs/ InP interface.*

At the second interface, the InGaAs layer is assumed to be terminated with As. *Anan et al.* [21] suggested that surface roughening at this interface is caused by the substitution of As by P atoms, not only at the surface but also deep into the InGaAs, forming a strained InGaAsP interfacial layer. In general, As tends to incorporate with Ga (or In) preferentially compared to P, because of its larger sticking coefficient. However, Ga-P bonds are stronger than Ga-As bonds (see table 3-4), so in this case, a P-As substitution may occur, resulting in an interfacial layer of InGaAsP (Figure 3-13a).

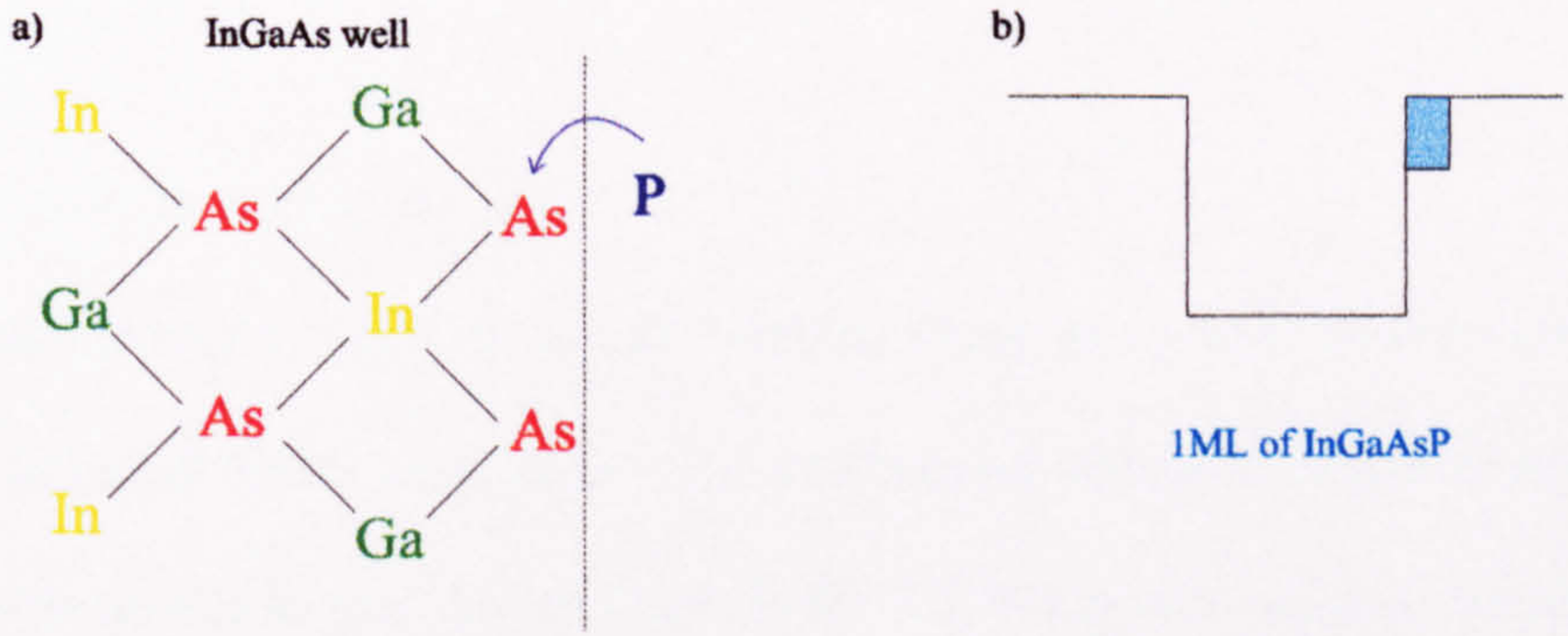

Figure 3-13 *a) Schematic of P atoms substituting for As atoms at the InGaAs well surface. b) Conduction band potential on insertion of a negatively strained $In_{0.53}GaAs_{0.5}P$ layer at the InGaAs/InP interface.*

In order to reproduce the experimental rocking curve, a 1ML and 3ML negatively strained $In_{0.53}Ga_{0.47}As_{0.5}P_{0.5}$ interfacial layer was introduced at the $In_{0.53}Ga_{0.47}As$/InP interface (Figure 3-13b)). The $In_xGa_{1-x}As_yP_{1-y}$ layer was more difficult to model as there were two group III and two group V atoms to be changed. As the overall strain in the MQWs is positive, introducing a negatively strained interfacial layer into the simulation will not fit the data as this shifts the satellite peaks to higher angles. *Benzaquen et al.* [6] also simulated a $In_{0.52}Ga_{0.48}As_{0.25}P_{0.75}$ quaternary layer under a biaxial tensile strain at the $In_xGa_{1-x}As$/InP interface and concluded that the peaks shifted to larger angles compared with the experimental case. Again the square well assumption does not correlate with the optical data. It can concluded that introducing a negatively strained layer into the simulation does not fit the experimental data.

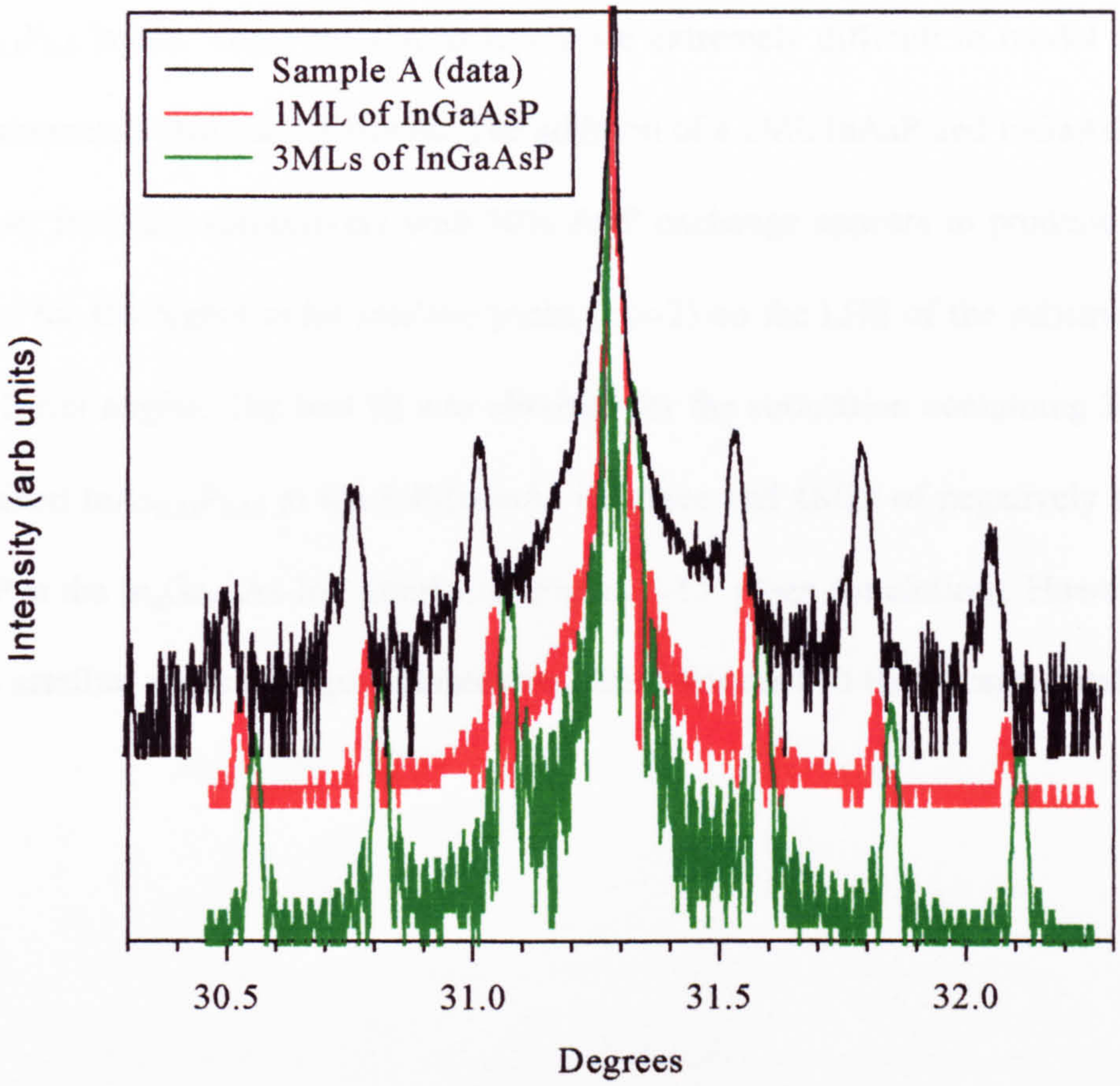

Figure 3-14 *XRD spectrum and simulations of a negatively strained $In_{0.53}GaAs_{0.5}P$ (reds) MLs and a 3ML $In_{0.53}GaAs_{0.5}P$ (green) at the InGaAs-InP interface.*

3) *Strained MLs on both sides of the well*

An alternative way of representing the average strain in a single period is to assume that InAsP and InGaAsP layers exist at the first and second interfaces respectively and are strained in opposite senses so that the net strain in the MQWs is still positive. Initially, 1ML of $InAs_{0.5}P_{0.5}$ and $In_{0.53}Ga_{0.47}As_{0.5}P_{0.5}$ at the first and second interfaces was simulated. This did not provide a good fit to the experimental data. The interfacial layers were then increased in width and Figure 3-15 shows simulations for various combinations of $InAs_{0.5}P_{0.5}$ and

$In_{0.53}Ga_{0.47}As_{0.5}P_{0.5}$ layers. These interfacial layers are extremely difficult to model as there are so many parameters that can be altered. The addition of a 2ML InAsP and InGaAsP at the lower and upper interface respectively with 50% As/P exchange appears to produce quite a good fit except for the higher order satellite peaks (m>-2) on the LHS of the substrate peak are shifted to lower angles. The best fit was obtained for the simulation containing 3MLs of positively strained $InAs_{0.31}P_{0.69}$ at the InP-InGaAs interface and 4MLs of negatively strained $In_{0.53}GaAs_{0.76}P$ at the $In_xGa_{1-x}As$-InP interfaces (Figure 3-15, green simulation). However, the LHS and RHS satellite peaks are equal in intensity which does not fit the experimental data.

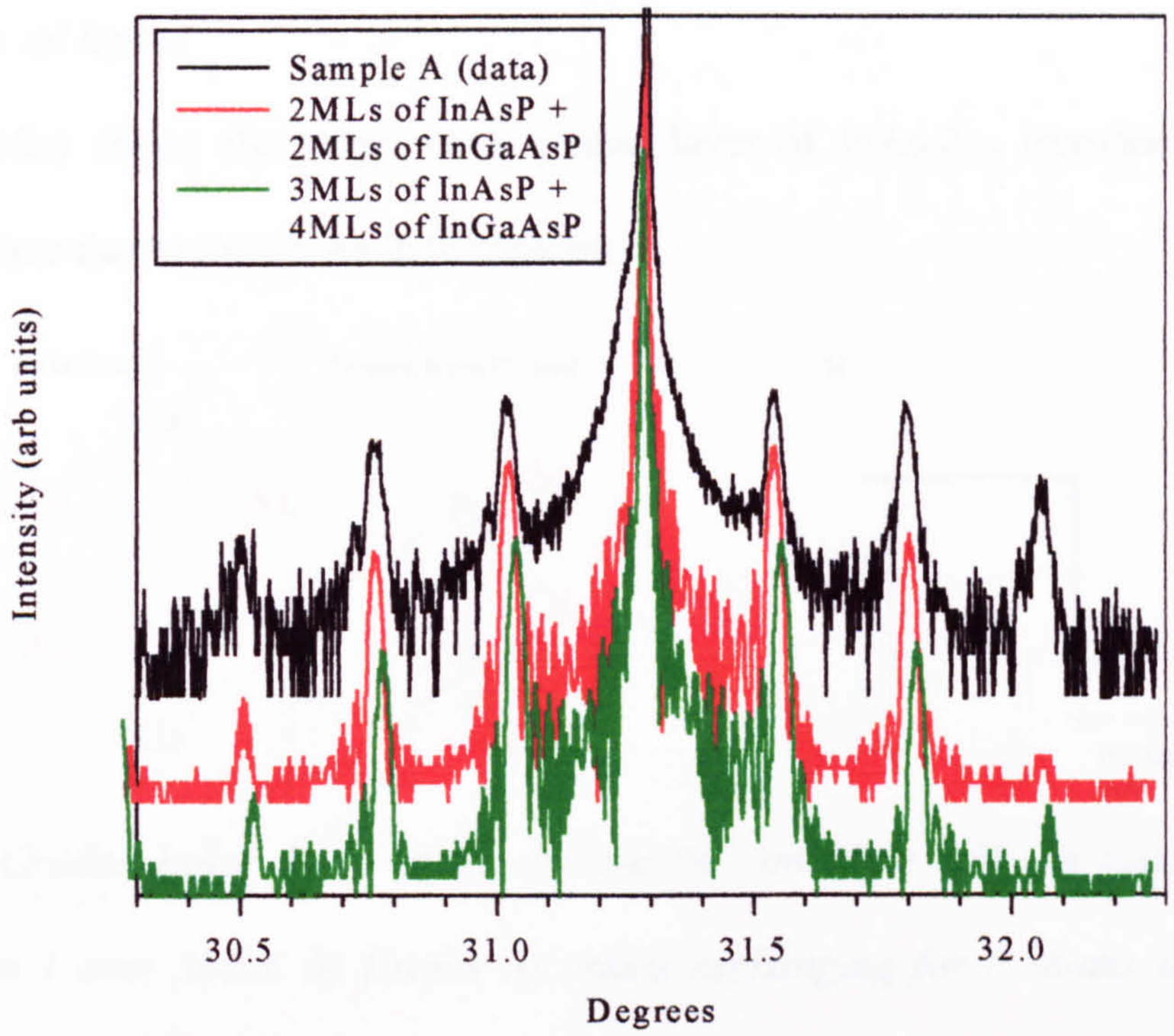

Figure 3-15 *XRD experimental rocking curve (black) and a simulation of a structure with 2MLs of positively strained $InAs_{0.5}P_{05}$ at the InP-InGaAs interface and 2MLs of negatively strained $In_{0.53}GaAs_{0.5}P_{0.5}$ at the $In_xGa_{1-x}As$-InP interfaces (red). The green curve shows the simulation for 3MLs of $InAs_{0.31}P_{0.69}$ at the first interface and 4MLs of $In_{0.53}GaAs_{0.76}P$ at the second interface.*

We can conclude on the basis of the simulations presented so far that the inclusion of simple MLs of InAsP and InGaAsP of various compositions does not give a satisfactory fit to the XRD data. A more realistic approach which should in principle lead to agreement with the optical data is to assume some grading at the interfaces and this is presented in the following section.

4) *Graded interfacial layers*

Figure 3-16a) shows the origin of a graded layer of $InAs_yP_{1-y}$ introduced at the InGaAs-InP interface due to excess As in the reactor.

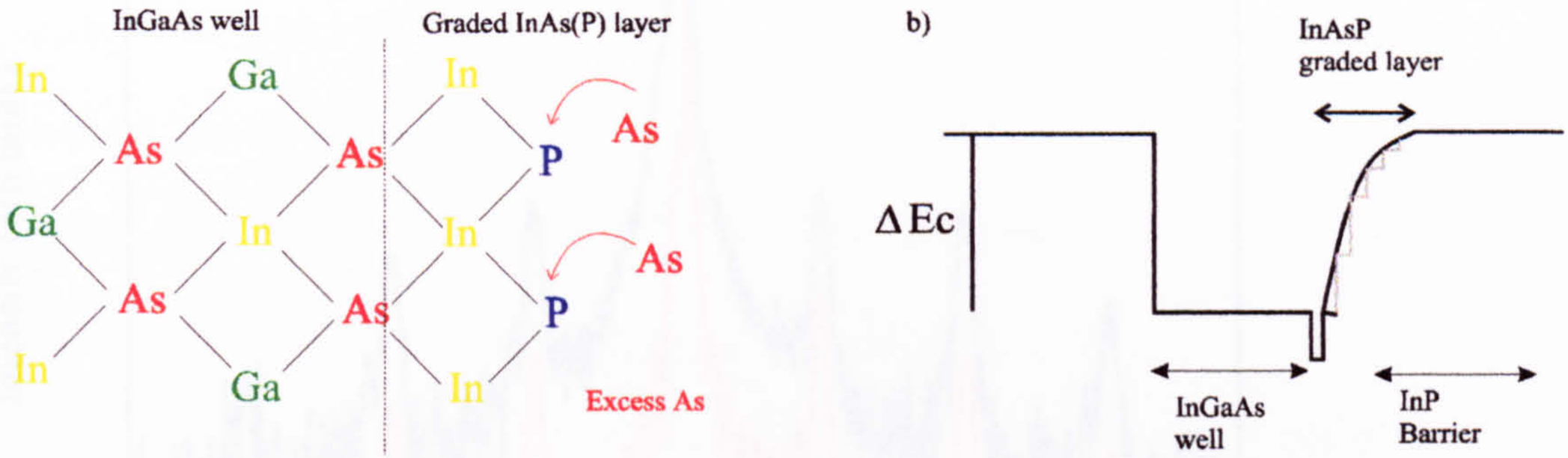

Figure 3-16 *a) Graded InAsP layer at the InGaAs/InP interface with As concentration varying from 0 to 1 over 3MLs. b) Excess As atoms exchanging for P atoms in the InP barrier.*

The graded interface represents exchange of As for P in the InP barrier with the As concentration, y, varying from 0 to 1 over 3 MLs beginning with a pure InAs layer. The In composition in $In_xGa_{1-x}As$ was decreased to x=0.50 in order to accommodate the large positive strain generated in the $InAs_yP_{1-y}$ graded interface. The resulting strain in the well is negative which increases the intensity of the peaks on the RHS of the zero order peak correlating well with the XRD data (figure 3-17). Overall, this simulation provided the best fit to the experimental data. The satellite peaks on the RHS were more intense than those on the LHS of the zero order peak in agreement with the experimental data. The graded interface in the well generates an asymmetric well profile as indicated in Figure 3-16b), the well becoming narrower at the bottom and wider at the top. This is consistent with the optical results.

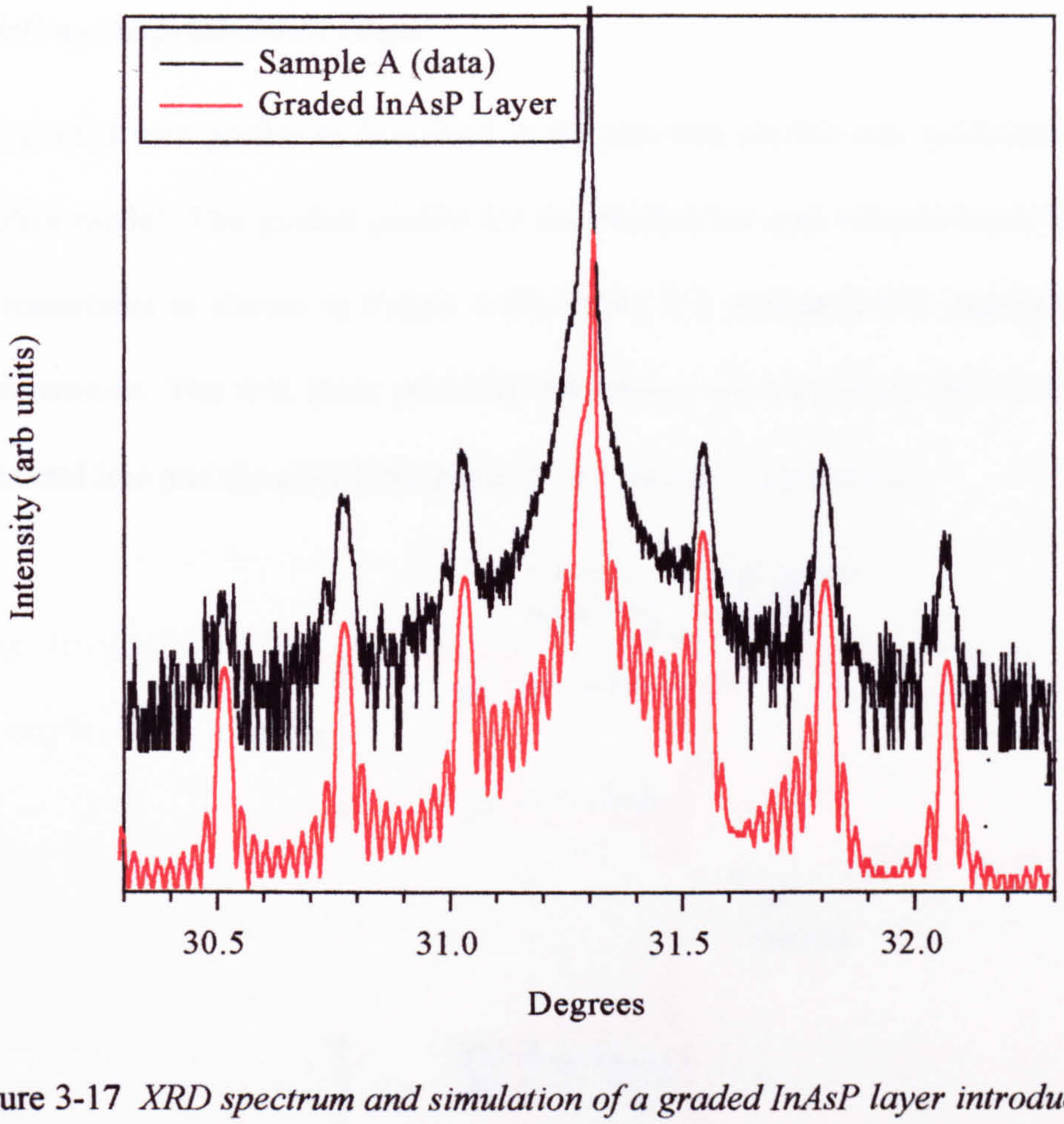

Figure 3-17 *XRD spectrum and simulation of a graded InAsP layer introduced at the InP-InGaAs interface*

The In-As bond is slightly stronger than the In-P bond [M12]. *Shuia et al.* [12] surmised that surface In atoms actively enhance the As-to-P substitution therefore As/P exchange occurs more readily at a InGaAs/InP interface. Thus As/P exchange is more likely to occur at the upper interface resulting in a graded positively strained interfacial layer. The next section outlines the self-consistency of the method by comparing this compositional variation deduced from the XRD results with the optical measurements.

3.4.3 Modelling the graded well shape

The graded well profile as described in the previous section was modelled using the transfer matrix model. The graded profile for the conduction and valence band, heavy and light hole transitions is shown in Figure 3-18. Table 3-5 compares the experimental and predicted transitions. The first three predicted transitions are very close (within 10meV) to the experimental line and the e2-lh2 transition is in reasonable agreement.

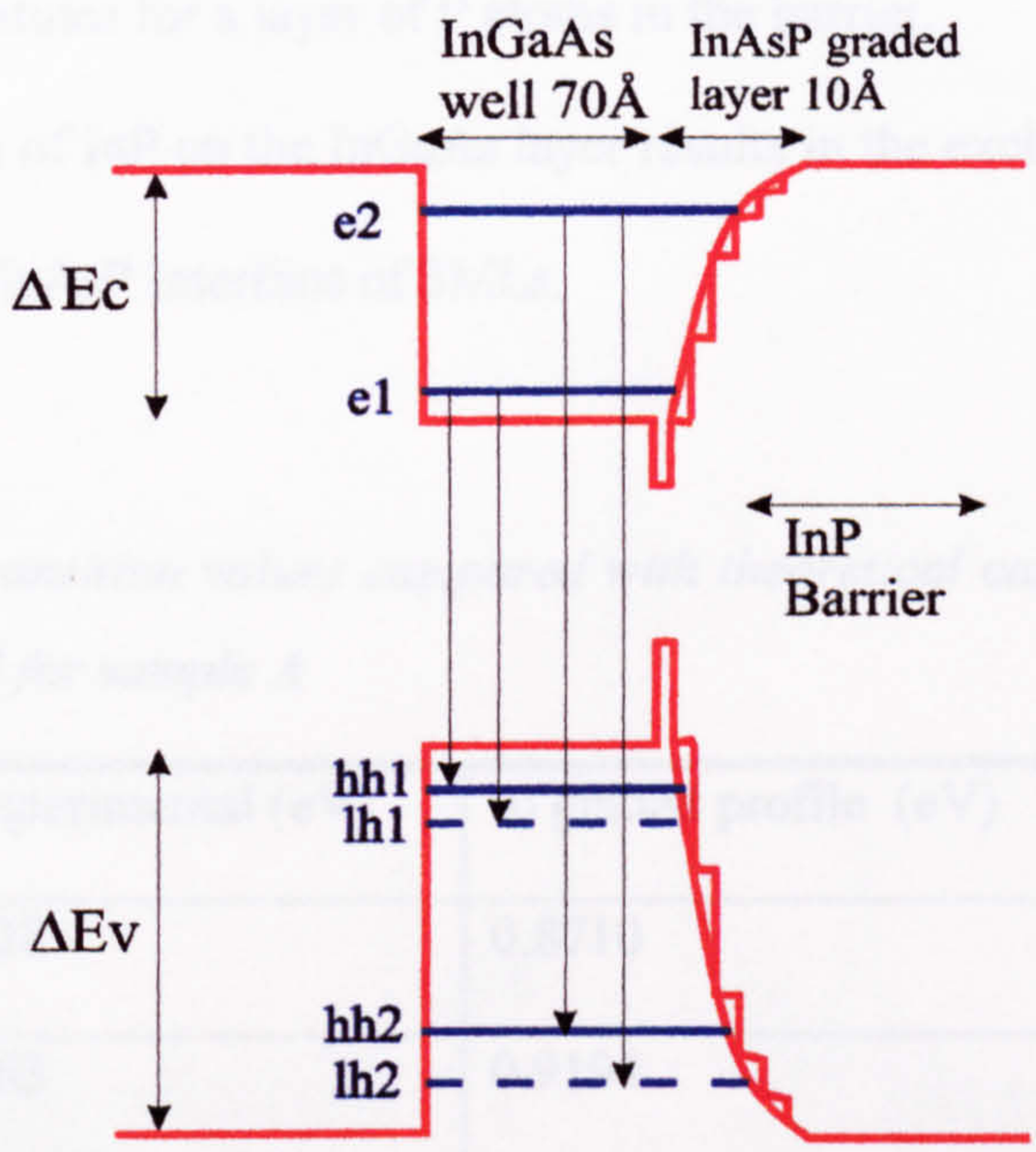

Figure 3-18 *Graded well profile for the conduction and valence band and corresponding transitions for sample A*

It can be concluded that the compositional grading is confined to the first three monolayers at the upper interface (InGaAs/InP). A layer consisting of In-As bonds is initially formed which could be due to;

1) As atoms from the surface of the InGaAs layer bonding with In atoms during the deposition of InP.
2) Incorporation of As, from solid depositions of As on the susceptor and reactor walls, leading to an In-As layer. When switching from an InGaAs well to growth of an InP barrier, the flow rates of all source gases change. It is possible that As takes some time to be purged from the system, even after the AsH_3 flow has being closed. As substitutes for a layer of P atoms in the barrier.

The subsequent deposition of InP on the InGaAs layer results in the exchange of the group V atoms leading to a graded InAsP interface of 3MLs.

Table 3-5 *Experimental transition values compared with theoretical calculated values for a graded well for sample A*

Transitions at 77K	a) Experimental (eV)	b) graded profile (eV)
e1-hh1	0.8828	0.8710
e1-lh1	0.9063	0.9194
e2-hh2	1.0422	1.0516
e2-lh2	1.2030	1.2472

Sample B - Figure 3-19 shows the experimental (004) reflection curve for sample B. Again the structure is assumed to be lattice matched but a slight shoulder on the high angle side of the InP peak indicates that the structure is under a small biaxial tensile strain. The first order peaks are clearly resolved whereas the second and third order peaks are weak and

asymmetric indicating a variation in the shape of the QWs throughout the structure. The period of the well and barrier is 164Å which is 6Å less than the intended value. The simulation shown in Figure 3-19 assumes that sample B consists of square wells, and that both the well and barrier material are lattice matched to InP producing a net zero strain in the simulation, i.e. $In_{0.533}Ga_{0.467}As/In_{0.756}GaAs_{0.530}P$. The satellites generated in the simulation are much weaker than the corresponding experimental satellites.

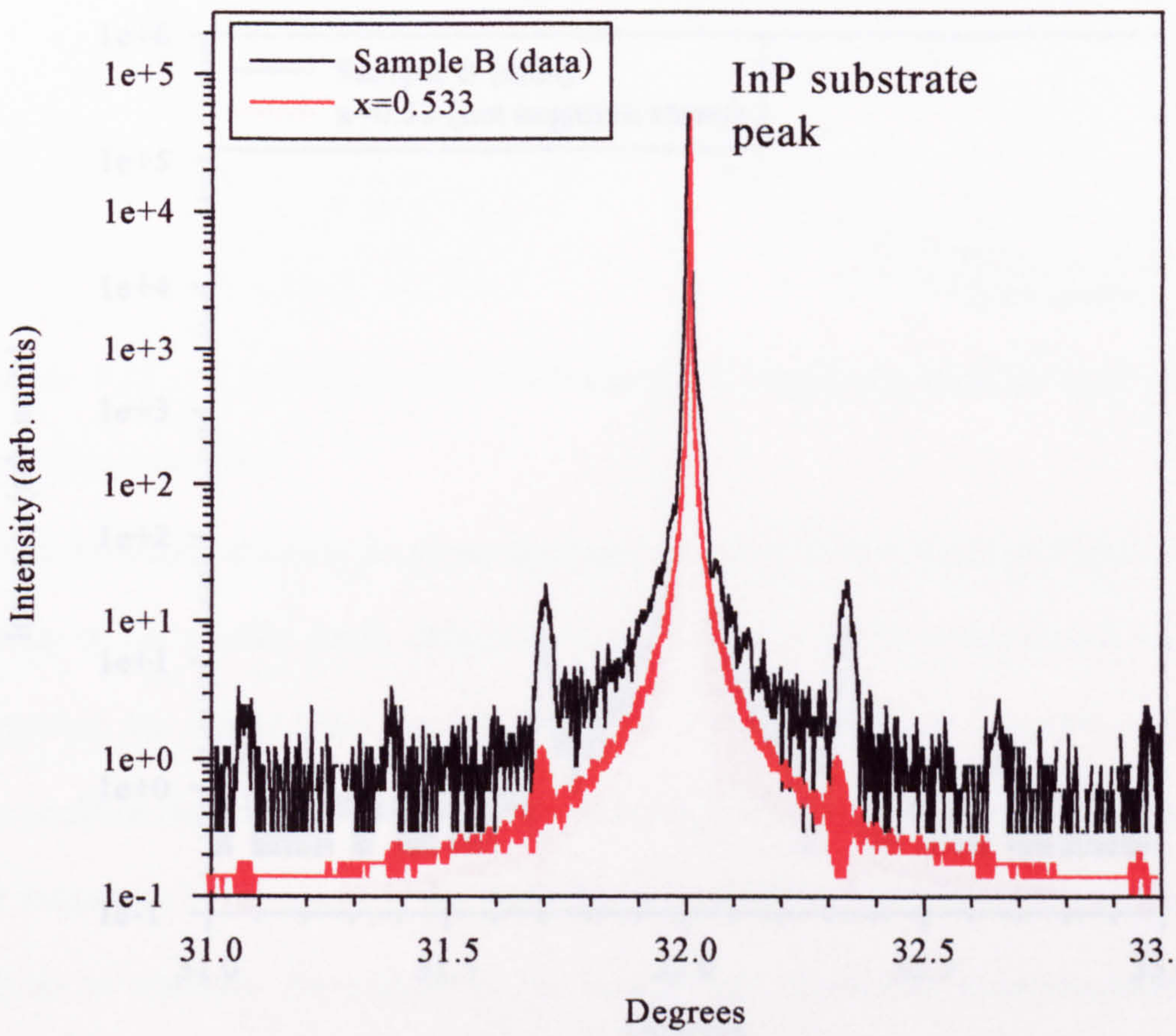

Figure 3-19 *Experimental (004) reflection rocking curve for sample B compared with a simulation using a square well.*

As the slight shoulder to the high angle side of the InP peak indicates an overall negative strain in the MQW, the In and As fraction were decreased in both the wells and

barriers yielding an overall negative strain (Figure 3-20). A shoulder to the high angle side appeared and the positions of the satellite peaks fit the data. However, the satellite peaks are much lower in intensity compared with the experimental peaks. A further increase in negative strain to increase the satellite intensities cannot be introduced into the layers as the satellite peaks move to higher angles. Graded layers of InGaAsP are simulated at the interfaces over 3MLs.

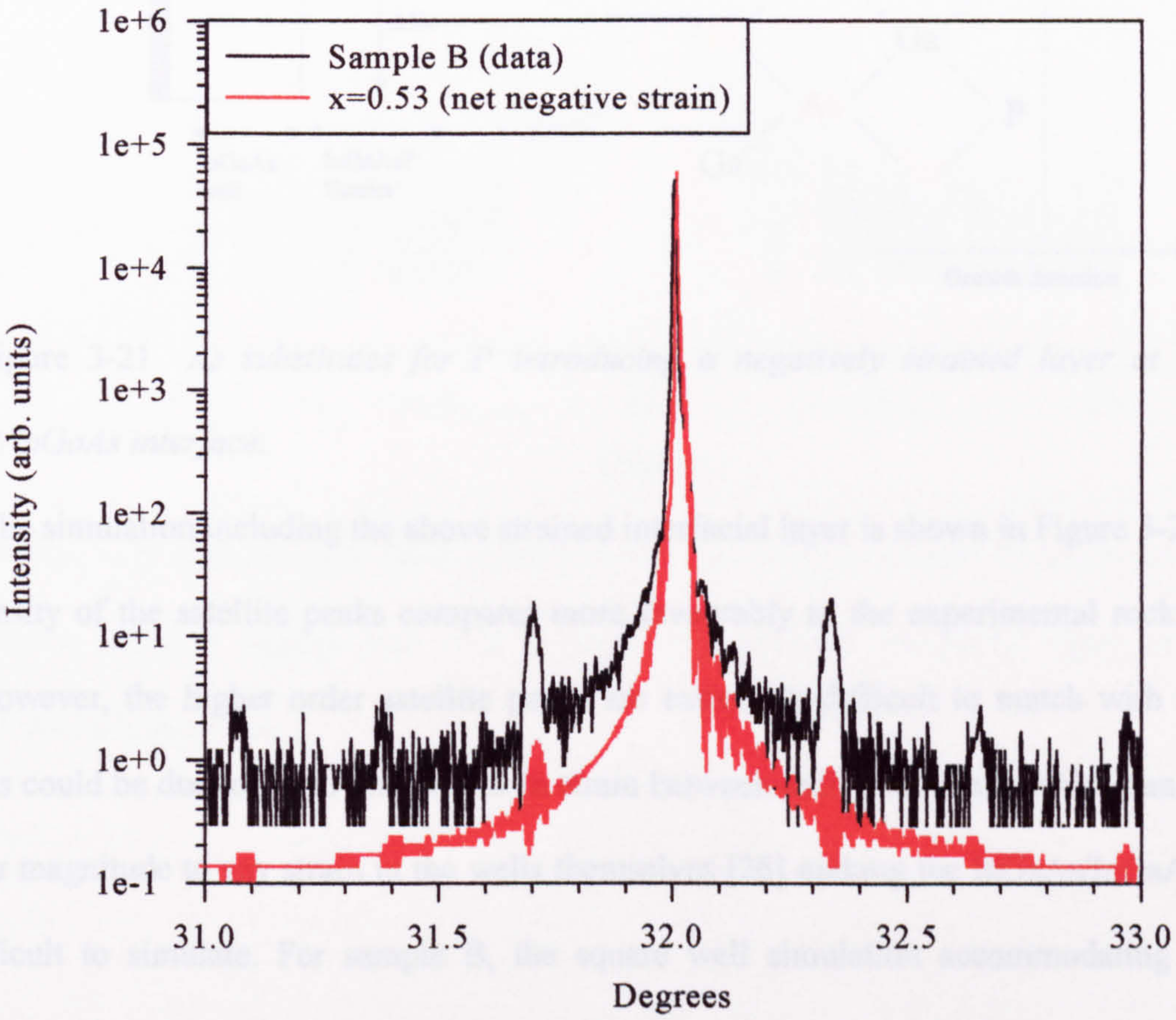

Figure 3-20 *Experimental (004) reflection rocking curve for sample B compared with a simulation using a square well and overall negative strain.*

In order to increase the intensity of the satellites, a negatively strained layer of InGaAsP is introduced at the InGaAsP/InGaAs interface as shown in Figure 3-21 a). The As

composition is increased to 62% (from 53%) which corresponds to an increased exchange of As (for P) in the interfacial layer as the As has a higher sticking coefficient compared to P. If the barrier layer is assumed to be terminated with a layer of P (bonded to In), As will readily substitute for P (InP bond is weaker than InAs bond) as shown in Figure 3-21 b).

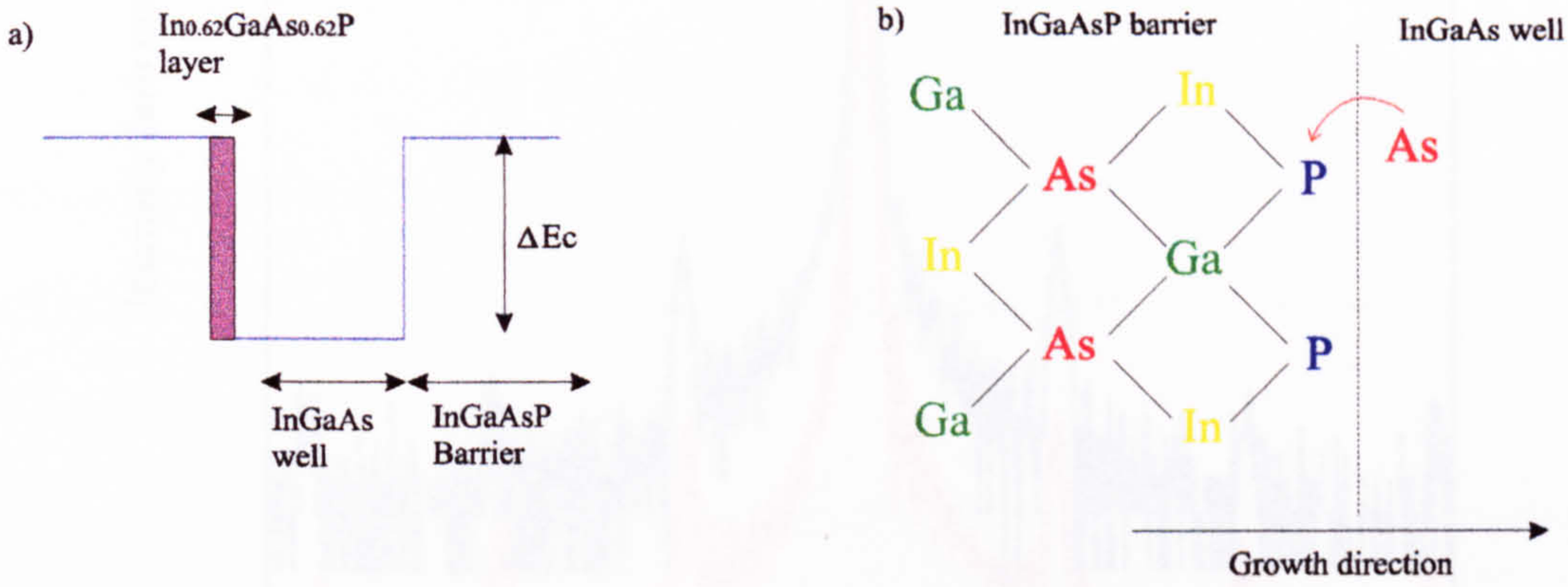

Figure 3-21 *As substitutes for P introducing a negatively strained layer at the InGaAsP/InGaAs interface.*

The simulation including the above strained interfacial layer is shown in Figure 3-22 . The intensity of the satellite peaks compares more favourably to the experimental rocking curve. However, the higher order satellite peaks are extremely difficult to match with the data. This could be due to small differences in strain between individual wells which can be of similar magnitude to any strain in the wells themselves [26] making the InGaAs/InGaAsP case difficult to simulate. For sample B, the square well simulation accommodating an additional tensile strained layer provided the best fit. The parameters used for the square well XRD simulation also give a good fit to the optical data. For the nominally lattice matched structure, the satellite peaks on the experimental (004) rocking curve are too weak to allow the spectrum to be unambiguously modelled.

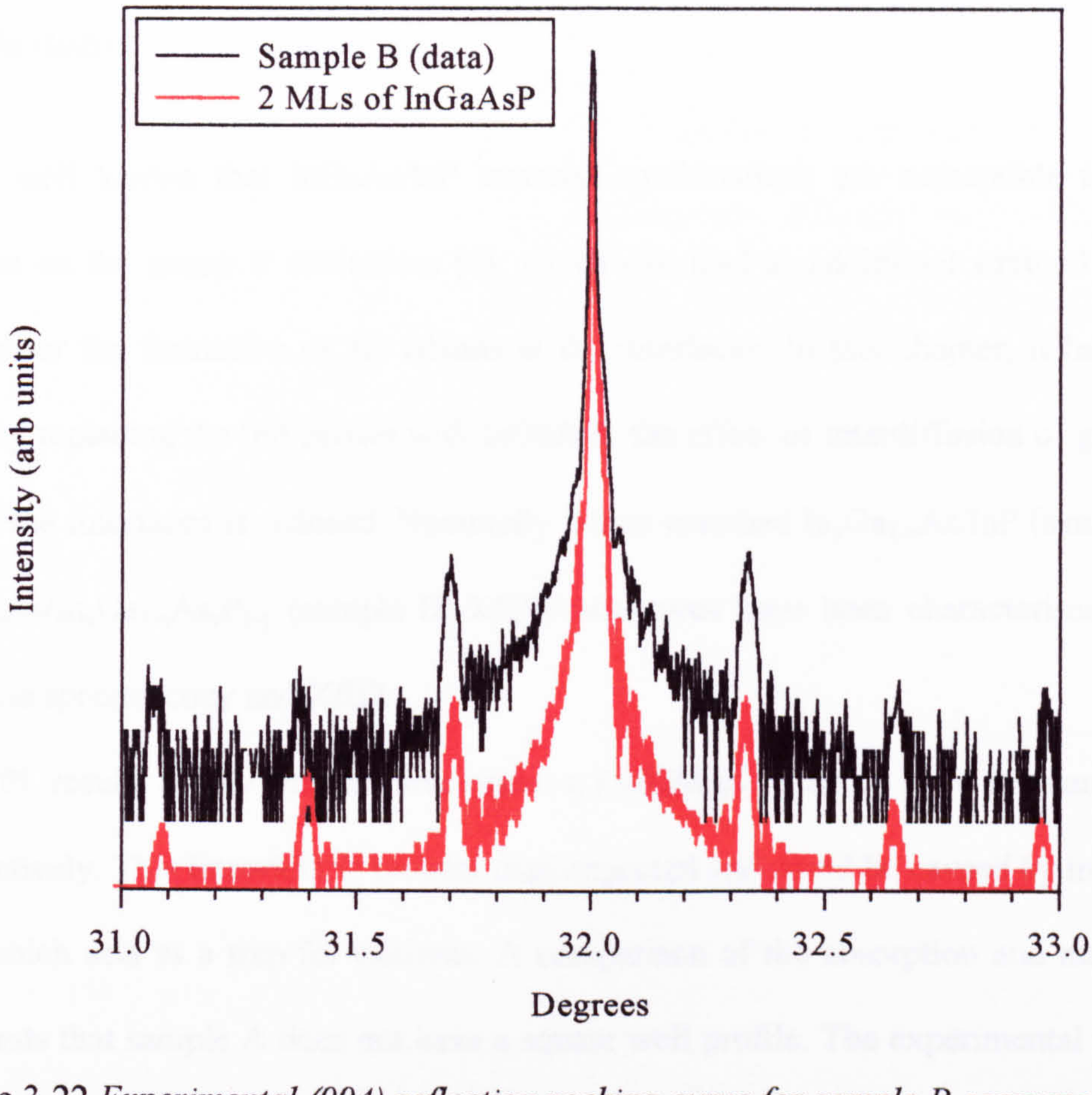

Figure 3-22 *Experimental (004) reflection rocking curve for sample B compared with a simulation using a square well and a negatively strained interfacial layer at the InGaAsP/InGaAs interface.*

3.5 Conclusions

It is well known that InGaAs/InP material combinations are susceptible to As/P interdiffusion on the group V sublattices [4], which can lead to additional strained layers, graded layers or the formation of 3D islands at the interfaces. In this chapter, it has been shown that by replacing the InP barrier with InGaAsP, the effect of interdiffusion of group V elements on the interfaces is reduced. Nominally lattice matched $In_xGa_{1-x}As/InP$ (sample A) and $In_xGa_{1-x}As/In_xGa_{1-x}As_yP_{1-y}$ (sample B) MQW structures have been characterised using PL, absorption spectroscopy and XRD.

The PL results at low temperatures reveal a FWHM of 12 and 8 meV for samples A and B respectively. This linewidth is broader than expected and could be caused by interface roughness which acts as a trap for excitons. A comparison of the absorption and modelled results suggests that sample A does not have a square well profile. The experimental e1-hh1 transition energy is higher than the corresponding theoretical energy whereas the experimental e2-hh2, e1-lh1 and e2-lh2 absorb at lower energies than predicted. The electron level shifts to a higher energy due to an effective narrowing at the bottom of the well and the higher lying electron levels shift to a lower energy due to carriers experiencing a 'wider' well at these energies. The optical transitions observed in the absorption spectra for sample B do not follow the same pattern as sample A. The e1-hh1 and e1-lh1 transitions emit at higher energies than the corresponding theoretical results. For both samples, non-parabolicity effects are considered to lead to only minor modifications in the optical transitions.

XRD measurements were employed to investigate the well composition and hence the well profile. The experimental (004) reflection rocking curve indicates that the InGaAs

well is under a slight negative strain but the net strain of the MQWs is positive as m=0 is situated to the low angle side of the InP peak. As outlined in the literature review at the beginning of the chapter, different groups have proposed different well profiles for InGaAs/InP depending on the growth conditions. Initially, rocking curves were simulated by introducing additional strained interfacial layers. These simulations gave a poor fit to the data. The best fit was provided by introducing an InAsP graded layer at the InGaAs-InP interface. Arsenic is easily incorporated into subsequently grown InP barrier material due to the high incorporation coefficient of As relative to P [21]. Also surface In atoms enhance the As-to-P substitution [12]. The graded interface represents an exchange of As for P in the InP barrier with As concentration, y, varying from 1 to 0 over 3 MLs. This graded well profile is then modelled using the transfer matrix model (Figure 3-12). The first three predicted transitions are very close (within 10meV) to the experimental line. The graded well is tapered becoming wider at the top which appears to fit the experimental data (optical and structural) well. The optical results are in better agreement with the new predicted transitions which vindicates the method used.

For the InGaAs/InGaAsP structure, the 004 simulations indicate a square well profile. A square well simulation accommodating a tensile strained interfacial layer at the InGaAsP/InGaAs interface provided the best fit to the simulation and PL results. Overall, sample B (InGaAsP barriers) provides the best optical results. This could be due to As being common to both well and barrier and hence the diffusion of As at the interface will be reduced.

The abruptness of the QW herterointerface can influence the properties of the heterostructure devices. If the well contains a rough or graded interface then the PL linewidth

increases and the electron mobility decreases which, for example, could affect threshold current densities in lasers and overlap integrals in optical modulators based on the quantum confined Stark effect (QCSE). The InGaAs/InGaAsP QWs exhibit sharper excitonic features which is attributed to sharper interfaces which is an advantage for both lasers and modulators.

3.6 References

[1] Y. -G. Zhao, Y. -H Zou, J. -J. Wang, Y.-D. Qin, X. -L. Huang, R. A. Masut, A. Bensada: Appl Phys Lett 72, (1), p97, (1998) [M120]

[2] L. Francesio, P. Franzosi, G. Landgren: J Phys D: Appl Phys 28, pA169, (1995) [24]

[3] T. Y. Wang, E. H. Reihlen, H. R. Jen, G. B. Stringfellow: J Appl Phys 66, (11), p5376, (1989) [16]

[4] W. P. Gillin, S. S. Rao, I. V. Bradley, K. P. Homewood, A. D. Smith, A. T. R. Briggs: Appl Phys Lett 63, (6), p797, (1993) [M54]

[5] M. H. Lyons, E. G. Scott, M. A. G. Halliwell: Inst Phys Conf Ser, no100, section 6, p473, (1989)

[6] R. Benzaquen, A. P Roth, R. Leonelli: J Appl Phys 79, (5), p2640, (1996) [13]

[7] R. Meyer, M. Hollfelder, H. Hardtdegen, B. Leneler, H. Luth: J Crys Growth, 124, p583, (1992) [1]

[8] G. Salviati, C. Ferrai, L. Lazzarina, F. Genova, C. Rigo, G. M. Schiavini, F. Taiariol: Inst Phys Conf Ser, no134, section 7, p471, (1993)

[9] K. Steubel, V. Harle, F. Scholz, M. Bode, M. Grundmann: J Appl Phys 71, (7), p3300, (1992) [20]

[10] A. Krost, J. Bohrer, H. Roehle, G. Bauer: Appl Phys Lett 64, (4), p469, (1993) [9]

[11] T. Y. Wang, E. H. Reihlen, H. R. Jen, G. B. Stringfellow; J Appl Phys 66, (11), p5376, (1989) [16]

[12] J. Hergeth, D. Grutzmacher, F. Reinhardt, P. Balk: J Crys Growth, 107, p537, (1991) [17]

[13] J. Camassel, J. P. Laurenti, S. Juillaget, F. Reinhardt, K. Wolter, H. Kurz, D. Grutzmacher: J Crys Growth, 107, p534, (1991) [19]

[14] G. -J. Shiau, C. -P. Chao, P. E. Burrows, S. R. Forrest: J Appl Phys 77, (1), p201, (1994) [12]

[15] J. M. Vandenberg, A. T. Macrander, R. A. Hamm, M. B. Panish: Phys Rev B, 44, (8), p3991, (1991) [18]

[16] J. Bohrer, A. Krost, D. Bimberg: Appl Phys Lett 60, (18), p2258, (1992) [11]

[17] R. Schwedler, F. Reinhardt, D. Grutzmacher, K. Wolter: J Crys Growth, 107, p531, (1991) [14]

[18] P. D. Brown, E. G. Bithell, C. J. Himphreys, P. J. Skevington, P. J. Cannard, G. J. Davies: Inst Phys Conf Ser, no134, section 6, p373, (1993)

[19] T. Anan, S. Sugou, K. Nishi, T. Ichihashi: Appl Phys Lett 63, (8), p1047, (1993) [21]

[20] D. Grutzmacher, K. Wolter, H. Jurgensen, P. Balk: Appl Phys Lett 52, p872, (1988) [16(19)]

[21] R. Schwedler, B. Gallmann, K. Wolter, A. Kohl, K. Leo, H. Kurz, S. Juillaguet, E. Massone, J. Camassel, J. P. Laurenti, F. H. Baumann: Appl Sur Sci, 63, p187, (1993) [M58]

[22] Quantum Well Lasers, P. S. Zory: Academic, San Diego, 1993 [M122(1)]

[23] T. Tanbun-Ek, R. A. Logan, N. A. Olsson, H. Temkin, A. M. Sergent, K. W. Wecht; Appl Phys Lett 57, p224, (1989) [22(2)]

[24] R. W. Martin, S. L. Wong, R. J. Nicholas, K. Satzke, M. Gibbons, E. J. Thrush: Semicond Sci Tech, 8, p1173 (1993) [M23]

[25] T. Odagawa, K. Nakajima, K. Tanaka, H. Nobuhara, T. Inoue, N. Okazaki, K. Wakao: Appl Phys Lett 63, p2996, (1993) [M50]

[26] G. Rowland, T. J. C. Hosea: J Appl Phys 83, (9), p4909, (1998) [M121]

[27] J. Dalfors, T. Lundstrom, P. O. Holtz, H. H. Radamson, B. Monemar, J. Wallin, G. Landgren: Appl Phys Lett 71, (4) p503, (1997) [M122]

[28] C. G. Cureton, E. J. Thrush, A. T. R. Briggs: J Crys Growth, 107, p549, (1991) [4]

[29] M. S. Skolnick, P. R. Tapster, S. J. Bass, A. D. Pitt, N. Apsley, S. P Aldred: Semicond Sci Tech, 1, p29 (1986) [M65]

[30] D. J. Westland, A. M. Fox, A. C. Maciel, J. F. Ryan, M. D. Scott, J. I. Davies, J. R. Riffat: Appl Phys Lett 50, (13) p839, (1987) [M68]

[31] H. C. Casey and M.B. Panish; Heterostructure lasers

[32] M. S. Skolnick, P. R. Tapster, S. J. Bass, N. Apsley, A. D. Pitt, N. G. Chew, A. G. Cullis, S. P. Aldred, C. A. Warwick: Appl Phys Lett 48, (21) p1455, (1986) [15]

[33] G. Bacher, C. Hartmann, H. Schweizer, T. Held, G. Mahler, H. Nickel: Phys Rev B, 47 (15) p9545 (1993)

[34] A. Guiner, R. Jullien: The Solid State; from superconductors to superalloys, Oxford Science Publications, (1989)

[35] W. G. Bi, C. W. Tu: J Appl Phys 78, (4), p2889, (1995) [22]

[36] G. Arnaud, J. Allegre, P. Lefebvre, H. Mathieu, L. K. Howard, D. J. Dunstan: Phys Rev B, 46, (23), p15 290, (1992) [M127]

[37] Properties of InP, EMIS, no6, An INSPEC publication (1991)

[38] M. Zachau et al. : Superlattices Microstruct. (UK) 5, p19 (1989) [Adachi 9]

[39] D. V. Lang et al.: Appl Phys Lett 50, p736, (1987) [Adachi 21]

[40] R. E. Cavicchi, D. V. Lang, D. Gershoni, A. M. Sergent, J. M. Vandenberg, S. N. G. Chu, M. B. Panish: Appl Phys Lett 54, (8), p739, (1988) [M46]

[41] M. P. C. M. Krijin; Semicond. Sci. Technol. 6 p27-31 (1991)

[42] S. Adachi: J Appl Phys 53, (12), p8775, (1982) [M20]

[43] R. L. Moon, G. A. Antypas, L. W. James: J Elec Mat 3, 3, p635 (1974) [InP 22]

[44] P. Rochon, E. Fortin: Phys Rev B, 12, (12), p5803 (1975) [InP74]

[45] C. Hermann, T. P Pearsall: Appl Phys Lett 38, (6), p450, (1981) [InP 78]

[46] P. Dawson, K. J. Moore, G. Duggan, H. I. Ralph, C. T. B. Foxon: Phys Rev B, 34, (8), p6007 (1986) [M72]

[47] J. W. Orton, P. W. Fewster, J. P Gowers, P. Dawson, K. J. Moore, P. j. Dobson, C. J. Curling, C. T. Foxon, K. Woodbridge, G. Duggan, H. I. Ralph: Semicond Sci Tech, 2, p597 (1987) [M63]

[48] C. Wetzel, R. Winkler, M. Drechsler, B. K. Meyer, U. Rossler, J. Scriba, J. P. Kotthaus, V. Harle, F. Scholz: Phys Rev B, 53, (3), p1038 (1996) [26]

[49] P. F. Fewster, C. J. Curling; : J Appl Phys 62, (10) p415, (1987) [E8]

[50] M. A. G. Halliwell, M. H. Lyons, M. J. Hill: J Crys Growth, 68, p523, (1984) [6(6)]

[51] J. M. Vanderberg, M. B. Panish, H. Temkin, R. A. Hamm: Appl Phys Lett 53, p1920, (1988) [18(8)]

[52] J. M. Vanderberg, A. T. Macrander, R. A. Hamm, M. P. Panish; Phys. Rev. B, 44, 8, p3991 (1991) [10]

[53] S. -W. Ryu, B. -D. Choe, W. G. Jeong: Appl Phys Lett 71, (12) p1670, (1997) [M123]

[54] J. M. Vandenberg, D. Gershoni, R. A. Hamm, M. P. Panish, H. Temkin: J Appl Phys 66, p3635, (1989) [10(19)]

4. Chapter 4 - $InAs_xP_{1-x}$/InP Quantum Wells

4.1 Introduction

$InAs_xP_{1-x}$/InP multiple quantum well (MQW) structures are proving to be a suitable materials combination for optoelectronic devices operating in the 1-1.3μm region. High quality, coherently strained samples can be grown, including optical modulators and quantum well lasers [1]. $InAs_xP_{1-x}$/InP MQWs exhibit sharper excitonic features, due to the lower level of strain relaxation [2, 3, 4, 5], than other pseudomorphically strained structures such as $InGa_xAs_{1-x}$/GaAs operating in this spectral region. The $InAs_xP_{1-x}$/InP heterostructure also has a larger conduction band discontinuity than $InGa_xAs_{1-x}$/GaAs which makes the former a preferable materials combination for optoelectronic devices. A high conduction band offset is required to prevent electrons tunnelling out of the wells under a strong electric field [6, 7].

4.1.1 Integration of optical devices

III-V based optoelectronic integrated circuits (OEICs) are the subject of intense interest for industrial applications and optical communication systems. The increasing demand for higher data rate systems for global telecommunications and the ever expanding internet has pushed technology towards monolithic integration of active and passive optical components fabricated on a single substrate. These offer a number of advantages over discrete components connected together which includes, a reduction in cost and size and an improvement in performance and reliability. The materials used in the manufacture of integrated devices must also be stable against thermal degradation as most integration processes require an anneal stage.

The majority of the OEICs were based on GaAs technology but with the advances made in bandgap engineering for InP based material, it has been possible to integrate devices working in the 1.3-1.55μm region by selective area control of the bandgap. This can be achieved by intermixing the wells and barriers in III-V QW heterostructures inducing a change in composition of the well/barrier layers and an increase in the bandgap.

Quantum Well Intermixing (QWI), is achieved by employing techniques such as Impurity Induced Disordering (IID) [8, 9, 10] and Impurity-Free Vacancy Disordering (IFVD) [8, 10]. These post-growth intermixing processes can be used to alter the bandgap of the MQW in selected regions, so bandgap tuned modulator-laser devices and bandgap shifted QCSE modulators and detectors can be formed using only one epitaxial step. In IID, dopants such as Fluorine and Boron are implanted into the structures and diffuse during the annealing stage causing intermixing. However, these impurities tend to form electron traps and introduce residual damage during implantation, making this technique unsuitable for bandgap tuned devices. Consequently, IID was not adopted for the present study. With IFVD, the sample is capped with SiO_2 and then annealed. SIMS measurements show that Ga readily diffuses into the dielectric cap leaving behind group III vacancies which then diffuse through the structure causing intermixing [11]. Published results show that intermixing leads to a blueshift of the bandgap energy in InGaAsP/InP QW which was attributed to P-As diffusion through the heterointerface. The intermixing process can be extended by selectively capping and annealing the MQW structure and then using the capping layer as a means to either enhance or prevent intermixing [12]. For both GaAs [13] and InP [14] based structures, the extent of the blue shift is dependent on the SiO_2 cap thickness.

4.1.2 Comparing Different Material Systems used for devices

The interdiffusion mechanisms have been studied in several III-V quantum well structures. The first intermixing studies were performed on GaAs/$Al_{1-x}Ga_xAs$ structures which operate in the 0.87-0.89μm wavelength region for 1<x<0.7. Interdiffusion processes for other systems such as $In_xGa_{1-x}As$/GaAs [15], $In_xGa_{1-x}As/In_xGa_{1-x}As_yP_{1-y}$ [9], $In_xGa_{1-x}As_yP_{1-y}$ /InP [13] and $InAs_yP_{1-y}$/InP [16] operating in the long-wavelength region have also been investigated. The interdiffusion process involves two stages: capping the sample and thermal annealing, which are described below.

SiO_2 and Si_3N_4 are the most commonly used capping layers and are deposited at a temperature of 300°C using plasma-enhanced chemical vapour deposition (PECVD). For Si_3N_4 layers, nitrogen and silane gases are mixed at a pressure of 1 Torr and a layer of Si_3N_4 is deposited at a rate of about $3Ås^{-1}$. For the SiO_2 layer, a mixture of silane and nitrous oxide gases at a pressure of 1 Torr is used to deposit the dielectric at a rate of about $6Ås^{-1}$. The $InAs_xP_{1-x}$/InP MQW samples studied in this chapter were capped using the above process.

The sample is then annealed either in a conventional furnace or a Rapid Thermal Anneal (RTA) processor [17]. Conventional furnaces can reach temperatures of 1000°C and tend to be used for relatively long anneal times (> 5 minutes). The RTA processor system automatically controls anneal temperature and time specified by the user, and anneal temperatures of up to 1250°C can be achieved for times up to a few minutes. The sample is placed on a silicon wafer and the temperature is monitored using an extended range thermocouple attached to the silicon wafer. The heating and cooling stage takes only a few seconds in contrast to the conventional furnace where the samples may take several minutes to reach the desired anneal temperature.

Annealing takes place in an inert gas (usually argon or nitrogen) atmosphere to aid cooling and prevent oxidation.

In order to promote, or in some cases, prevent post-growth intermixing in MQWs, other groups have used different capping layers and annealing techniques, some of which are described below.

a) **SiO_2 dielectric capping layer.** In GaAs/AlGaAs QW, interdiffusion of group III atoms causes a blue shift at anneal temperatures above 800°C [18]. *Ralston et al.* [19] have shown that selective capping of GaAs/AlGaAs superlattices with SiO_2 followed by RTA between 850-900°C for 15s resulted in an energy shift of about 61meV in the capped regions. In addition the excitonic features were still well resolved. Intermixing was attributed to the diffusion of Ga into the SiO_2 cap, accompanied by Ga vacancy diffusion through the active layer. For those regions not capped with SiO_2, the exciton transition energies were unaltered over the annealing temperature range. In contrast to GaAs/AlGaAs QWs which remain stable up to temperatures well beyond those normally used in epitaxial growth, QW materials operating at 1.5μm such as InGaAs/InGaAsP exhibit intermixing even at growth temperatures. *Marsh et al.* [9] have demonstrated blue shifts in P-based quaternary samples (InGaAs/InGaAsP) capped with SiO_2 and annealed in a conventional furnace for 30 minutes at temperatures ranging from 500 to 750°C. The blue shift was attributed to the diffusion of P into and As out of the wells due to group V vacancies generated by P desorption from the surface diffusing through the structure [8]. *Cao et al.* [13] subjected strained InGaAsP/InP MQW laser structures to RTA, with and without a SiO_2 cap. The RTA process was performed in a high purity nitrogen atmosphere at a temperature of 750°C for times of 30, 60, 90s. With a SiO_2 cap, the intermixing between the well and barrier was enhanced resulting in a 66meV blue shift. These authors also investigated

the influence of the deposited cap layer thickness on the degree of intermixing. The blue shift increased with increasing SiO_2 thickness but saturated for a SiO_2 cap layer as thin as 15nm. *Burkner et al.* [14] also reported a dependence of the blue shift on SiO_2 cap thickness for GaAs/AlGaAs and InGaAs/GaAs MQWs and found that the energy shift saturated with a much thicker SiO_2 cap of 235nm. *Nakashima et al.* [12] attributed the intermixing process observed in SiO_2 capped InGaAs/InP MQWs to the diffusion of the group V atoms with the well ultimately becoming an InGaAsP lattice matched layer. The InGaAs/InP system has two possible interdiffusion species, group III and group V atoms. These atoms diffuse at similar temperatures [20]. Higher temperatures are required to break Al-As and Ga-As than In-As and In-P bonds i.e. the melting point of the former pair is greater than the latter and so diffusion will commence at higher temperatures in these crystals. Most semiconductors are bound by covalent bonds but in the case of III-V semiconductors partial ionic bonding is also present [21]. The fractional ionicity is less in Al-As and Ga-As (than In-As or In-P) making these bonds more difficult to break. *Joyner et al.* [22, 23] have shown that annealing at temperatures between 500 and 640°C was sufficient to drive the group V species through the InGaAsP/InP interface causing a blue shift of the PL emission peak. *Mallard et al.* [24] studied layer diffusion of the four constituent elements in InGaAs/InGaAsP MQWs before and after annealing using energy dispersive x-ray (EDX) microanalysis. EDX linescans across the interfaces were obtained with a spatial resolution of 2nm. The linescans generated from x-ray signals, characteristic of the elements present, showed that the annealed interfaces had become more diffuse, revealing interfacial widths of 3 and 4nm for the group III and V elements respectively. This implied the diffusion rate of the group V elements exceeded that of the group III elements in the sample.

b) **Si_3N_4 dielectric capping layers.** These capping layers are also used to coat InP and GaAs based structures before annealing. Even though Ga atoms have a lower affinity for Si_3N_4 than SiO_2 layers, a blue shift of ~40meV was reported [25] for GaAs/AlGaAs structures coated with Si_3N_4 and annealed at 800°C. *Marsh et al.* [9] have demonstrated blue shifts of up to 25meV in P-based quaternary samples (InGaAs/InGaAsP) capped with Si_3N_4 and annealed in a conventional furnace for 30 minutes at temperatures ranging from 500 to 750°C.

Marsh et al. [8, 9] have also compared the intermixing in uncapped and capped (SiO_2 and Si_3N_4) P-based quaternary samples, annealed in a conventional furnace for 30 minutes at temperatures ranging from 500 to 750°C. In the case of the uncapped samples, blue shifts were attributed to P desorption creating vacancies at the sample surface, which diffuse through the structure causing interdiffusion at the interface. However, a slight difference in the measured energy shift between P-quaternary structures capped with SiO_2 or Si_3N_4 was observed for short RTA anneal times (< 30s). Disordering, leading to blue shifts of 15meV occurs with the Si_3N_4 coated samples and only a small shift of 5meV with the SiO_2 coated samples. This behaviour is reversed for GaAs based materials.

c) **No capping layer.** Another method used to enhance and in some cases prevent intermixing and which can lead to degradation of the sample, is thermal annealing of uncapped samples in P overpressure conditions. *Francis et al.* [26] annealed InGaAs/InGaAsP QWs in a gaseous phosphorus overpressure and demonstrated that the stoichiometry at the sample surface influences the amount of intermixing of the QWs located in the sample. *Marsh et al.* [8,9] observed blue shifts in uncapped P-based quaternary samples due to P desorption from the sample surface, similar to the results found by *Komiya et al.* [27]. To suppress P desorption, the uncapped samples were annealed in silica ampoules in a background ambient of P_4, for 30

minutes at 650°C. The exciton energy shift was reduced from 25 to 15meV. *Marsh and Komiya et al.* [8, 27] demonstrated that a phosphorus overpressure inhibits the desorption of phosphorus from the surface reducing the generation rate of vacancies. *Francis et al.* [28] have demonstrated a PL peak blue shift of 60meV for the InGaAs/InGaAsP samples annealed at 600°C for 4 hours in a P_4 ambient. The FWHM increased slightly from 22 to 30meV after diffusion, indicating that good structural quality was maintained after annealing. *Oshinowo et al.* [29] have reported that uncapped InGaAs/InP QWs annealed at 900°C for 1 minute can increase the QW emission energy by more than 300meV. The P desorption was suppressed by covering the epilayer side with a silicon wafer and the substrate side with an InP wafer when annealing the samples by RTA in a nitrogen atmosphere. *Fujii et al.* [20] annealed InGaAs/InP samples of different QW widths, from 500-640°C for 1-3 hours in a phosphine atmosphere and demonstrated by XRD that P diffuses from the InP layer and As from the InGaAs layer, changing the compositional profile of the QW. They also demonstrated that, after annealing, the narrowest well exhibited the greatest PL energy shift. *Francis et al.* [26] monitored group V interdiffusion of InGaAs/InGaAsP QWs by a combination of selective capping and changing the P pressure during the anneal. The degree of blue shift, resulting from the diffusion of group V atoms, can be controlled by altering the phosphorus pressure during the anneal but this varies in a non-linear way. An 80meV difference in blue shift between the uncapped and capped areas on the wafer was observed.

d) **Strained layers**. A consensus has not yet been reached regarding any dependence of the rate of interdiffusion at semiconductor heterointerfaces on the amount of strain in the structure. Strain effects on interdiffusion have been investigated with some groups reporting distinct changes in diffusion [31] while others do not [32]. For the InAsP/InP system, *Tweet et*

al. [33], have presented evidence for the existence of a 'critical strain' influencing the interdiffusion in $InAs_{1-x}P_x/InP$ heterostructures. If the strain is 1.9% or more ($x<0.4$) a substantial P-As intermixing occurs but if $x>0.4$ (decrease in strain), the intermixing is greatly increased. *Francis et al.* [30] investigated the intermixing of strained and unstrained InGaAsP/InGaAs QWs induced by thermal anneals with a P over-pressure. They showed that the diffusion through the QW heterointerfaces was slower in the presence of strain.

InAsP/InP MQW structures are prone to a slight amount of intermixing during growth. *Tweet et al.* [33] showed that the interdiffusion in InAsP/InP QWs is sensitive to growth temperature, as the P-As intermixing is a factor of 2 greater for samples grown at 620°C than 580°C. Purposely induced intermixing of the group V atoms in InAsP/InP QWs has not been extensively researched. *Sallese et al.* [34] have investigated diffusion in ultrathin InAs/InP strained layers. Their samples were not capped and too thin to compare directly with our work but a blue shift was observed after annealing above 700°C which was attributed to the interdiffusion of As into the InP and P into the InAs layer leading to an InAsP QW where the composition profile depended on both the interdiffusion process and on the initial InAs thickness. *Sallese et al.* [34] postulated that the intermixing may be a direct P-As site exchange process or successive hopping between neighbouring vacancy sites. They calculated an interdiffusion coefficient of $(7\pm0.5)\times10^{-17}cm^2s^{-1}$ at 830°C confirming that interdiffusion is more pronounced in (In,Ga)(As,P) than in (Al,Ga)As alloys for which a value of $1\times10^{-19}cm^2s^{-1}$ was calculated [25].

Several groups [19, 25, 35] have used a combination of PL and thermal annealing to determine the interdiffusion rate, D. They have monitored the shift in PL emission as a function of thermal anneal time and temperature. Comparing this shift with calculated values of the

emission energy, the value of D can be deduced. The calculated value of the emission energy is determined by modelling the post-diffusion group V profile assuming the diffusion obeys Fick's Law and then employing the transfer matrix model to determine the e1-hh1 transition. A detailed explanation of this procedure is given in section 4-2.

4.1.3 Aim

In this chapter InAsP/InP MQW structures designed to operate at 1.3μm have been subjected to IFVD to assess their potential for OEICs. Several optoelectronic devices, including optical modulators and QW lasers, have recently been demonstrated using InAsP based strained layer heterostructures [36, 37, 38] but very little work has been done on interdiffusion and bandgap changes that occur after post-growth annealing. The InAsP/InP samples studied here have been capped with SiO_2 and Si_3N_4 dielectric layers and subjected to annealing for various times and temperatures. The experimental results have been compared with modelled results and the diffusion coefficient deduced. The chapter is organised as follows. Section 4.2 describes the interdiffusion processes and equations. In section 4.2.2, the determination of the composition of $InAs_xP_{1-x}$ using PL, XRD and the transfer matrix model is outlined. Section 4.3 discusses the annealing process and PL results. Section 4.4 describes the implementation of the interdiffusion equations and how these are applied to the experimental results to obtain a value for the diffusion coefficient. Section 4.4.3 presents a comparison between samples A and B and finally, section 4.5 summarises the chapter.

4.2 Interdiffusion Processes and Equations

Photoluminescence and x-ray diffraction are non-destructive characterisation techniques which can be used to study the effects of intermixing in a QW before and after annealing. PL gives information about the excitonic transitions which depend on the well/barrier composition and well width, and XRD is used to examine the composition, thickness and morphology of annealed and unannealed layers. The measured shifts in the PL energies are compared with calculated values for the interdiffused wells in order to obtain values for the interdiffusion coefficient, D, as a function of temperature. The equations required for modelling the diffusion are assumed to obey Fick's Law [39]. A detailed explanation of the derivation of these equations is given in Appendix B.

In order to calculate the value of D for the intermixing of the well and barrier layers after annealing, the well profile must be calculated. Schrödinger's equation can then be solved for the resulting well profile to determine the energies of the confined states [15, 25, 35,]. The interdiffusion can be modelled by looking at the P or As profiles across the layers and examining the change. For the case of an InAsP/InP QW, only diffusion of P and As is considered. The interdiffusion is modelled using an error function profile [39, 40] of the P(As) composition, x, varying across the well centred at z=0 [35],

$$x(z) = x_0 + c_0\left[\frac{1}{2}erf\left(\frac{z-{}^{l_w}\!/_{2}}{2(Dt)^{\frac{1}{2}}}\right) - \frac{1}{2}erf\left(\frac{z+{}^{l_w}\!/_{2}}{2(Dt)^{\frac{1}{2}}}\right)\right] \qquad \text{Eq 4-1}$$

where D is the interdiffusion coefficient, t is the annealing time, l_w the well thickness, x_0 is the initial P barrier concentration, c_0 is the As composition in the well, erf(x) is the error function and $L_d = 2(Dt)^{\frac{1}{2}}$ is the diffusion length. The solution is symmetric about z=0. The equation is initially solved for $-\frac{1}{2}(l_w + l_b) \leq z \leq +\frac{1}{2}(l_w + l_b)$ as the diffusion of P(As) is confined to this region. Equation 4-1 is difficult to implement as many iterations have to be performed and so a simpler Boltzmann-like function has been evaluated which gives a good fit to the error function as shown in Figure 4-1.

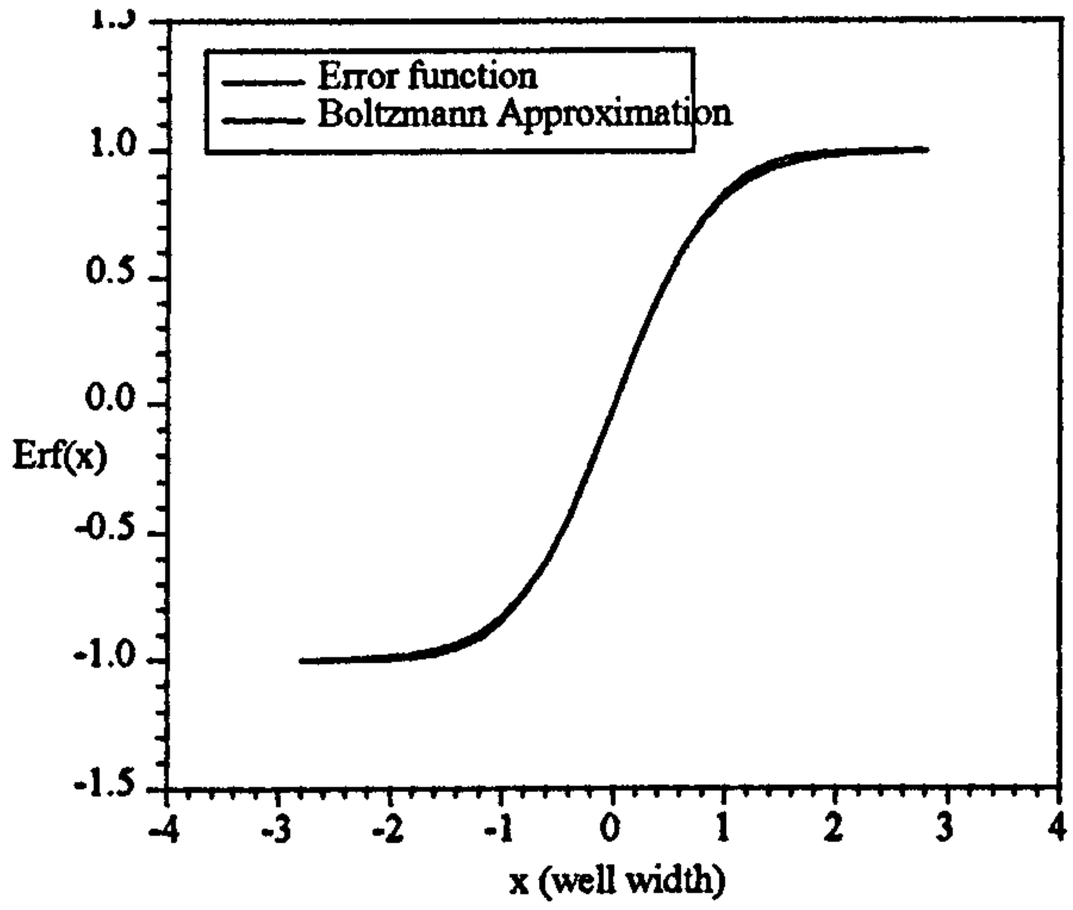

Figure 4-1 *A Boltzmann like function which has been evaluated to give a accurate fit to*

Eq 4-1

The Boltzmann-like function is shown in Eq 4-2,

$$erf(x) \approx \frac{2}{1+\exp\left(-\frac{X}{0.429}\right)} - 1 , \qquad \text{where } X = \left(\frac{z - {}^{l_w}/_2}{2(Dt)^{\frac{1}{2}}}\right) \qquad \text{Eq 4-2}$$

Substituting this approximation for the error function, Equation 4-1 can now be written,

$$x(z) = x_0 + c_0\left\{\left[1+\exp\left(-\frac{z - {}^{l_w}/_2}{0.858(Dt)^{\frac{1}{2}}}\right)\right]^{-1} - \left[1+\exp\left(-\frac{z + {}^{l_w}/_2}{0.858(Dt)^{\frac{1}{2}}}\right)\right]^{-1}\right\} \qquad \text{Eq 4-3}$$

The compositional profile can be solved by substituting incremental values of the diffusion length (L_d) into Eq 4-2. Once the As/P concentration profile has been calculated, the potential profile can be determined. The conduction band minimum and the valence band maximum at each point in the calculated profile are evaluated from an empirical relationship between the 300K unstrained bulk InAsP bandgap and the As/P concentration given by [41],

$$E^{300K} = 1.35 - 1.083(1 - x(z)) + 0.091(1 - x(z))^2 \qquad \text{Eq 4-4}$$

However, as InAsP/InP QWs are compressively strained, the hydrostatic and uniaxial strain as a function of composition must be taken into consideration.

The hydrostatic strain is calculated from,

$$\Delta E^H = 2a\left(\frac{C_{11} - C_{12}}{C_{11}}\right)\varepsilon_{//} \qquad \text{Eq 4-5}$$

and the uniaxial strain is calculated from,

$$\Delta E^U = b\left(\frac{C_{11} + 2C_{12}}{C_{11}}\right)\varepsilon_{//} \qquad \text{Eq 4-6}$$

where a and b are the deformation potentials and C_{11} and C_{12} are elastic coefficients which are well documented for III-V semiconductors [42]. C_{11} and C_{12} are calculated for the QWs strained here by linearly interpolating between the binary compounds. $\varepsilon_{//}$ is the in-plane strain and is calculated from the (004) ω-2θ rocking curve. Equation 4-3 then becomes,

$$E_g = 1.35 - 1.083(x(z)) + 0.091(x(z))^2 + \Delta E^H \pm \Delta E^U \qquad \text{Eq 4-7}$$

A conduction:valence band offset of 0.75:0.25 taken from *David et al.* [2], is assumed. The electron and heavy hole effective masses for the well are calculated again by linearly interpolating between the effective masses for InAs and InP for the appropriate value of the composition. By assuming that Fick's Law is obeyed with a constant diffusion coefficient, it is possible to model, using the interdiffusion equations and the transfer matrix (shoot) method (Appendix A), the position of the confined energy states as a function of diffusion length [15]. The diffusion length of the group V elements after each anneal can be determined from the graph. If the square of these (extracted) diffusion lengths is plotted against the anneal time, the diffusion coefficient for the intermixing can be evaluated from the gradient of the graph.

4.2.1 Samples

In this study, two undoped $InAs_xP_{1-x}$/InP MQW structures of different As compositions and well widths, both designed to operate in the 1.3μm region [36, 38], were subjected to dielectric capping and annealing for different times and temperatures. The InAsP/InP heterostructures were grown at the EPSRC III-V facility in Sheffield on (100) oriented, sulphur-doped InP substrates by MOCVD, using trimethlyindium as the group III source and AsH_3 and

PH_3 as the group V sources. The samples were grown at 600°C which is the lowest practical temperature that can be used with this machine using existing calibrations. Sample A (MR980) comprised of five nominally 70Å thick $InAs_xP_{1-x}$ wells, with $x = 0.38$, separated by 400Å InP barriers. Sample B (MR981) comprised of five nominally 40Å thick $InAs_xP_{1-x}$ wells, with $x = 0.44$, separated by 400Å InP barriers. Each sample was capped with a 600Å InP layer. The $InAs_xP_{1-x}$ QW growth rate was about 1.2μm/hour. For sample A, the growth time of the 70Å thick well was 16s and for sample B, the growth time of the 40Å well was 11.5s, leading to a total growth time of around 10 minutes for each sample. *Tweet et al.* [33] grew $InAs_xP_{1-x}$/InP QWs at 620°C and reported a diffusion coefficient for As/P atoms of $1.3x10^{-19}cm^2/s$ which would give a diffusion length of 1Å for every 1000Å of InAsP grown at the rate used here. It was therefore assumed that samples A and B (grown at slightly lower temperatures) had sharp well/barrier interfaces.

Before coating with a 0.1μm thick dielectric capping layer of SiO_2 or Si_3N_4 using PECVD, the emission energy of the sample was mapped across the wafer to reduce errors which might arise between a blue shift in energy due to interdiffusion and the uniformity of the sample. Structural analysis was also carried out using a Philips high resolution X-ray diffractometer to determine the average As composition and well/barrier width. After capping and annealing the sample, optical experiments were performed to determine the extent of the blueshift arising from the diffusion of the group V elements.

4.2.2 Determination of the As composition and well width for the $InAs_xP_{1-x}$/InP QWs

A unique fit to the XRD rocking curve data is difficult with simulations since different combinations of As composition and well/barrier thickness can give good fits, so an iterative method which combines XRD, the transfer matrix and the measured PL data was used in order to establish the composition of As and hence the well width. This method assumes a square well but this is a reasonable assumption given the low growth temperature. Below is an outline and a flow diagram (Figure 4-2) of the process,

- *Experimental data.* PL data yield the e1-hh1 transition. XRD yields values for mean lattice parameter (a) and period (p) and hence the hydrostatic strain can be determined.

- *Set up a spreadsheet.* Varying values of x in $InAs_xP_{1-x}$ and incorporating the information from XRD can be used to generate values of $E_g(InAs_xP_{1-x})$.

- *Transfer matrix model.* Use the value of the bandgap of $E_g(InAs_xP_{1-x})$ to calculate the potential band offsets which are substituted into the transfer matrix model to find e1-hh1 transition.

- *Comparing results.* Compare e1-hh1 calculated results with PL results. The corresponding composition value and hence well width from the closest matching e1-hh1 emission were used to simulate a square well rocking curve.

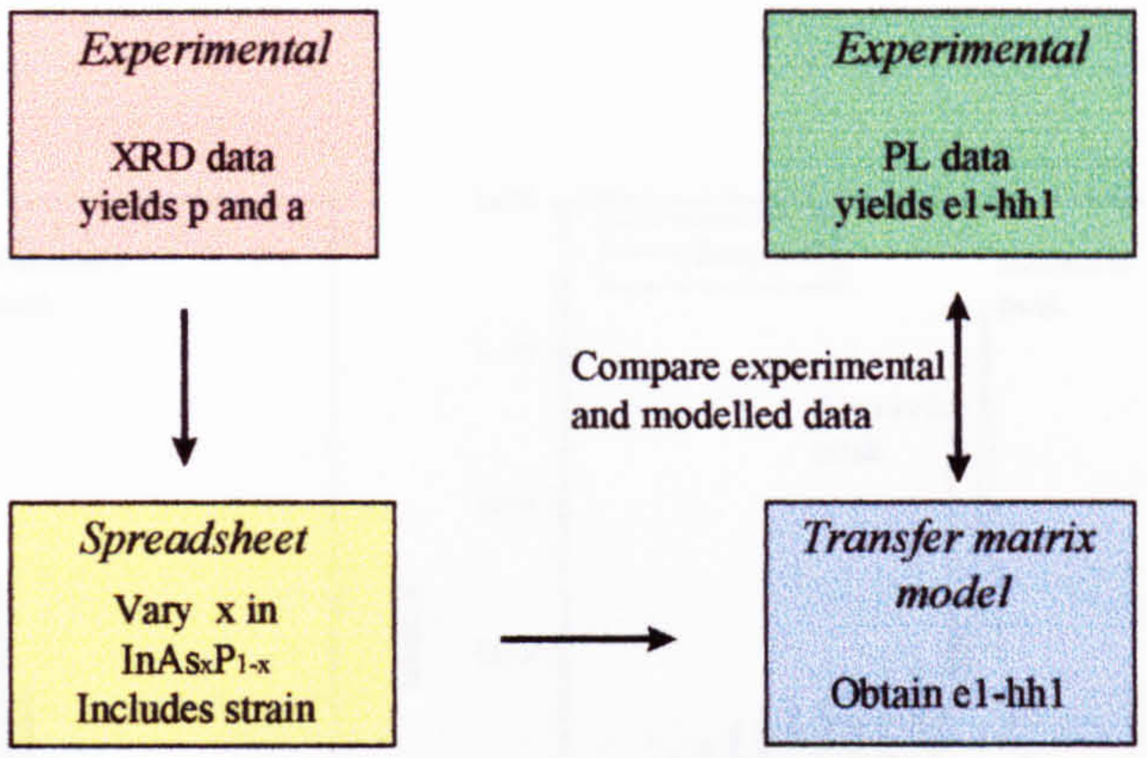

Figure 4-2 *Flow diagram showing the outline of the determination of the As composition and well width for the $InAs_xP_{1-x}$/InP QWs.*

4.2.3 Preliminary characterisation results for unannealed samples A and B

*4.*2.3.1 ***Photoluminescence***

Low temperature (10K) and room temperature (RT) PL spectra were obtained from unannealed pieces of samples A and B. At 10K, the e1-hh1 PL emission peak was located around 1.04 and 1.05eV for sample A and B respectively, with a variation of only 5meV across each wafer. One symmetrical luminescence peak was observed at each position with a FWHM of 15meV for sample A and 18meV for sample B. On increasing the temperature to 300K, the PL peak position shifted to lower energies by 53meV for sample A and 59meV for sample B. The integrated intensity decreased by about a factor of 20 over this temperature range while the FWHM increased to 28 and 36meV for samples A and B respectively.

4.2.3.2 *X-Ray Diffraction*

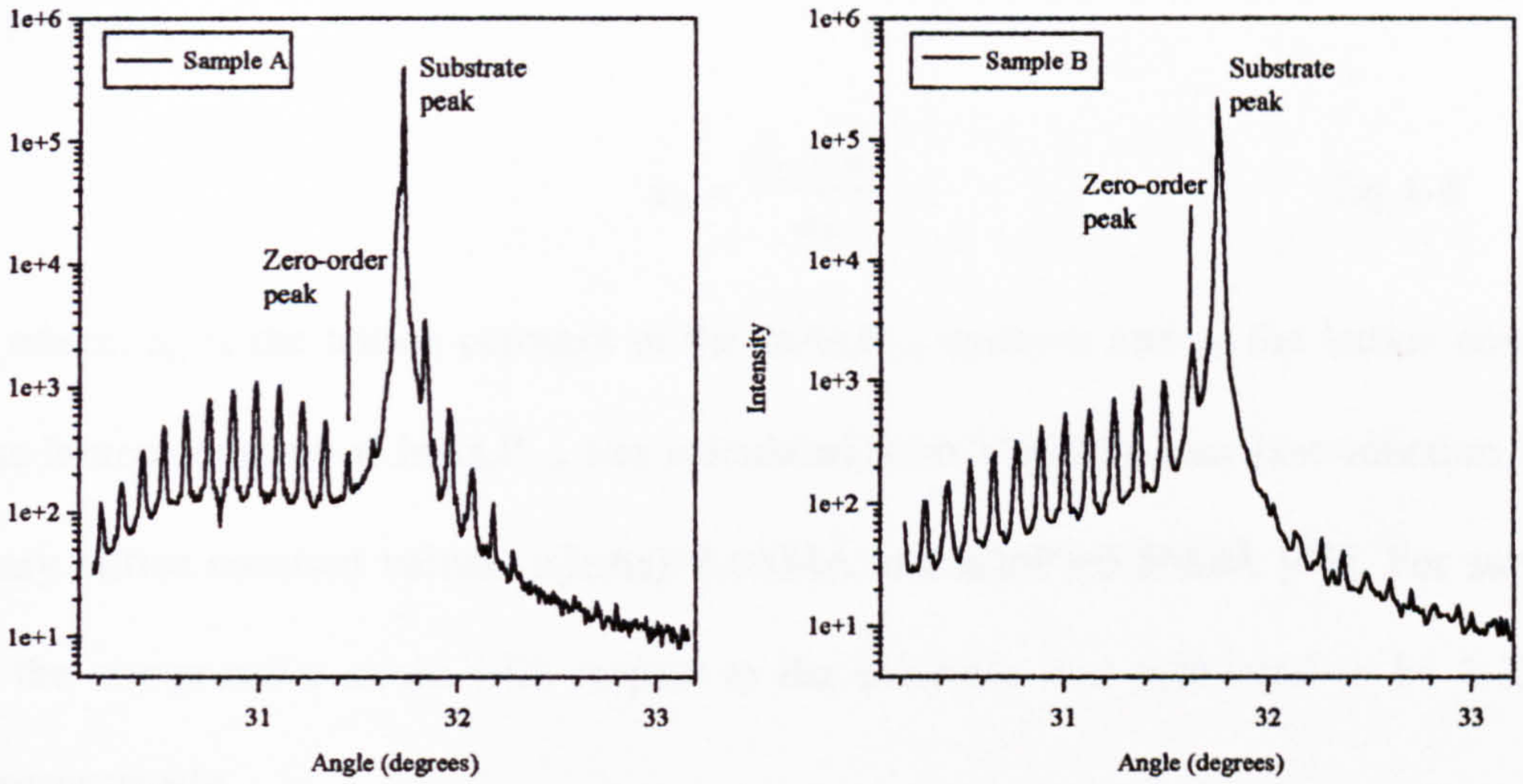

Figure 4-3 *The symmetric (004) rocking curves for sample A and sample B*

The symmetric (004) rocking curves for the samples are displayed in Figure 4-3. The most prominent feature is the sharp peak located at 31.67° arising from the InP substrate peak. The satellite peaks are also sharp and evenly spaced indicating good uniformity of thickness and composition throughout the MQW structure. The splitting, $\Delta\omega$, between the substrate and zero-order peak, corresponding to a reflection from the epilayer, is negative indicating that the samples are compressively strained, as expected. The angular separation between the zero-order and substrate peaks is proportional to the average lattice parameter, $\overline{a}$, in the MQW stack and yields values of 5.8894Å and 5.8853Å for samples A and B respectively. The angular separation of the satellite peaks is a measure of the period yielding values 465Å and 440Å for samples A and B respectively. The equations used to determine $\overline{a}$ and p were given in chapter 1.

The in-plane strain, $\varepsilon_{//}$, in the $InAs_xP_{1-x}$ epilayer with respect to the InP substrate was calculated using,

$$\varepsilon_{//} = \frac{a_L - a_S}{a_S} \qquad \text{Eq 4-8}$$

where, a_L is the lattice constant of the $InAs_xP_{1-x}$ epilayer and a_S the lattice constant of InP. The lattice constant of $InAs_xP_{1-x}$ was calculated from Vegard's Law [Introduction 1] using the binary lattice constant values, a(InAs)=6.0584Å and a(InP)=5.8688Å [41]. For samples A and B, the compressive strain with respect to the substrate was estimated to be 1.23% and 1.42% respectively.

Using the parameters, $\bar{a}$ and p, obtained from the XRD data and the in-plane strain obtained from Eq 4-8, these can be substituted into a series of equations to calculate the perpendicular strain and hence the uniaxial and hydrostatic strain, for a given value of x (Outline of process illustrated in Figure 4-2). The strain is included in the calculation of the $InAs_xP_{1-x}$ bandgap. Assuming a 75:25 ratio for the band offsets [2], the values of the CB and VB potentials and effective mass (linearly interpolated from the binaries) are substituted into the transfer matrix model to obtain the e1-hh1 confinement levels for the quantum well. These values are compared with the experimental PL emission and the corresponding compositional value, x, and hence the well width from the closest matching e1-hh1 emission is obtained. Table 4-1 shows the closest e1-hh1 emission energy value to the PL data and hence the corresponding value of x for sample B as highlighted.

Combining the values from this iterative process with XRD simulations, a self-consistent value of the composition, well and barrier width was deduced. A comparison of the measured and simulated x-ray data indicated that the well was almost square confirming that

there was negligible diffusion of As-P at the interfaces during growth. (Asymmetric grading of the first and second interface or symmetric grading of both interfaces did not produce good fits to the measured data). The XRD results also reveal that the period of the sample and the As composition differ slightly from the nominal values. For sample A, the As composition was 43%, l_w=65Å and l_b=400Å. For sample B, the As composition was 50%, l_w=40Å and l_b=400Å. It is important to obtain an accurate value of the As composition and well width in the unannealed samples as these values will be monitored after annealing.

Table 4-1 *Part of the spreadsheet used to obtain values of x and l_w for sample B*

x	l_w (Å)	l_b (Å)	a(InAsP) (Å)	a_l unstrained	$\varepsilon_{parallel}$	EH-EU (eV)	Eg(InAsP) bulk (eV)	E_g(10K) (eV)	Ec+Ev (eV)	e1-hh1 (eV)
0.46	43.8	396.5	6.0358	5.9560	-0.0122	0.01925	0.87107	0.95702	0.47590	1.0770
0.48	41.7	398.3	6.0430	5.5981	-0.0129	0.02015	0.85112	0.93676	0.49368	1.0647
0.50	**40.0**	**400.0**	**6.0503**	**5.9636**	**-0.0132**	**0.02104**	**0.83125**	**0.91650**	**0.51131**	**1.0538**
0.52	38.5	401.5	6.0576	5.9674	-0.0137	0.02194	0.81145	0.89624	0.52879	1.0430
0.54	37.0	403.0	6.0648	5.9711	-0.0142	0.02285	0.79172	0.87598	0.54612	1.0330

4.3 Rapid Thermal Annealing

The capped samples were annealed in a nitrogen atmosphere at 700°C for 30, 60 or 120s using a RTA. The Si_3N_4 cap was then removed by plasma etching and the SiO_2 by wet etching in Hydrogen Fluoride.

Following these treatments, there was no discernible energy shift, contrary to the result of *Cao et al.* [13] although their work used InGaAsP/InP MQWs where interdiffusion of the group III species may have been enhanced by use of the SiO_2 cap. It was concluded that higher temperatures and longer anneal times would be necessary to induce a measurable interdiffusion in the InAsP/InP QW. The remainder of this chapter deals with the results and conclusions deduced from conventional furnace anneals.

4.3.1 Annealing in a conventional furnace

Samples cut from wafers A and B were annealed in evacuated sealed glass ampoules at temperatures in the range 800-900°C for times between 2 and 30 minutes. Different pieces of sample A or B were used for each anneal obviating the need to map the wafer prior to the anneals. The energy shifts as a function of anneal time are displayed in Figure 4-4 for each sample at each anneal temperature. The PL peak of each annealed sample shifts to higher energies with increasing anneal time. A further two pieces of sample B, coated with SiO_2, were annealed at temperatures of 700°C for one hour and at 1000°C for 300s. After the anneals, the sample surfaces were apparently unchanged although there was a slight degradation of the Si_3N_4 coated epilayer surface at the highest temperatures and longest anneal times. The uncoated underside of the sample surface exhibited significant deterioration due to the P desorption from the surface.

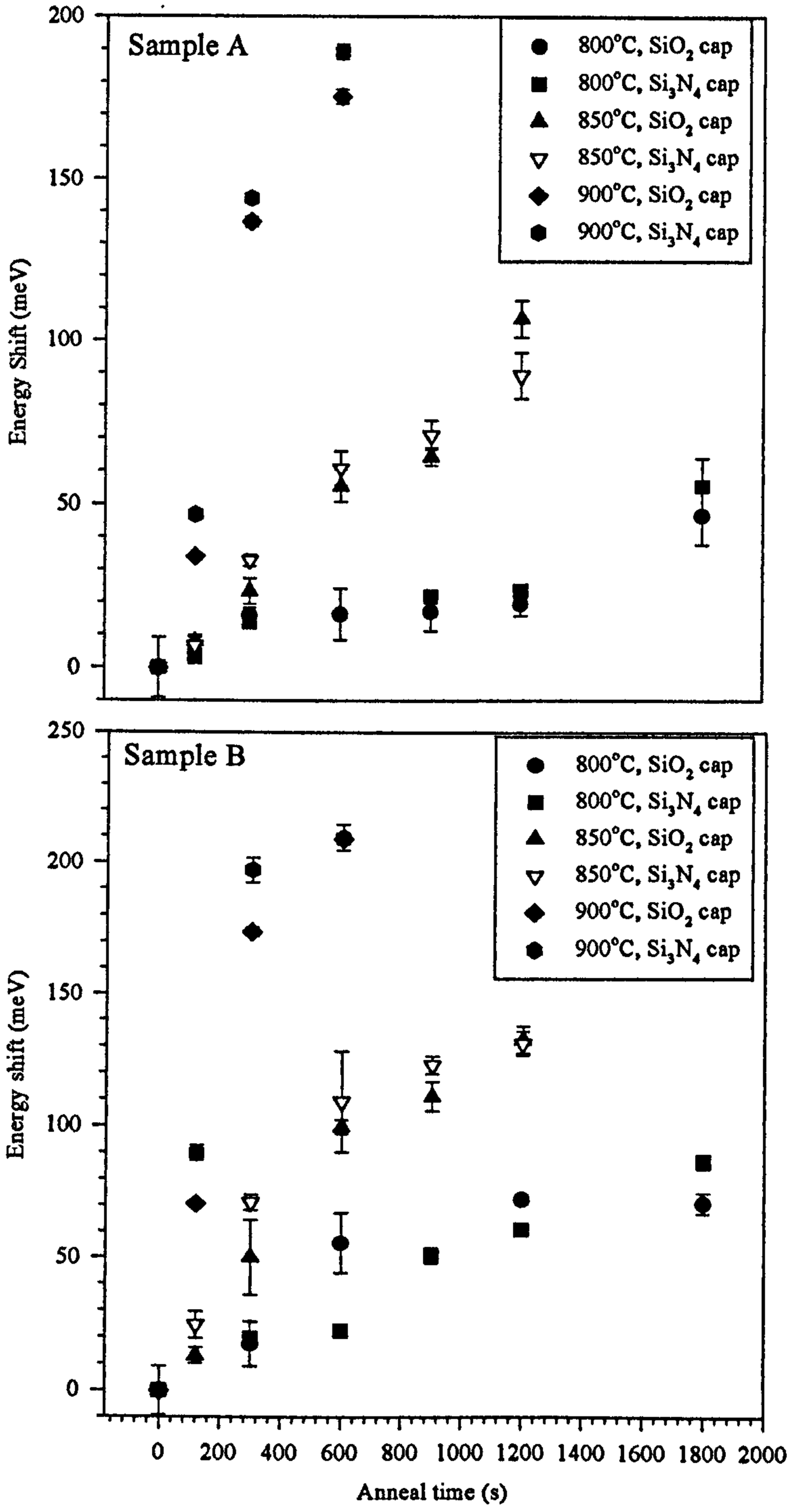

Figure 4-4 *Energy shift versus anneal time at different temperatures, for sample A and B capped with either SiO_2 or Si_3N_4. The error bars indicate the variation in the PL energy over the sample.*

4.3.2 Energy shifts

All samples exhibited an approximately linear blue shift of the emission peak after annealing which is attributed to the interdiffusion of As and P atoms across the heterointerfaces. The slope of the lines increases with anneal temperature but there were no significant differences between the measured blueshifts for the two types of dielectric cap. However, there were small differences in the blueshift across each sample and this is reflected in the error bars in the diagrams. Sample B exhibits a slightly larger gradient than sample A at each anneal temperature perhaps indicating a higher diffusion coefficient. Some saturation effects are evident for sample B which may be due to almost complete interdiffusion of the narrower wells.

4.3.3 PL peak shapes

For short annealing times at the lower temperatures the PL peaks remained symmetric indicating a uniform intermixing of the wells throughout the structure. After annealing at 800°C for the longest time (1800s), the PL peak obtained from sample A diminishes to about two thirds of its original intensity and a slight asymmetry is observed in the peak shape with a weak shoulder evident on the *high energy side*. This reduction in intensity implies that some degradation of the sample has occurred as a result of the annealing. A similar asymmetric feature was also observed for a sample subjected to anneals of 1200s at 850°C. However, for the samples annealed at 900°C, for 300s and 600s and capped with Si_3N_4 and SiO_2, a slight asymmetry is observed on the *low energy side* of the main peak.

Sample B exhibits similar results indicating non-uniformity of intermixing for longer anneal times and higher temperatures. Figure 4-5 shows low temperature (10K) emission

spectra obtained from pieces of sample B subjected to different annealing treatments. For the sample annealed at 800°C for 900s (spectrum b) there is a shoulder to the *high energy side* of the main peak at 1.1eV. Increasing the anneal time to 1800s, (spectrum c) makes the shoulder more pronounced. These results are consistent with non-uniform intermixing throughout the MQW structure. These asymmetric peaks appear, to some extent, to be dependent on the dielectric cap. For instance, a piece of sample B, capped with Si_3N_4 and annealed at 850°C for 1200s exhibited an asymmetric feature but the corresponding SiO_2 capped sample did not. In the case of the samples capped and annealed at 900°C for 600s, a slight shoulder was observed on the *low energy side* of the main peak in agreement with the results for sample A.

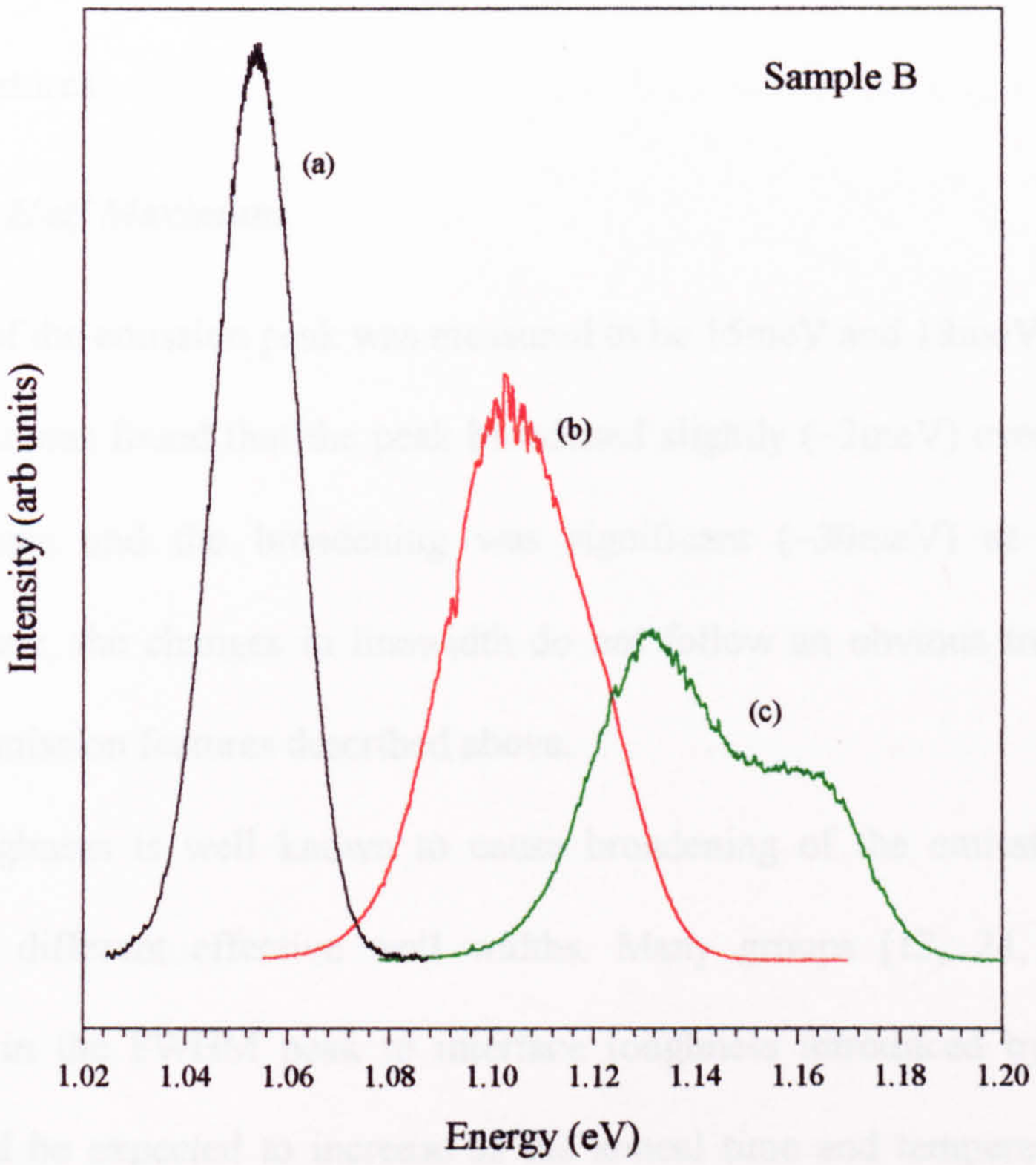

Figure 4-5 *Low temperature (10K) emission spectra obtained from sample B: a) an as-grown sample, b) a sample annealed at 800°C for 900s, capped with Si_3N_4 and c) a sample annealed at 800°C for 1800s, capped with Si_3N_4.*

Similar results were obtained for samples cut from wafer B. A sample annealed at a relatively low temperature of 700°C for 3600s exhibited a shift of 50meV. A shoulder was present on the high energy side of the main peak in agreement with the results obtained for samples annealed at 800 and 850°C. However, a sample annealed at a relatively high temperature of 1000°C for 300s showed a blueshift of 280meV with a clear shoulder on the low energy side of the main peak similar to the result obtained from the sample annealed at 900°C. These results imply that there are two different processes which can lead to non-uniform

broadening of the PL features; one occurring at higher anneal temperatures and the other at lower anneal temperatures.

4.3.4 Full Width at Half Maximum

The FWHM of the emission peak was measured to be 15meV and 18meV for samples A and B respectively. It was found that the peak broadened slightly (~3meV) even at the lowest annealing temperatures and the broadening was significant (~30meV) at higher anneal temperatures. However, the changes in linewidth do not follow an obvious trend due to the asymmetries in the emission features described above.

Interface roughness is well known to cause broadening of the emission peak since excitons experience different effective well widths. Many groups [13, 24, 29, 43] have attributed increases in the FWHM peak to interface roughness introduced by the diffusion process which would be expected to increase as the anneal time and temperature increased. *Mallard et al.* [9] observed an increase in spectral linewidth of 6meV for an InGaAs/InGaAsP sample after annealing, while *Cao et al.* [13] observed a larger increase of 30meV when annealing SiO_2 capped InGaAsP/InP MQWs at 750°C for times between 30s to 90s. These authors also observed a shoulder on the high energy side of the main peak similar to the work reported here. *Ghisoni et al.* [44] studied interdiffusion in AlGaAs/GaAs QWs by the IFVD process. They concluded, from TEM images, that interdiffusion had not only graded the aluminium concentration across the well/barrier interface, but had also introduced random fluctuations along the interface. Thus the decrease in intensity and broadening of the PL peak after annealing may be due to interface roughness or the introduction of impurities while the asymmetrical broadening of the peak is likely to arise from a well-to-well variation. In

principle, inadvertent impurities could also lead to an asymmetrical peak but this invariably yields only low energy shoulders and cannot account for all the results presented here.

4.3.5 High excitation power experiments

In order to distinguish between effects of interdiffusion which changes the shape of the confining potential and any impurities that may have been introduced as a result of the annealing process or even the growth process, further optical studies have been conducted. Performing a PL power or temperature variation experiment on the annealed samples should enable intrinsic and extrinsic processes to be distinguished. At high temperatures or excitation power, predominantly free excitonic emission (intrinsic) is detected. A power variation experiment was carried out on a piece of sample B, coated with SiO_2 and annealed at 700°C for 3600s. Using a combination of neutral density filters, the HeNe excitation power on the sample was varied from 1-7mW. Figure 4-6 shows that a high energy shoulder is present in all the spectra. The integrated intensity increases with increasing power while the PL peak remains the same shape, implying that the shoulder is due to an intrinsic rather than an extrinsic process. Consequently the asymmetry in the PL feature is ascribed to a non-uniform interdiffusion of the QWs causing a well-to-well variation.

An argon ion laser (λ=5145Å) was also used as the excitation source and the resulting spectrum is shown in Figure 4-6. Now, only a small shoulder is observed with the main peak centred at 1.09eV. Since the penetration depth of the argon ion laser is less than the HeNe laser and only the wells nearer the surface are being excited, then the dominant peak originates from the top wells and the shoulder originates from the wells located nearer the substrate, indicating that the latter wells have experienced more intermixing.

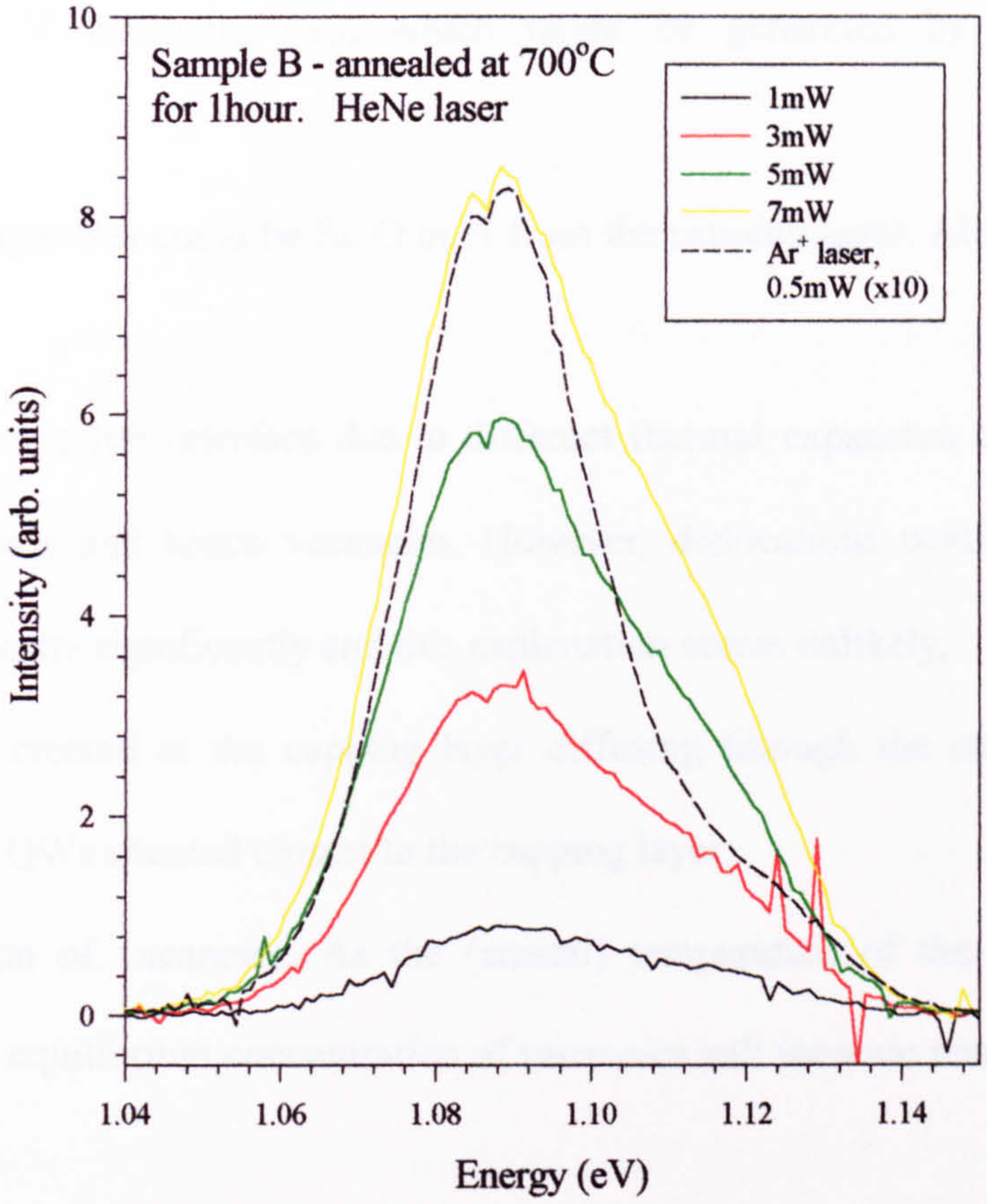

Figure 4-6 *PL spectra at 10K for sample B, annealed at 700°C for 1 hour. The main figure shows that the high energy shoulder on the main peak is retained after varying the HeNe excitation power. The dotted curve shows a smaller high energy shoulder on the main peak after being excited with the Argon ion laser.*

4.3.6 Sources of interdiffusion

The asymmetric peaks imply that non-uniform intermixing has taken place throughout the MQW structure. It would appear that annealing the sample at low (high) temperatures, an asymmetry on the high (low) energy side of the main PL peak emerges indicating that different QWs have experienced different amounts of intermixing. The interdiffusion is likely to be

mediated by group V vacancies (V_P) which might be generated by several different mechanisms:

a) IID. Sources of impurities could be Si, O or N from the capping layer. Alternatively, S from the substrate,

b) strain at the dielectric/InP interface due to different thermal expansion coefficients which generate dislocations and hence vacancies. However, dislocations would be expected to reduce the PL intensity significantly and this explanation seems unlikely,

c) IFVD. Vacancies created at the capping layer diffusing through the structure enhancing intermixing in the QWs situated closest to the capping layer,

d) Thermal generation of vacancies. As the (anneal) temperature of the semiconductor is increased then the equilibrium concentration of vacancies will increase resulting in enhanced intermixing [25].

The impurities that might be responsible for the interdiffusion of As and P via the IID process are Si, O or N from the capping layer or S from the substrate. Si acts as a donor in InP and is usually incorporated on indium lattice sites in InP and would be unlikely to generate V_P (in fact V_{In} would be more likely) although there has been one report by Schwarz *et. al.* [45] which concluded that there is interdiffusion of both sublattices in InGaAs/InP QWs when the Si doping level is around 5×10^{18} cm^{-3}. Alternatively an impurity such as Si may enhance vacancy creation through the IFVD mechanism and not directly interfere with the MQWs.

There is very little information on the behaviour of oxygen and nitrogen in InP. If they are fast diffusers in InP then they could be responsible for the interdiffusion processes observed in this work. Oxygen also acts as a deep donor in GaAs and InP forming non-radiative recombination centres [45] and therefore a decrease in intensity of the peaks will be seen.

However, no significant differences were found for the interdiffusion of As/P in the samples investigated here using dielectric caps containing N and O so it seems reasonable to assume that these atoms are not involved. It appears unlikely that impurities, dislocations or vacancies originating from the capping layer diffuse into the wells as the power variation experiment revealed that at the low anneal temperature, the wells nearer the substrate exhibited more interdiffusion. If the source of diffusion originated from the capping layer, we would expect the top wells to exhibit more intermixing even at low anneal temperatures.

Impurities or vacancies generated at the substrate could be responsible for enhancing interdiffusion of the wells located nearer the substrate at low anneal temperatures. S atoms from the substrate may diffuse through the active region. There have been a few studies of the diffusion of S in InP [47] but these gave conflicting results, suggesting that S is either a fast or a slow diffuser. *Dutt et al.* [48] showed that S atoms preferentially out-diffuse when used as a dopant in InP. Sulphur atoms may enhance vacancy creation which in turn enhances intermixing in the wells and barriers. However, from the high excitation power experiment, impurities diffusing into the active region are not responsible for the intermixing of the wells as the high energy shoulder did not saturate with increasing excitation power. Phosphorus vacancies generated at the lower substrate surface from existing impurities and or vacancies in the substrate after annealing may responsible for intermixing in the active region but this is difficult to prove.

It is concluded therefore that simple thermal generation of V_P is most likely responsible for the interdiffusion effects observed in this work. It might therefore be expected that the induced intermixing would be uniform throughout the wells. This cannot provide an explanation for the asymmetry shown in Figure 4.6 and further work is necessary to understand

the nature of the non-uniform interdiffusion although the asymmetrical peaks only occur following long anneals at both the low and high temperatures and clearly these treatments should be avoided for device applications.

4.4 Implementing the Interdiffusion Equations

The previous sections have demonstrated that capping and annealing induce blueshifts in the emission spectrum which are attributed to interdiffusion of As and P across the well/barrier interfaces. In the following sections the interdiffusion process is modelled using the equations introduced in section 4.2. The modelled profile is compared with optical data in a self-consistent way so that a diffusion length can be associated with each annealing treatment. By plotting the diffusion lengths deduced in this way against the anneal time, the diffusion coefficient corresponding to each anneal temperature can be established. Finally a comparison of the diffusion coefficients at each temperature can be used to calculate the diffusion coefficient as a function of temperature in the form [49],

$$D = D_0 \exp\left(\frac{-E_a}{k_B T}\right) \qquad \text{Eq 4-9}$$

where E_a is the activation energy for diffusion and D_0 is the pre-exponential factor, both being independent of temperature and characteristic of the diffusing constituent in a semiconductor material.

4.4.1 Results and Modelling for sample A

Assuming the diffusion of group V atoms obeys Fick's Law, Eq 4-2 can be modified to take into account the well width (65Å) and the initial As content in the well (43%), calculated in section 4.2.2,

$$x(z) = x_0 + 0.43\left\{\left[1+\exp\left(-\frac{z-32.5}{0.858(Dt)^{\frac{1}{2}}}\right)\right]^{-1} - \left[1+\exp\left(-\frac{z+32.5}{0.858(Dt)^{\frac{1}{2}}}\right)\right]^{-1}\right\} \qquad \text{Eq 4-10}$$

Incremental diffusion lengths were substituted into the composition equation (Eq 4-10) to obtain the well profile for varying diffusion lengths. Once the composition profile has been calculated, the potential well profile for the conduction band and valence band can be calculated from Eq 4-11,

$$E_0 = 1.35 - 1.083(1-x(z)) + 0.091(1-x(z))^2 + 0.0464(x(z)) + 0.0266 + 0.03168(1-x(z)) \qquad \text{Eq 4-11}$$

The first three terms of Eq 4-11 correspond to the bandgap of bulk $InAs_xP_{1-x}$ at 300K. As the bandgap is temperature dependent the next two terms allow the calculated bandgap to be compared directly with the measured PL data at 10K i.e the bandgap at 10K can be calculated as a function of the composition. The last term incorporates the effect of the hydrostatic and uniaxial strain (for heavy holes only) on the bandgap as a function of composition (Section 4.2). The strain at the centre of the well (z=0) is calculated and varied as a function of composition which has been generated from Eq 4-10.

Figure 4-7 illustrates the resulting potential well profile for the conduction band of the original square well and the diffused well. The figure shows the profile of the well as P diffuses into the well (and As diffuses out). As the InAsP/InP interdiffuses, the interface between the

two materials changes in profile from an abrupt to a graded interface. For the CB, the interdiffusion effectively narrows the well near the bottom but broadens it near the top and vice versa for the VB.

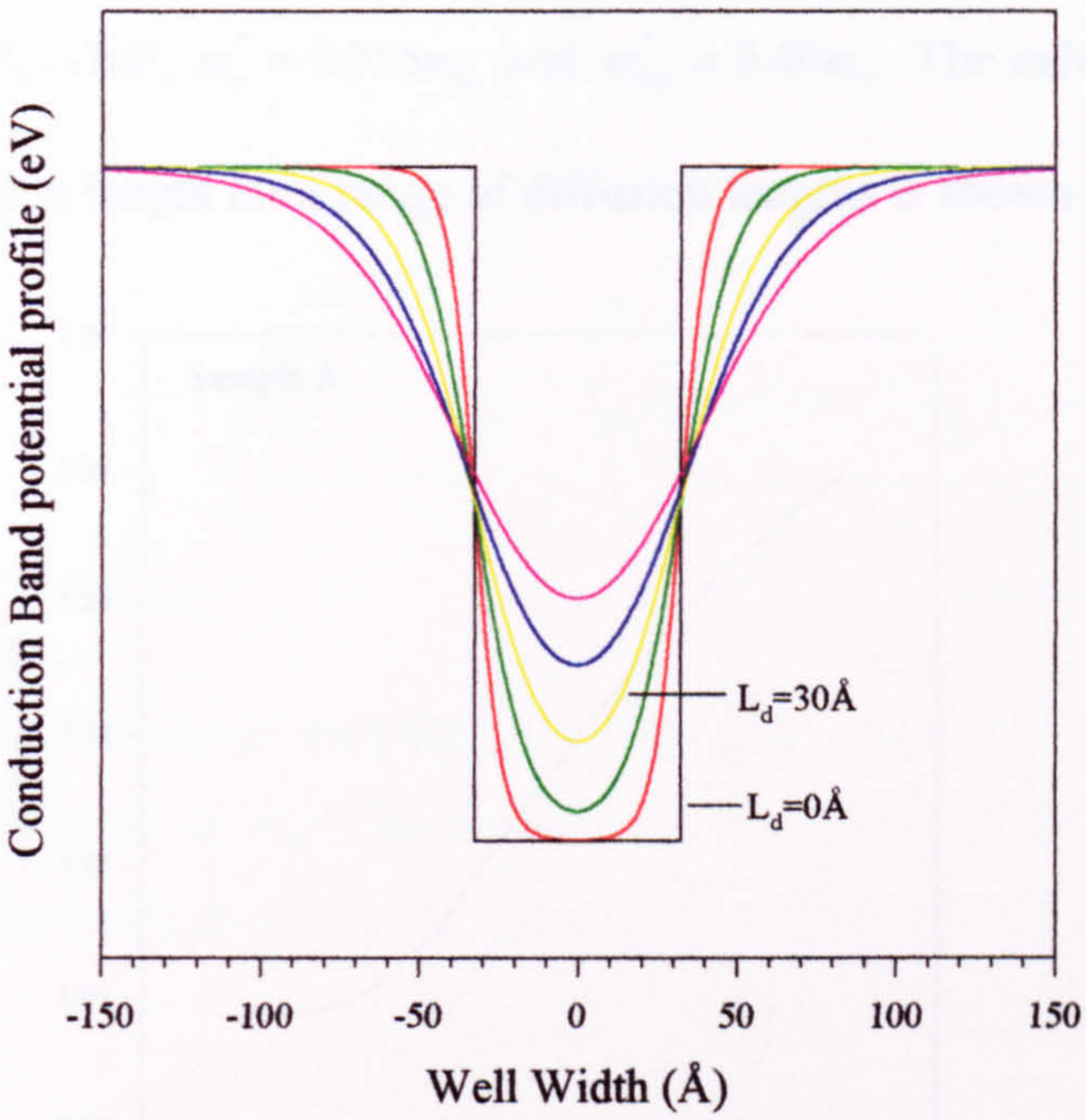

Figure 4-7 *The potential well profile for the conduction band of the original square well and the calculated diffused well is displayed for sample A. The diffusion lengths (L_d) have been indicated.*

The separation between the top of the CB and the bottom of the VB increases as the As/P diffuse. This will result in an increase in the e1-hh1 transition energy. Narrowing of the well potential will also increase the confinement energies adding to the blueshift. A small redshift would also be expected since the barrier height decreases with longer anneal times but this term is relatively small and has therefore been ignored.

The bandgap of $InAs_xP_{1-x}$ at the centre of the well (z=0), calculated for different values of x, can now be used to determine the e1-hh1 energy transitions by employing the transfer

matrix model. A CB:VB band offset ratio of 75:25 [2] was assumed and the electron and heavy hole masses for the well were calculated by linearly interpolating between InAs and InP. For the unannealed structures, the effective masses for InP of $m_e^* = 0.08m_0$ and $m_{hh}^* = 0.56m_0$ were adopted and for $InAs_{0.43}P_{0.57}$/InP, $m_e^* = 0.055m_0$ and $m_{hh}^* = 0.49m_0$. The calculated variation in the PL energy with diffusion length for a range of diffusion lengths is shown in Figure 4-8.

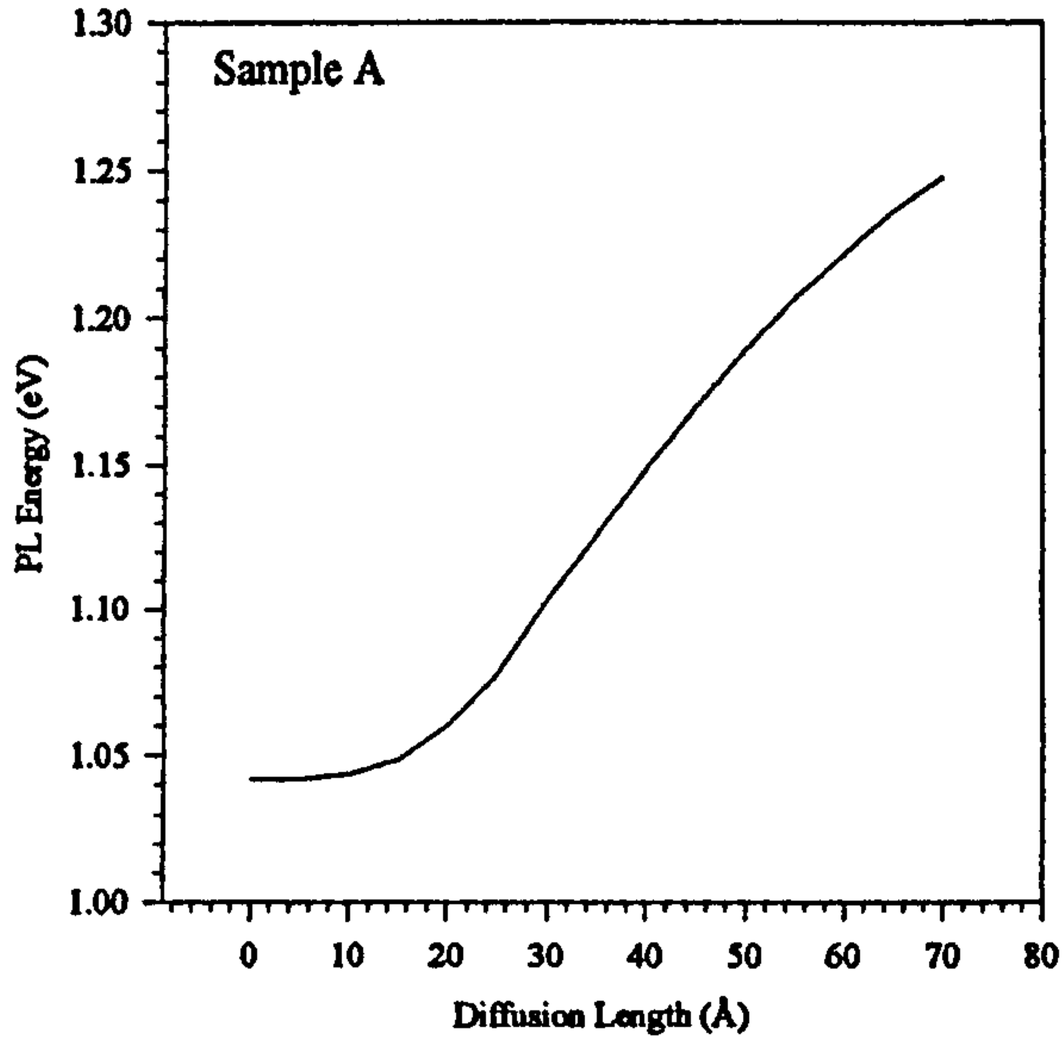

Figure 4-8 *Calculated variation in the PL emission energy against diffusion length for sample A.*

The e1-hh1 transition energy is sensitive to a diffusion length >15Å. The experimental PL emission energy recorded after each anneal for sample A can be used together with the calculated PL energy to determine the diffusion lengths for different anneal times. The experimental and calculated PL energies were plotted on the same graph as shown in Figure 4-9 a) and b) for sample A annealed at 800°C, capped with SiO_2 and Si_3N_4 respectively.

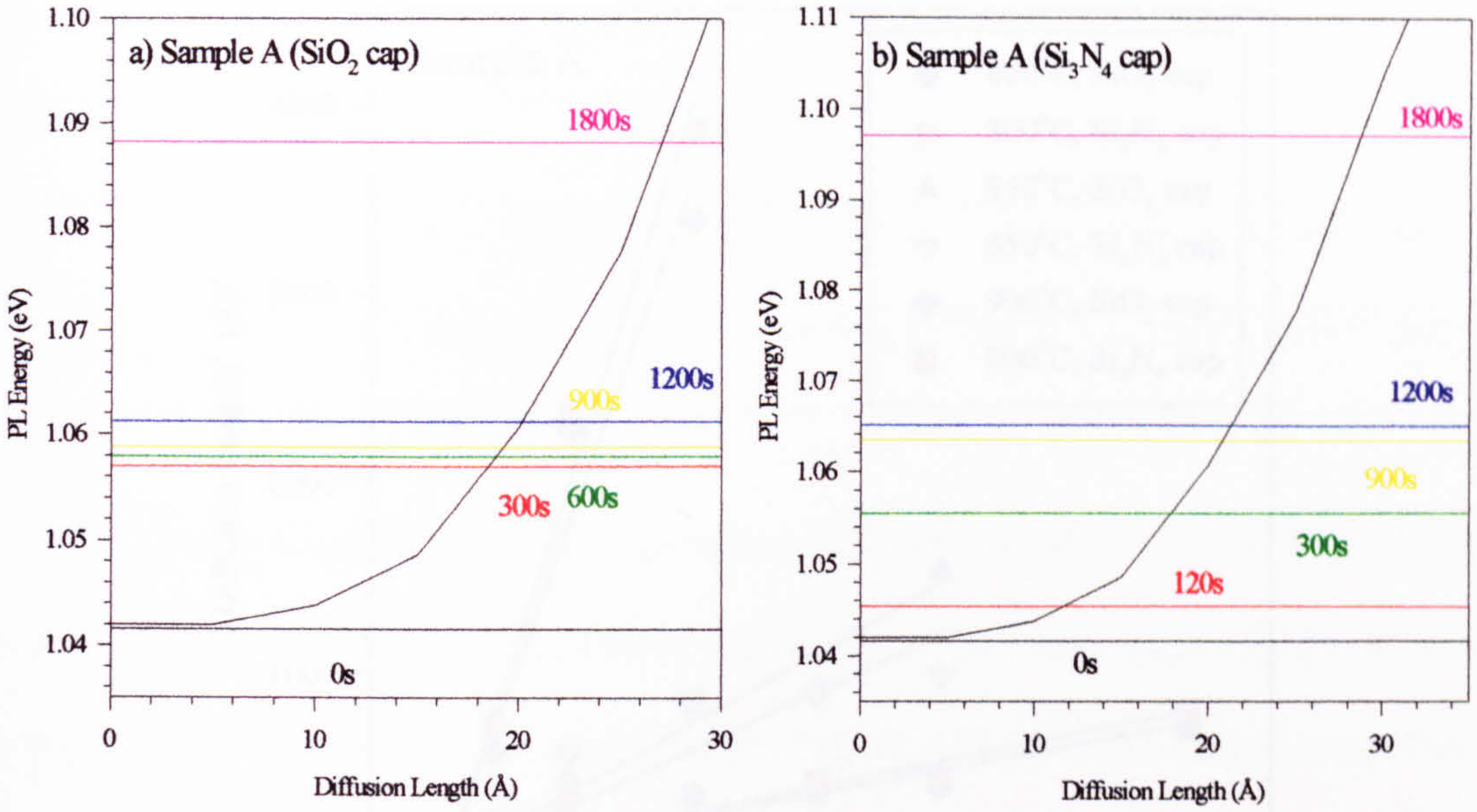

Figure 4-9 *Variation in the PL energy with diffusion length for sample A. The horizontal lines mark the position of the experimental PL emission for samples annealed at 800°C, capped with a) SiO_2 or b) Si_3N_4.*

The small difference of ~1meV between calculated and experimental e1-hh1 emission data at L_D=0 is a consequence of using the nearest integer value of x and the well width (l_w), (described in section 4.2.3). The diffusion length obtained from the intersection of the experimental and calculated energies can be used to determine the diffusion coefficient, D, for each anneal temperature. D is deduced from the slope of a plot of the square of the diffusion length against anneal time where the gradient =4D.

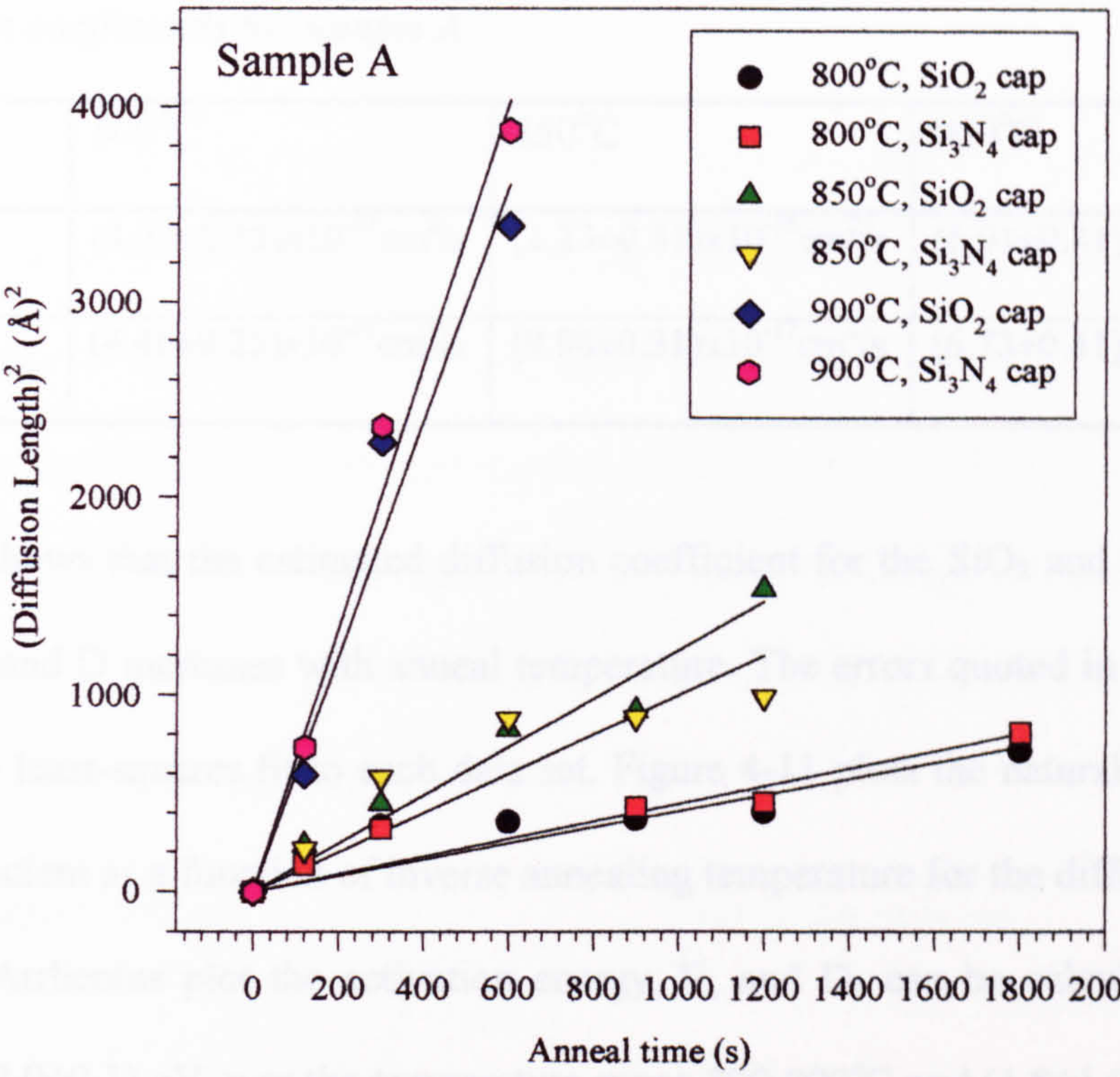

Figure 4-10 *Square of the diffusion length against anneal time for different anneal temperatures for sample A.*

Figure 4-10 shows a plot of the square of the diffusion length against anneal time for sample A at the three annealing temperatures. The slope in each case is nearly linear (=4D) implying that interdiffusion proceeds with a constant diffusion coefficient for each anneal temperature justifying the initial assumption of Fick's Law. Values of D deduced from Figure 4-10 are listed in Table 4-2.

Table 4-2 *Diffusion coefficients for sample A*

Dielectric cap	800°C	850°C	900°C
SiO_2	$(4.07\pm0.25)\times10^{-17}cm^2/s$	$(1.23\pm0.31)\times10^{-16}cm^2/s$	$(6.01\pm0.41)\times10^{-16}cm^2/s$
Si_3N_4	$(4.46\pm0.25)\times10^{-17}cm^2/s$	$(9.98\pm0.31)\times10^{-17}cm^2/s$	$(6.73\pm0.41)\times10^{-16}cm^2/s$

Table 4-2 shows that the estimated diffusion coefficient for the SiO_2 and Si_3N_4 capped samples is similar and D increases with anneal temperature. The errors quoted in this table are those given for the least-squares fit to each data set. Figure 4-11 plots the natural logarithm of the diffusion coefficient as a function of inverse annealing temperature for the different capping layers. From this Arrhenius plot the activation energy, E_a and D_0 can be calculated and are determined to be (2.9±0.1) eV over the temperature range 800-900°C and $(1.8\pm1.0)\times10^{-3}$ cm^2s^{-1} respectively.

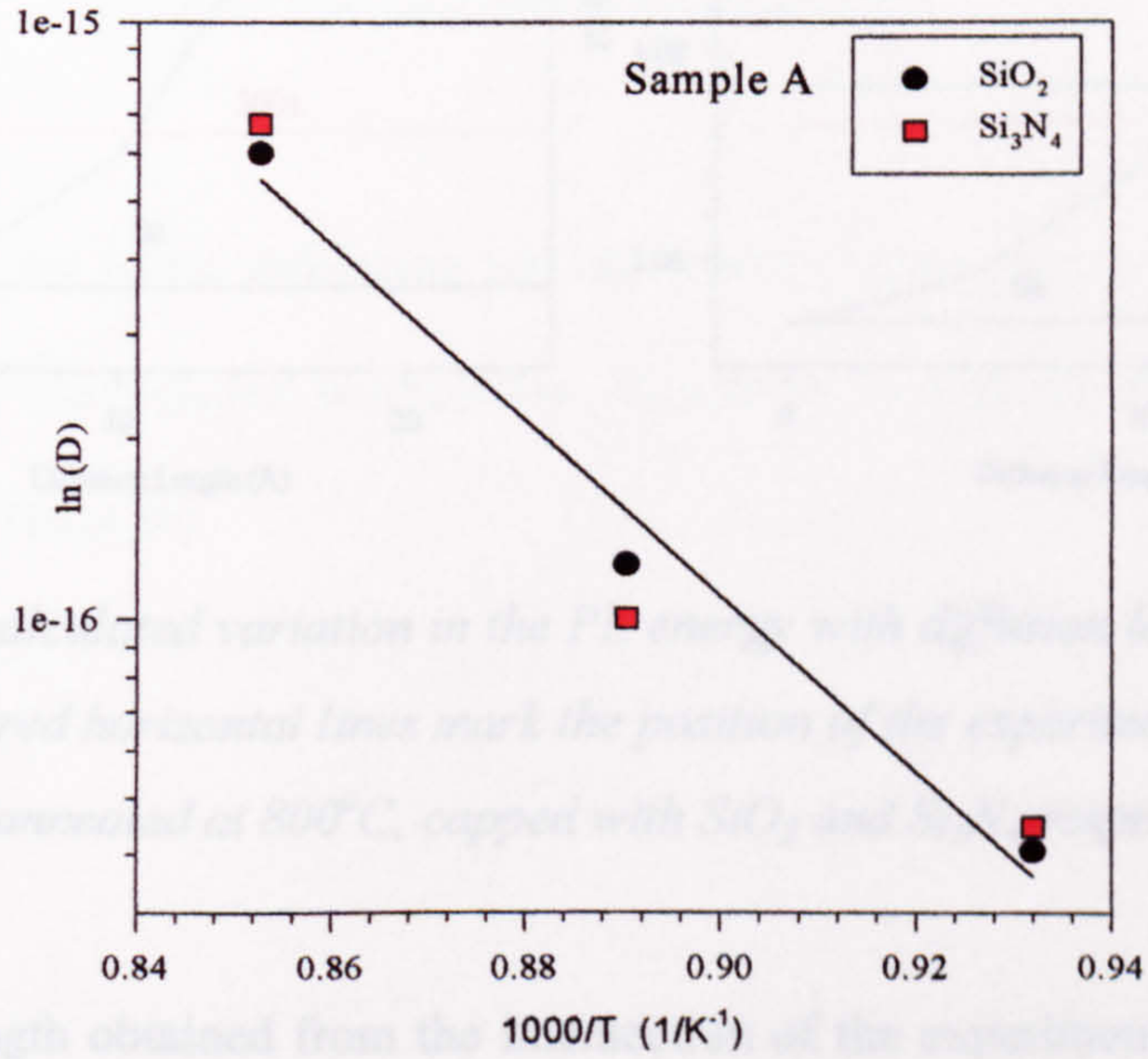

Figure 4-11 *Arrhenius plots of the diffusion coefficient for the SiO_2 and Si_3N_4 capped samples (Sample A)*

4.4.2 Results and Modelling for sample B

The same method is used to deduce the group V diffusion coefficient for sample B. The compositional profile equation (Eq 4.2) is used taking into account the well width (40Å) and the initial As content in the well (50%). Using these composition results the potential well profile for the conduction band minima and valence band maxima can now be calculated and the energy of the e1-hh1 transition calculated. The calculated PL energy and the PL emission energy recorded after each anneal for sample B are used together to determine the diffusion length for each anneal time as shown in Figure 4-12.

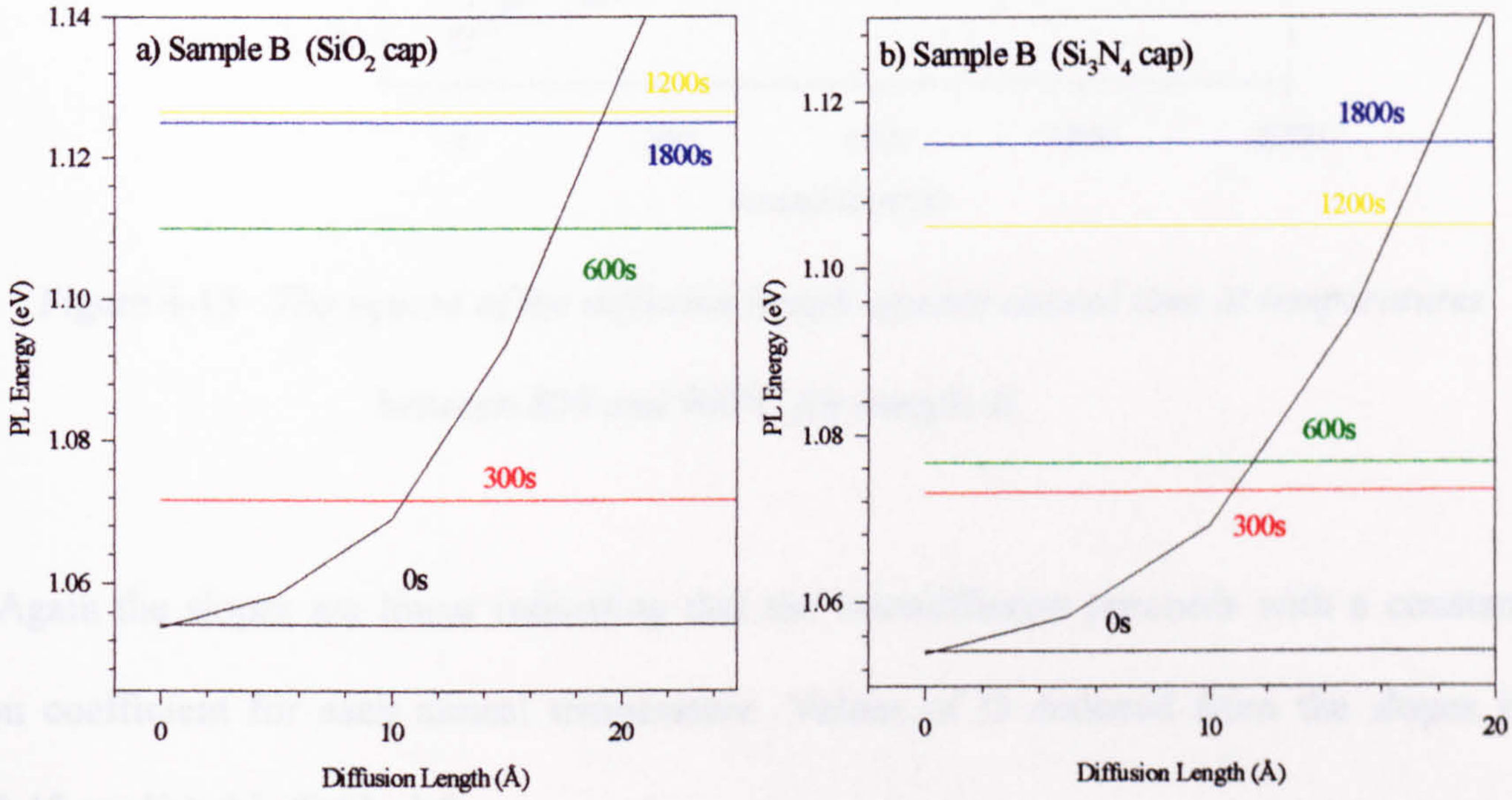

Figure 4-12 *shows the calculated variation in the PL energy with diffusion length (black line). The coloured horizontal lines mark the position of the experimental PL emission. a) and b) annealed at 800°C, capped with SiO_2 and Si_3N_4 respectively for sample B.*

The diffusion length obtained from the intersection of the experimental and calculated energies is used to determine the diffusion coefficient for each anneal time and temperature. The square of the diffusion coefficient is plotted against anneal time as shown in Figure 4-13.

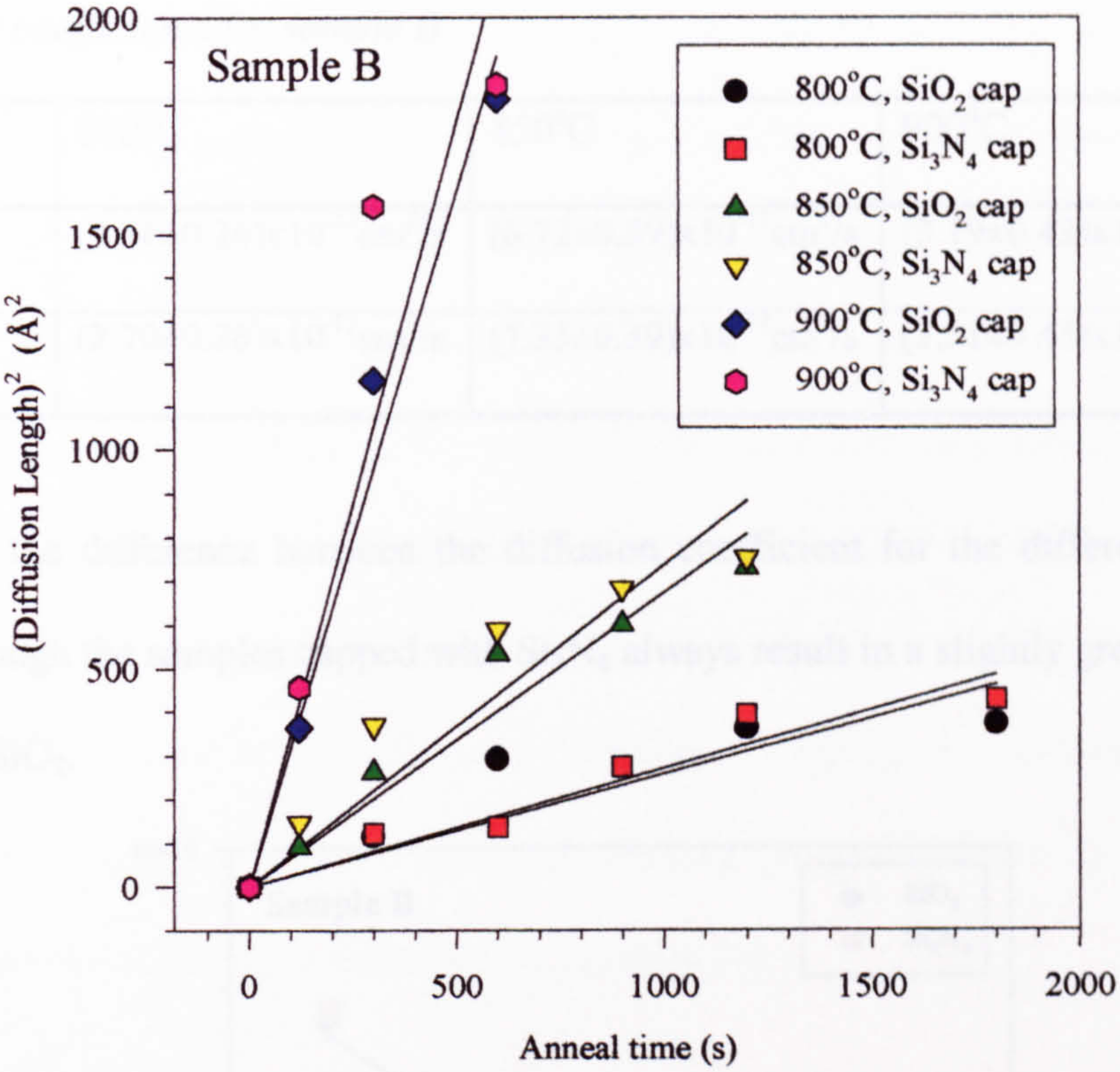

Figure 4-13 *The square of the diffusion length against anneal time at temperatures between 800 and 900°C for sample B.*

Again the slopes are linear indicating that the interdiffusion proceeds with a constant diffusion coefficient for each anneal temperature. Values of D deduced from the slopes in Figure 4-13 are listed in Table 4-3.

Table 4-3 *Diffusion coefficients for sample B*

Dielectric cap	800°C	850°C	900°C
SiO_2 Cap	$(2.56\pm0.26)\times10^{-17}cm^2/s$	$(6.72\pm0.39)\times10^{-17}cm^2/s$	$(3.19\pm0.43)\times10^{-16}cm^2/s$
Si_3N_4 Cap	$(2.70\pm0.26)\times10^{-17}cm^2/s$	$(7.35\pm0.39)\times10^{-17}cm^2/s$	$(3.51\pm0.43)\times10^{-16}cm^2/s$

Once again the difference between the diffusion coefficient for the different capping layers is small although the samples capped with Si_3N_4 always result in a slightly greater D than those capped with SiO_2.

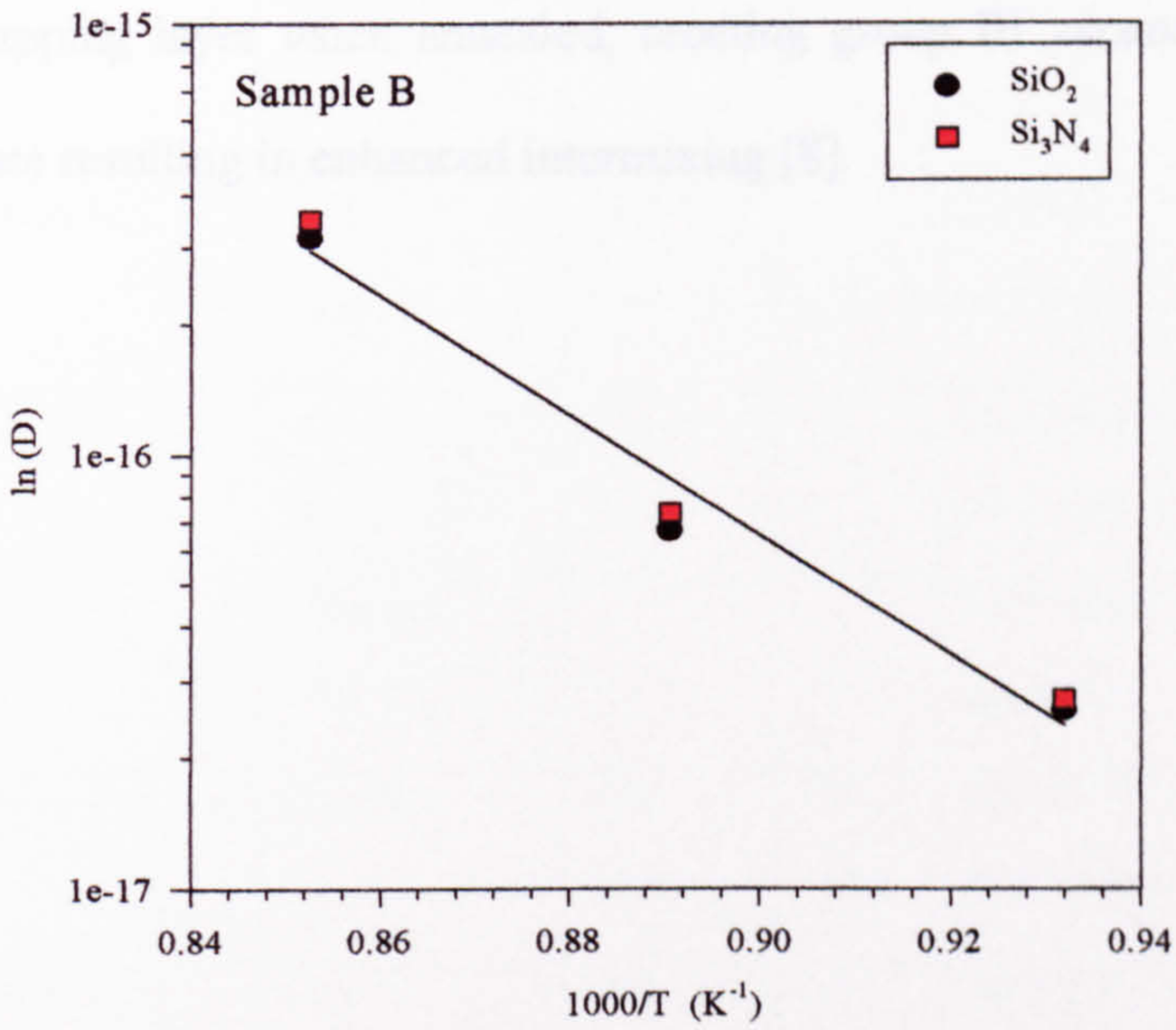

Figure 4-14 *Arrhenius plots of the diffusion coefficient for the SiO_2 and Si_3N_4 capped samples (Sample B)*

Figure 4-14 displays the calculated diffusion coefficient on an Arrhenius plot. The activation energy is calculated to be (2.7±0.1)eV over the temperature range 800-900°C and D_0 $=(1.8\pm1.1)\times10^{-4}\ cm^2s^{-1}$.

The activation energies are similar for samples A and B providing proof that As/P interdiffusion is a thermally activated process. The values of D_0 are reasonably close within experimental error. Estimates of D_0 deduced from other studies yield widely differing values ranging from $8x10^{-7}$ to $7x10^{10}cm^2s^{-1}$ (table 4-4). The large variation in D_0 might be attributed to vacancies or impurities in the wafer. Only some of the published data provides a suitable comparison with the present work, since (with the exception of the study by *Sallese et al.* [43] on very thin layers) other studies involve combinations which allow the possibility of group III interdiffusion which is known to be affected by dielectric capping. For example, Ga atoms migrate into a SiO_2 capping layer when annealed, creating group III vacancies which diffuse through the QW structure resulting in enhanced intermixing [8].

Table 4-4 *Values of E_a, D and D_0 calculated by other groups.*

Group [reference]	Structure	Diffusing elements	Annealing Conditions	Anneal temperature	Anneal time	Diffusion coefficient and E_a	D at 850°C cm^2s^{-1}
Sallese *et al.* [43] 1994	2ML of InAs on InP	As in InP	RTA - P desorp	830°C	5 mins	D_0=5.2x10^{-6} cm^2s^{-1} E_a=3.8eV	~(7±0.5)x10^{-17}
Gillin *et al.* [50] 1993	InGaAs/ InGaAsP group III - same concentration in wells and barrier	GroupV	RTA Si_3N_4	> 675°C	10-200s	D_0=23cm^2s^{-1} E_a=3.7eV	~9.13x10^{-16}
				< 675°C		D_0=5x10^{-10}cm^2s^{-1} E_a=1.7eV	
Schlesinger [26] 1986	AlGaAs/GaAs	Group III Al & Ga	Furnace SiN_x prevent As	850°C		D_0=2.4x10^{10}cm^2s^{-1} E_a=6.0eV	~4x10^{-19}
Oshinowo [29] 1992	$In_{0.53}GaAs/InP$	Group III/V	RTA N_2 atmosphere	900°C		D_0=8.6x10^{-8}cm^2s^{-1} E_a=2.6eV	~6.31x10^{-17}
Ralston [19]	GaAs/AlGaAs	Al / Ga	furnace SiO_2			D_0=13.99cm^2s^{-1} E_a=4.13eV	~7.3x10^{-18}
Ralston [19]	GaAs/AlGaAs	Al / Ga	Uncapped			D_0=2.06x10^{7}cm^2s^{-1} E_a=5.67eV	~7.4x10^{-19}
Bryan	InAsP/InP Sample A	group V	Capped	800-900°C	120-1800s	D_0=1.8x10^{-3}cm^2s^{-1} E_a=2.9±0.1eV	~1.1x10^{-16}
Bryan	InAsP/InP Sample B	group V	Capped	800-900°C	120-1800s	D_0=1.9x10^{-4}cm^2s^{-1} E_a=2.7±0.1eV	~7.0x10^{-17}

4.4.3 Comparisons between samples A and B

The diffusion coefficient deduced at the three anneal temperatures for sample A are larger by a factor of 1.5 than those for sample B however, this is not significant within experimental error. *Tweet et al.* [16] have suggested that the grown-in strain in pseudomorphic structures enhances the interdiffusion. These authors investigated strain dependent interdiffusion in InAsP layers grown on an InP substrate. *Fujii et al.* [20] concluded that strain suppresses diffusion. They studied diffusion in InGaAs/InP QWs by PL spectroscopy and suggested that the diffusion rate was determined by the movement of group V species across the heterointerface which is much lower than the diffusion rate in bulk InGaAs or InP layers. They concluded that diffusion through the interface was retarded by local strain. The strain energy was calculated to be of the same order of magnitude as E_a and they concluded that strain could have a significant effect upon the diffusion through the pre-exponential term. *Gillin et al.* [32] reported that strain did not affect the rate of diffusion in InGaAs/GaAs and InGaAs/InGaAsP QWs. The structures were designed so that there was a concentration gradient to drive diffusion on only one sublattice. These authors concluded that the diffusion constant does not change with time and therefore cannot change either with concentration or strain since these both vary with time. Furthermore, a study of a MQW sample with different In concentration in each well (and hence different initial strains) showed no change in the diffusion constant with strain. However, the small difference in the value of D between samples A and B is not sufficient to conclude that the strain significantly alters the rate of diffusion in differently strained samples, even though the initial strain at the centre of well for unannealed sample A is 1.37% (As = 0.43) and for unannealed sample B is 1.62% (As = 0.50). Interface roughness may account for the slight differences between D and D_0 measured for samples A and B. Potential fluctuations

could act as traps or sinks for vacancies or diffusing As atoms and hence retard the diffusion coefficient.

Even though the group V atoms appear to diffuse faster in sample A, sample B exhibits the greater blue shift. *Fujii* [20], *Francis* [30] and *Mallard* [24] *et al.* showed that diffusion was enhanced in thinner wells. *Mallard et al.* [24] concluded that greater blue shifts were observed in thinner wells due to the confinement energies being affected more by compositional changes at the interfaces. *Fujii et al.* [20] showed that the relationship between the PL energy shift was inversely proportional to the well width. This well width dependence has been confirmed by the results presented here as a larger blue shift was consistently observed for the sample with the narrower well (sample B).

The most important and interesting result seems to be that the value of the diffusion coefficient is independent of the capping layer. Other authors have shown that D depends on the composition of the capping layer, for example, Ga has an affinity for SiO_2 caping layer and hence the intermixing is increased. For the InAsP/InP material combination, no such dependence was found. The values of E_a, D_0 and D at each temperature are similar for both samples within experimental error implying that there is no significant difference between samples A and B. It is therefore concluded that the influence of strain and the different capping layers on the interdiffusion process on InAsP/InP MQWs is insignificant thus validating the application of Fick's Law.

4.5 Summary

The ability to continuously vary the effective band gap, in this case by post-growth annealing, and still retain the excitonic properties of the InAsP/InP QW structures is crucial to the integration of optical devices [19]. In this chapter, two InAsP/InP MQW structures (samples A and B) of differing well widths and compressive strain were subjected to capping and annealing in order to alter the bandgap and hence the emission energy. The resulting well potential was successfully modelled to an error shaped potential during the intermixing process, and the diffusion coefficient for the group V atoms at different temperatures was calculated. The optical results show that intermixing results in blue shifts of the e1-hh1 exciton line to the as-grown samples. The energy shift increases in an approximately linear way with anneal time obeying Fick's Law, for sample A, however, sample B showed some evidence of saturation. The QWs have undergone structural changes which manifest themselves as a change in the FWHM and/or symmetry of the PL peak.

A power variation PL experiment carried out on sample B (section 4.2.9) reveals that the asymmetry is due to intrinsic rather than extrinsic processes. The asymmetric peaks imply that non-uniform intermixing has taken place throughout the MQW structure. It would appear that annealing the sample at low (high) temperatures for longer anneal times reveals an asymmetry on the high (low) energy side of the main PL peak emerges. This may indicate that different QWs have experienced different amounts of intermixing. The activation energies for samples A and B are similar providing proof that the generation of vacancies and hence As/P intermixing is a thermally activated process.

The values of D and D_0 are also similar in both samples implying that the strain has no significant effect on the diffusion of the group V atoms in InAsP/InP QWs. A greater blueshift is always observed for sample B at each anneal time and temperature due to the narrower well width.

Post-growth annealing of InAsP/InP MQW structures has been executed with a view to integrating optical devices in the long wavelength region for telecommunications. Most of the initial OEICs were based on GaAs technology with applications in optical interconnects such as computing networks. This piece of work illustrates that InAsP/InP is a suitable candidate for OEICs as the pseudomorphically strained InAsP/InP structures can be subjected to annealing temperatures of up to 1000°C while still maintaining its excitonic properties.

4.6 References

[1] P. Desjardins, M. Beaudoin, R. Leonelli, G. L'Esperance, R. A. Masut; J. Appl. Phys., vol80, no2, p846 (1996) [A38]

[2] J.P.R. David, M. Hopkinson, P.N. Stavrinou, S.K. Haywood: J. Appl. Phys, vol78, no5, p3330 (1990) [A10]

[3] T.K. Woodward, T. Sizer II, T.H. Chiu,: Appl Phys Letts, vol58, p1366 (1991) [A10,2]

[4] H.Q. Hou, A.N. Cheng, H.H. Wieder, W.S.C. Chang, C.W. Tu: Appl Phys Letts, vol63, p1833 (1993) [A10,20]

[5] T.K. Woodward, T.H. Chiu, T. Sizer II: Appl Phys Letts, vol60, p2846 (1992) [A20]

[6] A.C. Bryce, J.H. Marsh, L.L Taylor, S.J. Bass, D.R P. Guy: Electron Lett vol27, no304 (1991) [A6,7]

[7] H.Q. Hou, C.W. Tu: J Electron Mat, vol21, no2, p137 (1992) [A13]

[8] J.H. Marsh; Semicond. Sci. Technol, vol8, p1136 (1993) [A5]

[9] J.H. Marsh, S.A. Bradshaw, A.C. Bryce, R. Gwilliam, R.W. Glew: J Electron Mat, vol20, no12, p973 (1991) [A6]

[10] S.A. Schwartz, P. Mei, T. Venkatesan, R. Bhat, D.M. Hwang, C.L. Schartz, M. Koza, L. Nazar, B.J. Skromme: Appl Phys Letts, vol53, p1051 (1988) [A7,3]

[11] W.D. Laidig, N. Holonyak Jr, M.D. Camras, K. Hess, J.J. Coleman, P.D. Dapkus, J. Bardeen: Appl Phys Letts, vol38, p3610 (1981) [A8,2]

[12] K. Nakashima, Y. Kawagughi, Y. Kawamura, H. Asahi, Y. Imamura: Jpn J Appl Phys, vol26, no10, pL1620 (1987) [A1]

[13] A. Cao, B.B. Elenkrig, J.G. Simmons, D.A. Thompson, N. Puetz: Appl Phys Letts, vol70, no25, p3419 (1997) [A28]

[14] S. Burkner, M. Maier, E. C. Larkins, W. Rothemund, E. P. O'Reilly, J. D. Ralston: J of Elec. Mat, vol24, no7, p805 (1995) [A67]

[15] L.V. Bradley, W.P. Gillin, K.P. Homewood, R.P. Webb: J. Appl. Phys, vol73, no4, p1686 (1993) [A30]

[16] D. J. Tweet, H. Matsuhata, R. Shioda, H. Oyanagi, H. Kamei; Jpn. J. Appl. Phys. 35, 4a, p2025 (1996) [A17]

[17] A. McKee, C.J. McLean, G. Lullo, A.C. Bryce, R.M. De La Rue, J.H. Marsh. C.C. Button: IEEE J Quant Electron, vol33, no1, p45 (1997) [A7]

[18] L.L. Chang, L.L. Koma: Appl Phys Letts, vol29, p138 (1976) [A16,1]

[19] J.D. Ralston, S. O'Brien, G.W. Wicks, L.F. Eastman: Appl Phys Letts, vol52, no18, p1511 (1988) [A19]

[20] T. Fuji, M. Sugawara, S. Yamazaki, K. Nakajima: J Cryst Gr, vol105 p348 (1990) [A18]

[21] J. C. Phillips; Bonds and Bands in Semiconductor, Academic Press (1973)

[22] C.H. Joyner, L.M. Ostar, A.G. Dentai: J Cryst Gr, vol121 p413 (1992) [A9]

[23] K. Mukai, M. Sugawara, S. Yamazaki: Phys Rev B, vol50, no4, p2273 (1994) [A16]

[24] R.E. Mallard, E. J. Thrush, R. W. Martin, S. L. Wong, R. J. Nicholas, R. E. Pritchard, B. Hamilton, N. J. Long, S. A. Galloway, A. Chew, D. E. Sykes, J. Thompson, K. Scarrott, J. M. Jowett, K. Satzke, A. G. Norman, G. R. Booker: Semicond. Sci. Technol. 8, p1156 (1993) [A12]

[25] T.E. Schlesinger, T. Kuech: Appl Phys Letts, vol49, no9, p519 (1986) [A26]

[26] C. Francis, F.H. Julien, J-Y. Emery, R. Simes, L. Goldstein: J. Appl. Phys, vol75, p3607 (1994) [A14,9]

[27] S. Komiya, T. Tanahashi, I. Umebu: Jpn J Appl Phys, vol24, no8, p1053 (1985) [A4]

[28] C. Francis, P. Boucard, F.H. Julien, J-Y. Emery, L. Goldstein: J. Appl. Phys, vol73, no3, p1944 (1995) [A14]

[29] J. Oshinowo, A. Forchel, D. Grutsmacher, M. Stollen, M. Heuken, K. Heime: Appl Phys Letts, vol60, no21 p2660 (1992) [A11]

[30] C. Francis, F.H. Julien, J-Y. Emery, R. Simes, L. Goldstein: J. Appl. Phys, vol75, no7, p3607 (1994) [A8]

[31] F. H. Baumann, J.-H. Huang, J. A. Rentschler, T. Y. Chang, A. Ourmazd: Phys. Rev. Lett. Vol73, p448 (1994) [A27,8]

[32] W. P. Gillin, D. J. Dunstan: Phys. Rev. B. vol 50, no11, p7495 (1994) [A66]

[33] D. J. Tweet, H. Matshuhata, P. Fons, H. Oyanagi, H. Kamei: Appl Phys Letts, vol70, no25, p3410 (1997) [A27]

[34] J. M. Sallese, S. Taylor, H. J. Buhlmann, J. F. Carlin, A. Rudra, R. Houdre, M. Ilegems: Appl Phys Letts, vol65, no3, p341 (1994) [A3]

[35] M. Ghisoni, P.J. Stevens, G. Parry, J.S. Roberts: Opt and Quant Electron, vol23, pS915, (1991) [A25]

[36] H. Shimizu, K. Kumada, N. Yamanaka, N. Iwai, T. Mukaihara, A. Kasukawa: Electron. Letts, vol34, no9, (1998) [A80]

[37] N. Iwai, T. Mukaihara, H. Shimizu, N. Yamanaka, K. Kumada, A. Kasukawa: Electron. Letts, vol34, no9, (1998) [A83]

[38] T. Mukaihara, N. Yamanaka, N. Iwai, T. Ishikawa, A. Kasukawa: Electron. Letts, vol34, no9, (1998) [A81]

[39] J. Crank, The Mathematics of Diffusion, Oxford at the Clarendon Press, 1979.

[40] H. Kato, M. Yokazawa, R. Kohara, Y. Okaabayashi, S. Takayanagi; Solid State Electron 12 p137 (1969)

[41] S. Adachi: : J. Appl. Phys, vol53, no12, p8775 (1982) [M20]

[42] Landolt-Bornstein, edited by Madelung, New Series, Group 3, vol17a, (Springer, Berlin 1982) p281; vol22a, (Springer, Berlin 1989) p107

[43] J. M. Sallese, J. F. Carlin, M. Gailhanou, M. Ilegems: Appl Phys Letts, vol71, no16, p2331 (1997) [A36]

[44] M. Ghisoni: (thesis), Post-growth bandgap engineering for optoelectronic integration (1992)

[45] S.A. Schwarz, P. Mei, T. Venkatesan, R. Bhat, D. M Hwang, C. L. Schwartz, M. Koza, L. Nazar, B. J. Skromme; Appl.Phys.Lett. 53, p1051 (1988) [A126]

[46] K. Akimoto, M. Kamada, M. Taira, M. Arai, N. Watanabe; J. Appl. Phys. 59 p2833 (1986)

[47] A. K. Chin, I. Caamlibel, T. T. Sheng, W. A. Bonner; Appl. Phys. Lett., vol56, no5, p495 (1983) [A128]

[48] B. V. Dutt, A. K. Chin, I, Camlibel, W. A. Banner; J. Appl. Phys. 56 p1630 (1984)

[49] B. Tuck; Introduction to diffusion in semiconductors, Peter Peregrinus Ltd. (1974)

[50] W. P Gillin, S. S. Rao, I. V, Bradley, K. P. Homewood, A. D. Smith, A. T. R. Briggs: Appl. Phys. Lett., vol63, no6, p797 (1999) [A63]

[51] A. Hamoudi, A. Ougazzaden, P. Krauz, K. Rao, M. Juhel, H. Thibierge: Jpn J Appl Phys, vol34, no1, p36 (1995) [A33]

[52] O. M. Khreis, W. P. Gillin, K. P. Homewood: Phys. Rev. B, vol55, no23, p15 813 (1997) [A82]

5. Chapter 5 - InAs/InP Quantum Dots

5.1 Introduction

Semiconductor quantum dots (QDs) represent the ultimate in low-dimensional engineering and, in principle, should exhibit superior electronic and optical properties compared with QWs due to 3D carrier confinement [1, 2, 3, 4]. In practice, QDs have proved impossible to fabricate successfully by photolithographic methods but recently self organised nanometer sized islands, which approximate to QDs, have been grown by depositing a thin layer of highly strained semiconductor on (001) substrates. Confining the electronic states in 3D results in a delta-function like density of states (DOS) as shown in Figure 5-1. The DOS diagram for QWs is also illustrated. Reducing the dimensions of the smaller band gap semiconductor impedes the motion of the carriers and favours the formation of excitons with increased binding energies and oscillator strength. Hence QDs should have higher photon emission efficiencies compared with QWs [5]. When QDs are used in a device, such as a laser, the reduced dimensionality is expected to result in low threshold current densities J_{th} which are temperature independent, and an increase in the differential gain. For bulk and QW lasers a critical threshold current must be delivered to achieve transparency and ultimately, lasing. Perhaps the most important advantage of moving to QD lasers, particularly at longer wavelengths, is the expected temperature independence of the threshold current. In QW lasers, thermally excited carriers spread into adjacent states at higher energies. In QD lasers the electronic states are discrete and well separated so that thermal spreading does not

occur. The threshold current is also strongly affected by Auger recombination, a major problem in long wavelength QW lasers, but which should be largely suppressed in QDs [6].

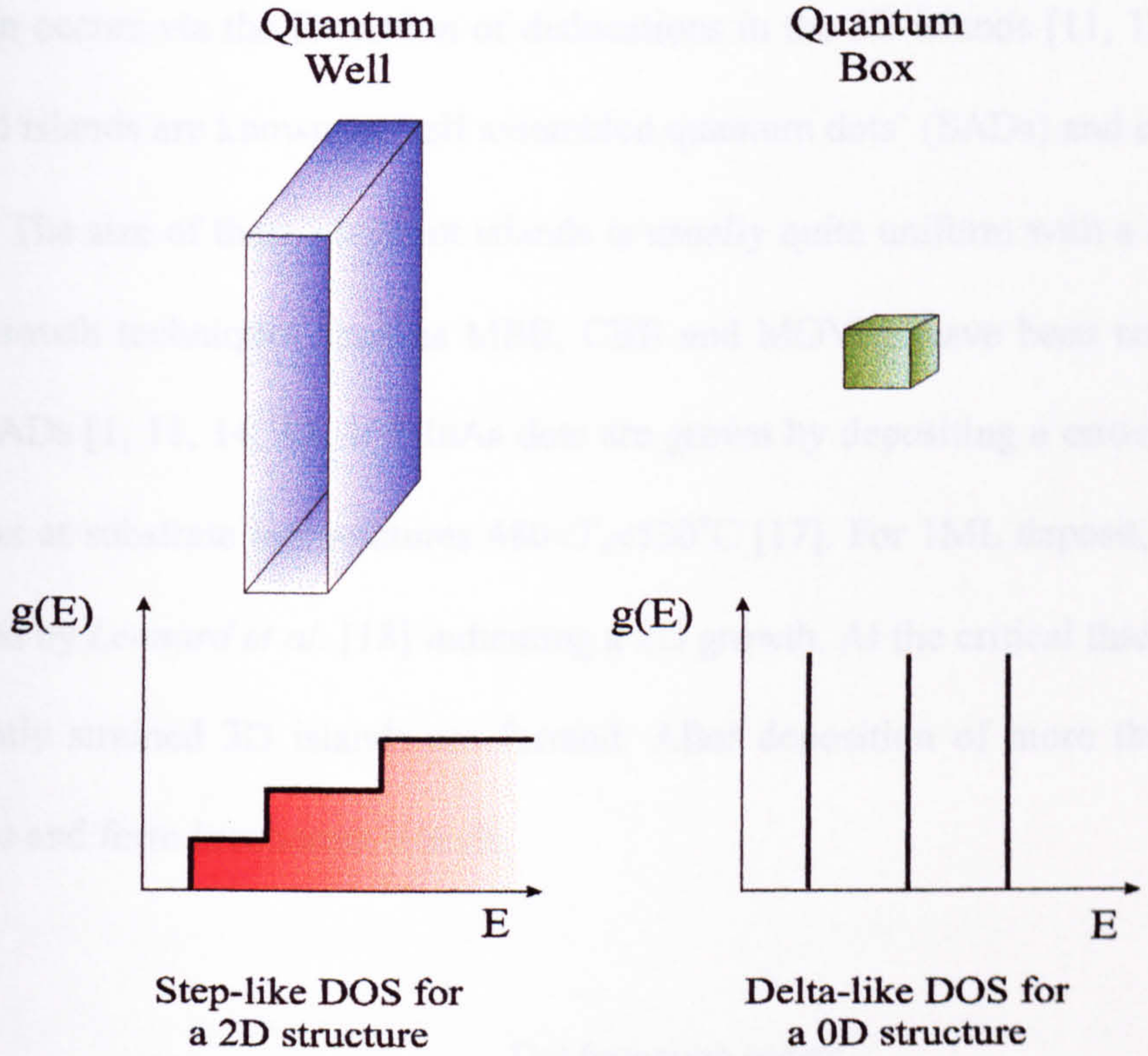

Figure 5-1 *Illustration of QW (2D) and QD (0D) crystal geometries with corresponding DOS function plotted against energy*

5.1.1 Growth of self-assembled QDs

The growth of these dots is thought to be governed by the Stranski-Krastanow (S-K) growth mode [7]. In this growth mode, the initial strained 2D-growth is followed by 3D growth when a critical strain is reached [8, 9, 10] and 3D islands are formed on top of a wetting layer as illustrated in Figure 5-2. The WL is effectively a thin QW in which excitons

can recombine producing a separate peak in the PL spectrum obtained under high excitation. The island formation process is thought to be driven by the reduction of the total surface strain energy of the layer-substrate system. If the coverage is further increased, the relaxation of strain occurs via the formation of dislocations in the 3D islands [11, 12]. The coherently strained islands are known as 'self assembled quantum dots' (SADs) and confine the carriers in 3D. The size of these coherent islands is usually quite uniform with a deviation of ~10% [13]. Growth techniques such as MBE, CBE and MOVPE have been successfully used to grow SADs [1, 11, 14, 15, 16]. InAs dots are grown by depositing a critical amount of InAs on GaAs at substrate temperatures $480<T_s<530^{o}C$ [17]. For 1ML deposit, flat terraces were observed by *Leonard et al.* [18] indicating a 2D growth. At the critical thickness (1.5-1.7ML) coherently strained 3D islands are formed. After deposition of more that 2MLs, the dots coalesce and form incoherent islands.

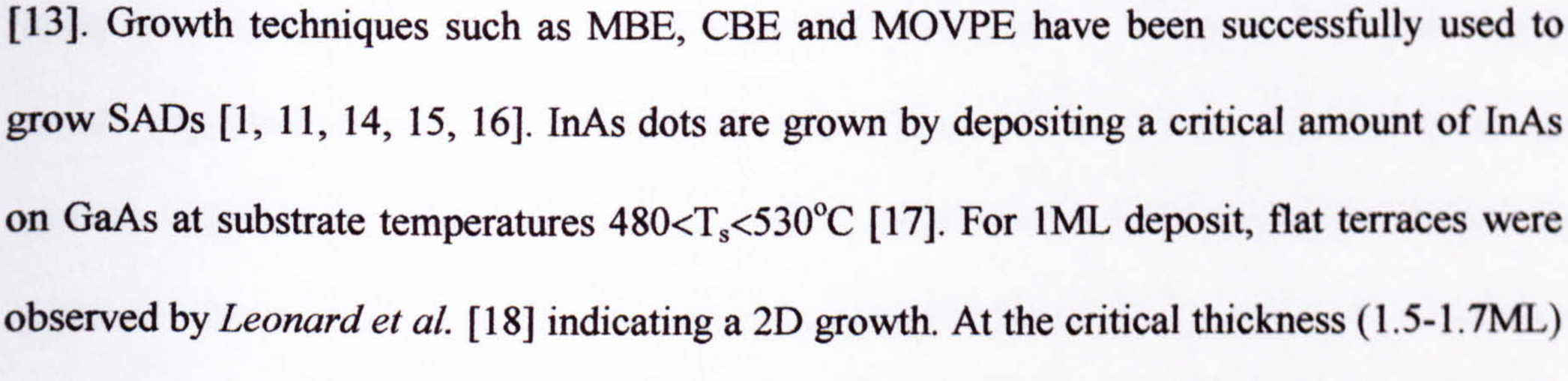

Figure 5-2 *Schematic diagram of QD formation. a) InAs layer is below critical thickness, t_c for dot formation so the layer remains 2D b) dots form when the critical thickness of InAs has been deposited and are connected by the WL c) capping layer covers dots*

Adatom diffusion is proportional to the surface temperature and depends on the strain field that develops as the islands are formed [6, 18] limiting the size of the islands and hence reducing the variation in size distribution. *Barabasi et al.* [19] has proposed a model based on Monte Carlo simulation indicating the existence of a strain assisted kinetic mechanism for island formation. The islands grow, reach a critical size and a strain field develops surrounding the island which at the critical island size generates a net current of adatoms away from the islands. This process stabilises the island size as the strain field also 'repels' newly deposited atoms. The combined kinetic effects of the adatom density, strain, and growth temperatures reduce the growth rate of large islands (energetically unstable) and promotes the nucleation of new islands (energetically favourable), leading to a narrower island size distribution. Continuing the deposition leads to island coalescence, which results in a drop of the island density.

Self organised InAs islands on a GaAs substrate is the most extensively studied system [1, 14, 15, 16, 20, 21] with emission wavelengths in the 1μm region at 10K. However, the study of growth of highly strained semiconductors on InP substrates allows the emission wavelength to be shifted to the technologically important 1.3-1.55μm range. This can be achieved by using InAs as the low bandgap material, which results in a high lattice mismatch of 3.2% when grown on InP [22, 24]. For InAs dots grown on InP, *Taskinen et al.* [7] have demonstrated S-K growth at a temperature of 500°C using source materials trimethylindium (TMIn), trimethylgallium (TMGa) and tertiarybutylarsine (TBAs) by atmospheric pressure MOVPE. 3D islands 10nm in height and 90nm in diameter are formed for InAs deposition thickness between 1.5-3MLs. These authors also studied the effects of growth temperature on areal density, size and uniformity of the islands. For 2ML of InAs deposited at a temperature

of 450°C, no 3D nucleation was observed. Small coherent islands were observed at 500°C, but at 600°C the average island size increased dramatically to 200nm in height and 500nm in diameter. Taking into account the density of these large islands the volume of material contained within the dots surpassed the volume of InAs deposited. *Taskinen et al.* [7] concluded that the growth mode was no longer S-K and As/P exchange was taking place resulting in atoms from the WL and underlying InP layer being incorporated into the InAs island. This suggests that in the case of InAs/InP dot formation the mechanism is not purely S-K strain growth but is also driven by kinetic factors such as adatom diffusion [23] and the dots are an $In_xAs_{1-x}P$ alloy. *Taskinen et al.* [7] also studied the effect of different thicknesses of InAs layers on the density and uniformity of the islands grown at T_s=500°C. The island density increased from $6x10^9cm^{-2}$ to $1.7x10^{10}cm^{-2}$ when the InAs deposition was increased from 1.5 to 4 MLs. In the case of 6ML deposition of InAs, the island density decreased to $1.3x10^{10}cm^{-2}$ due to island coalesence. *Ponchet et al.* [24, 25] have identified two different modes of island size and spatial distribution. For a deposit of 1.5 to 2ML, the average height is 7nm and the islands are randomly distributed. Above 2.5ML, the island height is only 3-4nm and the island volume is decreased by a factor 5, with a typical inter-dot distance of 40nm independent of the island density. The deposit formed elongated islands in the [110] direction implying a significant level of island-island interaction. It is suggested that the strong dependence of the island size on the total amount of deposited InAs is mainly due to long range interactions through the substrate. Both *Ponchet et al.* [25] and *Marchand et al.* [23] have grown dots with a growth interruption of 30s after the InAs deposition. If the InAs film grown on InP is left under a AsH_3 ambient, it will spontaneously reorganise by surface migration resulting in coherent InAs islands. *Yoon et al.* [28] demonstrated using AFM, for

the formation of InAs/InP QDs, that the increase in growth temperature from 550 to 600°C decreased the dot density and increased the dot size. This behaviour can be understood by enhancement of the adatoms surface diffusion at a higher temperature

From the above attempts at growing QDs, it can be seen that the surface morphology of the QDs varies extensively with growth temperature, amount of material deposited and V/III ratio. Characterisation of these dots by optical and structural techniques is crucial in the understanding and refinement of the growth mechanisms.

5.1.2 Optical Properties of QDs

The PL emission from a single dot is very narrow [14]. *Marzin et al.* [12] have measured a linewidth of 0.1meV for InAs dots grown on GaAs. However, the linewidth from an ensemble of dots is always broad (40-70meV [1, 13]) with a Gaussian shape since the peak is a convolution of the emission from approximately 10^6 QDs within the excitation area. Size uniformity and alloy content of the InAs dots correlate with inhomogeneous broadening of the PL emission peak. Achieving narrower luminescence lines for a large ensemble of QDs is a major goal for future device applications [28]. However, the delta-like DOS can, in principle, inhibit fast carrier relaxation resulting in the 'phonon bottleneck'. The phonon bottleneck effect was proposed by *Benisty et al.* [29] to explain the low emission intensities measured for photolithographically defined QDs. In an ideal QD, carriers can only relax via the discrete excited levels towards the ground state (GS). When the electronic intersublevel spacing is comparable to the energy of a longitudinal-optic (LO) phonon the relaxation rate should be fast ($\sim 10^{12} s^{-1}$). If the interband levels do not equal this critical LO

phonon energy (or multiples of it) due to the fluctuation in dot size and composition, relaxation occurs by a multiphonon process which is much slower and results in a build up of carriers at each level (phonon bottleneck). Acoustic phonon scattering provides an alternative relaxation process but this occurs at a much slower rate (~$10^8 s^{-1}$) again contributing to the phonon bottleneck [30]. Fast relaxation is critical for high speed devices [31]. If the phonon bottleneck is operative, higher energy peaks corresponding to recombination involving the excited states should be observed at all excitation densities. However, at low excitation densities, higher energy peaks are not observed [15, 32] indicating another relaxation mechanism is in operation.

In order to distinguish emission from a 0D system from that of a 2D system, two methods have been shown to be useful; level filling and lifetime measurements. If the excitation power density focused on the dots is increased new peaks appear at higher energies which arise from recombination of excitons associated with higher lying states in the dot. The small density of dots and the fact that each dot only accommodates two electrons in its ground state results in the higher lying levels being filled depending on the degeneracy of each state. The low recombination rate of carriers from the ground state (~1ns) together with the phonon bottleneck also increases the likelihood of recombination from the excited state. *Castillo et al.* [33] have shown that the excitation power density required to obtain significant level filling was relatively low, 40Wcm^{-2}. In order to observe comparable filling in QWs under the same experimental conditions, an excitation power density of 8kWcm^{-2} was required. Deconvolving the PL feature obtained under conditions of high excitation allows the separation of the ground and excited states to be estimated. *Fafard et al.* [22] measured a peak (state) separation of 60meV in InAs dots grown on an InP susbtrate

which is comparable with the energy level separation of 50-70meV in InAs/GaAs dots [14]. The second optical fingerprint of a QD is a temperature independent exciton radiative lifetime [33, 34]. Unfortunately, lifetime measurements using time-resolved PL (TRPL) could not be performed on these samples due to the lack of a fast detector operating at 1.55μm.

Due to the complexity of the dot formation mechanism associated with the chemical reactions of the surface, only a few reports on InAs/InP QDs have been published [7, 27, 36]. P atoms on the InP surface are easily exchanged by As atoms, when the InP surface is exposed to InAs (As/P exchange reaction), deteriorating the interface quality of the heterostructures. In the case of the InAs/InP QD, the local variation in the strain field around the dots may result in an even more complex As/P exchange reaction, significantly altering the kinetic processes of the QD formation.

In this chapter, different thicknesses of InAs layer have been deposited on standard or misorientated InP substrates to form $InAs_xP_{1-x}$ QDs. Scanning transmission-electron microscopy (section 5.2) and photoluminescence (section 5.3) techniques are used to investigate the properties of the QDs and wetting layer. The dots are then coated with SiO_2 and subjected to post growth annealing which has been found to blue shift and narrow the FWHM of the emission from the QD ensemble (section 5.5). Although blue shifts have been measured the detailed mechanisms are not precisely known but it is expected that interdiffusion processes play a major role [28].

5.1.3 Samples

The samples were grown in a horizontal MOCVD reactor at the EPSRC III-V growth facility at Sheffield University and represented the first attempt at growing InAs dots on InP in this reactor. The intention was to deposit different amounts of InAs at a low growth rate of 0.14μm/hr (approximately 0.4Å/s), onto a 50Å InP layer (same growth rate) and cap the InAs layer with 30Å of InP again grown at the slow growth rate in order to prevent diffusion of As into the P layer. The final layer was 500Å of InP grown at the standard rate of 1.24μm/hr (approximately 3.4Å/s). Two different types of wafer were used; one was the 'standard' 0.2° off (100) towards (110) substrate and the other was a 'misorientated' 2° off (100) towards (110) substrate. During growth the wafers were placed side by side in the reactor, with the 'major flat' facing in the upstream direction of the gas flow. Trimethylindium was used as the group III source and AsH_3 and PH_3 as the group V sources. The growth temperature was maintained at 600°C throughout and nominally 1.5 (4Å), 2 (6Å), 3 (9Å) and 4MLs (12Å) of InAs were deposited on InP. As these were the first dots to be grown by MOCVD in Sheffield, different substrate orientations and thicknesses of InAs layers were investigated to determine optimum growth conditions for 1.55μm RT emission.

5.2 Scanning Transmission-Electron Microscopy (STEM)

Cross-sectional Scanning Transmission-Electron Microscopy (STEM) and Energy Dispersive X-ray (EDX) have been employed to give structural information on capped dots. The experiment was carried out using the facility at Liverpool University. The 3ML InAs (0.2° substrate) dot sample is thinned to less than 2000Å using ion beam milling. An electron beam of energy ~100keV is scanned across the sample, which is sufficiently thin that spreading of the electron beam can be neglected, yielding a contrast image as shown in Figure 5-3(a). The micrograph image is not sharp enough to be able to estimate accurately the dot dimensions and the images are in any case likely to be dominated by strain and atomic number (Z) contrast. However, some darker regions of the image indicate the sites of the dots. In addition the STEM image cannot supply chemical information and so EDX analysis has been used which is compositionally sensitive, enabling the height of the capped QDs to be estimated.

Figure 5-(b) shows an EDX linescan excited by a 10Å wide, 100keV beam with 10Å steps taken along the growth direction. The position of the linescan is indicated by the black arrow. Other dots are indicated by white arrows. The FWHM of the As peak is taken to be an estimate of the height of the QD and yields a value of ~84Å. Another linescan with the electron beam traversing between the dots through the WL region also gives a value close to 84Å. Since the WL width and the height of the dot are the same, this implies that the dots do not sit on a thin InAs WL but lie within a 2D confining layer (CL) which has a thickness equal to the dot height. A similar conclusion was reached by *Siverns et al.* [36] for InAs dots grown on GaAs and has been confirmed by TEM [38] and cross-sectional STM studies [39].

Monitoring the P signal gives the inverse behaviour; the P signal drops in the region of the dot but does not reduce to the background level indicating that the composition of the QDs is InAsP and not InAs. This is consistent with the ideas of As/P exchange which can occur during the initial WL stage and the capping stage when the CL is formed. The width of the confining layer and the height of the dot are used in the transfer matrix model to estimate the composition of the dot and WL in section 5.3. Many studies of QD systems have utilised AFM images to ascertain the dot size and density. Uncapped versions of the samples studied here were grown but the images showed extremely large objects approximately 100nm high and 200nm across. Such "islands" are too large to give confinement effects and are inconsistent with the STEM images. It is thought that the large islands result from continued growth during the cool down stage (~ several minutes) as has been reported by *Wang et al.* [36]. The MOVPE system is not equipped to perform a rapid quench from the growth temperature and further AFM studies were abandoned (section 5.4).

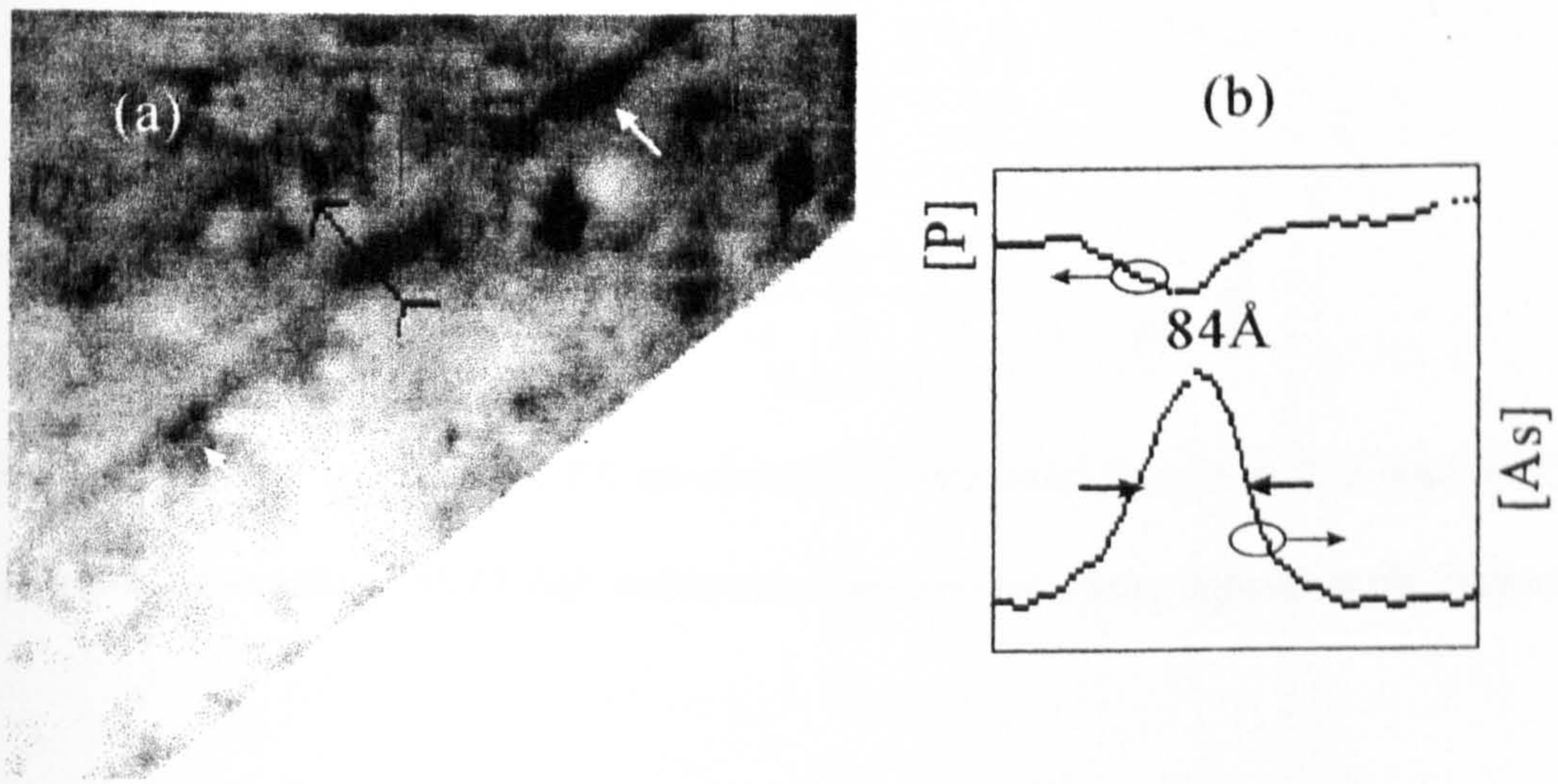

Figure 5-3 *(a) STEM image of the 3ML InAs/InP QD sample. (b) EDX linescan taken along the growth direction, which indicates that the dot height is approximately 84Å. QDs are indicated by the arrows.*

5.3 PL Results

5.3.1 Standard (0.2°) substrates

Figure 5-4 shows the low temperature spectra of the samples grown on the standard (0.2°) substrate for depositions of 1.5, 2, 3 and 4ML of InAs. Three peaks, labelled I, II and III can be clearly distinguished in each spectrum together with a weak signal at 1.42eV which is attributed to bandgap emission of the InP substrate.

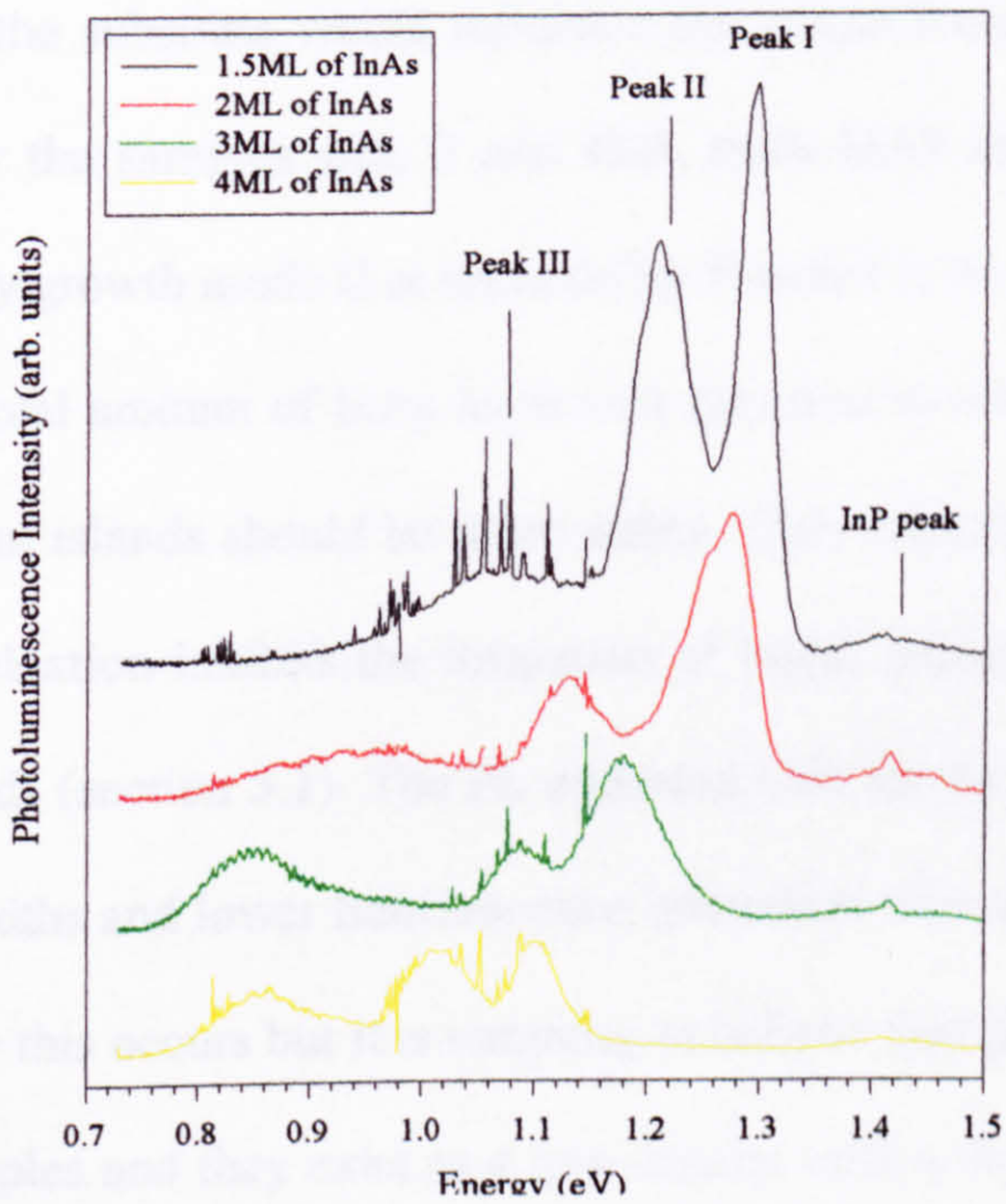

Figure 5-4. *Low temperature PL spectra (10K) obtained from 1.5, 2, 3 and 4ML of InAs deposited on standard (0.2°) InP substrate. The structure was capped with 530nm of InP.*

As the deposited InAs layer increases from 1.5-4ML, peaks I and II shift to lower energies, whilst peak III initially shifts and then remains constant around 0.85eV. By analogy

with other QD systems the lowest energy peak is attributed to emission from QDs and these results might indicate that the dot emission cannot be extended to longer wavelengths, at least for the growth conditions used here. The 4ML dot peak is similar in shape and intensity to the 3ML sample. However, the detector response is significantly reduced below 0.8eV which distorts the shape of the emission peak. Similar results were reported by *Taskinen et al.* [7] who observed a Gaussian-shaped feature for the deposition of 2MLs of InAs on InP at 500°C. The islands are probably composed of an alloy of $InAs_xP_{1-x}$ as an exchange of As from the WL and P from the substrate would influence the island formation by producing 'excess' material [27]. For the samples with 3 and 4ML thick InAs layers shown here, it would appear that they obey growth mode II as reported by *Ponchet et al.* [25]. These authors found that increasing the total amount of InAs leads to a decrease in island size despite the fact that the largest coherent islands should be more stable. They concluded that the kinetic process which governs nucleation inhibits the formation of larger islands and promotes the nucleation of smaller islands (section 5.1). The PL emission (III) for the 1.5 and 2ML InAs layers exhibit larger linewidths and lower luminescence intensities than the 3 and 4ML InAs samples. It is not clear why this occurs but it is tempting to believe that the dots are not fully formed for the former samples and they exist in a low density with a large size distribution [25]. With increasing InAs deposition the QDs achieve a more uniform size resulting in a narrower linewidth. *Tabata et al.* [40] also concluded that there is a transition from homogeneous flat layers to 3D islands after deposition of 2-3MLs of InAs when the substrate temperature >525°C. The PL results suggest that 3-4 MLs of InAs is the optimum deposit for the formation of dots under the growth conditions used in this work. Consequently the majority of the optical characterisation has focused on the 3ML sample. It is important to

remember that growth of InAs/InP QDs has not been so extensively studied as for the InAs/GaAs system. There is a variation in results from different groups perhaps indicating that the 'chemistry' of the formation of InAs/InP dots is more complicated and depends more heavily on growth conditions.

It is tempting to ascribe peaks I and II shown in Figure 5-4 to emission from the WL/CL but there are several possibilities for their origin:

(i) they arise from a WL/CL which has ML thickness fluctuations

(ii) one of the peaks involves impurities in the substrate

(iii) there are *two* WL/CL layers

(iv) both peaks involve QDs of different size/composition

Taskinen et al. [6] detected two WL peaks after deposition of 2MLs of InAs at 600°C. *Ponchet et al.* [23] found two peaks around 1.1eV similar to the results presented here but only for a sample where 1.5 ML of InAs was deposited. Increasing the amount of material to 2ML resulted in a single WL peak. Emission peaks I and II shown in Figure 5-4 have a FWHM of ~50-70meV which is considerably greater than the PL linewidth (~15meV) of the $InAs_xP_{1-x}$ QWs described in chapter 4. This makes it unlikely that the two peaks can be due to ML fluctuations as reported by some groups [7, 41]. Also, the peaks shift with different InAs depositions. However, the EDX measurements indicated that the WL/CL consists of an $InAs_xP_{1-x}$ alloy and it is possible that the composition of the WL/CL changes with increasing InAs deposition. This might allow for the possibility of ML fluctuations from different alloy compositions but the separation of the peaks remains constant making it seem unlikely that this is the origin of these emission features. A definitive experiment to determine whether there are ML fluctuations is to perform a PLE experiment. The results are shown in Figure 5-

5. This region of the spectrum is only partially covered by the range of the Ti/Sapphire laser (860-970nm) but it is clear that the same features are not evident in the spectra detecting at 1000nm (peak I) and 1350nm (peak II). In particular the feature around 1.33eV in the PLE spectrum detecting at 1000nm (peak I) is not present when detecting at 1350nm or at 1550nm. This shows that the peaks at 1.09 and 1.2 eV cannot be due to ML fluctuations of a single WL.

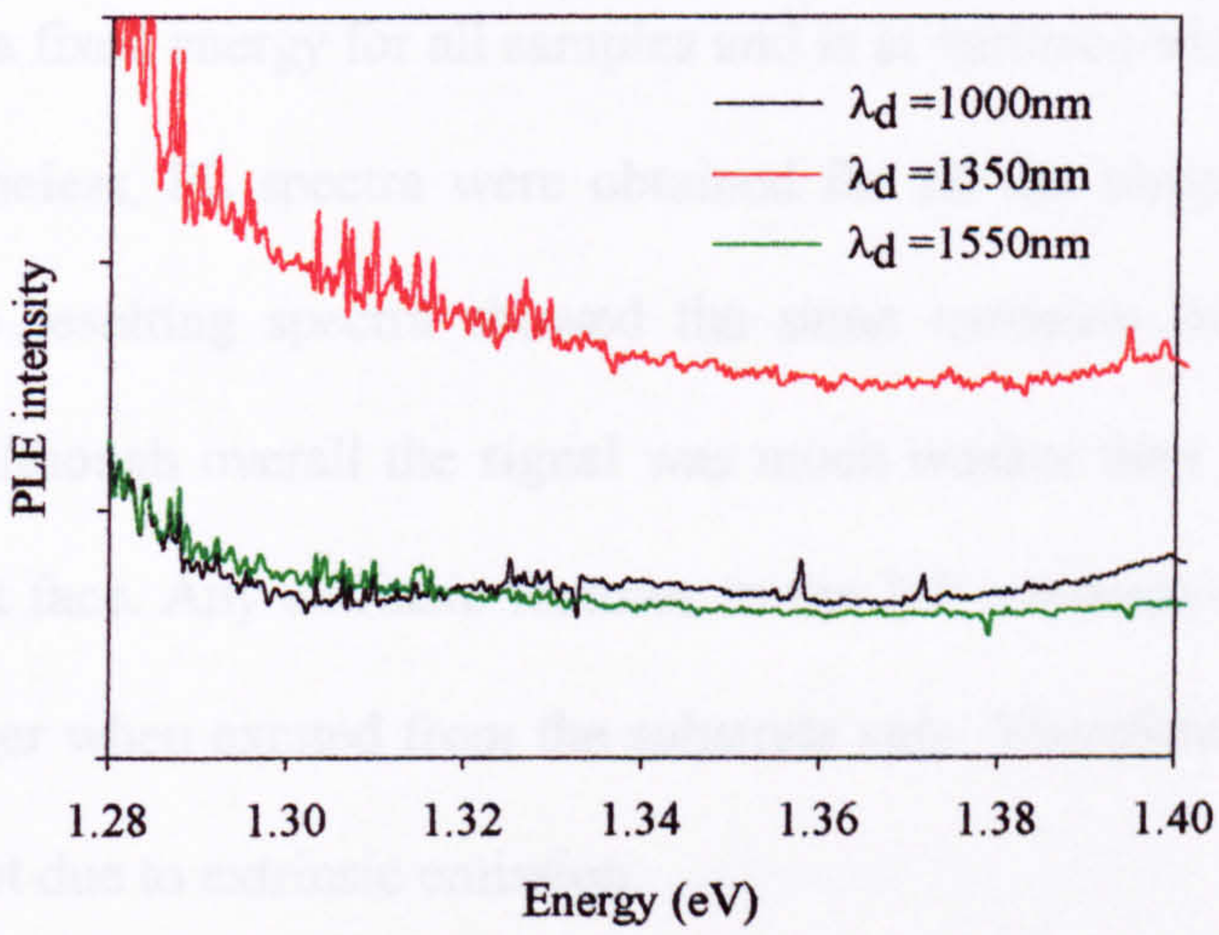

Figure 5-5 *PLE spectra detected at λ_d = 1000nm (peak I), 1350nm (peak II) and 1550nm (peak III).*

The transfer matrix model is employed to calculate the e2-hh2 transition for an InAsP QW of 70Å (STEM results) and 30% As (Figure 5-6). A value of 1.34eV is obtained which, within experimental error appears to indicate that the feature located at 1.33eV can be assigned to the e2-hh2 transition in a QW. Recently, PLE experiments performed on InAs/GaAs dots have given conflicting results. However, when PLE is carried out on QDs, the position of the higher lying peaks is dependent on the detection wavelength (λ_d) due to different sized dots being probed. If the detection wavelength is changed within the PL envelope, the dot peak

shifts. This is contrary to the PLE results obtained for a QW as the higher lying peaks remain stationary regardless of the position of the detection wavelength. Further PLE experiments would need to be carried out on the InAs/InP dots to clarify the PL emission.

Tabata et al. [40] found a defect band at 1.08eV, which they ascribed to a deep level complex involving a P vacancy in n-type InP substrates. This band falls in the same region of the spectrum as peaks I and II but is broader (~ 150 meV). Such a defect emission would in any case remain at a fixed energy for all samples and is at variance with the results shown in Figure 5-4. Nevertheless, PL spectra were obtained for all the samples exciting from the substrate side. The resulting spectra showed the same emission features with the same relative strengths, although overall the signal was much weaker than when the sample was excited on the front face. Any extrinsic features in the InP substrate would be expected to appear much stronger when excited from the substrate side. Therefore we conclude that the peaks I and II are not due to extrinsic emission.

A third possibility is that the two peaks have their origins in two independent WLs. *Zhukov et al.* [42] performed PLE on InGaAs/GaAs, in the range of energies higher than the QD emission band and obtained a distinct doublet shape of the line (WL 1 and WL 2) which was attributed to a coexistance of the 2D InGaAs layer regions with slightly different thickness. *Tabata et al.* [40] observed a red shift in the PL emission spectra when an InP substrate was annealed under As at temperatures of 550, 570, 575 and 600°C. They attributed this shift to As/P exchange at the surface which is known to lead to diffusion of As to a depth of about 5ML [40] and the generation of a thin 2D InAsP layer. An increase in thickness of the InAsP layer as the As penetrates more deeply into the substrate with increasing anneal temperature might explain the shifts observed in the samples studied here. This may account

for the origin of peak II and a limit of 15Å could be placed on the thickness of this WL. The origin of the peak I is attributed to the formation of an InAsP layer during the capping process by analogy with the InAs/GaAs system. It is well known in the InAs/GaAs system that there is dissolution of the islands and formation of a 2D confining layer during the capping process [37, 38]. It is assumed that a similar process operates here and an InAsP 2D layer (confining layer) is formed around the QDs. It is proposed that an increase in the InAs thickness provides more As in this confining layer and induces a red shift in the PL peak.

To obtain an estimate of the As composition for the WL and CL emission, the transfer matrix model has been employed. Figures 5-6 predicts the emission energies of $InAs_xP_{1-x}$ QWs with thicknesses in the range 4 to 70Å (from STEM) and x varying from 0 to 1. Strain has not been taken into account which introduces an error of ~4%. From these predictions, the WL has a composition of ~80% arsenic and the CL consists of 30% arsenic. An estimate of the dot composition can also be obtained by approximating it to a QW. This is justified on the grounds that the aspect ratio diameter: height is usually ~3 and confinement in the lateral direction is weak. If the height of the dot is ~70Å, then the corresponding As composition in the QD according to Figure 5-6 is ~63%.

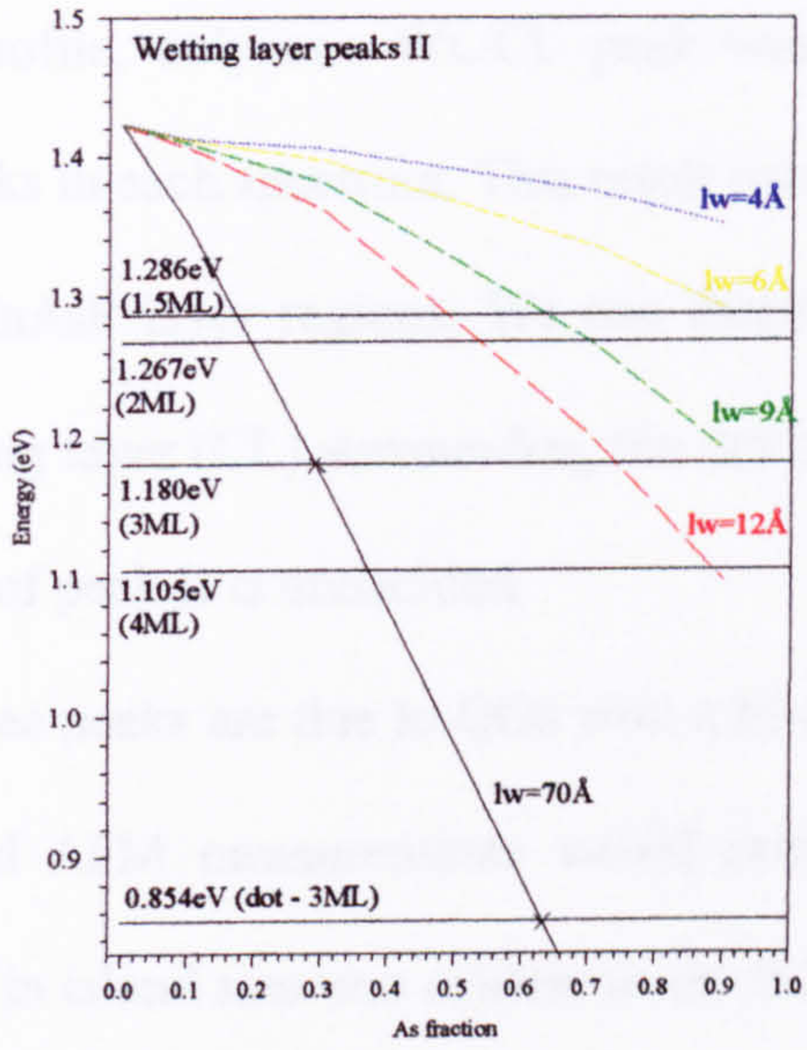

Figure 5-6 *The coloured curves indicate predicted transition energies modelled for a 4 to 70Å thick QW of $InAs_xP_{1-x}$ with x varying from 0 to 1, confined between InP barriers.*

For WL and CL, an InAsP well surrounded by InP with a band offset of 75:25 [43] has been assumed. However, a cross section through the WL/CL (Figure 5-7 a)) reveals that only one side of each 2D confining layer may be surrounded by InP. Taking this 'new' profile into account, the CB potential is illustrated in Figure 5-7 b).

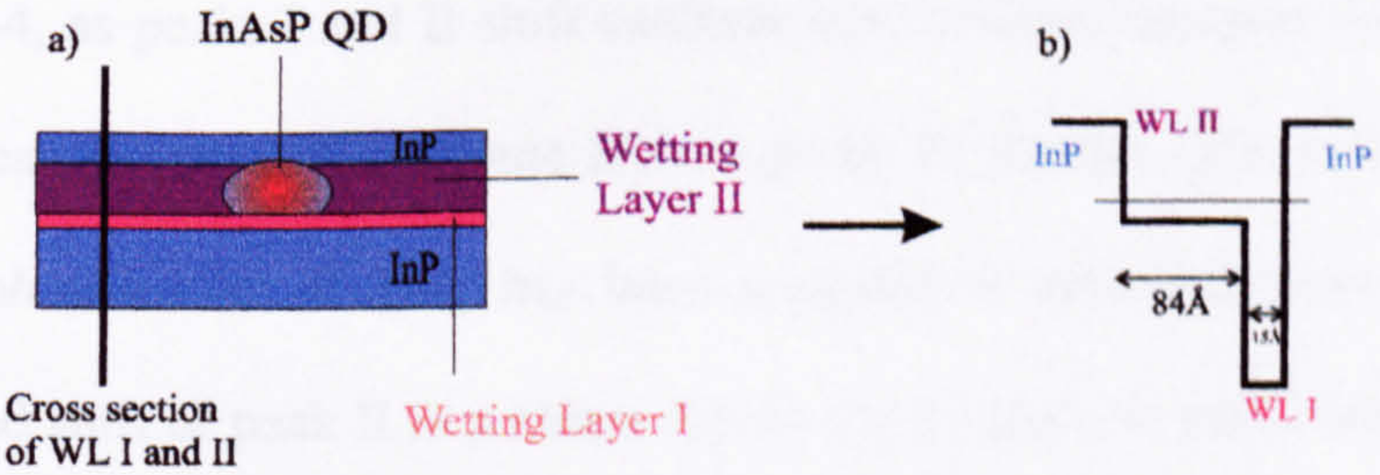

Figure 5-7 *a) Cross section of WL I and II surrounded by InP. b) CB potential profile for WL I and II.*

For the graded well profile, only one WL/CL peak would be observed which is contrary to the two WL/CL peaks in each spectrum. This result invalidates the possibility that there is a coexistance of 2D InAsP layer regions. We can therefore speculate that peak I originates from the 2D confining layer (CL) surrounding the dot after the InP capping layer has been deposited. The origin of peak II is undecided.

It is possible that all three peaks are due to QDs with a tri-modal size distribution. In principle this could occur and AFM measurements would provide a definitive answer. However, no obvious variation in island size was evident in the STEM images. *Johansson et al.* [44] observed a bi-modal distribution of InP islands on GaP at 580°C for 3.5 MLs of InP deposit. They conclude that the small islands could be the pre-stages on the way to fully developed islands. A bi-modal distribution has been reported by *Carlsson et al.* [10] for InP islands grown on $Ga_{0.5}In_{0.5}P$ barriers. These authors found a 2D to 3D growth mode transition on depositing 1.5-1.8MLs of InP on GaInP. For thicknesses greater than 1.8ML, a PL peak emerged at lower energies which was attributed to the evolution of larger islands. AFM experiments confirmed that the lower (higher) energy PL peaks originated from large (small) islands. However, the PL peak attributed to the small dots remained fixed but increased in width as more material was deposited. Even though this is inconsistent with the spectra shown in Figure 5-4, as peaks I and II shift continuously to lower energies with increasing InAs deposition, peak II may still originate from a group of smaller QDs and therefore, in agreement with *Johansson et al.* [44] has been assigned to emission from a small dot distribution. The red shift of peak II is perhaps due to the increase in small dot size and the changing composition of the confining layer [45]. No peak is observed between peaks II and

III implying that no intermediate island sizes are present which is similar to the results obtained by *Johansson et al.* [44].

As already seen, by increasing the amount of material deposited, the QD red shifts which is attributed to the change in QD size. *Zuhuhov et al.* [42] have shown that the energy of optical transitions in a QD are sensitive to the bandgap of the surrounding matrix. Substitution of a wider bandgap (InAlAs lattice matched to InP (Eg~1.5eV)) with a narrower bandgap (InGaAs lattice matched to InP (Eg~0.8eV)) matrix results in a red shift of the QD PL peak position. Replacing the matrix with a wider bandgap material can be used to increase the energy separation between the QD levels. Replacing the matrix material with a narrower bandgap material can be used to extend the QD emission range towards longer wavelengths. A similar analogy can be used here to explain the PL energy red shift. If peak I originates from the surrounding matrix, then as more InAs is deposited, the bandgap of the material matrix is reduced (PL peak will red shift) as P/As exchange creates a more arsenic rich CL layer (Figure 5-4). This decrease in the matrix bandgap will consequently cause the dot peaks to shift to lower energies. A combination of an increase in QD size and a decrease in the matrix bandgap may explain the red shift of the smaller dot (peak II) and the larger dot (peak III) as more InAs is deposited. The large QD peak ceases to shift after 3ML of InAs are deposited, perhaps indicating that the islands have reached a critical size.

To further investigate and confirm the origin of the PL peaks, a PL temperature variation (section 5.3.2) and a level filling (section 5.3.3) experiment were performed.

5.3.2 Temperature variation

An important property of QDs is the deep confining potential which contributes to the conservation of high radiative recombination efficiency at RT as opposed to the case of QWs [46]. By increasing the temperature, PL peaks originating from QWs or QDs will decrease in intensity at different rates, due to a variation in confinement potential and lateral movement of the carriers [45].

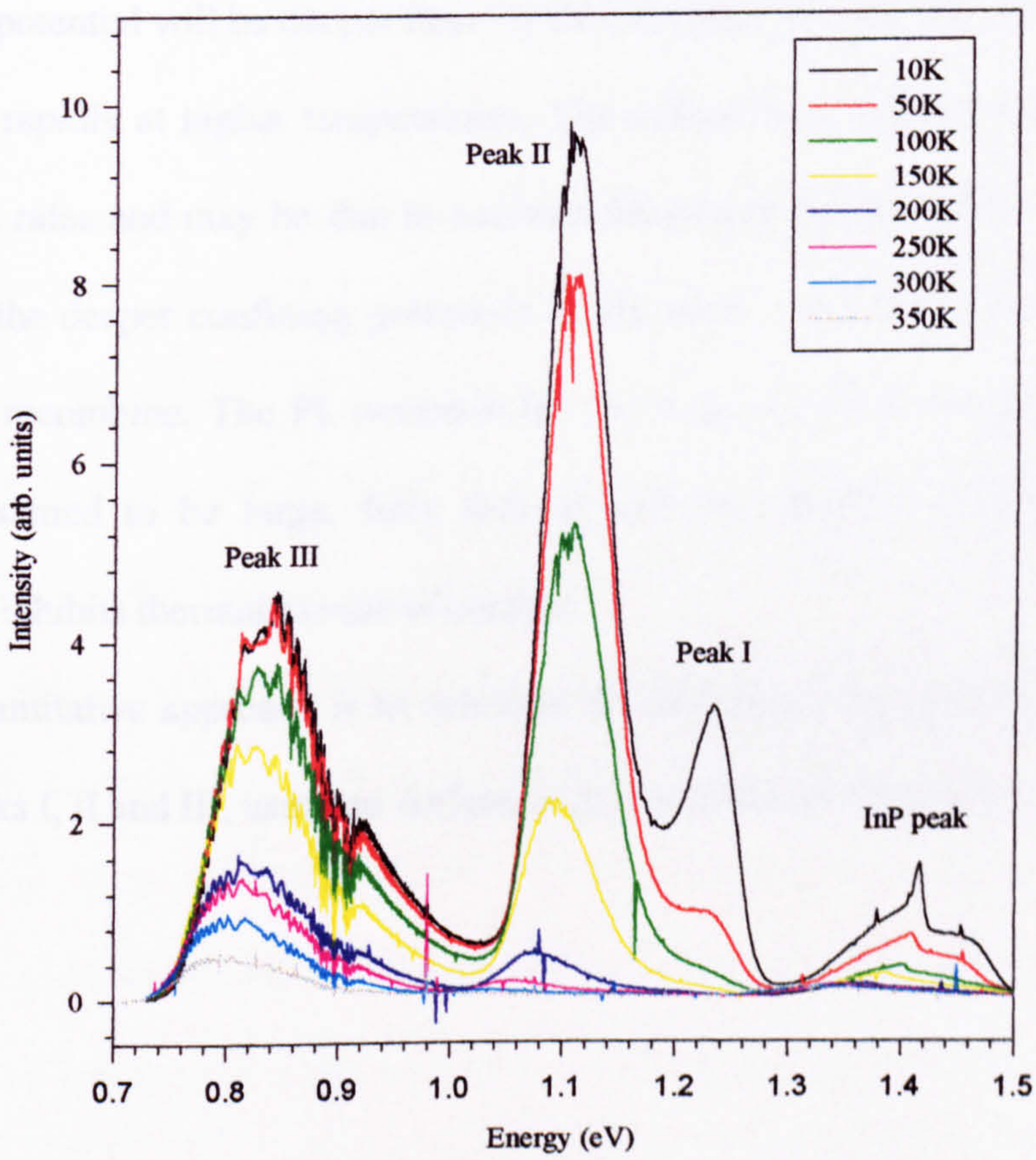

Figure 5-8 *PL spectra showing temperature variation for the 3ML InAs/InP sample. Note that the QD peak is still detectable at 350K.*

Figure 5-8 shows the spectra for the 3ML InAs/InP sample from 10K to 350K. With increasing temperature, the peaks I, II and III decrease in intensity. Peak III exhibits a red shift of about 60-70meV and the QD peak exhibits a smaller shift but this is due to the detector response which is significantly reduced below 0.8eV. This distorts the shape of the emission peak at the higher temperatures. Only the peak attributed to the large dot is detected at room temperature. If peak II originates from smaller dots, then it is reasonable to assume that the confining potential will be deeper than for the CL (peak I) and hence the PL intensity will decrease less rapidly at higher temperatures. The reduction in intensity of these peaks occurs at different rates and may be due to excitons becoming mobile within the 2D layer and relaxing into the deeper confining potentials of the small and large dot groups, where they subsequently recombine. The PL emission for the large dot peak remains at 350K as these dots are assumed to be large, fully formed with the deepest confining potential (~600meV) which inhibits thermal escape of carriers.

A more quantitative approach is to calculate the activation energies, E_a, for thermal emission from peaks I, II and III, using an Arrhenius plot as shown in Figure 5-9.

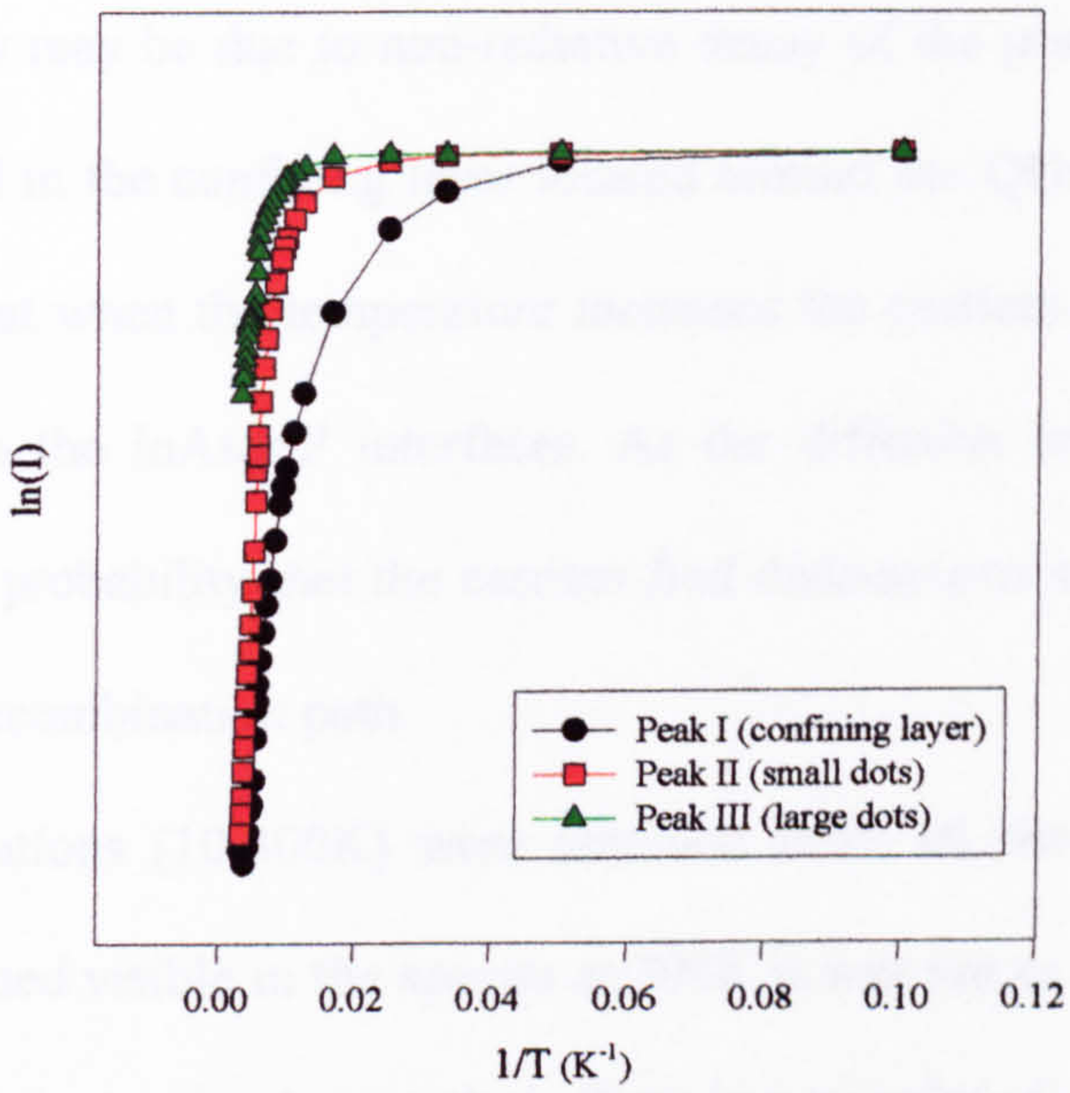

Figure 5-9 *Arrhenius plots for the emission peaks in a 3ML InAs/InP sample*

The activation energies are calculated to be 45, 96 and 345meV for CL, small dots and the large dots respectively. The E_a for the large dots is greater than the small dots (peak II) and peak I which is not unexpected given the much deeper confining potential associated with these dots. Previous studies of thermal escape from QW and QDs [47, 48] have yielded values which directly correlate with the energy difference between the optical transition and the barrier bandgap. This is approximately correct for the large QD emission if carriers/excitons are emitted into the smaller dots (peak II). As the temperature is increased excitons become free and transfer from CL to the small and large dot groups. A further increase in temperature will result in transfer of excitons from the smaller dots to the larger dots and hence at higher temperatures, the small dot PL peak disappears.

The high radiative recombination efficiency of the QDs at RT could also be due to the 3D carrier confinement preventing lateral diffusion of the carriers, reducing the probability of their recombination on defects such as dislocations [46]. The small decrease in

the large dot PL intensity may be due to non-radiative decay of the photogenerated carriers which are mainly created in the confining layer located around the QDs. The PL I intensity drop is due to the fact that when the temperature increases the carriers diffuse in the CL in the directions parallel to the InAs/InP interfaces. As the diffusion length increases with temperature, so does the probability that the carriers find dislocations and impurities which provide a non-radiative recombination path.

Temperature variations (10-300K) were obtained from all the other samples and while the dot peak remained visible in the spectra at 300K it was not as well defined as that for the 3ML sample. With increasing temperature, there is a transfer of carriers from the CL to the large and small QDs until, at room temperature, the only detectable emission is from the large QD layer.

5.3.3 Level Filling

As mentioned in section 5.1.2, a useful method for distinguishing emission from 0D and 2D systems is by increasing the excitation power density to monitor *level* filling. At low excitation intensity only GS levels are observed but as the pump power is increased high energy peaks will emerge which originate from the excited state (ES) transitions. The GS becomes filled with electrons and subsequent electrons in the QD must occupy higher energy states due to the Pauli exclusion principle, hence recombination of these carriers results in PL emission on the high energy side of the GS peak [49]. The DOS consists of a broadened delta function for each energy level allowed by lateral confinement. The proportion of carriers in semiconductor QDs that have a smaller lateral extension than the carrier diffusion

length is higher in QDs than QWs for the same excitation power. It is therefore expected that level filling (filling of the electronic states) should occur at lower excitation powers in QDs compared with QWs [32] as the dots have significant lateral quantisation.

The large QD emission remains almost Gaussian in shape when increasing the sample temperature from 10 to 350K. However, the peak shape is distorted due to the limitations of the Ge diode detector. A closer inspection of the dot PL spectrum at 10K does not reveal weak shoulders located on the high energy side of the main peak which could tentatively be ascribed to an excited state in the dot. However, an excited state may be obscured by some atmospheric absorption of the PL signal around 0.90±0.02eV. A power variation experiment is carried out at 10K to determine if high energy peaks originating from the ES transitions will emerge at higher excitation powers.

Figure 5-10 shows the 10K PL spectra for the 3ML InAs dot sample grown on a 0.2° InP substrate, obtained by increasing the excitation power from 10 to 300mW. The spectra have not been corrected for the spectral response of the system and display some atmospheric absorption of the PL signal around 0.90±0.02eV. At the low excitation power at 10K, the dominant peak is the GS dot emission centred at 0.85eV. As the excitation power is increased from 10 to 300mW, the large and small dot (peak III and II) PL intensities increase and broaden on the high energy side more rapidly than peak I. In fact, peak III and II appear to blue shift as the excitation power increases. This indicates that the sample has not undergone significant sample heating that might be expected for the higher excitation powers as the peaks would red shift.

The PL spectrum at 2mW has been scaled up to facilitate the comparison between the emission spectra taken at 2mW and 300mW. Peak III intensity has increased asymmetrically,

exhibiting a more pronounced broadening on the high energy side. A similar result is observed for peak II. This PL peak line has broadened to such an extent on the high energy side that it appears to have engulfed peak I. Peak I increases in intensity but does not exhibit the same high energy broadening. This broadening on the high energy side could indicate excited states in the dots, thus providing further confirmation that the PL peaks have been correctly assigned. The dot excited states are not as well resolved as for the InAs/GaAs dots studied by *Malik et al.* [32]. The FWHM of the ground state is very wide so the FWHM of the excited states will also be broad making it difficult to distinguish between individual excited states.

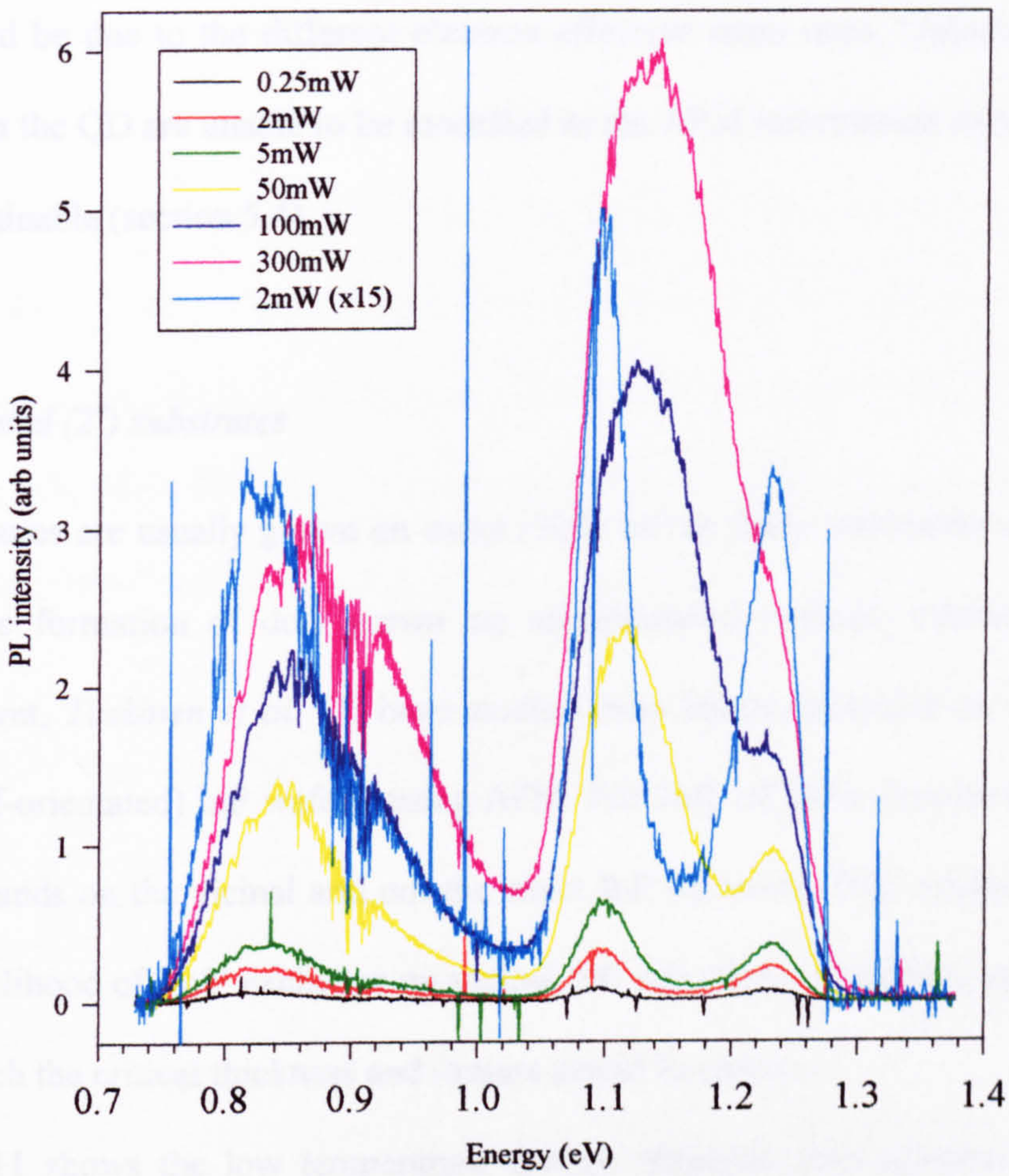

Figure 5-10 *10K PL spectra of 3ML InAs QDs at excitation powers between 1-300mW exhibiting ground state emission at of the larger dots ~0.84eV, the smaller dots at ~1.10eV and the confining layer at ~1.22eV.*

The nature of excited dot states is unclear as calculations of the electronic structure of QDs give conflicting results. For example, *Grundmann et al.* [13] have modelled transitions between only one electron GS state and various hole states, assuming a small pyramidal InAs QD in GaAs. These authors concluded from their calculations that the strain distribution in and around the dot does not depend on the actual size of the QD but on its shape. *Marzin and Bastard et al.* [50] predict at least two confined electron states for cone shaped dots. This

discrepancy could be due to the different electron effective mass used. Unfortunately, the confined levels in the QD are unable to be modelled as the AFM information on the shape of the dots is unobtainable (section 5.4).

5.3.4 Misorientated (2°) substrates

QD structures are usually grown on exact (100) InP or GaAs substrates using MBE. The study of the formation of dots grown on misorientated (vicinal) substrates is not extensive. However, *Taskinen et al.* [7] have studied InAs layers deposited on vicinal, (2° towards [011] off-orientated) InP wafers, using AFM. For 2ML of InAs deposited at 500°C, they observed islands on the vicinal and not the exact InP substrate. They attributed this to the increased likelihood of As/P exchange on vicinal InP substrates. Therefore, less material is required to reach the critical thickness and initiate island formation.

Figure 5-11 shows the low temperature spectra obtained from samples grown on misorientated (2°) substrates with 1.5, 2 and 4ML InAs dot layers. The weak peak at 1.42eV from the InP substrate is visible on each spectrum. A similar process is used in assigning the PL peaks on the vicinal substrate as for the standard substrate. For the 1.5ML InAs layer sample a broad peak located around 1.3eV is clearly visible with a shoulder on the low energy side. The shoulder may originate from small dots whereas the main peak originates from the confining layer. A weak broad peak situated at approximately 1.05eV is also visible and could indicate the onset of larger dot formation. The spectrum for the 2ML InAs layer sample exhibits two peaks; one strong PL peak located at 1.17eV and the other a weak broad peak at 0.98eV. As more InAs is deposited, the 2D confined layer increases in width and

becomes more As rich (As/P exchange) causing the peak to red shift and perhaps obscure the emission from the small dots. The spectrum of the 4ML InAs layer shows three peaks and resembles the spectrum obtained for the 4ML InAs grown on the standard substrate. The peaks are assigned in a similar manner as shown in Figure 5-4. The CL peak is located at a lower energy for growth on the 0.2° substrate compared with those grown on the 2° substrate but the large dot peak is located at the same position as the corresponding peak for the 4ML InAs deposit on the standard substrate.

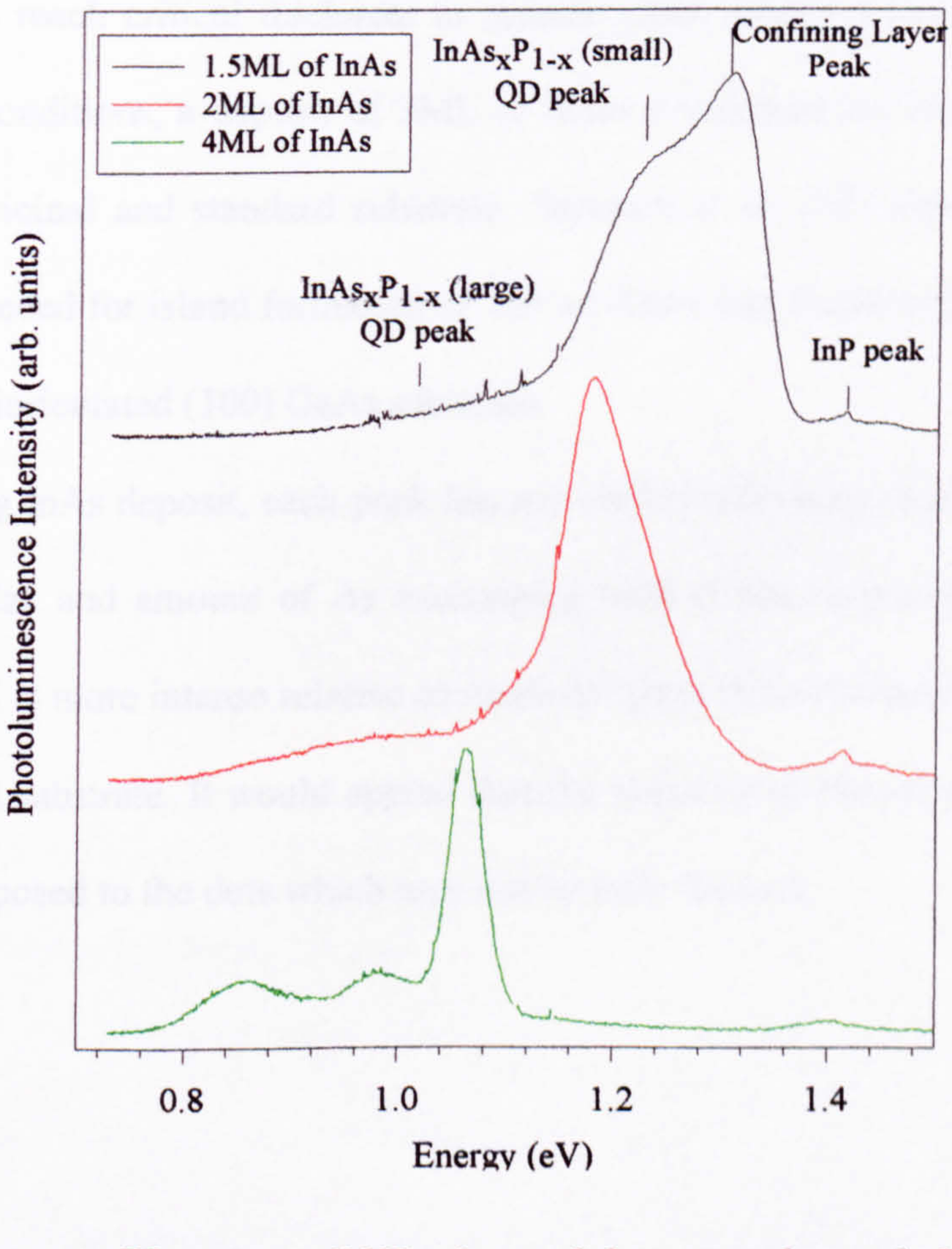

Figure 5-11 *Low temperature PL spectra (10K) obtained from samples with 1.5, 2, 3 and 4ML of InAs deposited on misorientated (2°) InP substrate. The structures are capped with 53nm of InP. Emission from QDs, the CL and the InP substrate are indicated in the figure.*

For InAs deposits of 1.5 and 2MLs, grown on either 0.2 and 2° offcut substrates, the broad weak peak at lower energies (<1.0eV) in Figure 5-4 and 5-11 appears to indicate emission from a small number of large islands. *Leon et al.* [51] have demonstrated that nucleation on step edges is energetically favourable unless kinetically limited by small diffusion lengths. QDs formed on stepped edges results in smaller average diameters and higher island densities for InGaAs/GaAs structures. In this case, for InAs deposited on InP, it appears that a similar amount of material has to be deposited on the vicinal substrate (and standard substrate) to reach critical thickness to initiate small island formation (peak II). Under these growth conditions, a deposit of 3ML or more is required for larger dots to be formed on both the vicinal and standard substrate. *Sopanen et al.* [52] observed that the threshold thickness needed for island formation of InP on GaAs was found to be ~2.5ML for both the 0.2° and 2° miorientated (100) GaAs substrate.

With increasing InAs deposit, each peak has red shifted indicating that the confining layer thickness, dot size and amount of As exchanging with P has increased. For a 4ML deposit of InAs, peak I is more intense relative to small dot peak (II) and also compared with peak I on the standard substrate. It would appear that the majority of carrier recombination occurs in the CL as opposed to the dots which may not be fully formed.

5.4 Atomic Force Microscopy (AFM)

The surface morphology of the dots can be viewed (*ex-situ*) using AFM in order to determine the effects of growth temperature and InAs deposition thickness and rate on the areal density, size, uniformity and spatial distribution of SADs. Uncapped 3ML InAs dots were grown on standard and misorientated InP substrates under the same growth conditions as before. The AFM revealed that the dots were extremely large, ranging from 84 to 243nm in height and 78 to 2000nm in length. The majority of islands were shaped like a truncated square based pyramid (with the apex missing). However, volume calculations of the dots revealed that much more material had been deposited than stated in the growth process. It is clear that such large structures cannot provide confinement for injected carriers. Further investigation revealed that the cool down time in the MOCVD reactor was at least 30s during which arsine gas continued to flow. It is likely that during this cool-down period additional As/P exchange took place resulting in the large islands evident in the AFM pictures [26]. At present it is not possible to reduce the cooling time and AFM could not be used to estimate the dot size and density.

According to *Barbabasi et al.* [19] the maximum strain energy was expected at the periphery of the dot base and therefore, the As/P exchange reaction would be increased along the periphery of InAs QDs as As/P exchange reactions are more enhanced in strained areas. *Yoon et al.* [27] suggested that if surface diffusion of free In atoms generated at the periphery of InAs QDs is sufficient, the adatoms will migrate in such a way that the total energy of the system decreases. The free In atoms will migrate towards the apex of the dot where the strain energy is minimal. This may explain our results. The generation of free In atoms migrating

towards the apex of the dots [36] may enhance the bonding with excess As in the reactor and hence substantially increase the size of the dots.

5.5 Annealing

InAs/GaAs self-assembled QD structures can be tuned to different emission wavelengths by post-growth annealing [51] treatments which induce interdiffusion of the group III atoms. There is a concomitant reduction in the emission FWHM of the dot ensemble which arises from the general increase in dot size for InGaAs/GaAs QDs and hence a narrower distribution of the dot sizes [28, 53-55]. Studies have also found that a larger blue shift can be obtained in QDs compared with QWs for the same value of the diffusion length. However, the emission intensity is decreased at higher anneal temperatures due to shallower confining dot potentials [32, 54]. Interdiffusion processes have been extensively studied for the GaAs/AlGaAs and InGaAs/GaAs QW structures.

Recently *Leon et al.* [28] *Xu et al.* [54] and *Malik et al.* [32] have investigated the PL emission energies of InAs/GaAs based QDs after post-growth thermal annealing. They have reported significant narrowing and blue shift of the luminescence emission of the SADs which they attributed to diffusion of group III elements. For anneals at different temperatures up to and including 850°C, *Xu et al.* [54] observed a large blue shift of 260meV and a narrowing from 79 to 21meV of the PL linewidth for QDs. Annealing at 850°C, a large decrease in the PL intensity was observed, implying a degradation in material quality. Subsequent TEM results show that the QDs disappear and combine with the WL to form a QW like structure. However, the mechanisms and processes which result in the change of

optical properties are not clearly understood. *Lobo et al.* [53] have concluded that the diffusing elements affect the PL emission (In diffuses from the dot to the barrier material whilst Ga diffuses in the opposite direction).

5.5.1 Samples and results after annealing

This section investigates the effects of post-growth thermal annealing on InAs QDs grown on InP. Samples from the 3ML InAs wafer grown on the standard (0.2°) off-axis InP substrate were capped with 0.1μm of SiO_2 on the epilayer and substrate side. The same post-growth annealing method was used as described in section 4. The samples were then annealed in a furnace at 800°C for 120, 300 or 600s or at 850°C for 600s.

Figure 5-12 compares the low temperature (10K) PL spectra for these samples with the unannealed original. Peak III attributed to the large QDs is observed to blue shift with increasing anneal time and temperature. The other two peaks located at 1.09eV and 1.18eV in the unannealed sample exhibit quite different behaviour again indicating that they do not both originate from two separate QW layers. Peak I which is thought to arise from the 2D confining layer formed during the InP capping process red shifts during annealing. By contrast the emission energy of peak II, attributed to small dots, remains roughly constant implying minimal interdiffusion of these dot during annealing.

Annealing at a higher temperature (850°C for 600s) results in only one detectable peak at 1.14eV although it is not clear from these measurements whether there is complete dissolution of the QDs following this treatment. Therefore a temperature variation (10 to 300K) experiment was carried out on each sample. In each case, as the temperature increased, the large dot peak blue shifted, decreased in intensity but remained clearly visible

up to temperatures of 300K. Peak I and II decreased in intensity as the temperature increased and peak I became undetectable by ~190K. At the highest anneal time and temperature, it is assumed that the large dots are still intact and remain dislocation free as an emission peak was observed at 300K. Confirmation would be needed in the form of a power variation experiment to determine the evolution of excited states which is characteristic of 0D behaviour [54].

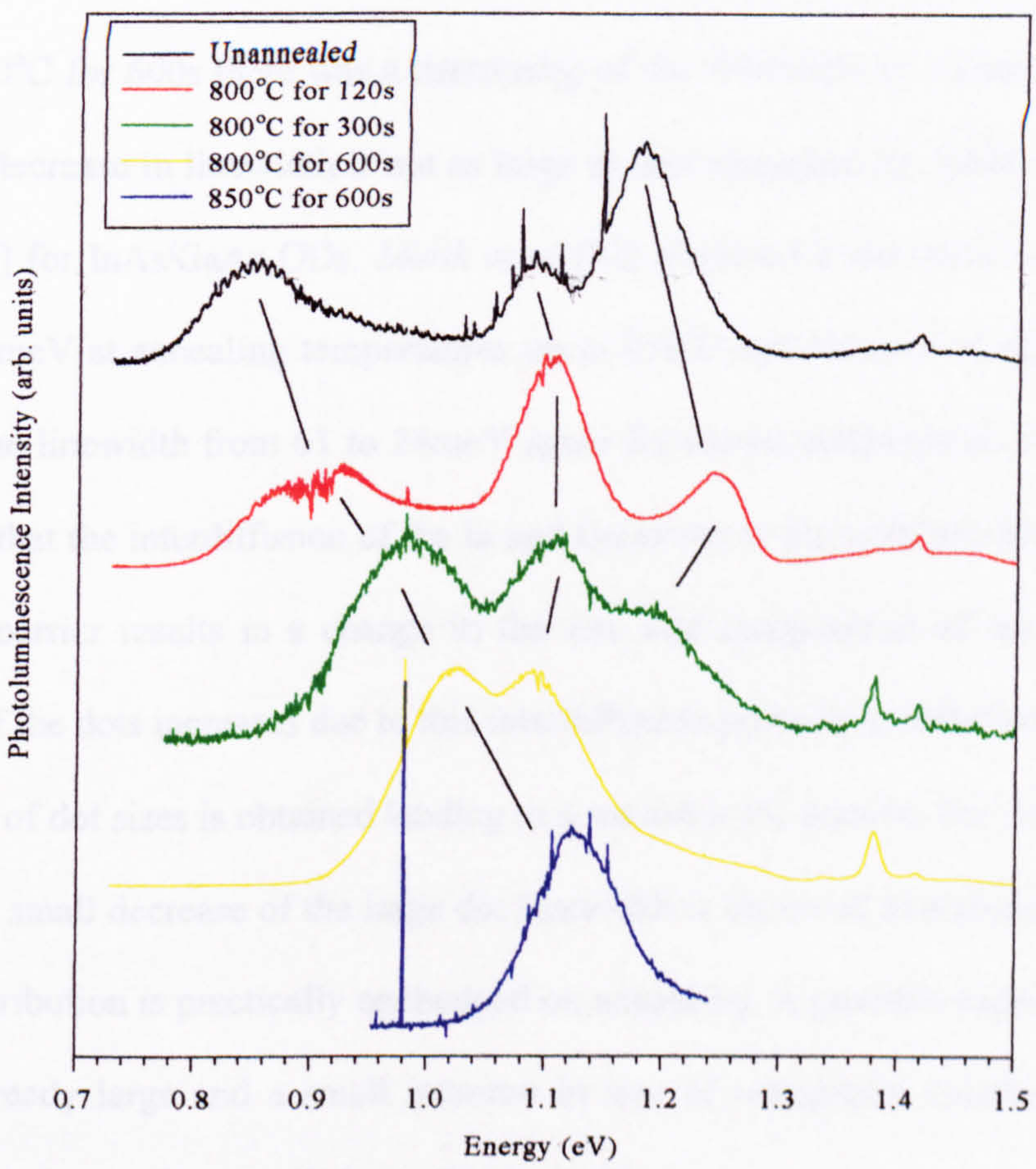

Figure 5-12 *Low temperature (10K) PL spectra for the 3ML InAs dot samples capped with SiO_2 annealed at 800°C for 120, 300 and 600s and at 850°C for 600s. Guide lines have been included.*

The large dot peaks are roughly Gaussian in shape after all the annealing treatments. As mentioned before, for the unannealed sample, the broad dot signal arises from the variation of the GS emission energy from the individual QDs implying that they are of different size (and composition) [57]. Annealing results in a narrowing of the inhomogeneously broadened PL peak perhaps correlating to a narrower size distribution of the dots [31, 53]. The FWHM is difficult to measure directly from the spectra as the peaks merged together on increasing the anneal time and temperature. However, for the sample annealed at 850°C for 600s there was a narrowing of the linewidth by 15meV (from 107 to 92meV). This decrease in linewidth is not as large as that measured by *Malik et al.* [32] and *Leon et al.* [28] for InAs/GaAs QDs. *Malik et al* [32] observed a narrowing of the FWHM from 55 to 12 meV at annealing temperatures up to 950°C and *Leon et al.* [28] observed a narrowing of the linewidth from 61 to 24meV again for anneal temperature of 950°C. Both papers suggest that the interdiffusion of the In and Ga atoms at the interface between the QD and the GaAs barrier results in a change in the size and composition of the QDs. As the effective size of the dots increases due to this interdiffusion process, an effective reduction in the distribution of dot sizes is obtained leading to a narrower PL feature. For the InAs on InP samples, only a small decrease of the large dot linewidth is observed and could indicate that the dot size distribution is practically unchanged on annealing. A possible explanation is that the dots are already large and a small increase in size of marginally smaller dots due to interdiffusion, leads to only a small change in linewidth.

Figure 5-13 shows the shift of the large dot peak, as a function of anneal time. The exciton transition blueshifts by 50, 138 and 179meV for anneal times of 120, 300 and 600s respectively at 800°C and exhibits a sub-linear dependence with increasing temperature. The

greatest blueshift of 273meV was observed for the anneal time and temperature of 850°C. The high energy shift of the luminescence line can be explained by reduced confinement potential after annealing due to the change in dot composition [58-60]. Even though no general agreement has been reached for the mechanisms involved in the blueshift of the dot peak, annealing would cause interdiffusion of the group V species as seen in QWs. In QWs, interdiffusion causes the abrupt interfaces to become graded, reducing the confining potential and hence a blueshift of the PL emission is observed. It is difficult to model the diffusion since there is no consensus on the size and strain or shape of the dots.

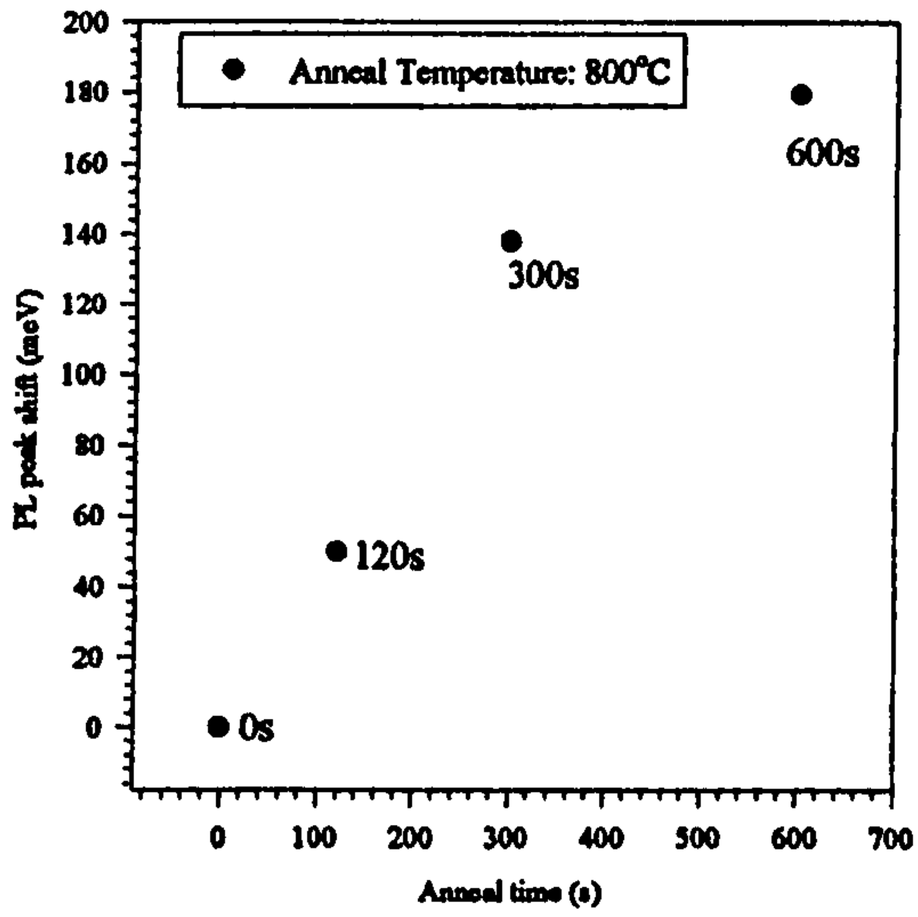

Figure 5-13 *The large QD PL peak energy shift as a function of anneal time for anneal temperature of 800°C*

After annealing it is reasonable to assume that the group V elements (P and As) have undergone diffusion as these elements are known to diffuse at temperatures as low as 500°C as detailed in chapter 4. Even during growth an enhanced As/P surface exchange process with increasing growth temperature has been observed [57]. For the large dots (peak III), as

the anneal time and temperature increases, more P from the underlying InP layer and CL will exchange with the As in the dots. This manifests itself as a significant blueshift of the large dot PL peak as shown in Figure 5-12, as the emission peak moves towards the InP bandgap energy. It would appear that the incorporation of P into the dot is the dominant process. If the large dots were significantly increasing in size, then the dot emission would shift to lower energies. However, only a small decrease in the linewidth is observed on annealing indicating that the dot size distribution remains almost unchanged. A similar conclusion was reached by *Malik et al.* [32]. (The sub-linear dependence of the blue shift with increasing temperature could signify the As/P exchange between the dots, CLs and barriers reaching a limit).

The small dot peak (peak II) does not appear to significantly shift to lower or higher energies with increasing anneal time. Two conflicting effects could be occurring 1) a change in the small dot composition due to As/P exchange results in a shallower confining potential and hence a blueshift in the emission and 2) as the As/P exchange rate increases for higher anneal times and temperatures, this could lead to an effective increase in the dot size and/or island coalescence of a small proportion of the smaller islands resulting in a red shift of the PL emission. This would also reduce the small island PL intensity and increase the larger island intensity as observed in Figure 5-12. Hence the above effects may actually cancel each other which results as the PL peak remaining stationary even after annealing. After annealing at 800°C for 300s, the intensity of peak II is lower than the large dot peak indicating that exciton recombination is greater in the latter. After annealing at 850°C for 600s, the solitary peak may represent the luminescence from a set of similar sized islands rather than a bimodal distribution as previously observed.

The red shift of the CL emission peak could be explained by the increase of the As/P exchange between the CL and the dot layer as the anneal *time is increased. This could have* two effects a) the effective 'well width' of the 2D layer will increase and b) arsenic (from the dots) replacing the P in the CL causes a reduction in the compressive strain and hence leads to a decrease in the bandgap [23]. Both these result in a PL shift to lower energies. The reduction in intensity and finally the disappearance of the CL peak can be explained by considering the average QD separation [51]. If the InAs dots increase in size due to the diffusion and incorporation of P the average separation of the dots will decrease. Hence the carriers are more easily recaptured into the dot from the CL and the intensity of the CL emission decreases until its emission can no longer be detected under these experimental conditions.

In summary, As/P interdiffusion causes the large dot peak to shift to higher energies with increasing (anneal/growth) temperature [57]. It would appear from the optical spectra in Figure 5-12 that, as the anneal time and temperature is increased, the three peaks culminate in a single peak which is still observed at 350K for the sample annealed at 850°C implying that the dots remain intact and dislocation free.

5.6 Conclusions

Different ML thicknesses of InAs were deposited on standard and misorientated (100) InP substrate by MOCVD at 600°C to obtain $InAs_xP_{1-x}$ QDs which emit at 1.55μm at room temperature. Only a limited optical analysis in the form of PL temperature variation and level filling experiments could be performed on the dots due to their long wavelength emission.

For the 1.5, 2, 3 and 4 ML InAs dots grown on 0.2° off (001) InP substrate, three peaks could be clearly identified in the 10K PL spectrum. The signal located at the lowest energy was ascribed to the emission from large QDs, the next PL peak was ascribed to the emission from small dots and finally, the third peak was attributed to emission from 2D confining layers. It was concluded that 3ML was the optimum InAs deposit for the formations of QDs grown at a temperature of 600°C. Information on the actual dot shape and CL dimensions was difficult to obtain but EDX linescans revealed that the height of the QD and also the width of the confining layer was ~84Å. This indicates that the QDs are embedded in the confining layer rather than 'sitting' on top. This was used as a guideline to the thickness of CL and the height of the large dots. A composition of 30% As in CL and 61% As in the large dots was calculated.

1.5, 2 and 4 ML InAs layers were deposited on vicinal substrates. In each case the dot peaks were not as intense as the corresponding emission from the dots grown on the standard substrate. It appears that a similar amount of material needs to be deposited on the vicinal and standard substrate to reach critical thickness for island formation.

Temperature variation and level filling were performed on the 3ML InAs/InP sample grown on the standard substrate. In the temperature variation experiment (10K-350K), the

large dot peak remained clearly visible up to a temperature of 350K, whereas the small dot (peak II) and CL peak disappeared at lower temperatures. Activation energies for CL, small dots and large dots were evaluated to be 45, 96 and 345meV respectively. Carrier escape from the CL commenced at a lower temperature than for the small and large dots. As the temperature increases, carriers escaping from CL could be captured by the small and large dots deeper confining potential where they recombine. As the temperature was increased, the small dot peak was reduced in intensity indicating that carriers may be escaping from the small dots into the large dots. The strong luminescence from QDs, even at high temperatures, can be attributed to a deeper confinement potential which reduces thermal carrier escape, a stronger exciton binding energy from the confinement in 3D and an enlarged oscillator strength which is a property of reduced dimensionality. Increasing the excitation energy from 0.2mW to 300mW resulted in the small and large dot peak broadening on the high energy side indicating excited states in the dots. Peak I did not exhibit the same behaviour, hence confirming that the two lower PL peaks originate from a bi-modal distribution of dots and the third peak originates from a QW layer.

Blueshifts in the PL emission from the 3ML InAs QDs were observed as a result of post-growth annealing. Low temperature PL revealed that the large dot peak blue shifted with increasing anneal time, up to 273meV for the anneal time 600s and temperature of 850°C, and the PL linewidth decreased by ~15meV indicating a more uniform distribution in dot size. The large dot PL emission remained strong at temperatures up to 350K implying that the dots remain intact and dislocation free. The blueshift is attributed to the As/P intermixing resulting in changes in composition of the dot. The small dot peak appeared not to shift which could be due to an increase in dot size cancelling out a decrease in As in the dot due to

the As/P exchange. The CL peak disappeared with increasing anneal time. Annealing at 850°C for a 600s, resulted in one PL signal which was attributed to the lowest energy state on the surface. PL measurements indicate that the annealed structures remained as dots.

From the optical and structural results, it would appear that by depositing 3MLs of InAs on InP at 600°C, QDs can be successfully grown which emit at 1.55μm at room temperature.

5.7 References

[1] L. Goldstein, F. Glas J. Y. Marzin, M. N. Charasse, G. Le. Roux; Appl. Phys. Lett. 47 (10) p1099 (1985) [D73]

[2] D. Leonard, M. Krishnamurty, C. M. Reaves, S. P. Densbaars, P. M. Petroff: Appl. Phys. Lett. 63 (23) p3203 (1993) [D77]

[3] M. Grundmann, R. Heitz, N. Ledentsov, O. Stier, D. Bimberg, V. M. Ustinov, P. S. Kop'ev, Zh. I. Alferov; Superlatt. and Microstruc. 19 (2) p81 (1996) [D48]

[4] H. Lee, R. Lowe-Webb, W. Yang, P. C. Sercel; Appl. Phys. Lett. 72 (7) p812 (1998) [D90]

[5] M. Grundmann, J. Christen, N. N. Ledentsov, J. Bohrer, D. Bimberg, S. S. Ruvimov, P. Werner, U. Richter, U. Gosele, J. Heydenreich; Phys. Rev. Lett. 74 (20) p4043 (1995) [D30]

[6] P. S. Zory Jr.: Academic Press (1993)

[7] M. Taskinen, M. Sopanen, H. Lipsanen, J. Tulkki, T. Tuomi, J. Ahopelto; Sur. Sci. 376 p60 (1997) [D60]

[8] A. Kurtenbach, K. Eberl, T. Shitara; Appl. Phys. Lett. 66 (3) p361 (1994) [D205]

[9] M. Sopanen, H. Lipsanen, J. Ahopelto; Appl. Phys. Lett. 67 (25) p812 (1995) [D206]

[10] N. Carlsson, W. Seifert, A. Petersson, P. Castrillo, M. E. Pistol, L. Samuelson; Appl. Phys. Lett. 65 (24) p3093 (1994) [D72]

[11] V. A. Shchukin, N. N. Ledentsov, P. S Kop'ev, D. Bimberg; Rev. Lett. 75 (16) p2968 (1995) [D85]

[12] J. Y. Marzin, J.-M. Gerard, A. Izrael, D. Barrier, G. Bastard; Phys. Rev. Lett. 73 p716 (1994) [D22,3]

[13] S. Farfard, D. Leonard, J. M. Merz, P. M. Petroff; Appl. Phys. Lett. 65 (11) p1388 (1994) [D66]

[14] M. Grundmann, N. N. Ledentsov, O. Stier, D. Bimberg, V. M. Ustinov, P. S. Kop'ev, Zh. I. Alferov; Appl. Phys. Lett. 68 (7) p979 (1995) [D88]

[15] M. Grundmann, R. Heitz, N. Ledentsov, O. Stier, D. Bimberg, V. M. Ustinov, P. S. Kop'ev, Zh. I. Alferov, S.S. Ruvimov, P. Werner, U. Gosele, J. Heydenreich; Supperlatt and Microstruc. 19 (2) p81 (1996) [D89]

[16] Y. Arakawa, H. Sakaki; Appl. Phys. Lett. 40 (11) p939 (1982) [D65]

[17] D. Leonard, M. Krishnamurty, S. Fafard, J. L. Merz, P. M. Petroff; J. Vac. Sci. Technol. B 12 (2) p1063 (1993) [D78]

[18] J. Singh; Physics of semiconductors and their heterostructures; McGraw-Hill (1993)

[19] A.-L. Barabasi; Appl. Phys. Lett. 70 (19) p2565 (1997) [D62]

[20] Y. Hasegawa, H. Kiyama, Q. K. Xue, T. Sakurai; Appl. Phys. Lett. 72 (18) p2265 (1998) [D86]

[21] D. Leonard, K. Pond, P. M. Petroff; Phys. Rev. B 50 (16) p11 687 (1994) [D80]

[22] S. Farfard, Z. Wasilewki, J. McCaffrey, S. Raymond, S. Charbonneau; Appl. Phys. Lett. 68 (7) p991 (1995) [D20]

[23] H. Marchand, P. Desjardins, S. Guillon, J.-E. Paultre, Z. Bougrioua, R. Y.-P. Yip, R. A. Masut; Appl. Phys. Lett. 71 (4) p527 (1997) [D16]

[24] A. Ponchet, A. Le Corre, H. L'Haridon, B. Lambert, S. Salaun, J. Groenen, R. Carles; Solid-State Electronics 40 (1-8) p615 (1996) [D21]

[25] A. Ponchet, A. Le Corre, H. L'Haridon, B. Lambert, S. Salaun; Appl. Phys. Lett. 71 (4) p527 (1997) [D17]

[26] Y. Nonogaki, T. Iguchi, Y. Fujiwara, Y. Takeda; Appl. Surf. Sci. 117 p665 (1997) [D19]

[27] S. Yoon, Y. Moon, T.-W. Lee, E. Yoon, Y. D. Kim; ; Appl. Phys. Lett. 74 (14) p2029 (1999) [D242]

[28] R. Leon, Y. Kim, C. Jagadish, M. Gal, J. Zou, D. J. H. Cockayne; Appl. Phys. Lett. 69 (13) p1889 (1996) [D25]

[29] H. Benistry, C. M. Sotomayor-Torres, C. Weisbuch; Phys. Rev. B. 44 (19) p10 945 (1991) [D207]

[30] P. D. Wang, C. M. Sotomayor-Torres; J. Appl. Phys. 74 (8) p5047 (1993) [D59]

[31] R. Heitz, M. Grundmann, N. Ledentsov, L. Eckey, M. Veit, D. Bimberg, V. M. Ustinov, A. Yu. Egorov, A. E. Zhukov, P. S. Kop'ev, Zh. I. Alferov; Appl. Phys. Lett. 68 (3) p361 (1996) [D201]

[32] S. Malik, C. Roberts, R. Murray, M. Pate; Appl. Phys. Lett. 71 (14) p1987 (1997) [D110]

[33] P. Castrillo, D. Hessman, M.-E. Pistol, S. Anand, N. Carlsson, W. Seifert, L. Samuelson; Appl. Phys. Lett. 67 (13) p1905 (1995) [D94]

[34] H. Yu, S. Lycett, C. Roberts, R. Murray; Appl. Phys. Lett. 69 (26) p4087 (1996) [D200]

[35] G. Wang, S. Fafard, D. Leonard, *J. E. Bowers, J. L. Merz,* P. M. Petroff; Appl. Phys. Lett. 64 (21) p2815 (1993) [D204]

[36] B. Wang, F. Zhao, Y. Peng, Z. Jin, Y. Li, S. Liu; ; Appl. Phys. Lett. 72 (19) p2433 (1998) [D222]

[37] P. D. Siverns, S. Mailk, G. McPherson, D. Childs, C. Roberts, R. Murray, B. A. Joyce, H. Davock; Phys. Rev. B 58 (16) p R10 127 (1998) [D211]

[38] U. Woggan, W. Langbein, J. M. Hvam, A. Rosenauer, T. Remmele, D. Gerthsen; Appl. Phys. Letts. 71 (3) p377 (1997) [D217]

[39] W. Wu, J. R. Tucker, G. S. Solomon, J. S. Harris, Jr.; Appl. Phys. Letts. 71 (8) p1083 (1997) [D217]

[40] A. Tabata, T. Benyattou, G. Guillot, M. Gendry, G. Hollinger, P. Viktorovitch; J. Vac. Sci. Technol. B 12 (4) p2299 (1994) [D216]

[41] J. F. Carlin, R. Houdre, A. Rudra, M. Ilegems; Appl. Phys. Lett. 59 (23) p3018 (1991) [D100]

[42] A. E. Zhukov, V. M. Ustinov, A. R. Kovsh, A. Yu Egorov, N. A. Maleev, N. N. Ledentsov, A. F. Tsatsul'nikov, M. V. Maximov, Yu G. Musikhin, P. S. Kop'ev, D. Bimberg, Zh I. Alferov; Semicond. Sci. Technol. 14 p575 (1999) [D229]

[43] J. P. R. David, M. Hopkinson, P. N. Stavrinou, S. K. Haywood; J. Appl. Phys. 78 (5) p3330 (1995) [A10]

[44] J. Johansson, W. Seifert, T. Junno, L. Samuelson; J of Cryst. Growth 195 p546 (1998) [D289]

[45] V. M. Ustinov, E. R. Weber, S. Ruvimov, Z. Lilliental-Weber, A. E. Zhukov, A. Yu. Egorov, A. R. Kovsh, A. F. Tsatsul'nikov, P. S. Kop'ev; Appl. Phys. Lett. 72 (3) p362 (1998) [D231]

[46] B. Lambert, A. Le Corre, V. Drouot, H. L'Haridon, S. Loualiche; Semicond. Sci. Technol. 13 p143 (1998) [D223]

[47] G. Bacher, H. Schweizer, J. Kovac, A. Forchel, H. Nickel, W. Schlapp, R. Lösch; Phys. Rev. B. 43 (11) p9312 (1991) [E19]

[48] J. D. Lambkin, D. J. Dunstan, K. P. Homewood, L. K. Howard, M. T. Emeny; Appl. Phys. Lett. 57 (19) p1986 (1990) [300]

[49] D. Hessman, P. Castrillo, M.-E. Pistol, C. Pryor, L. Samuelson; Appl. Phys. Lett. 69 (6) p749 (1996) [D22]

[50] J.-Y. Marzin, G. Bastard; Sol. Stat. Commun. 92 p437 (1994) [D33,20]

[51] R. Leon, C. Lobo, A. Clark, R. Bozek, A. Wysmolek, A. Kurpiewski, M. Kaminska; J. Appl. Phys. 84 (1) p248 (1998) [D104]

[52] M. Sopanen, H. Lipsanen, J. Ahopelto; Appl. Phys. Lett. 67 (25) p3768 (1995) [D152]

[53] C. Lobo, R. Leon, S. Fafard, P. G. Piva; Appl. Phys. Lett. 72 (22) p2850 (1998) [D105]

[54] S. J. Xu, X. C. Wang, S. J. Chua, C. H. Wang, W. J. Fan, J. Jiang, X. G. Xie; ; Appl. Phys. Lett. 72 (25) p3335 (1998) [D101]

[55] H. Yu, C. Roberts, R. Murray; ; Appl. Phys. *Lett. 66 (17) p2253 (1995)* [D75]

[56] K. Nakashima, Y. Kawaguchi, Y. Kawamura, H. Asahi, Y. Imamura; Jpn. J. Appl. Phys. 26, (10) 1987 [A1]

[57] J.-J. Shen, A. S. Brown, R. A. Metzger, B. Sievers, L. Bottomley, P. Eckert, W. B. Carter; J. Vac. Sci. Technol. B, 16 (3) p1326 (1998) [D103]

[58] A. O. Kosogov, P. Werner, U. Gosele, N. N. Ledenstov, D. Bimberg, V. M. Ustinov, A. Yu. Egorov, A. E. Zhukov, P. S. Kop'ev, N. A. Bert, Zh. I. Alferov; ; Appl. Phys. Lett. 69 (20) p3072 (1996) [D102]

[59] R. Leon, D. R. M. Williams, J. Krueger, E. R. Weber, M. R. Melloch; Phys. Rev. B, 56 (8) pR4336 (1997) [D016]

[60] R. Leon, S. Fafard, D. Leonard, J. L. Merz, P. M. P:etroff; ; Appl. Phys. Lett. 67 (4) p521 (1995) [D209]

6. Conclusions and Future Work

The work described in chapters 3-5 is an investigation of InP-based QWs and QDs, which emit in the technologically important wavelength region of 1.3-1.55μm. Although InP based QWs are crucial to the telecomms industry largely empirical solutions have been found to deal with grading of interfaces involving use of quaternary InGaAsP material. This work has confirmed that unintentional grading of the QW interfaces occurred in lattice-matched $In_{0.53}Ga_{0.47}As$/InP QWs due to As/P exchange at the interface. A combination of optical and structural measurements showed that grading at the InGaAs well interfaces can be overcome by substituting an InP barrier with a P-based quaternary barrier.

There have been many investigations of deliberate grading of QW interfaces for integrated optics applications. These rely on interdiffusion caused either by thermal generation of vacancies or enhanced generation of vacancies by use of a dielectric cap. There is evidence that the caps generate group III vacancies but their effect on interdiffusion of the group V species has not been tested. In chapter 4 the interdiffusion of InAsP/InP MQWs by intermixing the well and barrier material using post-growth annealing techniques was investigated. Significant blueshifts could be induced in the emission energy whilst retaining strong excitonic emission. This was attributed to As/P exchange at the interface and appears to happen even during the growth process. The degree of intermixing can be controlled by altering the annealing time and temperature. However, the process was independent of the type of dielectric cap and suggests that it is due to thermal generation of vacancies. The activation energy for interdiffusion and diffusion coefficients deduced from optical and structural measurements are in reasonable agreement with previously reported values.

There is currently a great deal of interest in self-assembled quantum dots. In chapter 5 it was demonstrated that InAsP QDs can be grown by depositing a few MLs of InAs on an InP substrate by MOCVD. An ensemble of QDs was formed with the optimum deposit of 3MLs of InAs for these growth conditions which resulted in room temperature emission around 1.5μm. These structures should in principle offer advantages over QW lasers at these longer wavelengths; lower threshold currents which are also temperature independent and the suppression of Auger recombination.

6.1 Chapter 3

Latticed matched InGaAs/InP is a suitable material combination for optoelectronic devices such as long wavelength semiconductor lasers and modulators [1]. Growth of high quality heterointerfaces has been the key factor in improving the properties of these devices. However, the cross contamination of fluxes due to incomplete switching or the memory effect creates a compositionally graded layer with built in strain deforming the shape of the well [2], thus making it difficult to calculate and predict the optical properties of the resultant non-square well potential. Further strain and other effects of compositional grading can result in increased nonradiative recombination at the heterointerfaces. The additional interfacial layers and grading at the interfaces is attributed to As/P exchange as As has a high incorporation coefficient relative to P [3]. Growth interruption techniques [2] are one of the most commonly used methods to reduce the exchange process or eliminate three-dimensional islands which result during growth.

A good fit for the square well approximation to the experimental results was not obtained for the InGaAs/InP MQW, indicating that the well was graded at the interface.

Rather than an attempt to minimise intermixing by an elaborate growth sequence, a structure where the InP barriers are replaced by InGaAsP was adopted. The quaternary barriers were still lattice matched to InP. For the InGaAs/InGaAsP MQW, a much better agreement between experimental and calculated energy levels was obtained. InGaAsP barriers were substituted for InP barriers as both group V elements were common to the well and the (InGaAsP) barrier so even if some intermixing occurred, it resulted in improved heterointerfaces and hence MQW device quality.

The next step would be to incorporate biaxial strain in the QW layers as it is beneficial to devices such as semiconductor lasers. By introducing strain into the QW system, lasers operating at both 1.3 and 1.55μm can be achieved with a reduced threshold current and improved differential gain [4, 5]. *Vandenberg et al.* [6] suggested that incorporating strain into such layers would allow the valence band properties to be engineered; splitting the valence *band degeneracy* at the Brillouin zone centre by introducing compressive strain into the active region of a semiconductor laser reduces *Auger* recombination and intervalence band absorption (IVBA). An additional benefit of introducing strain is the alteration of the valence band effective masses, which leads to a reduction in the in-plane density of states. This reduces the laser threshold current and improves the temperature sensitivity.

Replacing InGaAs with InGaAsP in the well region forming structures such as InGaAsP/InP [7], gives more design freedom, as strain can be incorporated into the InGaAsP layer by independently changing the QW thickness and composition for a given emission wavelength. Compressive strain (1-1.5%) is large enough to reduce the density of states below a third of that of the unstrained wells, which in turn increases differential gain as light

hole and heavy hole subbands are split at an optimum well width. For tensile-strained wells emitting at 1.55μm, the well width would need to be greater than 15nm. However, these wide wells would degrade the differential gain due to the accumulation of conduction subbands in the well [7].

6.2 Chapter 4

Controlled intermixing of the QWs by post-growth annealing can be achieved by IFVD or IILD processes and leads to changes in the bandgap of the structure [8]. The bandgap of the intermixed alloy is usually larger than that of the original structure, thus providing a route to form low-loss optical waveguides and bandgap shifted modulators, lasers and detectors using only one epitaxial step. The increase in bandgap leads to a reduction in the refractive index [9].

The results obtained using IFVD on InAsP/InP QWs have shown to be capable of producing large blueshifts of the band edge while still retaining clearly definable room temperature excitonic characteristics. However, annealing for longer times results in asymmetric PL peaks which have been attributed to different wells undergoing different amounts of intermixing. In all cases, the sample consisting of the narrower wells experienced the greatest blueshift even though these wells were subjected to more strain which appeared to retard the interdiffusion of As and P.

The InAsP has recently become an interesting alternative system for optical devices operating in the 0.9-1.6μm range. In particular, InAsP/InGaAsP compressively strained QW layers emitting at 1.3μm have a larger CB offset (if compared to the InGaAsP/InP system), which will improve the lasing characteristics at high temperature due to the smaller electron

leakage in an optical confinement layer [10]. More recently, tensile strained InGaP layers have been alternated with InAsP in the heterostructure to compensate for the compressive strain of the InAsP layers. This leads to InAsP/InP/InGaP and ternary InAsP/InGaP strain compensated QW lasers [emitting at 1.55 and 1.3 μm] and modulators which exhibit improved characteristics with respect to the more common devices based on the InGaAsP/InP system [11]. For the successful fabrication of these devices, an understanding of the As/P interdiffusion is essential as described in chapter 4.

6.3 Chapter 5

The electronic and structural properties of self-assembled QDs have attracted much attention recently due to interest in both their fundamental properties and device applications. However, most of the research has been focused on InAs/GaAs QDs emitting at wavelengths of 1.3μm. Successful growth of InAs(P) QDs on standard InP substrates at growth temperatures of 600°C has been demonstrated in chapter 5. 3MLs of InAs deposited on InP formed dots which emitted at ~1.5μm, at room temperature, making them suitable for optoelectronic devices operating at this wavelength. The strong luminescence (at ~1.5μm) at room temperature is due to a deep confinement potential of the dots and a larger exciton binding energy due to strong spatial confinement of the excitons in the InAs(P) QDs. Two other peaks observed on the PL spectrum were assigned to a distribution of smaller InAs(P) dots and an InAsP confining layer. The local variation in the strain field round the dots makes the As/P exchange reaction complicated to solve.

Progressing a stage further involves placing the QDs in the active region of a semiconductor device such as a laser or diode. It is an important development since Auger

recombination, which is highly temperature sensitive, represents the major loss mechanism in 1.55μm devices and should be minimised in a QD structure. According to *Arakawa and Sakaki et al.* [12] the QDs in the active region would lead to lower threshold currents in lasers due to the delta-like DOS. The threshold current increases with temperature in QW lasers but remains temperature independent for QD lasers.

In-plane QD lasers have been fabricated by several groups but several problems have arisen. The ground state of the QDs does not lase at room temperature. *Moritz et al.* [13] fabricated an optically pumped QD laser using self-assembled InP dots on InGaP. At low pump powers lasing occurred from the WL, but at higher powers lasing from the QDs eventually dominated. At higher temperatures, non-ground state lasing which required higher threshold currents seemed to take over. It has been difficult to achieve lasing in QD lasers due a low density of dots in the active region. The size distribution of dots leads to inhomogeneously broadened optical spectrum which may deteriorate the laser properties [13] and increase the threshold current. However, by increasing the number of QD layers in the active region and using a vertical cavity geometry (vertical cavity surface emitting laser, VCSEL) to reduce cavity losses, it may be possible to obtain lasing from the ground state at room temperature. *Saito et al.* [14] demonstrated an increase in gain in the active region of QD-VCSELs by stacking 10-period $In_{0.5}Ga_{0.5}As$ dot/$Al_{0.25}Ga_{0.75}As$ layers, resulting in the first demonstration of QD-VCSEL lasing at room temperature by current injection. The matching of the cavity mode with narrow bandwidth light emission from QDs should result in a high performance light source with very low threshold current [14].

The advantages of utilising InAs/InP QDs in the active region of devices are a) the emission wavelengths are extended to the telecommunication range at ~1.55μm and b) the

effective masses of carriers in the strained InAs quantum structures grown on InP are smaller than those grown on GaAs, and their energy levels are further apart [15], improving the thermal stability of the devices. In order to fabricate lasers, operating around 1.55μm, it is necessary to design a waveguiding layer for optical confinement [13]. *Moritz et al.* [13] achieved this by embedding the GaInP layer with the QDs within a 0.7μm thick AlInP cladding layer. *Fafard et al.* [16] investigated InAs QDs grown on an InP substrate instead of GaAs, with AlInGaAs barriers. They demonstrated electrical injection of carriers at room temperature in InAs/AlInGaAs/InP QD laser diode emitting at ~1.5μm. The electroluminescence covered a broad range from 1.3 to 1.6μm, due to the inhomogeneous size broadening of the probed QDs. For this system, the high degree of control demonstrated for the InAs/GaAs system has not yet been achieved.

This work on InP based QDs has been extended in our group as P-I-N diodes incorporating a single InAs/InGaAsP QD layer have been fabricated and have exhibited strong electroluminescence over a wide range of input currents [17]. The composition of these QDs is assumed to be InAsP. *Murray et al* [17] demonstrated that 10 times more light was emitted by a InAs QD layer compared with a QW device consisting of 60 InGaAs wells. With increased power the QW device exhibited saturation effects which were attributable to heating and a loss of efficiency. Similar but less dramatic effects were observed for the QD device.

Many groups have moved on to investigating InP based QDs due to their potential to be used in long wavelength devices (Chapter 5). More detailed studies of the growth kinetics combined with specific growth sequences are now needed to bring the depth of understanding of these dots in line with InAs QDs grown on GaAs.

6.4 References

[1] K. Steubel, V. Harle, F. Scholz, M. Bode, M. Grundmann: J Appl Phys 71, (7), p3300, (1992) [20]

[2] Anan [M21] T. Anan, S. Sugou, K. Nishi, T. Ichihashi: Appl Phys Lett 63, (8), p1047, (1993) [21]

[3] Hergeth [M17] J. Hergeth, D. Grutzmacher, F. Reinhardt, P. Balk: J Crys Growth, 107, p537, (1991) [17]

[4] S. Shim, E. H. Lee; Appl Phys Lett 63, (17), p2387, (1993) [M22]

[5] T.-A. Ma, Z.-M. Li, T. Makino, M. S. Wartak; IEEE J. of Quant. Elect. 31 (1) p29 (1995) [M24]

[6] J. M. Vandenberg, S. N. G. Chu, R. A. Hamm, M. P. Panish, H. Temkin; Appl Phys Lett 63, (8), p1047, (1993) [M21,1]

[7] S. Seki, T. Yamanaka, W. Lui, K. Yokoyama; J Appl Phys 75, (3), p1299, (1994) [M25]

[8] J.H. Marsh; Semicond. Sci. Technol, vol8, p1136 (1993) [A5]

[9] M. Ghisoni, P. J. Stevens, G. Parry, J. S. Roberts; Optical and Quant. Electronics, 23 pS915 (1991) [A25]

[10] C. Lamberti, S. Bordiga, F. Boscherini, S. Mobilio, S. Pascarelli, L. Gastaldi, M. Madella, C. Papuzza, C. Rigo, D. Soldani, C. Ferrai, L. Lazzarini, G. Salviati; J. Appl. Phys. 83 (2) p1058 (1998) [A200]

[11] N. Iwai, T. Mukaihara, H. Shimizu, N. Yamanaka, K. Kumada, A. Kasukawa; Electron. Letts. 34 (9) p 890 (1998)[A83]

[12] Y. Arakawa, H. Sakaki; Appl. Phys. Letts. 40 (11) p939 (1982) [D65]

[13] A. Moritz, R. Wirth, A. Hangleiter, A Kurtenbach, K. Earl; Appl. Phys. Letts. 69 (2) p212 (1996) [D241]

[14] H. Saito, K. Nishi, I. Ogura, S. Sugou, Y. Sugimoto; Appl. Phys. Letts. 69 (21) p3140 (1996) [D240]

[15] S. Fafard, Z. R. Wasilewski, J. MaCaffrey, S. Raymond, S. Charboneau; Appl. Phys. Letts. 68 p991 (1996) [D242,5]

[16] S. Fafard, Z. R. Wasilewski, C. Ni, Allen, D. Picard, P. G. Piva, J. P. McCaffrey; Superlatt and Microstruc. 25 (1/2) p87 (1998) [D243]

[17] R. Murray, C. Bryan, C. Button, D. Spikes, G. Hill; MRS Proceedings, San Francisco, Spring Meeting, 1999 (to be published)

Appendix A

Transfer Matrix Method

In this appendix the one dimensional transfer matrix method used to calculate the confined levels in an arbitary shaped quantum well, otherwise known as the 'Shooting method' is described.

Description of Particles moving in a box

In a one dimensional potential, such as the potential in the growth direction, the carrier wavefunction (supressing the bloch state part) is described by the envelope wavefunction ψ and is determined by the Schrodinger Wave equation;

$$\nabla^2\psi + \frac{2m^*}{\hbar^2}(E-V)\psi = 0 \qquad [A1]$$

where m* is the effective mass of the carrier, V is the potential experienced by the carrier and E is the energy of the carrier.

In one dimension the solutions are;

$$\psi(x) = Ae^{ikx} + Be^{-ikx} \qquad \text{for E>V} \qquad [A2]$$

where $k = \sqrt{\frac{2m^*}{\hbar^2}(E-V)}$

$$\psi(x) = Ae^{Kx} + Be^{-Kx} \qquad \text{for E<V} \qquad [A3]$$

where $K = \sqrt{\frac{2m^*}{\hbar^2}(V-E)}$

now suppose the carrier is in a region where E>V (equation A2) and consider the carrier traveling in the region and reflecting at the boundaries. (This analysis is identical to that of light moving through regions of different refractive index [1]).

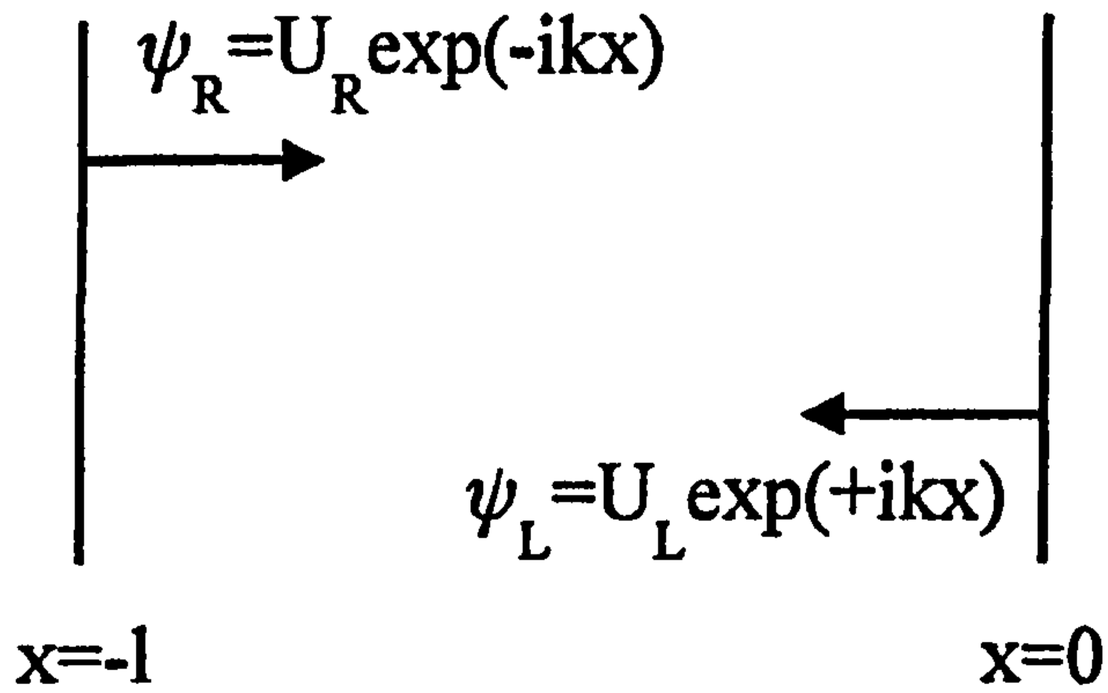

Figure A-1 : *Particle waves travelling in a region x=-l to x=0*

For semiconductors ψ and 1/m*.dψ/dx must be continuous especially at the boundaries [2] and;

Waves to the right

$$\psi_R = U_R e^{-ikx} \quad [A3]$$

$$\frac{1}{m^*}\frac{\partial \psi_R}{\partial x} = -\frac{ik}{m^*} U_R e^{-ikx} \quad [A4]$$

at x=0;

$$\psi(0) = U_R + U_L \quad [A7]$$

$$\frac{1}{m^*}\frac{\partial \psi}{\partial x}\bigg|_{x=0} = \frac{ik}{m^*}(-U_R + U_L) \quad [A8]$$

Waves to the left

$$\psi_L = U_L e^{+ikx} \quad [A5]$$

$$\frac{1}{m^*}\frac{\partial \psi_L}{\partial x} = \frac{ik}{m^*} U_L e^{+ikx} \quad [A6]$$

at x=-l;

$$\psi(-l) = U_R e^{ikl} + U_L e^{-ikl} \quad [A9]$$

$$\frac{1}{m^*}\frac{\partial \psi}{\partial x}\bigg|_{x=-l} = \frac{ik}{m^*}(-U_R e^{ikl} + U_L e^{-ikl}) \quad [A10]$$

$$\text{so } U_R + U_L = \psi(0) \text{ and } U_L + U_R = \frac{m^*}{ik}\left(\frac{1}{m^*}\frac{\partial \psi}{\partial x}\bigg|_{x=0}\right) \quad [A11\text{-}12]$$

hence adding and substracting A11 and A12;

$$U_L = \tfrac{1}{2}\psi(0) + \tfrac{1}{2}\frac{m^*}{ik}\left(\frac{1}{m^*}\frac{\partial\psi}{\partial x}\bigg|_{x=0}\right) \qquad \text{[A13]}$$

and

$$U_R = \tfrac{1}{2}\psi(0) - \tfrac{1}{2}\frac{m^*}{ik}\left(\frac{1}{m^*}\frac{\partial\psi}{\partial x}\bigg|_{x=0}\right) \qquad \text{[A14]}$$

substituting A13 & A14 into A9:

$$\begin{aligned}\psi(-l) &= \tfrac{1}{2}\psi(0)\left[e^{-ikl} + e^{ikl}\right] + \tfrac{1}{2}\frac{m^*}{ik}\left(\frac{1}{m^*}\frac{\partial\psi}{\partial x}\bigg|_{x=0}\right)\left[e^{-ikl} - e^{ikl}\right] \\ &= \psi(0)\cos kl + \frac{m^*}{k}\left(\frac{1}{m^*}\frac{\partial\psi}{\partial x}\bigg|_{x=0}\right)\sin kl\end{aligned} \qquad \text{[A15]}$$

and substituting A13 & A14 into A10;

$$\begin{aligned}\frac{1}{m^*}\frac{\partial\psi}{\partial x}\bigg|_{x=-l} &= \tfrac{1}{2}\psi(0)\left[e^{-ikl} - e^{ikl}\right] + \tfrac{1}{2}\frac{m^*}{ik}\left(\frac{1}{m^*}\frac{\partial\psi}{\partial x}\bigg|_{x=0}\right)\left[e^{-ikl} + e^{ikl}\right] \\ &= \frac{-k}{m^*}\psi(0)\sin kl + \left(\frac{1}{m^*}\frac{\partial\psi}{\partial x}\bigg|_{x=0}\right)\cos kl\end{aligned} \qquad \text{[A16]}$$

therefore the wavefunctions and derivatives at x=-l can be related to those at x=0 by the matrix equation;

$$\begin{pmatrix}\psi(-l) \\ \frac{1}{m^*}\frac{\partial\psi}{\partial x}\big|_{x=-l}\end{pmatrix} = \begin{pmatrix}\cos kl & {}^{m^*}\!/_{k}\sin kl \\ -{}^{k}\!/_{m^*}\sin kl & \cos kl\end{pmatrix}\begin{pmatrix}\psi(0) \\ \frac{1}{m^*}\frac{\partial\psi}{\partial x}\big|_{x=0}\end{pmatrix} \qquad \text{[A17]}$$

Now consider a three layered structure;

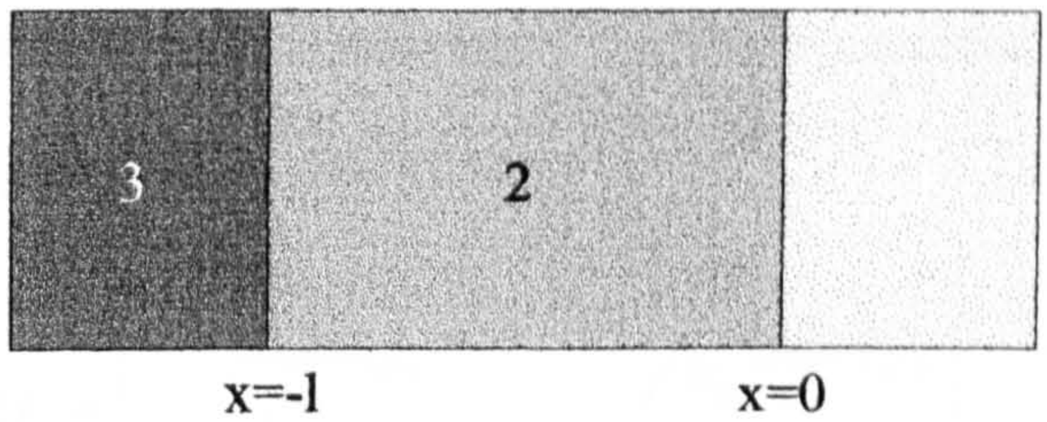

Figure A-2 : *A three layered structure*

Equation A-17 described how to find ψ(-l) given ψ(0), but since ψ and 1/m*.dψ/dx must be continuous across a boundary ψ and 1/m*.dψ/dx are also known in regions 1 & 3, even if m* in these regions is different.

For an arbitary number of layers;

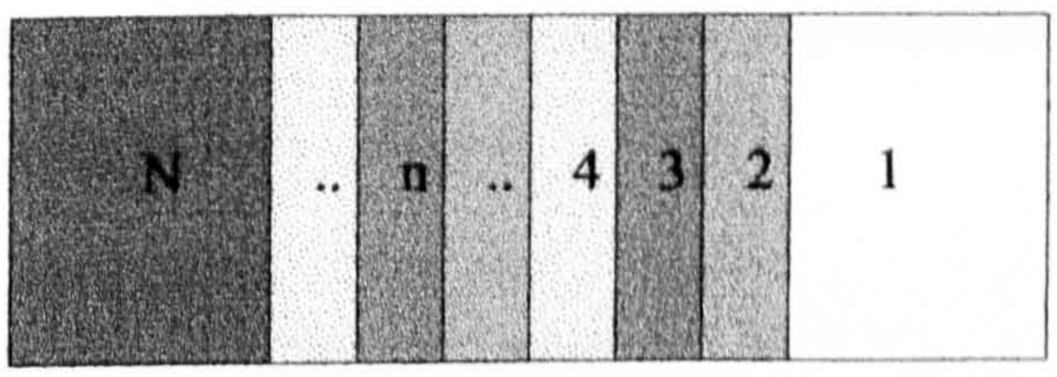

Figure A-3 : *A structure with N layers*

$$\begin{pmatrix} \psi_N \\ \frac{1}{m_N^*}\frac{\partial\psi}{\partial x}\Big|_N \end{pmatrix} = M \begin{pmatrix} \psi_1 \\ \frac{1}{m_1^*}\frac{\partial\psi}{\partial x}\Big|_1 \end{pmatrix} \qquad [A18]$$

where the matrix M is the combination of all the matrix elements of the layers $M_{N-1}...M_n...M_4M_3M_2$, and the individual matrix elements have values of k, l, and m* applicable to the particular layer;

(for E>V)
$$M_n = \begin{pmatrix} \cos k_n l_n & {m_n^*}/{k_n} \sin k_n l_n \\ -{k_n}/{m_n^*} \sin k_n l_n & \cos k_n l_n \end{pmatrix} \qquad [A19]$$

However, only the case where E>V and $\psi \sim e^{ikx}$ has been considered so far. If E<V then $\psi \sim e^{kx}$ and using a similar analysis;

(for E<V)
$$M_n = \begin{pmatrix} \cosh k_n l_n & {m_n^*}/{k_n} \sinh k_n l_n \\ -{k_n}/{m_n} * \sinh k_n l_n & \cosh k_n l_n \end{pmatrix} \qquad [A20]$$

The 'Shooting' Method

To find the confined states in a semiconductor structure consider reflection and transmission of carriers of a particular energy (and wavevector) through the desired structure. Only the amplitude (A) of the waves need to be taken into account to obtain the reflection (r) and transmission (t) coefficients.

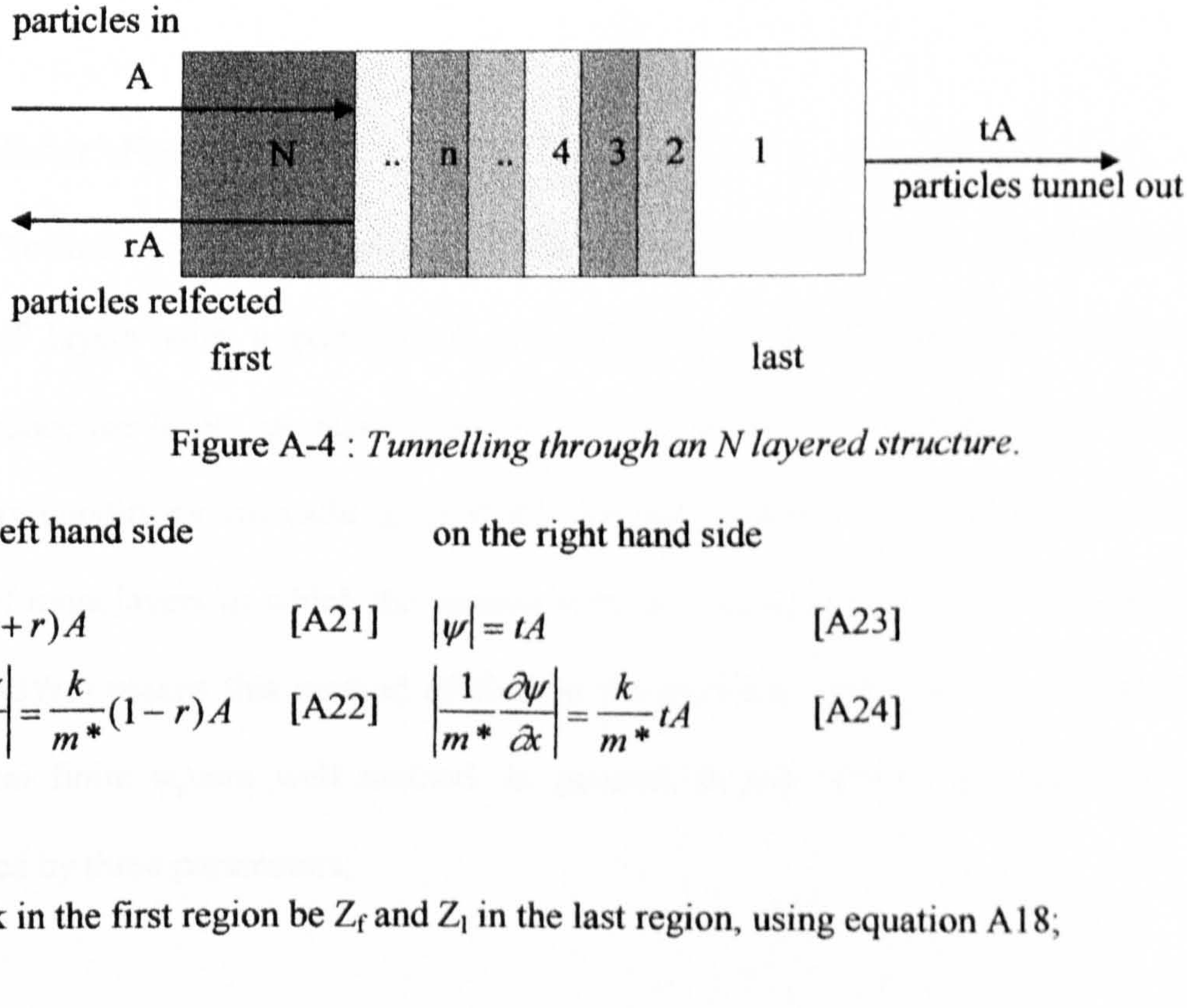

Figure A-4 : *Tunnelling through an N layered structure.*

on the left hand side

$$|\psi| = (1+r)A \qquad [A21]$$

$$\left|\frac{1}{m^*}\frac{\partial\psi}{\partial x}\right| = \frac{k}{m^*}(1-r)A \qquad [A22]$$

on the right hand side

$$|\psi| = tA \qquad [A23]$$

$$\left|\frac{1}{m^*}\frac{\partial\psi}{\partial x}\right| = \frac{k}{m^*}tA \qquad [A24]$$

let m*/k in the first region be Z_f and Z_l in the last region, using equation A18;

$$\begin{pmatrix} (1+r)A \\ 1/Z_f\,(1-r)A \end{pmatrix} = M\begin{pmatrix} tA \\ 1/Z_i\,tA \end{pmatrix} = \begin{pmatrix} A & B \\ C & D \end{pmatrix}\begin{pmatrix} tA \\ 1/Z_i\,tA \end{pmatrix} \qquad [A25]$$

hence $(1+r)=t(A+B/Z_i)$ [A26]

and $(1-r)=Z_f(C+D/Z_i)$ [A27]

implying that $t=2/(A+B/Z_i+Z_fC+Z_fD/Z_i)$ [A28]

Therefore the probability of a carrier with a particular energy (and wavevector k) being transmitted through the structure is T where;

$$T=t^2=4/(A+B/Z_i+Z_fC+Z_fD/Z_i)^2 \qquad [A29]$$

Consequently the energies for which there is a maximum in the transmission coefficient correspond to a maximum tunneling current. Hence the carriers must be resonant with a tunelling (i.e. confined) state.

The 'Shoot' Program

To find the confined states in an arbitary potential well shape, consider the QW as a series of layers with a potential V and effective mass m* associated with each. For convenience the layers are taken to be the same thickness as a monolayer (~3Å). Since the boundary conditions are valid for a slowly varying potential, decomposing the QW into a series of monolayers in which the composition only changes slightly between layers (as for graded QWs) makes this method of finding the confined states just as valid as the semi-analytical finite square well method. In general, in the 'shoot' program, each layer is described by three parameters;

Length of layer: L

Potential : V

effective mass : m*

(The lowest point in the potential well is chosen to have V=0, so the barriers always have positive potential. In the valence band the same applies, so it is not necessary to use negative effective masses).

These parameter define $k = \sqrt{2m^*/\hbar^2 (E - V)}$, Z=m*/k and the transfer matrix M for the layer;

$$M = \begin{pmatrix} \cos kl & Z \sin kl \\ -\sin kl / Z & \cos kl \end{pmatrix}$$ if E>V (or sinh and cosh elements if E<V)

To evaluate the quantum well structure , the transfer matrices of all the layers need to be combined, remembering to begin with the last layer (to be grown) and end with the first. Once the quantum well matrices have been combined, the transmission coefficient for a range of energies (0 to barrier height) can be evaluated according to equation B29, using the coefficients Z_f, Z_l for the very first and last layers in the whole structure, which are usually the barrier layers. The maxima of the transmission coefficient correspond the energies of the confined states.

References

[1] Hecht 'Optics' - Addison-Wesley Publishing company (1987)

[2] M. G. Burt; J. Phys. Cond. Matter 4 6651 (1992)

Appendix B

Error Function Solution to the Interdiffusion Problem

The error function solution for the interdiffusion of the well/barrier used in chapter 4 is derived. The derivation assumes that the diffusion process is Fickain i.e. the diffusion coefficient is independent of time and concentration, and that the process is isotropic (the diffusion coefficient of As and P is identical). Using this assumption, the diffusion can be regarded in terms of As or P distribution in the InAsP/InP well/barrier system.

Consider a bar of finite length containing a uniform concentration, C_0, of As atoms which on anneal time, t, diffuse into the barriers on either side, which at t=0 have a zero As concentration. The solution of such a problem is outlined in Crank [1] and Tuck [2].

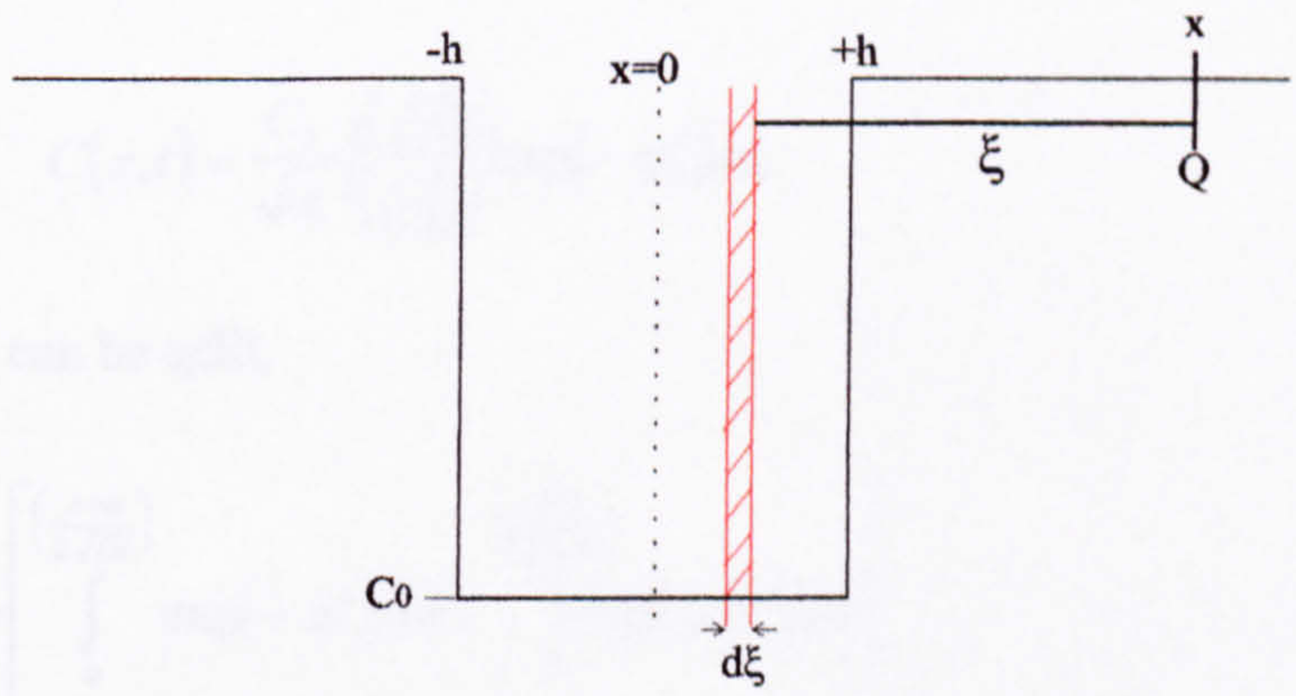

Figure B-1 *Schematic diagram of problem solved in the text*

The finite bar of As contained within the region $-h\langle x\langle+h$, is illustrated in Figure B-1. The solution considers the bar to be composed of a number of independent line sources of width $d\xi$, and then combines the corresponding infinite number of elementary solutions. Each elemental source has a concentration strength $C_0.\ d\xi$. After time, t, the concentration

due to an individual line source at a point Q, a distance ξ, from the source is thus given by the standard Fickian solution for a plane source,

$$\frac{C_0}{2\sqrt{\pi Dt}}\exp\left(\frac{-\xi^2}{4Dt}\right)d\xi \qquad \text{[B-1]}$$

The total concentration at Q will be that due to the sum of all the line source solutions i.e. between x-h and x+h. Thus the concentration at position x at time t, C(x,t) can be written as the integral of Eq. [7-1] between the aforementioned limits,

$$C(x,t) = \int_{(x-h)}^{(x+h)} \frac{C_0}{2\sqrt{\pi Dt}}\exp\left(-\frac{\xi^2}{4Dt}\right)d\xi \qquad \text{[B-2]}$$

if $\eta = \xi / 2\sqrt{Dt}$ is substituted this then yields,

$$C(x,t) = \frac{C_0}{\sqrt{\pi}}\int_{\left(\frac{x-h}{2\sqrt{Dt}}\right)}^{\left(\frac{x+h}{2\sqrt{Dt}}\right)}\exp(-\eta 2)d\eta \qquad \text{[B-3]}$$

The integral can be split,

$$C(x,t) = \frac{C_0}{\sqrt{\pi}}\left[\int_0^{\left(\frac{x+h}{2\sqrt{Dt}}\right)}\exp(-\eta^2)d\eta - \int_0^{\left(\frac{x-h}{2\sqrt{Dt}}\right)}\exp(-\eta^2)d\eta\right] \qquad \text{[B-4]}$$

The mathematical function known as the error function, denoted by erf(x) which has the following properties is now used,

$$erf(x) = \frac{2}{\sqrt{\pi}}\int_0^x \exp(-\eta^2)d\eta \qquad \text{[B-5]}$$

$$erf(-x) = -erf(x); \quad erf(0) = 0; \quad erf(\infty) = 1$$

It thus follows that the solution of above is:-

$$C(x,t) = \frac{C_0}{2} erf\left(\frac{x+h}{2\sqrt{Dt}}\right) - \frac{C_0}{2} erf\left(\frac{x-h}{2\sqrt{Dt}}\right) \qquad \text{[B-6]}$$

This form can also be arrived at by looking at the diffusion of P from the barrier. The solution for the P distribution, $C_P(x,t)$ will be given by,

$$C_P(x,t) = C_{P,barrier} - Eq\,7.6 \qquad \text{[B-7]}$$

where $C_{P,barrier}$ is the concentration in the barrier (this is taken as the base level). The reason that in Eq B-6 C_0, the As well concentration, is still valid in this case is because this also defines the difference in P concentrations between the well and barrier.

Writing this out in full then gives,

$$C(x,t) = x_0 - \left[\frac{C_0}{2} erf\left(\frac{x+{}^{l_w}\!/_{2}}{2\sqrt{Dt}}\right) + \frac{C_0}{2} erf\left(\frac{x-{}^{l_w}\!/_{2}}{2\sqrt{Dt}}\right) \right]$$

which finally yields Eq 4.1 as shown in Chapter 4,

$$C(x,t) = x_0 + \left[\frac{C_0}{2} erf\left(\frac{x-{}^{l_w}\!/_{2}}{2\sqrt{Dt}}\right) - \frac{C_0}{2} erf\left(\frac{x+{}^{l_w}\!/_{2}}{2\sqrt{Dt}}\right) \right]$$

when solved between $-{}^{1}\!/_{2}(L_w + L_B) \le x \le {}^{1}\!/_{2}(L_w + L_B)$, where L_B is the barrier width, this produces the P profile of the intermixed well/barrier system which is subsequently used to calculate the confined energy levels.

7.1.1 References

[1] J. Crank: 'The Mathematics of Diffusion' [Oxford]

[2] B. Tuck: 'Introduction to diffusion in semiconductors' [Peter Peregrinus Ltd. 1974]

List of publications

"1.55μm emission from InAs/InP self-assembled quantum dots"

R. *Murray, C. Bryan, C. Button, D. Spikes, G. Hill*

MRS Proceedings, San Francisco, Spring Meeting, 1999 (to be published)

"Influence of segregation in quantum well structures"

R. Murray, C. Bryan, H. Yu, S. Lycett

J. Mater. Sci. - Mater. Electron. 7 341 (1996)

Acknowledgements

I have so many people to thank and express my appreciation so I think a good place to start is with my supervisor, Ray Murray, who has been a great help, very patient and a fountain of knowledge over the years professionally and personally. Gareth Parry, Tim Jones and Bruce Joyce who were always very approachable, helpful and kind.

The members of the optical characterisation lab. Past members - Andrew Dewdney and Sam Lycett for very useful discussions and experimental expertise. Hai Ping again for experimental help. Present members - Surama (for being so helpful), Dave and Phil for all their help and also creating such a good working environment and endless cups of tea and chocolates.

Chris Button for the growth of the samples and Geoff Hill (both from Sheffield University) for the processing of the samples. X-ray experiments and analysis - Linda Hart, Juan Fernandez and Jean Micheal Hartmann.

Other people I have come into contact with who provided knowledge and laughter: Jim Neave, Jing, Eng Soon, Pippa Steans, Nick Woods, Rhys, Omar Naji, Joe Eggeling, Chris Mulcahy, Gavin Bell. Office friends who have put up with me so well and deserve a big thank you: Mark Ashwin, Rhian P, Christine Roberts, Steve Cussell, Paul Stavrinou.

Fourth floor friends and colleagues- Garry Rumbles, Jo Clarke, Kathryn Atherton, Gary Keogh, Andrew De Mello, Laura Magnani. Hockey club friends from Imperial College and Chiswick Ladies (especially Mel De Souza) and 'outside' friends who deserve a special mention - Ben James, Andrew Barber, Graham Brown, Chris Pease and Martin Reed.

And then some very special friends who I hope to always be in contact with - Anna Lees, Andrew Avery, Darren Holmes Alex Aquino, James Belk and more recently, Rob Van Dalen (endless laughter !) and Mark Whitehead.

Special and best friends - Jane Key and Phil Siverns. These two have stood by me every inch of the way and they mean more to me then they will ever know.

Mum, Dad, Claire and Grandma for their unfailing support and love.

This work was funded by an EPSRC studentship.